

Control of the optical interface of color centers in diamond

Brevoord, J.M.

DOI

[10.4233/uuid:de64a49e-9cfb-4865-a5ce-f506cafd4460](https://doi.org/10.4233/uuid:de64a49e-9cfb-4865-a5ce-f506cafd4460)

Publication date

2025

Document Version

Final published version

Citation (APA)

Brevoord, J. M. (2025). *Control of the optical interface of color centers in diamond*. [Dissertation (TU Delft), Delft University of Technology]. <https://doi.org/10.4233/uuid:de64a49e-9cfb-4865-a5ce-f506cafd4460>

Important note

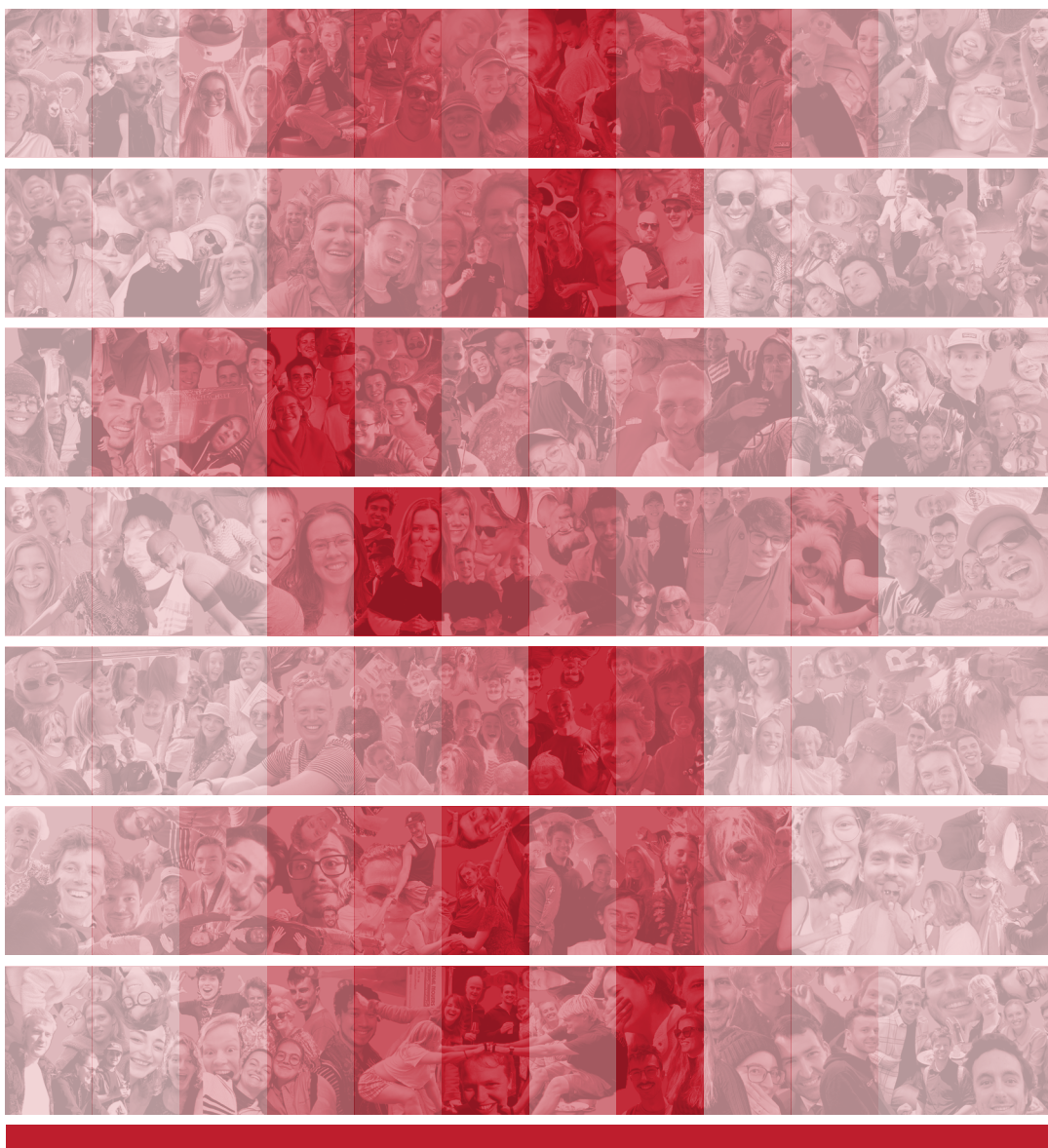
To cite this publication, please use the final published version (if applicable).
Please check the document version above.

Copyright

Other than for strictly personal use, it is not permitted to download, forward or distribute the text or part of it, without the consent of the author(s) and/or copyright holder(s), unless the work is under an open content license such as Creative Commons.

Takedown policy

Please contact us and provide details if you believe this document breaches copyrights.
We will remove access to the work immediately and investigate your claim.



Julia Maria Brevoord

Control of the optical interface of color centers in diamond



CONTROL OF THE OPTICAL INTERFACE OF COLOR CENTERS IN DIAMOND

Dissertation

for the purpose of obtaining the degree of doctor
at Delft University of Technology,
by the authority of the Rector Magnificus, Prof. dr. ir. T.H.J.J. van der Hagen,
Chair of the Board for Doctorates,
to be defended publicly on
Thursday, 11th December 2025 at 12:30 o'clock

by

Julia Maria BREVOORD

Master of Science in Applied Physics,
Master of Science in Applied Mathematics,
University of Twente, Enschede, The Netherlands,
born in IJsselham, The Netherlands.

This dissertation has been approved by the promotor:
Prof. dr. ir. R. Hanson

Composition of the doctoral committee:

Rector Magnificus	Chairperson
Prof. dr. ir. R. Hanson	Delft University of Technology, Promotor
Dr. ir. T. H. Taminiau	Delft University of Technology, Copromotor

Independent members:

Prof. dr. ir. L. M. K. Vandersypen	Delft University of Technology
Prof. dr. R. Riedinger	University of Hamburg, Germany
Prof. dr. ir. A. Brinkman	University of Twente
Dr. M. Blaauboer	Delft University of Technology
Prof. dr. ir. T. van der Sar	Delft University of Technology, reserve member



Copyright	© 2025 by Julia Maria Brevoord
Cover design	Studio Angelineau (Delft)
Printed	Gildeprint (Enschede)
ISBN	978-94-6518-173-8

An electronic version of this dissertation is available at
<http://repository.tudelft.nl/>.

For my grandmother
Simply the best

CONTENTS

Summary	ix
Samenvatting	xi
1 Introduction	1
1.1 Introducing quantum	2
1.2 Thesis outline	3
Bibliography	5
2 Methods for SnV centers in diamond as a quantum network node	7
2.1 Remote photon-mediated entanglement generation	8
2.1.1 Photon-mediated entanglement protocols.	8
2.1.2 Spin-photon interfaces	9
2.1.3 Encoding of the quantum information.	10
2.2 State of the Art: the Nitrogen-Vacancy center	11
2.3 Group-IV vacancy centers.	12
2.3.1 Electronic level structure.	13
2.3.2 Electron spin qubit.	14
2.3.3 Coherence of group-IV vacancy centers	15
2.3.4 Efficiency of the optical spin-photon interface.	17
2.4 The Tin-Vacancy center as a quantum node	19
2.4.1 SnV center creation	20
2.4.2 SnV center optical challenges	21
2.4.3 Inhomogeneous distribution.	22
2.4.4 Optical stability	23
2.4.5 Charge state and resonance frequency preparation	26
2.5 Tin-Vacancy center node in a metropolitan quantum network	28
2.5.1 Quantum Frequency Conversion	29
2.5.2 Data availability statement.	33
Bibliography	34
3 Laser-cut patterned, micrometer-thin diamond membranes with coherent color centers for open microcavities	41
3.1 Introduction	42
3.2 Fabrication of diamond microdevices.	43
3.2.1 Sample preparation	44
3.2.2 Patterning	44
3.2.3 Color center creation.	45
3.2.4 Device release etch.	46
3.2.5 Bonding	46

3.2.6	Fabrication results	47
3.3	Scanning cavity microscopy.	47
3.3.1	Cavity loss model	48
3.3.2	Cavity finesse measurements	49
3.3.3	Frequency splitting of the polarization cavity modes.	52
3.4	Optically coherent color centers	54
3.5	Conclusion	57
3.6	Acknowledgement	57
3.6.1	Author contributions.	57
3.6.2	Data availability statement.	58
3.7	Appendix	58
3.7.1	Outline of fabrication	58
3.7.2	Bonding of microdevices to cavity mirror	60
3.7.3	Experimental setup: room temperature microcavity	60
3.7.4	Experimental methods: finesse measurements and cavity fiber properties	61
3.7.5	Experimental methods: hybrid cavity modes	63
3.7.6	Experimental methods: polarization splitting	63
3.7.7	Experimental methods: PLE scans	63
3.7.8	Measurements on the laser-cut microdevice	65
3.8	Additional data	66
3.8.1	Creation of NV centers.	66
3.8.2	Fabrication of EBL microdevices	67
3.8.3	Fabrication of laser-cut microdevices	67
3.8.4	SnV centers in laser-cut microdevices	67
3.8.5	NV centers in EBL microdevices	69
3.8.6	NV centers in laser-cut microdevices.	71
	Bibliography	73
4	Heralded initialization of charge state and optical transition frequency of di- amond tin vacancy centers	79
4.1	Introduction	80
4.2	Experimental setup	80
4.3	Dynamics of charge state and resonance frequency.	81
4.4	Probe pulses for charge-state and resonance-condition detection	82
4.5	Optical Rabi driving.	83
4.6	Real-time heralding of charge state and optical-transition frequency	85
4.7	Optical Ramsey experiment using real-time heralding	88
4.8	Conclusion and outlook.	89
4.9	Acknowledgement	89
4.9.1	Author contributions.	90
4.9.2	Data availability statement.	90

4.10	Supplementary material	90
4.10.1	Fabrication method	90
4.10.2	Experimental set-up	90
4.10.3	Correlations between the heralding signal and the readout signal	91
4.10.4	Initialization fidelity	92
4.10.5	Optical pulse characterization and optimization.	92
4.10.6	CRC optical Ramsey interferometry measurements	93
4.10.7	CRC linescans	93
	Bibliography	94
5	Large-range tuning and stabilization of the optical transition of diamond tin-vacancy centers by <i>in situ</i> strain control	97
5.1	Introduction	98
5.1.1	Inhomogeneous distribution.	99
5.2	SnV center strain theory.	100
5.3	Diamond waveguide device for strain tuning	100
5.4	Strain simulation of the diamond device	101
5.5	Tuning range via local strain engineering	103
5.6	Optical resonant frequency stability	103
5.7	Conclusion and outlook.	105
5.8	Acknowledgement	105
5.8.1	Author contributions.	105
5.8.2	Data availability statement.	106
5.9	Supplementary material	106
5.9.1	Device fabrication	106
5.9.2	Experimental set-up	107
5.9.3	Voltage pulse calibration.	108
5.9.4	Frequency shift as a function of voltage	109
5.9.5	FEM simulations.	109
	Bibliography	110
6	Quantum Frequency Conversion of single photons from a Tin-Vacancy center in diamond	115
6.1	Introduction	116
6.2	Methods & Results	117
6.2.1	Quantum Frequency Converter	117
6.2.2	Conversion efficiency and bandwidth	117
6.2.3	QFC noise characterization	119
6.2.4	Conversion of single SnV ⁻ center photons	120
6.3	Conclusion	123
6.4	Acknowledgement	124
6.4.1	Data availability statement.	124
	Bibliography	125

7	Conclusions and outlook	129
7.1	Summary	130
7.2	Scaling quantum links	131
7.2.1	Improving the memory	131
7.2.2	Improving the entanglement rate	132
7.3	SnV-based photonics chip	133
7.3.1	Deterministic placement of SnV centers	133
7.3.2	Diamond nanophotonics fabrication	134
7.3.3	Hybrid integration	134
7.3.4	Photonic packaging	135
7.4	Other platforms	136
7.5	Going the distance	136
7.6	The quantum eco system	137
7.7	Epilogue	137
	Bibliography	138
	Acknowledgements	143
	List of Publications	153
	Curriculum Vitae	155

SUMMARY

Quantum networks offer capabilities beyond the reach of classical systems, enabling intrinsically secure communication, enhanced sensing, and the sharing of quantum states for distributed quantum computation. Optically active spins in solids, where stationary qubits are entangled with flying photonic qubits, enable the creation of entangled links for transmitting quantum information over large distances. However, realizing such links at high rates and with high fidelity remains a central challenge, while both are essential for scaling to practical quantum applications. Although the nitrogen-vacancy (NV) center in diamond has been extensively studied for such networks, its limited coherent photon emission rate constrains entanglement generation rates and thus network scalability. The tin-vacancy (SnV) center in diamond offers significant advantages: it intrinsically emits a higher fraction of coherent photons, and its inversion symmetry renders it first-order insensitive to charge noise, enabling integration into nanophotonic structures that can further enhance its coherent emission. This makes the SnV center a promising platform for building large-scale quantum networks.

This thesis addresses four major challenges in realizing scalable quantum networks with SnV centers. First, to further enhance the coherent photon emission, a novel laser-cutting technique is developed to realize micrometer-thin diamond devices, which are laser-cut into arbitrary lateral shapes. These devices are bonded to cavity mirrors and placed inside a cryogenic, fiber-based Fabry-Pérot microcavity, which can increase the coherent emission and thus the entanglement rate. The optical properties of the embedded color centers remained preserved during the fabrication.

In the second project, high-fidelity initialization of the negatively charged state and optical transition frequency is achieved using a real-time logic decision scheme based on photon counting during resonant excitation, enabling heralded initialization and improved optical coherence verified by optical Ramsey interferometry, as well as tuning of the optical frequency over the inhomogeneous linewidth of an individual SnV center.

Third, local strain engineering of suspended diamond waveguides allows shifting of optical resonances of SnV centers over a significant portion of the inhomogeneous distribution, while real-time feedback on the applied strain stabilizes the resonance frequency and mitigates spectral wandering over time. This allows for the generation of indistinguishable photons from different SnV centers.

Lastly, a highly efficient, low-noise quantum frequency converter is implemented to shift single photons from the visible 619 nm to 1480 nm in the telecom S-band, enabling low-loss transmission of photons entangled with the spin of the SnV center over long distances. Together, these advances move the SnV center closer to practical deployment in large-scale quantum networks.

SAMENVATTING

Kwantumnetwerken bieden mogelijkheden die buiten het bereik van klassieke systemen liggen, zoals intrinsiek veilige communicatie, verbeterde metrologie en het delen van kwantumtoestanden voor gedistribueerde kwantumberekeningen. Optisch actieve spins in vaste stof, waarbij stationaire qubits verstrengeld zijn met vliegende fotonische qubits, maken verstrengelde verbindingen mogelijk om kwantuminformatie over grote afstanden over te brengen. Het realiseren van zulke verbindingen met hoge snelheid en betrouwbaarheid blijft echter een centrale uitdaging en is cruciaal voor opschaling naar praktische kwantumtoepassingen. Er is veel onderzoek naar het stikstof-gatcentrum (NV-centrum) in diamant hiervoor gedaan, maar de lage emissiesnelheid van coherente fotonen beperkt de verstrengelingsnelheid en dus de schaalbaarheid van het netwerk. Het tin-gatcentrum (SnV-centrum) in diamant biedt voordelen: het genereert een groter deel coherente fotonen en is dankzij zijn inversiesymmetrie in eerste orde ongevoelig voor elektronische ruis. Daardoor kan het geïntegreerd worden in nanofotonische structuren, die de coherente emissie verder kunnen versterken. Het SnV-centrum vormt daarmee een veelbelovend platform voor grootschalige kwantumnetwerken.

Dit proefschrift behandelt vier uitdagingen in de realisatie van schaalbare kwantumnetwerken met SnV-centra. Allereerst is een nieuwe lasertechniek ontwikkeld om micrometer dunne diamantapparaatjes in willekeurige vormen uit te snijden. Deze dunne diamantapparaatjes worden gebonden aan een caviteitsspiegel en geplaatst in een cryogene, fiber gebaseerde Fabry-Pérot-microcaviteit, die de coherente emissie en daarmee de verstrengelingsnelheid verhoogt. De optische eigenschappen van de kleurcentra blijven behouden tijdens deze nieuwe fabricage techniek.

In het tweede project wordt een methode geïntroduceerd om SnV-centra betrouwbaar te initialiseren in zowel hun negatieve ladingsstaat als hun optische frequentie. Dit gebeurt met een realtime beslissingsprotocol gebaseerd op fotontelling tijdens resonante excitatie, wat leidt tot verbeterde optische coherentie, bevestigd met Ramsey-interferometrie, evenals het afstemmen van de optische frequentie binnen de inhomogene lijnbreedte van een individueel SnV-centrum.

Een derde aanpak richt zich op plaatselijke vervorming van vrijhangende diamanten golfgeleiders. Hiermee kunnen de optische resonanties van SnV-centra verschoven worden over een groot deel van de inhomogene verdeling. Realtime terugkoppeling stabiliseert de resonantiefrequentie en vermindert spectrale drift over tijd, wat de generatie van identieke fotonen uit verschillende SnV-centra mogelijk maakt.

Tot slot is een efficiënte, ruisarme kwantumfrequentieconverter (KFC) geïmplementeerd om enkele fotonen spectraal te verschuiven van het zichtbare 619 nm naar 1480 nm in de telecom S-band. Hiermee is de kans dat een foton, verstrengeld met de spin van een SnV-center, verloren gaat over een lange afstand aanzienlijk verminderd. Gezamenlijk brengen deze vooruitgangen van het SnV-centrum ons dichterbij praktische toepassingen in grootschalige kwantumnetwerken.

1

INTRODUCTION

*I'm sending my condolence
I'm sending my condolence to fear
I'm sending my condolence
I'm sending my condolence to insecurities
- Benjamin Clementine*

1.1. INTRODUCING QUANTUM

The origins of quantum mechanics lie in the early 20th century, when classical physics failed to explain the experimental results. These anomalies led to the idea that energy must be quantized, meaning that energy is discrete. A single energy packet is called a *quantum*. As the theory matured through the work of pioneers like Planck, Einstein, Bohr, Heisenberg and Schrödinger, it introduced a profoundly different view of nature. A world where particles can exist in *superposition*, occupying multiple states simultaneously rather than being in a single definite state, and where distant particles can exhibit *entanglement*, displaying correlations that defy classical explanation. Entangled particles cannot be described independently; instead, their joint state is inseparable, such that measuring one particle instantaneously determines the state of the other, regardless of the distance between them¹.

The birth of quantum mechanics concepts provided the theoretical tools to understand and predict the behavior of matter and light at atomic and subatomic scales. This understanding sparked the emergence of the first generation of quantum-based technologies. The discovery of population inversion led to the invention of the laser², and insights into the electronic band structure of solid-state materials paved the way for the creation of the transistor³. While these technologies rely fundamentally on quantum principles, they do not exploit quantum superposition or entanglement directly. These inventions are known as the Quantum 1.0 technology.

In the second half of the 20th century, scientists realized the control of individual atoms and photons, allowing them to explore the quantum principles of superposition and entanglement. The idea arose to use two-level quantum systems to store information. The ability to isolate and control individual quantum systems opened the door to combining quantum physics with information theory, laying the foundation for the field of quantum information science⁴. This led to the emergence of Quantum 2.0 technologies, which actively exploit superposition and entanglement as operational resources. The field now encompasses four major pillars: **quantum computing**, which promises exponential speed-ups for specific tasks; **quantum sensing**, which leverages quantum properties to achieve more measurement precision than classical sensors; **quantum simulation**, aimed at understanding complex quantum systems by building controllable analogues; and **quantum communication**, which enables intrinsic secure transmission of information using quantum entanglement and no-cloning principles⁵.

In this thesis, we focus on developing technology to realize a large-scale quantum network. These networks have applications in both the quantum communication and quantum computation pillars. Such a network consists of quantum nodes separated by large distances, interconnected through entangled links^{6,7}. Quantum information can be transmitted over these links by leveraging entanglement. At each node, there are *stationary qubits* that process and store quantum information, while *flying qubits* can be used to send quantum states over large distances. Photons are ideal flying qubits as they preserve the quantum information even at room temperature and travel with low

loss through optical channels. The challenge is to efficiently couple the quantum information from the stationary qubit onto the flying qubit. Therefore, a good interaction between your stationary qubit and your photon is required. There are different systems that can realize such stationary qubits, for example, trapped ions, cold atoms, quantum dots, rare-earth ions, and color centers⁸.

In this thesis, we use color centers in diamond, a material notable for its wide band gap of approximately 5.5 eV. This large band gap ensures that the electronic levels of defects are well defined and spectrally isolated, enabling optical transitions over a broad wavelength range. Furthermore, the diamond crystalline structure can result in symmetry of the electronic structure of the defect, resulting in more stable quantum systems. The nitrogen-vacancy (NV) center in diamond was the first solid-state defect in diamond that was employed to demonstrate quantum applications⁹. The NV center consists of a nitrogen atom substituting for one of two adjacent missing carbon atoms in the diamond lattice. It has enabled key proof-of-principle experiments in quantum information science¹⁰⁻¹⁷. However, when scaling toward large multi-node quantum networks, the NV center faces two significant challenges. First, the NV center emits a relatively low fraction of photons suitable for quantum networking purposes. Second, the NV center is sensitive to charge noise, due to the presence of a permanent dipole. This prevents the integration of NV centers in nanophotonic devices. Therefore, the group-IV color centers in diamond gained more attention. These color centers contain a group-IV element from the periodic table (Si, Ge, Sn, or Pb) positioned between two missing carbon atoms in the diamond lattice. The resulting symmetry configuration eliminates the permanent dipole, rendering these centers first-order insensitive to charge noise and thus more compatible with nanophotonic integration¹⁸⁻²⁴. This unique combination of stability and integration potential paves the way for innovative device architectures and holds great promise to enable a new generation of scalable, high-performance quantum network nodes.

1.2. THESIS OUTLINE

This thesis presents a series of experimental advances toward realizing scalable quantum networks using solid-state spin-photon interfaces, with a focus on the tin-vacancy (SnV) center in diamond. Each chapter addresses key challenges, as outlined below:

- **Chapter 2** provides the theoretical foundation and experimental background relevant for remote photon-mediated entanglement generation using solid-state spin-photon interfaces. It presents the SnV center in diamond as a promising platform for scalable quantum networks. The chapter discusses challenges related to the optical stability of the SnV center and introduces the theory of quantum frequency conversion (QFC) as a method to enable long-distance entanglement over metropolitan-scale fiber networks.
- **Chapter 3** introduces a novel laser-cutting technique for patterning arbitrary shapes into diamond. Combined with established techniques for fabricating micrometer-thin diamond membranes, this method enables the creation of dia-

mond devices with custom geometries. These devices are designed for open microcavity experiments. These micrometer-thin diamond devices are bonded to a dielectric Bragg mirror, and scanning cavity microscopy is used to investigate the cavity finesse. Low-temperature confocal microscopy further confirms the presence of optically coherent NV and SnV centers within these structures.

- **Chapter 4** explores a heralded initialization scheme for preparing the SnV center in a desired charge state and at a desired optical transition frequency. This scheme involves a combination of laser excitation, photon detection, and real-time logic. By applying this initialization protocol to photoluminescence excitation measurements, coherent optical driving, and optical Ramsey measurements, the enhancement of the optical coherence is studied. Moreover, the protocol explores deterministic preparation of the optical transition frequency across the inhomogeneous linewidth.
- **Chapter 5** focuses on the large-range tuning and active stabilization of the SnV center's optical transition frequency via local strain control. Diamond devices are designed and fabricated such that mechanical strain can be controllably applied locally to SnV centers embedded in suspended diamond waveguides. Furthermore, dynamic strain control is implemented to stabilize the optical transition frequency in real-time through a feedback loop, mitigating spectral wandering.
- **Chapter 6** details the implementation of quantum frequency conversion (QFC) to shift single photons emitted by the SnV center from 619 nm to 1480 nm in the telecom S-band. The QFC setup is characterized in terms of conversion efficiency and added noise. The single photon statistics are investigated by a second-order correlation function $g^{(2)}(\tau)$. The temporal profiles of the converted photons is used to confirm the SnV origin of the converted photons.
- **Chapter 7** concludes the thesis and provides an outlook on the remaining challenges to scaling the SnV center platform to large-scale quantum networks.

BIBLIOGRAPHY

- [1] S. Hawking, *A brief history of time* (Bantam Books, 1989).
- [2] J. L. Bromberg, *The Birth of the Laser*, *Physics Today* **41**, 26 (1988).
- [3] J. Bardeen and W. H. Brattain, *The Transistor, A Semi-Conductor Triode*, *Phys. Rev.* **74**, 230 (1948).
- [4] M. A. Nielsen and I. L. Chuang, *Quantum Computation and Quantum Information* (Cambridge University Press, 2000).
- [5] J. P. Dowling and G. J. Milburn, *Quantum technology: the second quantum revolution*, *Philosophical Transactions of the Royal Society of London. Series A: Mathematical, Physical and Engineering Sciences* **361**, 1655 (2003).
- [6] H. J. Kimble, *The quantum internet*, *Nature* **453**, 1023 (2008).
- [7] S. Wehner, D. Elkouss and R. Hanson, *Quantum internet: A vision for the road ahead*, *Science* **362**, 6412 (2018).
- [8] D. D. Awschalom, R. Hanson, J. Wrachtrup and B. B. Zhou, *Quantum technologies with optically interfaced solid-state spins*, *Nature Photon* **12**, 516 (2018).
- [9] M. W. Doherty *et al.*, *The nitrogen-vacancy colour centre in diamond*, *Physics Reports* **528**, 1 (2013).
- [10] B. Hensen *et al.*, *Loophole-free Bell inequality violation using electron spins separated by 1.3 kilometres*, *Nature* **526**, 682 (2015).
- [11] P. C. Humphreys *et al.*, *Deterministic delivery of remote entanglement on a quantum network*, *Nature* **558**, 268 (2018).
- [12] C. Bradley *et al.*, *A Ten-Qubit Solid-State Spin Register with Quantum Memory up to One Minute*, *Phys. Rev. X* **9**, 3 (2019).
- [13] M. Pompili *et al.*, *Realization of a multinode quantum network of remote solid-state qubits*, *Science* **372**, 6539 (2021).
- [14] J. Randall *et al.*, *Many-body-localized discrete time crystal with a programmable spin-based quantum simulator*, *Science* **374**, 6574 (2021).
- [15] S. L. N. Hermans *et al.*, *Qubit teleportation between non-neighbouring nodes in a quantum network*, *Nature* **605**, 663 (2022).
- [16] M. H. Abobeih *et al.*, *Fault-tolerant operation of a logical qubit in a diamond quantum processor*, *Nature* **606**, 884 (2022).
- [17] A. J. Stolk *et al.*, *Metropolitan-scale heralded entanglement of solid-state qubits*, *Science Advances* **10**, 44 (2024).

- [18] A. Sipahigil *et al.*, *An integrated diamond nanophotonics platform for quantum-optical networks*, *Science* **354**, 6314 (2016).
- [19] G. Thiering and A. Gali, *Ab Initio Magneto-Optical Spectrum of Group-IV Vacancy Color Centers in Diamond*, *Physical Review X* **8**, 021063 (2018).
- [20] C. Bradac, W. Gao, J. Forneris, M. E. Trusheim and I. Aharonovich, *Quantum nanophotonics with group IV defects in diamond*, *Nat. Commun.* **10**, 5625 (2019).
- [21] N. H. Wan *et al.*, *Large-scale integration of artificial atoms in hybrid photonic circuits*, *Nature* **583**, 226 (2020).
- [22] A. E. Rugar *et al.*, *Narrow-Linewidth Tin-Vacancy Centers in a Diamond Waveguide*, *ACS Photonics* **7**, 9 (2020).
- [23] L. Li *et al.*, *Heterogeneous integration of spin–photon interfaces with a CMOS platform*, *Nature* **630**, 70 (2024).
- [24] M. Pasini *et al.*, *Nonlinear Quantum Photonics with a Tin-Vacancy Center Coupled to a One-Dimensional Diamond Waveguide*, *Phys. Rev. Lett.* **133**, 023603 (2024).

2

METHODS FOR SNV CENTERS IN DIAMOND AS A QUANTUM NETWORK NODE

This chapter outlines the theoretical framework and experimental techniques relevant to remote photon-mediated entanglement generation using solid-state spin-photon interfaces. We begin by reviewing entanglement protocols and the principles of encoding quantum information. Particular attention is given to the nitrogen-vacancy (NV) center and group-IV vacancy centers in diamond, with a focus on the tin-vacancy (SnV) center as a promising candidate for scalable quantum networks. We describe the electronic structure, spin properties, and optical interface efficiency of these centers, and discuss the methods for SnV center creation and the optical challenges of SnV centers, including spectral inhomogeneity, instability, and charge state control. Finally, we explore quantum frequency conversion for the integration of SnV centers in a metropolitan-scale quantum network.

2.1. REMOTE PHOTON-MEDIATED ENTANGLEMENT GENERATION

2

In the absence of direct physical interactions between spatially separated quantum nodes, the generation of entanglement between *stationary qubits* needs a mediating carrier, often referred to as a *flying qubit*^{1,2}. Photons are particularly well-suited as a flying qubit as they can transmit quantum information over long distances with relatively low loss and weak interaction with the environment in already deployed optical fibers³. Furthermore, photons are compatible with room-temperature operation, benefitting from an established telecommunication infrastructure, and can be detected at the single-photon level using widely available detection technologies.

The generation of remote entanglement typically proceeds via a qubit state-selective interaction between the stationary qubit and a photon, which entangles the stationary qubit with the photon. This spin-photon entanglement serves as an intermediate resource which can then be used to generate heralded entanglement between 2 remote stationary qubits. Heralding mechanisms are particularly advantageous as they provide resilience against photon loss: entanglement is confirmed only upon successful detection events, thereby preserving the fidelity of the entangled state when the probability of false heralding, due to e.g., dark counts, is sufficiently limited^{4,5}.

Once entangled links between individual nodes are established and a memory is present to store the state, they can be combined to distribute entanglement over a quantum network⁶. These networks offer a platform for a range of quantum technologies, including distributed quantum computing⁷, quantum communication^{1,8,9}, quantum-enhanced metrology¹⁰, and quantum teleportation between nodes that are not directly connected¹¹.

The specific realization of photon-mediated remote entanglement is dependent on the physical hardware implementation of the quantum systems involved. In the following, several representative protocols for the generation of remote entanglement via photons are discussed, with a focus on their underlying principles, operational characteristics, and suitability for integration into quantum network architectures.

2.1.1. PHOTON-MEDIATED ENTANGLEMENT PROTOCOLS

One way to categorize different photon-mediated remote-entanglement protocols is by considering how the photonic qubit travels between the quantum nodes. In the tutorial work of Beukers, Pasini, and Choi et al., these different ways of photon-mediated remote-entanglement protocols are outlined¹². One widely employed approach is the detected-in-midpoint protocol, in which photons that have been individually entangled with stationary qubits at two separate nodes are directed towards a midpoint. At this midpoint, the remote entanglement is realized by a joint measurement, by performing a Bell-state measurement, on the two photons. A successful detection event heralds the entanglement of the remote stationary qubits, depending on the initial spin-photon

entanglement and the indistinguishability of the interfering photons.

An alternative scheme to realize photon-mediated remote entanglement is the sender-receiver protocol, wherein a photon entangled with a stationary qubit at the first node is sent to the second quantum node, where it interacts with the stationary qubit of the second node through a spin-photon interface. This interaction mechanism can, for example, involve a spin-selective reflection from a cavity. The photon is measured after it has interacted with the second spin-photon interface, and the detection serves to project the two stationary qubits into an entangled state. While this protocol does not require an intermediate station, different to the detection in the midpoint protocol, this approach introduces a longer optical path, as the photon has to travel the full distance between the two stationary qubits, whereas for the detection in the midpoint protocol, this is half. Consequently, both the optical loss and the classical communication time are doubled.

A third class of protocols involves a source-in-midpoint, where a central photon source emits entangled photons to two separate nodes. At each node, the photons interact with the local stationary qubits through a spin-photon interface, after which a photonic measurement can establish entanglement between the two stationary qubits. This protocol eliminates the need for initial spin-photon entanglement at the nodes, which is advantageous for some applications, e.g., satellite-assisted entanglement protocols.

Experimental realizations are achieved for the sender-receiver protocol using trapped atoms in optical cavities¹³ and using SiV centers in diamond¹⁴. The detector-in-midpoint has been experimentally realized using the NV center¹⁵, atoms¹⁶, quantum dots¹⁷, and trapped ions¹⁸. Each of these protocols exhibits advantages and limitations that are dependent on the specific characteristics of the quantum hardware used.

2.1.2. SPIN-PHOTON INTERFACES

Photon-mediated entanglement protocols rely on a good spin-photon interface: that is, an interaction mechanism in which the properties of the photon are influenced by the quantum state of the stationary qubit. This spin-selective interaction of the photon with the spin is the foundation for the generation of entanglement between the stationary and flying qubit and can be realized through various mechanisms.

One widely used approach to achieving a spin-photon interaction relies on spin-selective spontaneous emission. In this scheme, the system is excited to an excited state via an optical π -pulse. If the excitation and subsequent spontaneous emission processes are dependent on the spin state, the emitted photon becomes entangled with the spin. For example, when the spin is initially prepared in an equal superposition state, and the optical excitation pulse couples selectively to one of the spin state components, the emission yields a spin-photon entangled state. When the emitted photons entangled with a spin are desired to be used for the generation of entanglement between different stationary qubits, the which-path information needs to be erased, whose effectiveness

depends on the indistinguishability of the photons. The indistinguishability of the photons is constrained by the optical properties of the photons.

2

In addition to spin-photon interaction based on spin-selective spontaneous emission, an alternative class of spin-photon interfaces involving the use of conditional gates enabled by cavity quantum electrodynamics (cQED), can be identified. In these schemes, a strong, coherent interaction between the photon and the spin system is required to realize a conditional gate. This interaction can be enhanced by embedding the emitter in an optical cavity, where the interaction light is confined in the cavity. One such example is conditional amplitude reflection, where the cavity is tuned into resonance with an optical transition that is spin-state dependent. Depending on the spin state of the emitter, an incoming photon is either reflected or transmitted by the cavity, effectively realizing a conditional gate between the stationary and flying qubits¹⁹.

Another method is conditional phase reflection, implemented in the so-called overcoupled cavity regime, where one of the cavity mirrors is more reflective than the other. In this configuration, the response of the cavity is conditional on the spin state: the incoming photon is either reflected directly or enters the cavity and acquires a phase shift upon reflection. This can result in a π -phase shift of the reflected photon.

2.1.3. ENCODING OF THE QUANTUM INFORMATION

To transmit quantum information across a quantum network, information must be encoded in the degrees of freedom of the flying qubits. Several encoding schemes have been developed to realize this, including Fock-state encoding (based on the number of photons, typically the presence or absence of a photon), time-bin encoding (using the temporal mode of the photon), polarization encoding (based on the polarization of the photon), dual-rail encoding (using distinct spatial modes), and frequency encoding (distinguishing photons by their spectral characteristics). A single degree of freedom is chosen for encoding quantum information, while all other degrees of freedom are unchanged. This is critical for Bell-state measurements, as the full visibility of photon interference relies on photons being in an indistinguishable form. In this section, we focus on the Fock-state and time-bin encoding as the former has been widely used for experiments with the nitrogen-vacancy (NV) center entanglement experiments, while the time-bin encoding becomes advantageous when high photon rates are available (e.g., tin-vacancy qubits in diamond), which relaxes the technical requirements.

Fock-state encoding represents quantum information in the photon number basis, typically using the vacuum and single-photon states, as photodetectors are usually non-photon-number resolving. This encoding is conceptually simple and enables heralded entanglement using single-photon detection (single-click), which means that the entanglement generation rate scales linearly with photon detection efficiency. This is in contrast to encodings that require two-photon detection, for which the success probability scales quadratically with loss. As a result, Fock-state encoding is particularly attractive in regimes where overall photon collection and detection efficiency is low.

However, Fock-state encoding introduces technical challenges. Photon loss changes the quantum state to the vacuum (zero-photon) state, which is part of the encoding space. This degrades the fidelity of the entangled state. In addition, the phase of the entangled state is dependent on the relative phase between the optical modes. This necessitates either precise knowledge of the relative phase or active stabilization of the optical paths throughout the duration of the experiment. While this adds significant experimental overhead, successful implementations have been demonstrated^{3,6}. Moreover, the fidelity of entangled states using Fock-state encoding is inherently limited by the probability α that both emitters are initialized in the bright state, which limits the fidelity of the single click protocol to be $F = 1 - \alpha$.

Time-bin encoding encodes quantum information into a temporal mode of a single photon. In the simplest two-basis state space, the photon can either be detected in an early or a late time-bin, corresponding to the logical states. Bell-state measurements in this encoding scheme require two-photon detection (double-click), which means that the probability of successful heralding scales quadratically with photon detection efficiency. While this is a disadvantage in low-efficiency regimes, time-bin encoding offers benefits. Most notably, it relaxes the requirement for the optical phase stabilization that is critical in Fock-state and polarization encodings. This makes time-bin encoding particularly attractive for high-rate systems, where the photon generation rate is sufficiently high to compensate for the lower per-attempt success probability.

2.2. STATE OF THE ART: THE NITROGEN-VACANCY CENTER

The nitrogen-vacancy (NV) center in diamond was the first solid-state defect that was employed to demonstrate quantum applications. This defect consists of a substitutional nitrogen atom adjacent to a vacant carbon site in the diamond lattice. Since nitrogen is a common impurity during diamond growth, NV centers can form naturally in synthesized diamonds. The negatively charged NV center is a spin-1 system.

NV centers have played a pivotal role in advancing the field of solid-state quantum information processing. The NV center has demonstrated milestone experiments in the field of quantum communications, sensing, and simulations. Key achievements include the first demonstration of a loophole-free Bell test²⁰, the realization of a multi-node quantum network⁶, quantum teleportation between two non-adjacent nodes¹¹, and heralded entanglement over a metropolitan quantum network³. Moreover, NV center-based systems have demonstrated the ability to control surrounding spins, enabling the implementation of quantum registers²¹, which allowed for fault-tolerant operations²². At room temperature, the NV center has long coherence times²³ and a small quantum register based on ¹³C nuclei and the electron of an NV center was demonstrated²⁴; the room temperature operation is of special interest for quantum sensing applications. In addition, NV center-based systems have been used in the quantum simulation of a discrete time-crystal, showcasing their versatility beyond communication applications²⁵. More recently, universal high-fidelity quantum gates were demonstrated with an NV center-based system, showing a single qubit gate fidelity of 99.999(1)% and a two-qubit

gate fidelity of 99.93(5)%²⁶.

These demonstrations have served as proof-of-principle validations of the fundamental quantum network concepts. However, they have also highlighted the limitations of NV center-based experiments. Only about 3% of the NV center's photonic emission occurs through the zero-phonon line (ZPL). This portion of the emission happens without phonon interactions. These photons can be indistinguishable and thus can be used for entanglement generation. However, this low ZPL emission limits the entanglement rate.

In addition, the NV center exhibits a permanent electric dipole moment, which makes it sensitive to fluctuating electric fields, such as those generated by surface charges. This sensitivity reduces its compatibility with nanophotonic structures, which are otherwise desirable for increasing the photon collection efficiency and enhancing the emission in the ZPL in photonic cavities.

As the NV center is not compatible with nanophotonic structures, it is challenging to address a number of qubits per node. A larger number of controllable qubits per node is advantageous for multiplexed entanglement generation and for establishing entanglement with multiple remote nodes simultaneously. This motivates the exploration of alternative color centers that can be integrated with nanophotonic structures and that exhibit more favorable optical and material properties for scalable quantum networking.

2.3. GROUP-IV VACANCY CENTERS

Group-IV color centers in diamond are a family of optically active defects consisting of two adjacent carbon vacancies in the diamond lattice, with a group-IV element—such as silicon (Si), germanium (Ge), tin (Sn), or lead (Pb)—positioned symmetrically between them, see Fig. 2.1a. This split-vacancy configuration exhibits a D_{3d} symmetry, which includes an inversion symmetry at the group-IV atom position.

The symmetry properties of the group-IV centers have been theoretically determined through *ab initio* simulations²⁷, and later confirmed experimentally²⁸. A result of this inversion symmetry is the absence of a permanent electric dipole, which renders the group-IV color centers first-order insensitive to electronic field fluctuations. The intrinsic robustness to charge noise allows for integration in nanophotonic structures^{19,29,30}. This opens a whole new toolbox of possibilities to enhance the efficiency of the spin-photon interface, enabling enhanced photon collection efficiencies, Purcell enhancement of the emission in the ZPL, and greater scalability in the number of addressable qubits per quantum node due to its compatibility with nanophotonic integration.

2.3.1. ELECTRONIC LEVEL STRUCTURE

For quantum applications, the negatively charged group-IV centers are of interest. Unless stated otherwise, all references to group-IV centers throughout this thesis refer to this negatively charged charge state. These centers host electrons originating from carbon dangling bonds, the atom itself and from a donor in the diamond. Because of a one-electron difference between the number of electrons and available electron states, the spin and orbital dynamics can be effectively described by a hole with spin- $\frac{1}{2}$. The electronic energy level structure of these spin- $\frac{1}{2}$ systems is qualitatively similar for all group-IV centers.

Fig. 2.1c schematically illustrates the level structure of the group-IV defects in diamond. Both the ground and excited states are spin-doublet, orbital-doublet states, and while the overall level structure is shared, the interaction strengths vary depending on the specific group-IV element.

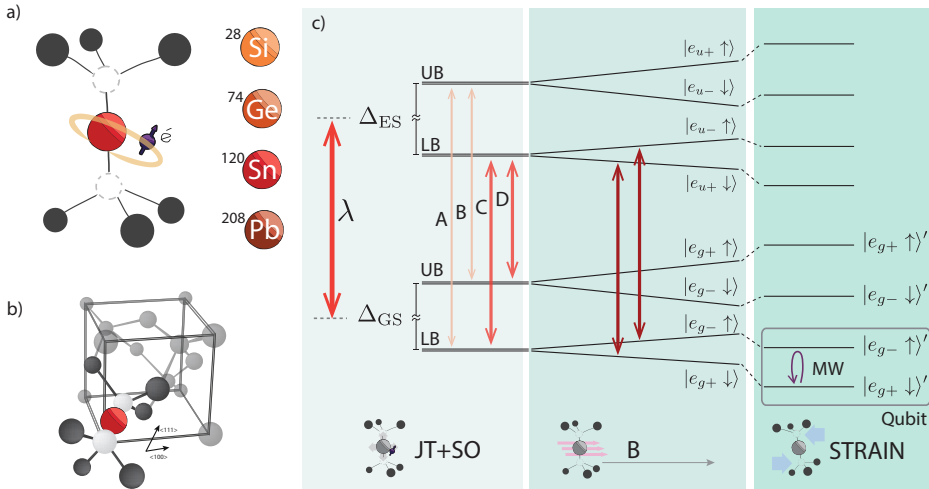


Figure 2.1: **Group-IV vacancy centers in diamond.** (a) Schematic of a group-IV color center in diamond, consisting of two adjacent carbon vacancies, with a group-IV atom symmetrically positioned between the vacancies. The desired optically active, negatively charged state forms upon electron capture. (b) A schematic of the color center within the diamond unit cell. The symmetry axis is along the <111> diamond crystallographic direction. (c) Energy level structure of a group-IV center: the ground and excited states are split by Jahn-Teller (JT) and spin-orbit (SO) interactions, yielding doubly degenerate lower (LB) and upper (UB) branches. A magnetic field (B) further lifts these degeneracies. Strain shifts the branches further. Adapted from Pasini³¹.

The ground and excited states have an opposite wavefunction parity; the ground state exhibits even parity (g), while the excited state is odd (u). The degeneracy of the orbital branches of ground and excited states is lifted by a combination of spin-orbit coupling (SOC) and the Jahn-Teller (JT) effect, resulting in Lower (LB) and Upper (UB) Branches. The spin-orbit coupling couples the electron spin with its orbital angular momentum,

Color center	λ_{ZPL} [nm]	τ [ns]	Δ_{GS} [GHz]	Δ_{ES} [GHz]
SiV	737 ³²	1.8 ³³	50 ³⁴	260 ³⁴
GeV	602 ³⁵	6 ³⁶	170 ³⁷	1120 ³⁸
SnV	619 ³⁹	4.5-8 ⁴⁰	822 ⁴¹	3030 ⁴⁰
PbV	550 ⁴²	4.4 ⁴²	3870 ⁴²	6920 ^{27*}
NV	637 ⁴³	12.3 ⁴⁴	-	-

Table 2.1: Properties of group-IV vacancy centers and the NV center, where λ_{ZPL} is the typical ZPL emission wavelength, τ is the lifetime of the optically excited state and Δ_{GS} (Δ_{ES}) the splitting of the ground (excited) state orbital branches of unstrained emitters. The NV center has no ground and excited state splitting. * The values with a star are based on ab initio calculations.

and scales with atomic number such that heavier elements (e.g., Sn and Pb) exhibit stronger SOC. This results in a larger splitting between the LB and UB of the ground and excited states. The splitting between the LB and UB of the ground (excited) states is denoted as the ground (excited) state splitting, $\Delta_{\text{GS(ES)}}$. The Jahn-Teller effect describes the geometrical distortion of the nuclei of the group-IV defects due to spontaneous symmetry breaking of the electronic wavefunction. For each group-IV defect, the spin-orbit coupling and the strength of the Jahn-Teller effect are different, resulting in different ground and excited state splitting.

In the presence of an external magnetic field, both the electron spin and the orbital angular momentum experience the Zeeman effect, and this lifts the spin degeneracy, resulting in eight spin-orbital energy levels.

In Tab. 2.1, the typical emission wavelength, optical lifetime, and ground and excited state splitting are given.

2.3.2. ELECTRON SPIN QUBIT

The spin qubit subspace is defined within the LB of the ground state, see Fig. 2.1c. For the spin-photon interface, we consider the LBs of the ground and excited states. The spin-conserving optical transitions are indicated in Fig. 2.1c by the dark red arrows in the middle panel.

Initialization of the electron spin into a known qubit state relies on optical spin pumping, which is a spin-flipping process under continuous resonant excitation. The electron spin is optically excited via a spin-conserving transition; if a spin-flip occurs during the decay, the electron ends up in the opposite ground state, which is no longer resonant with the driving field. This spin-pumping process effectively initializes the spin in the opposite spin state. The probability of such spin flips is characterized by the cyclicity of the transition, which quantifies how many optical cycles occur before a spin flip happens.

Readout of the spin qubit is achieved by applying a resonant laser pulse that drives one of the spin-conserving transitions. Detection of fluorescence indicates that the electron

was in the corresponding spin state. For high-fidelity initialization and readout, the spin-conserving transitions must be spectrally well-separated, significantly more than the optical linewidth. This can be achieved by an external magnetic field.

Controlling the spin qubit is non-trivial because the qubit is defined within an orbital branch. Direct transition from one qubit state to the other is forbidden by selection rules. However, strain in the diamond lattice mixes the orbital components of the qubit states, enabling direct control using a microwave-frequency electromagnetic field. The magnetic component of the microwave field mixes the orbitals, allowing coherent spin rotations. In the absence of strain, optical Raman schemes can be used for spin control, but they typically suffer from lower fidelities⁴⁵.

2.3.3. COHERENCE OF GROUP-IV VACANCY CENTERS

Efficient encoding of quantum information for quantum network applications requires that both the optical transition and the qubit subspace remain coherent over the relevant interaction timescales. For group-IV color centers in diamond, phonons are the dominant source of decoherence, which can alter the state of the system between the orbital branches in the ground and the excited states.

The main contributing phonon process responsible for decoherence are the direct phonon transitions that matches the orbital state splitting energy. This process promotes an electron from the LB to the UB at a rate γ_+ . The electron can subsequently decay back to the LB via phonon emission with a rate γ_- ⁴⁶,

$$\gamma_+ = 2\pi\chi\rho\Delta_{\text{GS}}^3 n(\Delta_{\text{GS}}, T), \quad (2.1)$$

$$\gamma_- = 2\pi\chi\rho\Delta_{\text{GS}}^3 [n(\Delta_{\text{GS}}, T) + 1], \quad (2.2)$$

where χ is proportional to the phonon-electron interaction frequency, and ρ is proportional to the phononic density of states, and $n(\Delta_{\text{GS}}, T)$ is the thermal population of the phonons matching the energy difference of the orbital states Δ_{GS} at a given temperature T , which follows the Bose-Einstein distribution,

$$n(\Delta_{\text{GS}}, T) = \frac{1}{e^{\Delta_{\text{GS}}/k_b T} - 1}, \quad (2.3)$$

where k_b is the Boltzmann constant. We focus on the ground state orbital splitting Δ_{GS} , as the decoherence is limited by the smallest splitting, which is the ground state splitting. As can be seen from Eq. 2.2, the rate γ_+ can be reduced by increasing the energy difference of the orbital state, Δ_{GS} , or decreasing the temperature, thereby suppressing the thermal phonon occupation.

To quantify the decoherence, we introduce two timescales: the depolarizing time T_1 , describing how fast an eigenstate decays to another eigenstate, and the dephasing time T_2^* , characterizing how fast the phase of a superposition is lost. In the low-temperature regime, $k_b T \ll \Delta_{\text{GS}}$, the thermal population of phonons that can drive the transition from the LB to the UB vanishes. In this case, the rate from LB to UB is the

limiting rate that determines the timescale at which the state is depolarized, resulting in,

$$T_1^{\text{orbit}} = \frac{1}{\gamma_+}. \quad (2.4)$$

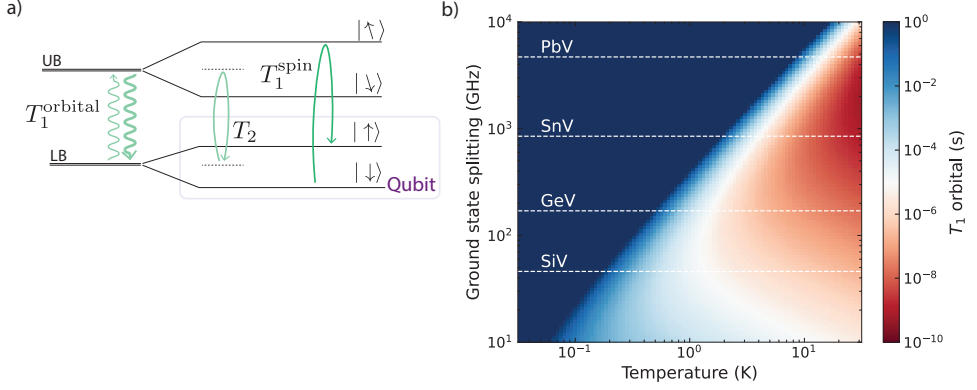


Figure 2.2: **Dephasing induced decoherence of group-IV vacancy centers in diamond.** (a) A schematic overview of the dephasing mechanisms and their relevant timescales. (b) The orbital relaxation time, T_1^{orbital} , due to phonon dynamics at varying temperature and ground state splitting. The T_1^{orbital} is simulated using $\chi\rho = 4.6 \times 10^{-9} \text{ GHz}^{-2}$, extracted from T_2^* measurements performed at $T \sim 4 \text{ K}$ ⁴⁷. Figure adapted from Pasini³¹.

Using Eq. 2.2 and Eq. 2.4, we can simulate T_1^{orbit} as a function of the temperature and the ground state splitting, which is depicted in Fig. 2.2b. The white dashed lines indicate the ground state splitting of the unstrained group-IV color centers. A clear transition is visible where the phonon processes are suppressed due to temperature. The plot reveals that to suppress phonon-induced depolarization, SiV and GeV color centers require temperatures below 1 K to achieve a T_1^{orbital} of about 10 ms, while SnV centers reach this regime below 1.7 K. This enables SnV center operation without requiring a dilution refrigerator, thereby reducing both system complexity and cost.

Fig. 2.2a shows that the spin dephasing time, T_2 mixes the phase of the spin. In the work of Harris et al., they show that this is due to a stochastic phase accumulation, which results in T_2 being limited by the orbital depolarizing time, T_1^{orbit} ⁴⁸. However, not every phonon interaction will cause a spin-flip, so the $T_1^{\text{spin}} > T_1^{\text{orbit}}$. This depends on the probability of a spin-flip occurring when a spin cycle is performed. We refer to the cyclicity, η^{spin} , as the average number of spin cycles before a spin-flip occurs. This results in $T_1^{\text{spin}} = \eta^{\text{spin}} T_1^{\text{orbit}}$.

In addition, for a coherent spin-photon interface, the coherence of the optical transition needs to be longer than the lifetime of the excited state.

There are 3 strategies to minimize γ_+ and enhancing the coherence, namely by,

1. Reducing the phononic density of states, by creating an environment where the phonons are not allowed, e.g., reducing the size of the host diamond and embedding color centers in nanodiamonds⁴⁹ or in phononic crystals⁵⁰,
2. Increasing the ground state splitting by selecting defects with larger ground state splitting (e.g., SnV or PbV) or applying large strain,
3. Decreasing the temperature to suppress thermal phonons.

2.3.4. EFFICIENCY OF THE OPTICAL SPIN-PHOTON INTERFACE

As introduced in Sec. 2.1.1, several spin-photon interfaces rely on the spin state-dependent excitation, where a laser pulse selectively excites the system based on the spin state. The emitted photon, resulting from the spontaneous decay of the excited state, acts as a flying qubit, provided that the photon is coherently emitted. In this section, we address the efficiency of the coherent photon emission process for the group-IV color centers.

First, the emission needs to happen in a radiative way, and we define the ratio of emission into the radiative decay path compared to all decay paths (radiative + non-radiative) as the quantum efficiency, η_{QE} . The quantum efficiency is different for all group-IV defects and depends on the molecular-like electronic orbitals of the defect.

Even when decay is radiative, coherence can be lost due to phonon interactions. The coupling between electronic and vibrational degrees of freedom leads to phonon sideband (PSB) emission. This is the decay via a phonon-assisted transition. The electronic and vibronic structures are intrinsically coupled, as modifications in the electronic configuration induce slight displacements of the nuclear positions through Coulomb interactions, which we can describe as a harmonic oscillator. The harmonic oscillator has quantized allowed vibrational modes. The Born-Oppenheimer approximation states that the change in electronic states happens at a much faster timescale than the nuclear motion. As a result, the radiative decay occurs when the nucleus has not been displaced. This affects which transitions are allowed, which are depicted in Fig. 2.3, as vertical transitions. According to the Frank-Condon principle, the probability of a transition occurring depends on the overlap of the vibrational wavefunction. The zero-phonon line (ZPL) transitions are the ones that are without the absorption or emission of a phonon. The other transitions we refer to as the emission in the phonon-side band (PSB). The probability that an emitted photon is coherent, i.e., emitted in the ZPL without phonon interaction, is quantified by the Debye–Waller factor:

$$\eta_{DW} = \frac{\gamma_{ZPL}}{\gamma_{ZPL} + \gamma_{PSB}}, \quad (2.5)$$

where γ_{ZPL} and γ_{PSB} are the ZPL and PSB emission rates, respectively. Heavier group-IV atoms induce greater lattice distortion, generally reducing η_{DW} ²⁷. Nevertheless, due to their inversion symmetry, group-IV centers exhibit significantly higher Debye–Waller factors than NV centers, as a result of a weaker electron-phonon coupling which gives rise to more overlap of the ground and excited states.

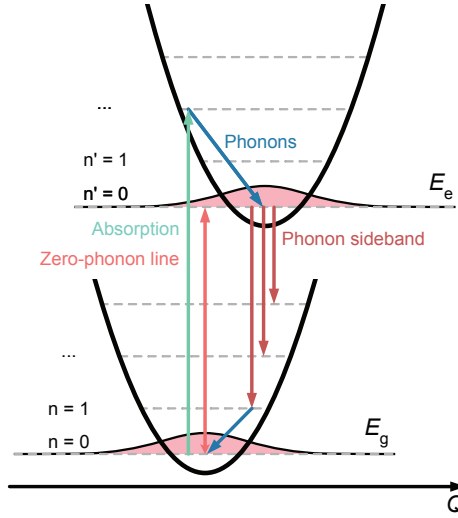


Figure 2.3: **Frank-Condon diagram** The ground and excited state energy levels of the vibronic potentials. The vertical transitions are the ZPL (green) and the PSB (dark red). Adapted from^{51,52}.

Within the ZPL, transitions can occur from the lower branch (LB) of the excited state to either the LB or the upper branch (UB) of the ground state. The C-transition, linking the excited and ground LB states, is especially of interest as it maintains the qubit subspace, contrary to transitions involving the UB, which suffer from rapid phonon-induced spin decoherence. The branching ratio into the desired C-transition is defined as,

$$\eta_{BR} = \frac{\gamma_C}{\gamma_{ZPL}}. \quad (2.6)$$

The overall coherent emission probability is the product of the quantum efficiency, the Debye-Waller factor, and the branching ratio,

$$\eta_{\text{coherent}} = \eta_{QE} \eta_{DW} \eta_{BR}. \quad (2.7)$$

Table 2.2 summarizes these quantities for group-IV centers and the NV center, where it can be seen that the SnV color center has the highest ratio of coherent emission compared to the other group-IV color centers.

Group-IV color centers offer multiple advantages over the NV center. The inversion symmetry of group-IV centers provides first-order insensitivity to electric field fluctuations, facilitating integration into nanophotonic structures. Due to the high ground state splitting, the SnV center has coherent spin control below 1.7 K, which allows for operation in a Helium-4 system rather than a dilution refrigerator. Recent work has shown that applying strain can further increase the operating temperature⁶¹. Most notably, the high ratio of coherent emission of the SnV center directly enhances

Center center	η_{QE}	η_{DW}	η_{BR}	$\eta_{coherent}$
SiV	0.1-0.3 ^{30,33}	0.65 ⁵³	2/3 ³⁴	0.04-0.13
GeV	0.2 ⁵⁴	0.6 ⁵⁵	$\approx 2/3$ [†]	0.08
SnV	0.8 ⁵⁶	0.57 ⁵⁷	0.8 ⁵⁸	0.36
PbV	-	0.34 ^{27*}	-	-
NV	>0.8 ⁵⁹	0.026 ⁶⁰	1	0.021-0.026

Table 2.2: The fraction of coherent emission of the group-IV color centers and the NV center. * The values with a star are based on ab initio calculations. † The branching ratio for the GeV has been estimated to be similar to the SiV and the SnV centers.

heralded entanglement generation rates, making it a strong candidate for scalable quantum networks.

2.4. THE TIN-VACANCY CENTER AS A QUANTUM NODE

Over the past few years, significant experimental progress has been made in establishing the SnV center in diamond as a promising platform for quantum network nodes. A range of experimental demonstrations has confirmed the suitability of the SnV center for scalable quantum technologies. Initial studies have achieved the spectral identification of the SnV center^{56,62,63}, followed by the observation of transform-limited optical transition linewidths^{39,40}. Techniques for deterministic depth control, such as shallow implantation and overgrowth, have also been demonstrated^{64,65}, as well as the integration of SnV centers into nanodiamonds⁶⁶. Further advancements include the integration of optically coherent SnV centers into photonic structures such as waveguides⁶⁷⁻⁶⁹, and photonic crystal cavities^{29,70,71}, along with open micro-cavities⁵⁸.

Charge-state control has been achieved through both electrostatic gating⁷² and optical fields⁵⁷, and heralded charge state initialization protocols⁶⁵. Moreover, single-shot readout has been demonstrated^{57,73,74}. Tuning of the optical transitions has been demonstrated through second-order Stark tuning^{75,76}, and strain engineering⁷⁷⁻⁷⁹. The demonstration of narrow inhomogeneous distribution of the optical resonance frequencies^{80,81}, and sub-picosecond optical excitation⁸², were shown. Two-photon quantum interference from a single emitter in a waveguide under resonant excitation⁶⁷ and from 2 emitters in different setups under off-resonant excitation⁸¹, have also been shown. Furthermore, large-scale CMOS integration has been reported⁷⁹.

On the spin side, strongly coupled nuclear spins have been identified^{83,84}, and recently, the high-fidelity spin control has been demonstrated^{41,61,85}. In addition, the control of a nearby ¹³C nuclear spin for a quantum memory register has been demonstrated⁷³.

This overview highlights the rapid development of the SnV center as a solid-state qubit platform. In the following sections, we will further discuss the optical characteristics of the SnV center. While the SnV center offers several desirable features, its

performance is still influenced by the solid-state environment. In the remainder of this section, we will discuss the SnV center creation and primary challenges affecting the optical behavior, along with approaches to mitigate these effects.

2.4.1. SnV CENTER CREATION

The creation of SnV centers in diamond can be implemented in various ways; different applications have different requirements. Creating SnV centers in diamond typically involves three main steps: tin ion implantation, defect generation, and annealing. Several review papers offer comprehensive overviews of color center creation in diamond^{86–89}. This section describes the key steps of SnV center creation, including its advantages and limitations.

TIN ION IMPLANTATION

The substrate quality is critical, and depending on the intended application must be chosen with care. Minimal strain is desirable to avoid inhomogeneous broadening. For nanophotonics, low dislocation density and smooth surfaces are preferred and essential for chemical vapour deposition (CVD) overgrowth methods, and low impurity levels are beneficial to avoid decoherence.

During ion implantation, three key parameters can be adjusted: ion dose, implantation energy, and implantation angle. The reported SnV center creation yield ranges from 2–5%^{63,90}. Depending on the desired emitter density and environmental purity (i.e., minimal nearby Sn ions or vacancies), implantation doses typically range from $5 \cdot 10^9$ ions/cm² to $5 \cdot 10^{11}$ ions/cm².

The implantation energy, together with the implantation angle, determines the final depth of the Sn ions. Simulations using the Stopping and Range of Ions in Matter (SRIM) simulations estimate both the implantation depth, and vertical and lateral spread, as well as the number of vacancies generated per implanted ion. Higher energies allow deeper placement, but increase positional uncertainty and lattice damage.

To improve the depth precision, shallow implantation followed by CVD diamond overgrowth can be used. The low-energy implantation minimizes crystal damage and vertical spread, while high-temperature CVD diamond growth simultaneously acts as an annealing step. Controlled growth rates allow placement of emitters at predefined depths. For optimal coupling to photonic waveguides and cavities — typically around 200 nm in height — SnV centers must be positioned on the order of 30 nm accuracy. Achieving this level of control of the diamond growth rate remains technically challenging. However, low-energy implantation minimizes vertical spread, aiding in accurate positioning.

DEFECT CREATION

Vacancies are introduced in the diamond crystal during the ion implantation and can become mobile during annealing, combining with Sn ions to form SnV centers. This is a conventional way to create SnV centers. However, studies on other color centers show

that additional electron irradiation significantly enhances conversion to defect centers. For instance, Schröder et al. demonstrated a tenfold improvement of SiV center creation yield after electron irradiation and annealing⁹¹, and similar results have been reported for NV centers⁹² using transmission electron microscopy (TEM) beams.

Alternatively, femtosecond laser pulses can be used as electron irradiation for vacancy generation. These pulses ionize molecules in the air, where resulting electrons are then accelerated by subsequent laser pulses⁹³. The latter two techniques allow for targeted vacancy creation, making them suitable for site-specific SnV center formation.

ANNEALING

Annealing mobilizes self-interstitials and vacancies at temperatures above 800 °C, healing implantation damage and facilitating SnV center formation²⁸. The annealing parameters, such as temperature, pressure, and duration, are crucial. Diamond, being a metastable phase of carbon, can graphitize during annealing, particularly in the presence of contamination or crystallographic defects⁹⁴. To avoid this, annealing is typically performed either:

- **High vacuum** ($<10^{-6}$ mbar)⁷⁸,
- **High pressure** ($>$ several GPa), often referred to as high-pressure high-temperature (HPHT) annealing⁵⁶, or
- **Atmospheric pressure** with a constant flow of gas (e.g., argon, hydrogen, or nitrogen)⁹⁵.

The specific combination of duration and temperature determines the extent of crystal healing. Alternatively, high temperatures reached during CVD overgrowth can serve as an in-situ annealing step, eliminating the need for a separate furnace anneal. Typically, extensive acid cleaning is performed to remove any formed graphite. This can be done using a tri-acid clean (mixture of 1:1:1 ratio of H₂SO₄ (97 %):HNO₃ (65 %):HClO₄ (60 %)) at 120 °C for one hour.

2.4.2. SnV CENTER OPTICAL CHALLENGES

The optical properties of the SnV center in diamond are influenced by its surrounding environment. Local strain and interactions with phonons can shift the frequency and broaden the linewidth of the optical transition, thereby limiting spectral stability and coherence. In addition to these static effects, dynamic environmental fluctuations—such as changes in the local charge distribution—can lead to time-dependent spectral diffusion of the optical transition. Lastly, the negatively charged SnV center can transition into other charge states (e.g., SnV⁰ or SnV⁻²), which have different energy level schemes, resulting in an effective optically "dark" SnV center. Fig. 2.4 illustrates the impact of strain, phononic interactions, and charge dynamics on the optical behavior of the SnV center.

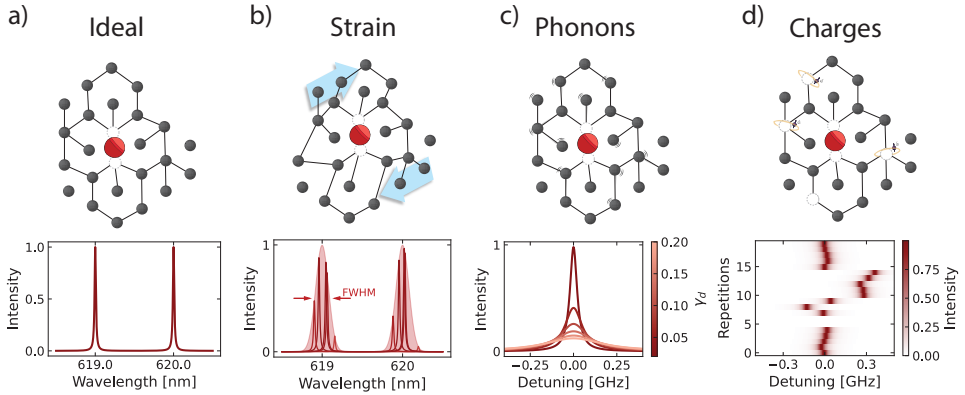


Figure 2.4: **Optical response of the SnV center to the environment.** (a) A perfect diamond lattice, consisting of a single SnV center. (b) Local changes in strain environment result in SnV centers having different resonance frequencies; this distribution of resonance frequencies is called the inhomogeneous distribution. (c) Phonons in the system broaden the optical transition. (d) A dynamic charge environment causes the resonance frequency to spectrally jump in time. Adapted from Pasini³¹.

2.4.3. INHOMOGENEOUS DISTRIBUTION

SnV centers embedded in diamond experience varying local strain environments, which arise from intrinsic structural features of the diamond, such as crystallographic defects, dislocations, or residual damage from ion implantation. These strain variations lead to shifts in the optical resonance frequencies, resulting in a distribution of resonance frequencies across different SnV centers within a single diamond sample. This distribution is referred to as the inhomogeneous distribution.

As introduced in Sec. 2.1.1, many entanglement protocols rely on the indistinguishability of the emitted photons. Depending on the number of SnV centers in the diamond (implantation dose) and the structural properties of the diamond, it is often challenging to identify multiple SnV centers with identical optical resonance frequencies. The ratio of the inhomogeneous distribution to the tuning range provides a measure of this difficulty. For example, Li et al. report that 40% of the resonance frequencies are in a window of ≈ 20 GHz. Görlitz et al. observe an inhomogeneous distribution linewidth of 15 GHz in a High-Temperature-High-Pressure (HPHT) annealed diamond⁴⁰. Even narrower distributions have been reported by Narita et al.⁸⁰ and Bushmakina et al.⁸¹, where both report on an inhomogeneous distribution linewidth of 4 GHz, where the diamond samples in the former study have been HPHT annealed. In addition to the annealing conditions, the implantation energy plays a critical role: higher implantation energies cause more crystal lattice damage, which, if not fully repaired during annealing, can significantly broaden the inhomogeneous distribution. Despite these advancements, even the narrowest reported inhomogeneous distributions remain over two orders of magnitude broader than the transform-limited linewidth of the SnV center optical transition, emphasising the challenge of finding SnV centers with the same resonance

frequency.

Several approaches have been proposed and demonstrated to address this challenge:

1. **Spectral tuning of individual emitters**, using either DC-Stark tuning^{75,76}, magnetic field tuning, charge-resonance checks⁶⁵, and strain fields⁷⁷⁻⁷⁹,
2. **Quantum frequency conversion (QFC)**, where the frequency of the emitted photon is converted to a target wavelength, through nonlinear optical processes^{3,96},
3. **Temporal techniques**, which rely on high-resolution photon arrival-time detection to reduce the spectral indistinguishability requirement⁹⁷,
4. **Improved material engineering**, aimed at reducing the structural defects that contribute to inhomogeneous broadening.

The first approach, using charge-resonance check, is discussed in Chap. 4. The approach involving local strain engineering is further discussed in Chap. 5, while tuning using QFC is elaborated on in Chap. 6.

2.4.4. OPTICAL STABILITY

Changes in the local environment can alter the optical resonance frequency of SnV centers. As discussed in Sec. 2.4.2, phonon interactions contribute to broadening of the optical transition, and temperature fluctuations can shift the optical resonance⁴⁰. However, when the cryostat is stabilized at a low enough temperature to ensure good optical coherence, these factors become negligible in terms of optical stability.

More significant are charge-related dynamics. One such process is charge-state dynamics, in which the SnV^- center ionizes to an optically inactive state, SnV^{2-} . Experiments suggest that this is a one-photon process in which an electron from the valence band goes to the ground state of the SnV center, ionizing the SnV center to the optically inactive SnV^{2-} . High-energy off-resonant laser pulses can restore the desired charge state (SnV^-) probabilistically. In our experiments, a green laser at 515 nm is used for this purpose. Other studies have shown that shorter-wavelength light, such as blue lasers near 450 nm, can initialize the desired charge state more efficiently⁵⁷.

In addition to the ionization of the SnV center, shifts in the optical resonance frequency can also arise from fluctuations in the surrounding charge environment⁹⁸. Charges trapped in nearby defects can be captured or released, altering the local electric field and inducing a shift in the SnV center transition frequency. While SnV centers are first-order insensitive to electric fields due to their inversion symmetry, they are still susceptible to second-order effects. Considering only the effect of the second order, the transition level energy changes with $\Delta\alpha/r^4$, where $\Delta\alpha$ is the second-order polarizability and r the distance between the charge trap and the SnV center. Experimentally, $\Delta\alpha$ is determined to be -5.1×10^{-5} GHz/(MV/m)²⁷⁵. A trap within a few Ångströms can cause frequency shifts of several GHz. The dynamics of the charge traps can also be stochastically altered by high-energy off-resonant laser light, which is used for the

initialization of the charge state of the SnV center. Both processes can be detrimental to the generation of indistinguishable photons.

2

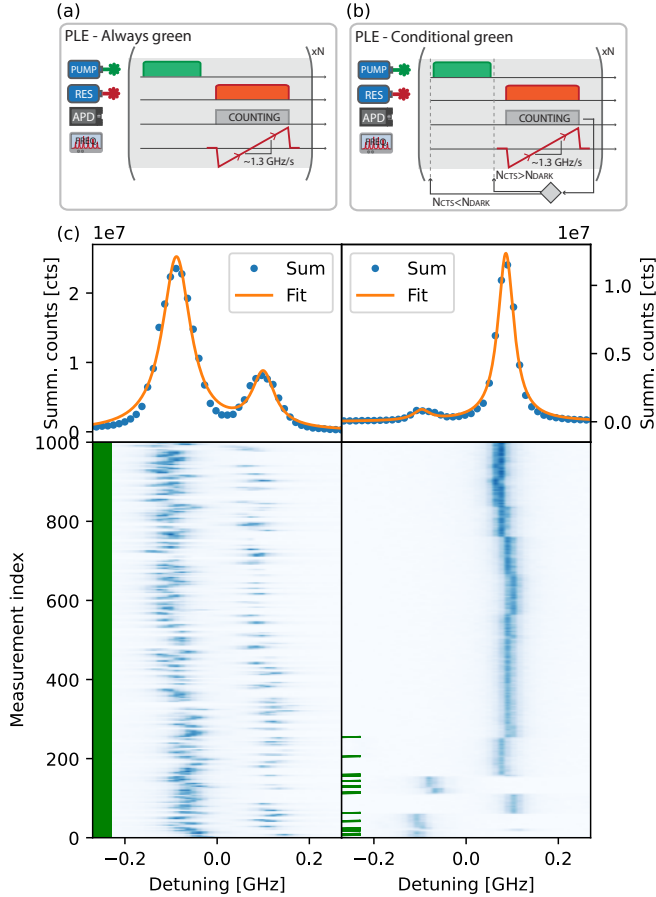


Figure 2.5: **Spectral instability of the SnV center.** (a) Pulse sequence PLE scan: always green. (b) Pulse sequence PLE scan: conditional green. (c) Fluorescence from 1000 PLE scans over the optical transition at a scan rate of 1.3 GHz/s. Left: An off-resonant green pulse is applied before every scan. Right: A green pulse is only applied when no fluorescence peak is detected in the previous scan. Green lines indicate scans preceded by a green pulse. Top panels: Sum of all scans fitted with a double Lorentzian. FWHMs for the always-green case are 74 ± 2 MHz and 60 ± 4 MHz; for the conditional-green case, 44 ± 12 MHz and 41 ± 2 MHz. Mean FWHMs of individual fits are 36 MHz (always green) and 32 MHz (conditional green).

These dynamic processes can be compensated for in post-processing; however, this significantly reduces the overall rate. A more scalable approach involves real-time control. Demonstration of the real-time initialization is discussed in Chap. 4. In the remainder of this section, we give more background on the mechanisms allowing for this heralded initialization.

We depict the effect of using an off-resonant green laser in Fig. 2.5c, where the PSB fluorescence of a SnV center is depicted when a resonant laser is scanned over the resonant transition. On the left side of the figure, an off-resonant green laser pulse is applied before every laser scan. A clear bi-stable state is visible. In contrast, in the right panel, the green pulse is only applied conditionally when no peak is detected, indicating the SnV center is likely in a dark charge state. This conditional initialization maintains the resonance of this SnV center for about 20 minutes. In the top panels, we plot the summed signal of the 1000 scans and we fit it with a double Lorentzian. The difference between the full-width-half-maximum (FWHM) of the summed scans and the mean FWHM of individual scans quantifies the spectral diffusion. In the always-green case, the FWHM of the fitted summed curves are 74 ± 2 MHz and 60 ± 4 MHz compared to a mean FWHM of 36 MHz for individual scans. In the conditional case, the FWHM of the fitted summed counts is significantly closer to the mean of the individual fitted curves of 32 MHz, at 44 ± 12 MHz and 41 ± 2 MHz, indicating improved spectral stability. Ideally, one uses an off-resonant laser pulse when the SnV center is in the optically dark state to minimize the spectral diffusion caused by the off-resonant laser pulse.

Although the optical instability of the SnV center is significantly less when only an off-resonant green pulse is applied when the SnV center is in an optically dark state, the charge environment is shuffled around, causing the resonance frequency to shift. To quantify the effect of green light, we perform a slow PLE scan where we alternate a high-power off-resonant green laser pulse with a red laser pulse, we repeat this n times (>1000), and then change the frequency of the red laser. This approach samples the range of resonance frequencies the SnV center can have after charge reshuffling. The resulting spectrum, shown in Fig. 2.6b, reveals a broadened FWHM of 312 ± 26 MHz. This demonstrates that while the intrinsic linewidth can be as narrow as ~ 34 MHz, charge dynamics induced by green laser pulses can result in the SnV center's resonance frequency being in a range more than an order of magnitude wider.

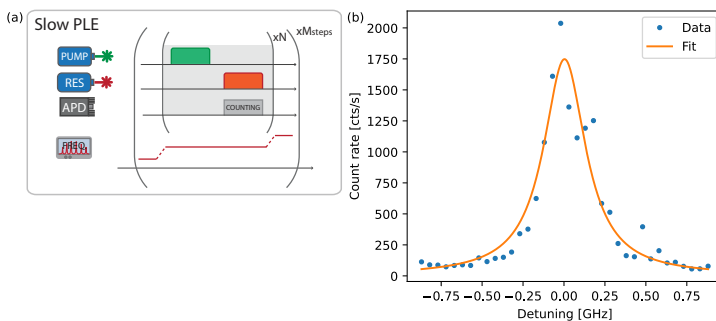


Figure 2.6: **Slow PLE.** PLE spectrum acquired by alternating high-power off-resonant green and resonant red laser pulses, probing the full range of frequency shifts induced by charge reshuffling. The fitted Lorentzian has a FWHM of 312 ± 34 MHz.

This effect highlights a trade-off: while green pulses are essential for charge-state initialization, they can also affect the spectral stability. In the following section, we discuss how the frequency distribution observed during slow scanning can be exploited while still preserving narrow linewidths during fast scans.

2

2.4.5. CHARGE STATE AND RESONANCE FREQUENCY PREPARATION

To make use of the broad, slow PLE linewidth compared to the narrow FWHM when scanning fast, we need to find a way to check whether the SnV center resonance is at the desired optical resonance frequency. In other words, we require a method to selectively initialize the SnV center at a specific resonance frequency within the broader distribution induced by high-power off-resonant green laser pulses.

To this end, we introduce a probing scheme, where a resonant pulse is used to test whether the SnV center is both in the optically bright state and resonant with the desired frequency. The SnV center will emit more photons during the resonant test pulse when it is in the optically bright state and resonant with the driving field. When the SnV center is not on resonance, it will emit fewer photons. To evaluate the feasibility of this approach, we implement a pulse scheme, see Fig. 2.7a, and we correlate the photon counts detected in two consecutive resonant pulses. The first pulse serves as the probe and tests the charge-resonance condition of the SnV center.

Fig. 2.7b shows histograms of photon counts from two subsequent resonant pulses. In the ideal case, we would expect a Poisson distribution centered around a mean count value for both pulses. However, we do see the contribution of other phenomena. On the left side of the histogram, a Poisson distribution with a mean around 5 photon counts corresponds to the optically dark state. On the right side, the distribution of high-count events (>20 counts) reflects the optically bright state. This distribution is not a pure Poissonian, the asymmetry can be explained by (1) ionization during the pulse, (2) charge-induced spectral diffusion.

Ionization leads to a nonzero probability for low photon counts, even when the system starts in the bright state, while on the other hand, spectral diffusion contributes to the asymmetry in the bright state distribution. When the SnV center is slightly detuned from the driving field frequency, the emission rate decreases, resulting in a Poisson distribution with a lower mean number of photons. The probability of having that lower number of photon counts is related to the Lorentzian distribution of Fig. 2.6b. This is proportional to the probability of the emitter having a specific resonance frequency after applying an off-resonant green laser pulse. However, since detuning (both red and blue detuned) always leads to a lower photon count, the probability of observing a given mean photon count follows a truncated (or "half") Lorentzian,

$$P_{\text{HL}}(x) = \begin{cases} \frac{A}{\pi} \cdot \frac{\gamma}{(x - x_0)^2 + \gamma^2} & \text{if } x \leq x_0 \\ 0 & \text{if } x > x_0, \end{cases} \quad (2.8)$$

where $P_{\text{HL}}(x)$ is the probability of observing a mean photon count x , A the normalization constant, the FWHM corresponds to 2γ , and x_0 is the expected photon count at resonance. The resulting total photon count distribution, $F(x)$, is a product of the "half" Lorentzian with Poisson distribution corresponding to the bright state and the Poisson distribution with mean photon numbers corresponding to the dark state,

$$F(x) = A_1 \text{Pois}(c_{\text{dark}}) + A_2 P_{\text{HL}} \text{Pois}(c_{\text{bright}}), \quad (2.9)$$

where $A_{1,2}$ are normalization factors, and $\text{Pois}(c_{\text{dark}}(\text{bright}))$ correspond to a Poisson probability mass function with a mean number of photon counts corresponding to the dark (bright) state. The resulting model is plotted as the solid line in Fig. 2.7b. The distribution for the second pulse differs slightly due to ionization during the first pulse, increasing the contribution of dark-state events.

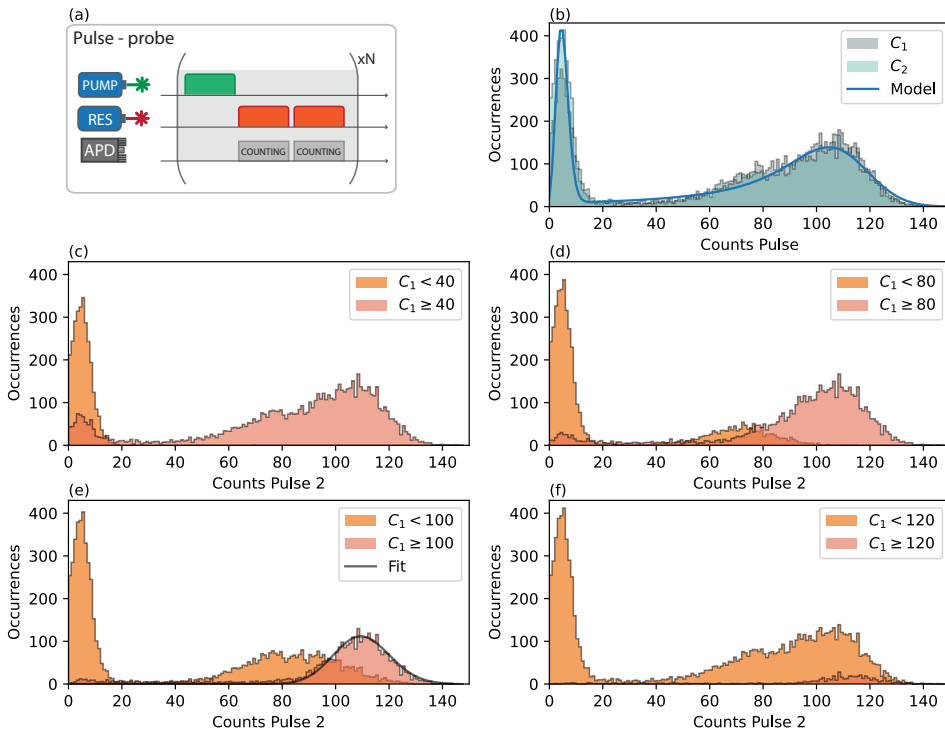


Figure 2.7: **Pulse probe histograms.** (a) Pulse sequence. (b) Histogram of photon counts from two subsequent resonant pulses. The solid line is a model including contributions from dark counts, a truncated Lorentzian-weighted Poisson distribution for slightly off-resonant emission, and ionization effects. (c–f) Conditional histograms of photon counts in the second pulse, depending on the number of photons detected in the first pulse.

We want to minimize the contributions of the optically dark state and the spectral diffusion. In Fig. 2.7c–f, we plot a histogram of the number of photon counts detected during pulse 2, conditioned on a minimum number of counts in the first pulse. Comparing

Fig. 2.7b with Fig. 2.7c, where a relatively low condition photon number is picked (40), we see that the dark count contribution is reduced. Increasing the threshold further (e.g., >100 counts in Fig. 2.7e) yields a near-Poissonian distribution, minimizing the contribution of spectral diffusion and the optically dark state. However, this comes at the cost of a lower success probability. With very high thresholds, the number of occurrences drops significantly (Fig. 2.7f). While this conditioning is currently applied during post-processing, it illustrates the potential of real-time filtering to herald the charge and resonance state.

For real-time decision making, we use a microcontroller. We implement a state machine that applies a resonant red pulse, which probes the number of photon counts. If the count exceeds a predefined threshold, the experimental sequence is started. Otherwise, a green off-resonant pulse is applied to reshuffle the charge environment, and the probe step is repeated. This process is repeated until the threshold is met and the experimental sequence is started. We employ two thresholds: a “repump” threshold to distinguish between the dark and bright states (typically set just above the dark-state background), and a “pass” threshold to check whether the resonance condition is met. If the first is met but not the second, the system remains in the bright state but is not sufficiently on-resonance, so the probe is repeated. This protocol is referred to as the Charge-Resonance Check (CR-check). The specific threshold values determine the overall sequence rate at which the CR-check is passed. In Chap. 4, we evaluate the performance of this scheme in detail for SnV centers.

2.5. TIN-VACANCY CENTER NODE IN A METROPOLITAN QUANTUM NETWORK

Building on the understanding of the optical properties of the SnV center, we now turn to its applicability to long-distance quantum networks. Establishing entanglement over long distances using photons as flying qubits requires a transmission medium. Existing telecom fiber infrastructure offers an attractive solution for this, as it enables long-distance connectivity, flexible routing between nodes and is optimized for low-loss transmission⁹⁹.

However, as shown in Fig. 2.8, photons emitted by SnV centers at 619 nm experience significant attenuation in silica fibers—around 10 dB/km. This high loss severely limits the achievable entanglement rates over long distances. To overcome this, one can convert the photons to a wavelength range where fiber transmission loss is minimal. Crucially, this conversion must preserve the quantum information encoded in the photon.

This process, known as Quantum Frequency Conversion (QFC), has been successfully demonstrated for various quantum network applications^{3,100–102}. The QFC set-up used for this work is discussed in Chap. 6 and this set-up is based on the work of Stolk and van der Enden et al.³, in which photons from NV centers at 637 nm were converted to telecom wavelengths (1588 nm) using a 1064 nm pump laser.

Applying the same conversion scheme to photons from SnV centers at 619 nm, combined with a 1064 nm laser, results in output photons at 1480 nm, as shown in Fig. 2.8. While this wavelength experiences slightly higher attenuation than the converted NV photons (0.33 dB/km vs. 0.25 dB/km), it still represents a substantial improvement over the original 10 dB/km loss at 619 nm. In the following sections, we provide a detailed discussion of the QFC mechanism and its implementation.

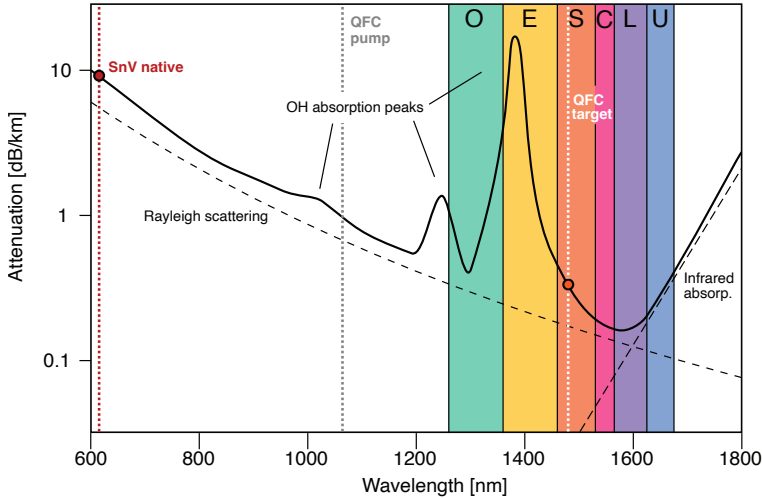


Figure 2.8: **Attenuation of light in silica optical fiber.** The primary loss mechanisms —Rayleigh scattering, OH-absorption, and infrared absorption— are indicated by black dashed lines. The O, E, S, C, L, and U telecom bands correspond to wavelength regions of low attenuation, provided that OH absorption in the E band is mitigated. The SnV center emission at 619 nm lies in a high-loss region compared to the telecom bands. Quantum frequency conversion using a 1064 nm pump shifts the SnV photons to 1480 nm, placing them in the S-band, where fiber attenuation is significantly lower. Adapted from van der Enden¹⁰³.

2.5.1. QUANTUM FREQUENCY CONVERSION

Frequency conversion of light arises from the interaction of electromagnetic waves with a nonlinear medium (NLM). In such materials, the polarization density \mathbf{P} exhibits a nonlinear response to an applied electric field \mathbf{E} (e.g., light). In the following sections, we discuss how this nonlinear behavior enables frequency conversion. Specifically, we focus on three-wave mixing (TWM) in a nonlinear material, leading to difference-frequency generation (DFG), in which two input modes—photons from SnV centers at 619 nm and pump photons at 1064 nm—are converted into photons at a target wavelength of 1480 nm. We also outline the conditions required for efficient frequency conversion and introduce the concept of birefringent phase matching.

DIFFERENCE-FREQUENCY GENERATION (DFG) THEORY

For a detailed treatment of nonlinear optics and TWM, we refer to^{104–106}, which form the basis of this section. In a linear, homogeneous, dispersion-free dielectric medium, the

polarization \mathbf{P} induced by an electric field \mathbf{E} is given by,

$$\mathbf{P} = \epsilon_0 \chi \mathbf{E}, \quad (2.10)$$

where ϵ_0 is the vacuum permittivity and χ is the electric susceptibility. In a nonlinear dielectric, the electric susceptibility becomes electric field-dependent, and the electric susceptibility can be expanded as,

$$\chi = \chi^{(1)} + \chi^{(2)} \mathbf{E} + \chi^{(3)} \mathbf{E}^2 + \dots, \quad (2.11)$$

where $\chi^{(n)}$ is the n-th order electric susceptibility. Combining Eq. 2.10 and Eq. 2.11 yields,

$$\begin{aligned} \mathbf{P} &= \mathbf{P}^{(1)} + \mathbf{P}^{(2)} + \mathbf{P}^{(3)} + \dots \\ &= \epsilon_0 \chi^{(1)} \mathbf{E} + \epsilon_0 \chi^{(2)} \mathbf{E}^2 + \epsilon_0 \chi^{(3)} \mathbf{E}^3 + \dots. \end{aligned} \quad (2.12)$$

We consider an incoming electric field with two frequency components to an NLM that can be described as,

$$\mathbf{E}(t) = E_1 e^{-i\omega_1 t} + E_2 e^{-i\omega_2 t} + c.c., \quad (2.13)$$

where the subscript 1 (2) represents the light from the first (second) frequency component, and "c.c." stands for the complex conjugate of prior terms. Substituting this into Eq. 2.12, we find that the polarization contains terms oscillating at new frequencies,

$$\begin{aligned} \mathbf{P}(t) &= \epsilon_0 \chi^{(1)} \left[E_1 e^{-i\omega_1 t} + E_2 e^{-i\omega_2 t} + c.c. \right] + \\ &\quad \epsilon_0 \chi^{(2)} \left[E_1^2 e^{-2i\omega_1 t} + E_2^2 e^{-2i\omega_2 t} + 2E_1 E_2 e^{-i(\omega_1 + \omega_2)t} + 2E_1 E_2 e^{-i(\omega_1 - \omega_2)t} + c.c. \right] + \\ &\quad 2\epsilon_0 \chi^{(2)} \left[E_1 E_1^* + E_2 E_2^* \right] + \dots. \end{aligned} \quad (2.14)$$

From this result, it can be seen that the polarization in the medium starts to oscillate with frequencies differing from the input wave due to the nonlinear electric susceptibility. Considering the second-order contribution, we decompose the polarization into its frequency components,

$$P^{(2)}(t) = \sum_n P(\omega_n) e^{-i\omega_n t}, \quad (2.15)$$

we obtain,

$$P^{(2)}(t) = P(2\omega_1) e^{-2i\omega_1 t} + P(2\omega_2) e^{-2i\omega_2 t} + P(\omega_1 + \omega_2) e^{-i(\omega_1 + \omega_2)t} + P(\omega_1 - \omega_2) e^{-i(\omega_1 - \omega_2)t} + P(0), \quad (2.16)$$

where we can recognize different non-linear processes,

$$\begin{aligned} P(2\omega_1) &= \epsilon_0 \chi^{(2)} E_1^2 && \text{Second Harmonic Generation (SHG),} \\ P(2\omega_2) &= \epsilon_0 \chi^{(2)} E_2^2 && \text{Second Harmonic Generation (SHG),} \\ P(\omega_1 + \omega_2) &= 2\epsilon_0 \chi^{(2)} E_1 E_2 && \text{Sum-Frequency Generation (SFG),} \\ P(\omega_1 - \omega_2) &= 2\epsilon_0 \chi^{(2)} E_1 E_2^* && \text{Difference-Frequency Generation (DFG),} \\ P(0) &= 2\epsilon_0 \chi^{(2)} (E_1 E_1^* + E_2 E_2^*) && \text{Optical Rectification (OR).} \end{aligned} \quad (2.17)$$

The terms in the second-order polarization drive oscillations of the polarization in the medium with different frequencies than the input waves. For this work, we are interested in the DFG process where ω_1 is the SnV photon frequency, ω_{SnV} , and ω_2 the pump light frequency, denoted as ω_{pump} . The light that is generated by the DFG process has the target frequency $\omega_{\text{target}} = \omega_{\text{SnV}} - \omega_{\text{pump}}$.

To assess the efficiency of the DFG process, we need to know what the electric field is that is generated by the oscillating polarization, non-linear term of the polarization $P^{(2)}$, by solving the wave equation for a lossless, non-magnetic, and nonlinear dielectric. This relation is derived from Maxwell's equations where the polarization, \mathbf{P} , is considered a source to the system,

$$\nabla^2 \mathbf{E} + \frac{\boldsymbol{\epsilon}_r}{c^2} \frac{\partial^2 \mathbf{E}}{\partial t^2} = -\mu_0 \frac{\partial^2 P^{(2)}}{\partial t^2}, \quad (2.18)$$

where $\boldsymbol{\epsilon}_r$ is the frequency-dependent dielectric tensor, which is for an isotropic medium the refractive index $n = \sqrt{|\boldsymbol{\epsilon}|}$, c is the speed of light and μ_0 is the vacuum permeability. Continuing to follow the derivation of Boyd¹⁰⁴ the solutions are of the form of a plane wave along the z -axis: $E_m(z, t) = A_m(z)e^{i(k_m z - \omega_m t)} + c.c.$, where $A_m(z)$ is the amplitude of the wave with mode number m along z . We assume that the pump light is strong, and thus we consider the amplitude of the pump wave constant throughout the process (undepleted pump approximation). The solutions to Eq. 2.18 given by Boyd¹⁰⁴ for our DFG process are,

$$\frac{dA_{\text{SnV}}(z)}{dz} = \frac{2i\omega_{\text{SnV}}^2 d_{\text{eff}}}{k_{\text{SnV}}c^2} A_{\text{pump}}(z) A_{\text{target}}(z) e^{i\Delta k z}, \quad (2.19a)$$

$$\frac{dA_{\text{target}}(z)}{dz} = \frac{2i\omega_{\text{target}}^2 d_{\text{eff}}}{k_{\text{target}}c^2} A_{\text{pump}}^*(z) A_{\text{SnV}}(z) e^{i\Delta k z}, \quad (2.19b)$$

where $\Delta k = k_{\text{SnV}} - k_{\text{target}} - k_{\text{pump}}$ is the phase mismatch, d_{eff} is the effective nonlinear coefficient, proportional to χ , which is dependent on the propagation and polarization direction of the three waves and is material specific. We can evaluate the amplitude of the wave after passing through a medium of length, L , by integrating Eq. 2.19b over z ,

$$\begin{aligned} A_{\text{target}}(L) &= \kappa_{\text{target}} A_{\text{pump}}^* A_{\text{SnV}} \int_0^L e^{i\Delta k z} dz \\ &= \kappa_{\text{target}} A_{\text{pump}}^* A_{\text{SnV}} \frac{e^{i\Delta k L} - 1}{i\Delta k}, \end{aligned} \quad (2.20)$$

where we introduce $\kappa_{\text{target}} = \frac{2i\omega_{\text{target}}^2 d_{\text{eff}}}{k_{\text{target}}c^2}$ for readability. The intensity of the target wave is proportional to the modulus squared of the amplitude of the wave,

$$\begin{aligned} I_{\text{target}}(L) &\propto |A_{\text{target}}(L)|^2 \\ &\propto (|\kappa_{\text{target}}| |A_{\text{pump}}| |A_{\text{SnV}}|)^2 \left| \frac{e^{i\Delta k L} - 1}{i\Delta k} \right|^2 \\ &\propto |\kappa_{\text{target}}| |A_{\text{pump}}| |A_{\text{SnV}}|^2 L^2 \text{sinc}^2 \left(\frac{\Delta k L}{2} \right). \end{aligned} \quad (2.21)$$

It can be seen that the intensity is maximized when the phase matching condition is satisfied,

$$\text{Phase matching condition: } \Delta k = k_{\text{SnV}} - k_{\text{pump}} - k_{\text{target}} = 0. \quad (2.22)$$

Additionally, energy conservation must hold,

$$\text{Conservation of energy condition: } h\omega_{\text{target}} = h\omega_{\text{SnV}} - h\omega_{\text{pump}}, \quad (2.23)$$

where h is the Planck constant. However, achieving both conditions simultaneously is nontrivial. Substituting the dispersion relation, $k_i = \frac{n_i\omega_i}{c}$, into the phase matching condition, Eq. 2.22, where n is the refractive index, we obtain,

$$\begin{aligned} \Delta k &= \frac{1}{c} \left(n_{\text{SnV}}\omega_{\text{SnV}} - n_{\text{pump}}\omega_{\text{pump}} - n_{\text{target}}\omega_{\text{target}} \right) \\ &= \frac{1}{c} \left(n_{\text{SnV}}(\omega_{\text{target}} + \omega_{\text{pump}}) - n_{\text{pump}}\omega_{\text{pump}} - n_{\text{target}}\omega_{\text{target}} \right) \\ &= \frac{1}{c} \left(\omega_{\text{target}}(n_{\text{SnV}} - n_{\text{target}}) + \omega_{\text{pump}}(n_{\text{SnV}} - n_{\text{pump}}) \right), \end{aligned} \quad (2.24)$$

where in the second line we substituted ω_{SnV} using the conservation of energy condition $\omega_{\text{SnV}} = \omega_{\text{target}} + \omega_{\text{pump}}$. The phase matching conditions says $\Delta k = 0$. However, under normal dispersion, where $n(\omega)$ increases with frequency, $n_{\text{SnV}} > n_{\text{pump}} > n_{\text{target}}$, so we know that $n_{\text{SnV}} - n_{\text{target}} > 0$ and $n_{\text{SnV}} - n_{\text{pump}} > 0$, which shows that Eq. 2.24 cannot be equal to 0, hence, this equation cannot possess a solution.

BIREFRINGENT PHASE MATCHING (CRITICAL PHASE MATCHING)

There are ways to overcome this challenge, and this is the reason for all the current technology relying on non-linear optics, e.g., electro-optic modulators and tunable lasers. To overcome this, we use birefringent phase matching (also known as critical phase matching), which exploits the anisotropic refractive index of birefringent crystals. In such materials, light experiences different refractive indices depending on polarization and propagation direction relative to the optical axis, which is dependent on the crystal structure of the material. For light propagating in direction \vec{k} , we can define a plane consisting of the optical axis and \vec{k} . When the polarization of the light is perpendicular to this plane, we call it ordinary light, which experiences a refractive index n_o . For extraordinary light polarized in the plane formed by \vec{k} and the optical axis, the effective refractive index, $n_e(\theta)$, depends on the angle, θ , between the optical axis and \vec{k} ,

$$\frac{1}{n_e(\theta)^2} = \frac{\sin^2(\theta)}{\bar{n}_e^2} + \frac{\cos^2(\theta)}{n_o^2}, \quad (2.25)$$

where $\bar{n}_e^2 = n_e(\pi/2)$ is the principal value of the extraordinary refractive index.

By adjusting the angle θ , the refractive index of the extraordinary light is changed and can achieve phase matching. In practice, normal incidence of the light on the crystal is preferred, and simulations can determine how to cut the crystal such that phase matching is achieved. Next to small-angle tuning, we make use of the temperature

dependence of the birefringence of the material to realize the phase matching.

A drawback of birefringent phase matching is that the extraordinary light experiences spatial walk-off; the propagation is no longer along \vec{k} , which results in the ordinary and extraordinary light to diverge in the medium. This limits the interaction length and prevents the implementation of structures to confine the light and enhance the interaction, such as waveguides. To achieve high conversion efficiency, we enhance the pump light intensity using an optical cavity. The performance of this approach is analyzed in detail in Chap. 6.

2.5.2. DATA AVAILABILITY STATEMENT

The datasets of the data shown in this chapter and the Python software for analysis and plotting are publicly available on 4TU.ResearchData under Ref. ¹⁰⁷.

BIBLIOGRAPHY

- [1] H. J. Kimble, *The quantum internet*, Nature **453**, 1023 (2008).
- [2] S. Wehner, D. Elkouss and R. Hanson, *Quantum internet: A vision for the road ahead*, Science **362**, 6412 (2018).
- [3] A. J. Stolk *et al.*, *Metropolitan-scale heralded entanglement of solid-state qubits*, Science Advances **10**, 44 (2024).
- [4] L.-M. Duan, M. D. Lukin, J. I. Cirac and P. Zoller, *Long-Distance Quantum Communication with Atomic Ensembles and Linear Optics*, Nature **414**, 6862 (2001).
- [5] C. Simon and W. T. M. Irvine, *Robust Long-Distance Entanglement and a Loophole-Free Bell Test with Ions and Photons*, Physical Review Letters **91**, 110405 (2003).
- [6] M. Pompili *et al.*, *Realization of a multinode quantum network of remote solid-state qubits*, Science **372**, 6539 (2021).
- [7] N. H. Nickerson, J. F. Fitzsimons and S. C. Benjamin, *Freely Scalable Quantum Technologies Using Cells of 5-to-50 Qubits with Very Lossy and Noisy Photonic Links*, Phys. Rev. X **4**, 041041 (2014).
- [8] W. J. Munro, K. Azuma, K. Tamaki and K. Nemoto, *Inside Quantum Repeaters*, IEEE Journal of Selected Topics in Quantum Electronics **21**, 3 (2015).
- [9] M. Ruf, N. H. Wan, H. Choi, D. Englund and R. Hanson, *Quantum networks based on color centers in diamond*, Journal of Applied Physics **130**, 070901 (2021).
- [10] C. L. Degen, F. Reinhard and P. Cappellaro, *Quantum Sensing*, Reviews of Modern Physics **89**, 3 (2017).
- [11] S. L. N. Hermans *et al.*, *Qubit teleportation between non-neighbouring nodes in a quantum network*, Nature **605**, 663 (2022).
- [12] H. K. Beukers *et al.*, *Remote-Entanglement Protocols for Stationary Qubits with Photonic Interfaces*, PRX Quantum **5**, 010202 (2024).
- [13] S. Daiss *et al.*, *A Quantum-Logic Gate between Distant Quantum-Network Modules*, Science **371**, 6529 (2021).
- [14] C. M. Knaut *et al.*, *Entanglement of nanophotonic quantum memory nodes in a telecom network*, Nature **629**, 573 (2024).
- [15] H. Bernien *et al.*, *Heralded entanglement between solid-state qubits separated by three metres*, Nature **497**, 86 (2013).
- [16] J. Hofmann *et al.*, *Heralded Entanglement Between Widely Separated Atoms*, Science **337**, 6090 (2012).
- [17] A. Delteil *et al.*, *Generation of Heralded Entanglement between Distant Hole Spins*, Nature Physics **12**, 218 (2016).

- [18] D. L. Moehring *et al.*, *Entanglement of Single-Atom Quantum Bits at a Distance*, *Nature* **449**, 7158 (2007).
- [19] M. K. Bhaskar *et al.*, *Experimental demonstration of memory-enhanced quantum communication*, *Nature* **580**, 60 (2020).
- [20] B. Hensen *et al.*, *Loophole-free Bell inequality violation using electron spins separated by 1.3 kilometres*, *Nature* **526**, 682 (2015).
- [21] C. Bradley *et al.*, *A Ten-Qubit Solid-State Spin Register with Quantum Memory up to One Minute*, *Phys. Rev. X* **9**, 3 (2019).
- [22] M. H. Abobeih *et al.*, *Fault-tolerant operation of a logical qubit in a diamond quantum processor*, *Nature* **606**, 884 (2022).
- [23] E. D. Herbschleb *et al.*, *Ultra-long coherence times amongst room-temperature solid-state spins*, *Nat Commun* **10**, 1 (2019).
- [24] P. Neumann *et al.*, *Multipartite Entanglement Among Single Spins in Diamond*, *Science* **320**, 5881 (2008).
- [25] J. Randall *et al.*, *Many-body-localized discrete time crystal with a programmable spin-based quantum simulator*, *Science* **374**, 6574 (2021).
- [26] H. Bartling *et al.*, *Universal high-fidelity quantum gates for spin qubits in diamond*, *Phys. Rev. Appl.* **23**, 034052 (2025).
- [27] G. Thiering and A. Gali, *Ab Initio Magneto-Optical Spectrum of Group-IV Vacancy Color Centers in Diamond*, *Physical Review X* **8**, 021063 (2018).
- [28] U. Wahl *et al.*, *Direct Structural Identification and Quantification of the Split-Vacancy Configuration for Implanted Sn in Diamond*, *Phys. Rev. Lett.* **125**, 045301 (2020).
- [29] A. E. Rugar *et al.*, *Quantum Photonic Interface for Tin-Vacancy Centers in Diamond*, *Phys. Rev. X* **11**, 031021 (2021).
- [30] A. Sipahigil *et al.*, *An integrated diamond nanophotonics platform for quantum-optical networks*, *Science* **354**, 6314 (2016).
- [31] M. Pasini, *Nanophotonics with Diamond Color Centers*, Ph.D. thesis (2024).
- [32] E. Neu *et al.*, *Low-temperature investigations of single silicon vacancy colour centres in diamond*, *New J. Phys.* **15**, 043005 (2013).
- [33] J. N. Becker and C. Becher, *Coherence properties and quantum control of silicon vacancy color centers in diamond*, *Phys. Status Solidi A* **214**, 11 (2017).
- [34] C. J. Hepp, *Electronic Structure of the Silicon Vacancy Color Center in Diamond*, PhD Thesis, school Universität des Saarlandes, Saarlandes (2014).

- [35] T. Iwasaki *et al.*, *Germanium-Vacancy Single Color Centers in Diamond*, Scientific Reports **5**, 12882 (2015).
- [36] M. Bhaskar *et al.*, *Quantum Nonlinear Optics with a Germanium-Vacancy Color Center in a Nanoscale Diamond Waveguide*, Phys. Rev. Lett. **118**, 22 (2017).
- [37] P. Siyushev *et al.*, *Optical and Microwave Control of Germanium-Vacancy Center Spins in Diamond*, Physical Review B **96**, 081201 (2017).
- [38] E. A. Ekimov *et al.*, *Germanium-Vacancy Color Center in Isotopically Enriched Diamonds Synthesized at High Pressures*, JETP Letters **102**, 11 (2015).
- [39] M. E. Trusheim *et al.*, *Transform-Limited Photons From a Coherent Tin-Vacancy Spin in Diamond*, Phys. Rev. Lett. **124**, 023602 (2020).
- [40] J. Görlitz *et al.*, *Spectroscopic investigations of negatively charged tin-vacancy centres in diamond*, New J. Phys. **22**, 013048 (2020).
- [41] I. Karapatzakis *et al.*, *Microwave Control of the Tin-Vacancy Spin Qubit in Diamond with a Superconducting Waveguide*, Phys. Rev. X **14**, 031036 (2024).
- [42] P. Wang *et al.*, *Transform-Limited Photon Emission from a Lead-Vacancy Center in Diamond above 10 K*, Physical Review Letters **132**, 073601 (2024).
- [43] L. Robledo *et al.*, *High-Fidelity Projective Read-out of a Solid-State Spin Quantum Register*, Nature **477**, 574 (2011).
- [44] N. Kalb, P. C. Humphreys, J. J. Slim and R. Hanson, *Dephasing Mechanisms of Diamond-Based Nuclear-Spin Memories for Quantum Networks*, Physical Review A **97**, 062330 (2018).
- [45] R. Debroux *et al.*, *Quantum Control of the Tin-Vacancy Spin Qubit in Diamond*, Physical Review X **11**, 4 (2021).
- [46] K. D. Jahnke *et al.*, *Electron-Phonon Processes of the Silicon-Vacancy Centre in Diamond*, New Journal of Physics **17**, 043011 (2015).
- [47] S. Niese, *Measuring Microwave Pulse Induced Heating Using Decoherence of the Tin-Vacancy Spin in Diamond*, Master's thesis, Delft University of Technology (2022).
- [48] I. B. W. Harris and D. Englund, *Coherence of group-IV color centers*, Phys. Rev. B **109**, 085414 (2024).
- [49] F. Feuchtmayr *et al.*, *Enhanced spectral density of a single germanium vacancy center in a nanodiamond by cavity integration*, Appl. Phys. Lett. **123**, 2 (2023).
- [50] K. Kuruma *et al.*, *Controlling interactions between high-frequency phonons and single quantum systems using phononic crystals*, Nat. Phys. **21**, 77 (2025).

- [51] G. Wolfowicz *et al.*, *Quantum guidelines for solid-state spin defects*, *Nat Rev Mater* **6**, 10 (2021).
- [52] A. M. Stramma, *The Tin-Vacancy Centre in Diamond: A Coherent Spin-Photon Interface for Quantum Network Nodes*, PhD Thesis, Cambridge University (2024).
- [53] A. Dietrich *et al.*, *Isotopically Varying Spectral Features of Silicon-Vacancy in Diamond*, *New Journal of Physics* **16**, 11 (2014).
- [54] R. Høy Jensen *et al.*, *Cavity-Enhanced Photon Emission from a Single Germanium-Vacancy Center in a Diamond Membrane*, *Physical Review Applied* **13**, 064016 (2020).
- [55] Y. N. Palyanov, I. N. Kupriyanov, Y. M. Borzdov and N. V. Surovtsev, *Germanium: A New Catalyst for Diamond Synthesis and a New Optically Active Impurity in Diamond*, *Scientific Reports* **5**, 14789 (2015).
- [56] T. Iwasaki *et al.*, *Tin-Vacancy Quantum Emitters in Diamond*, *Phys. Rev. Lett.* **119**, 253601 (2017).
- [57] J. Görlitz *et al.*, *Coherence of a charge stabilised tin-vacancy spin in diamond*, *npj Quantum Inf* **8**, 45 (2022).
- [58] Y. Herrmann *et al.*, *Coherent Coupling of a Diamond Tin-Vacancy Center to a Tunable Open Microcavity*, *Phys. Rev. X* **14**, 041013 (2024).
- [59] I. P. Radko *et al.*, *Determining the Internal Quantum Efficiency of Shallow-Implanted Nitrogen-Vacancy Defects in Bulk Diamond*, *Optics Express* **24**, 24 (2016).
- [60] D. Riedel *et al.*, *Deterministic Enhancement of Coherent Photon Generation from a Nitrogen-Vacancy Center in Ultrapure Diamond*, *Phys. Rev. X* **7**, 031040 (2017).
- [61] X. Guo *et al.*, *Microwave-Based Quantum Control and Coherence Protection of Tin-Vacancy Spin Qubits in a Strain-Tuned Diamond-Membrane Heterostructure*, *Phys. Rev. X* **13**, 041037 (2023).
- [62] A. E. Rugar, C. Dory, S. Sun and J. Vučković, *Characterization of optical and spin properties of single tin-vacancy centers in diamond nanopillars*, *Phys. Rev. B* **99**, 205417 (2019).
- [63] S. D. Tchernij *et al.*, *Single-Photon-Emitting Optical Centers in Diamond Fabricated upon Sn Implantation*, *ACS Photonics* **4**, 10 (2017).
- [64] A. E. Rugar *et al.*, *Generation of Tin-Vacancy Centers in Diamond via Shallow Ion Implantation and Subsequent Diamond Overgrowth*, *Nano Lett.* **20**, 3 (2020).
- [65] J. M. Brevoord *et al.*, *Heralded initialization of charge state and optical-transition frequency of diamond tin-vacancy centers*, *Phys. Rev. Applied* **21**, 5 (2024).

- [66] S. Sachero, R. Waltrich, E. Corte, S. D. Tchernij and A. Kubanek, *Creation of Negatively Charged GeV and SnV centers in Nanodiamonds via Ion Implantation*, (2025), arXiv:2503.19490.
- [67] J. Arjona Martínez *et al.*, *Photonic Indistinguishability of the Tin-Vacancy Center in Nanostructured Diamond*, *Phys. Rev. Lett.* **129**, 17 (2022).
- [68] M. Pasini *et al.*, *Nonlinear Quantum Photonics with a Tin-Vacancy Center Coupled to a One-Dimensional Diamond Waveguide*, *Phys. Rev. Lett.* **133**, 023603 (2024).
- [69] A. E. Rugar *et al.*, *Narrow-Linewidth Tin-Vacancy Centers in a Diamond Waveguide*, *ACS Photonics* **7**, 9 (2020).
- [70] K. Kuruma *et al.*, *Coupling of a single tin-vacancy center to a photonic crystal cavity in diamond*, *Applied Physics Letters* **118**, 230601 (2021).
- [71] K. C. Chen *et al.*, *A scalable cavity-based spin–photon interface in a photonic integrated circuit*, *Optica Quantum* **2**, 2 (2024).
- [72] T. Lühmann *et al.*, *Charge-State Tuning of Single SnV Centers in Diamond*, *ACS Photonics* **7**, 12 (2020).
- [73] H. K. Beukers *et al.*, *Control of Solid-State Nuclear Spin Qubits Using an Electron Spin-1/2*, *Phys. Rev. X* **15**, 021011 (2025).
- [74] E. I. Rosenthal *et al.*, *Single-Shot Readout and Weak Measurement of a Tin-Vacancy Qubit in Diamond*, *Phys. Rev. X* **14**, 041008 (2024).
- [75] L. De Santis, M. Trusheim, K. Chen and D. Englund, *Investigation of the Stark Effect on a Centrosymmetric Quantum Emitter in Diamond*, *Phys. Rev. Lett.* **127**, 14 (2021).
- [76] S. Aghaeimeibodi, D. Riedel, A. E. Rugar, C. Dory and J. Vučković, *Electrical Tuning of Tin-Vacancy Centers in Diamond*, *Phys. Rev. Applied* **15**, 6 (2021).
- [77] G. Clark *et al.*, *Nanoelectromechanical Control of Spin–Photon Interfaces in a Hybrid Quantum System on Chip*, *Nano Letters* **24**, 4 (2024).
- [78] J. M. Brevoord *et al.*, *Large-range tuning and stabilization of the optical transition of diamond tin-vacancy centers by in situ strain control*, *Appl. Phys. Lett.* **126**, 17 (2025).
- [79] L. Li *et al.*, *Heterogeneous integration of spin–photon interfaces with a CMOS platform*, *Nature* **630**, 70 (2024).
- [80] Y. Narita *et al.*, *Multiple Tin-Vacancy Centers in Diamond with Nearly Identical Photon Frequency and Linewidth*, *Phys. Rev. Applied* **19**, 024061 (2023).
- [81] V. Bushmakina *et al.*, *Two-Photon Interference of Photons from Remote Tin-Vacancy Centers in Diamond*, (2024), arXiv:2412.17539.

- [82] C. G. Torun *et al.*, *SUPER and subpicosecond coherent control of an optical qubit in a tin-vacancy color center in diamond*, (2023), arXiv:2312.05246.
- [83] R. A. Parker *et al.*, *A diamond nanophotonic interface with an optically accessible deterministic electronuclear spin register*, *Nat. Photon.* **18**, 156 (2024).
- [84] I. B. Harris *et al.*, *Hyperfine Spectroscopy of Isotopically Engineered Group-IV Color Centers in Diamond*, *PRX Quantum* **4**, 040301 (2023).
- [85] E. I. Rosenthal *et al.*, *Microwave Spin Control of a Tin-Vacancy Qubit in Diamond*, *Phys. Rev. X* **13**, 031022 (2023).
- [86] J. M. Smith, S. A. Meynell, A. C. Bleszynski Jayich and J. Meijer, *Colour centre generation in diamond for quantum technologies*, *Nanophotonics* **8**, 11 (2019).
- [87] C. Bradac, W. Gao, J. Forneris, M. E. Trusheim and I. Aharonovich, *Quantum nanophotonics with group IV defects in diamond*, *Nat. Commun.* **10**, 5625 (2019).
- [88] S. Mi, M. Kiss, T. Graziosi and N. Quack, *Integrated photonic devices in single crystal diamond*, *J. Phys. Photonics* **2**, 042001 (2020).
- [89] L. V. H. Rodgers *et al.*, *Materials challenges for quantum technologies based on color centers in diamond*, *MRS Bulletin* **46**, 7 (2021).
- [90] E. van Leeuwen, *Fabrication of a Nano-Electro-Mechanical System to strain individual tin-vacancy centres in diamond*, Master's thesis, Delft University of Technology (2023).
- [91] T. Schröder *et al.*, *Scalable focused ion beam creation of nearly lifetime-limited single quantum emitters in diamond nanostructures*, *Nat Commun* **8**, 15376 (2017).
- [92] D. Farfurnik *et al.*, *Enhanced concentrations of nitrogen-vacancy centers in diamond through TEM irradiation*, *Appl. Phys. Lett.* **111**, 12 (2017).
- [93] Y.-C. Chen *et al.*, *Laser writing of coherent colour centres in diamond*, *Nature Photon* **11**, 77 (2017).
- [94] F. P. Bundy, *The P, T phase and reaction diagram for elemental carbon*, 1979, *Journal of Geophysical Research: Solid Earth* **85**, B12 (1980).
- [95] T. Baba *et al.*, *Annealing Time Dependence on Creation of SiV, GeV, and SnV in Diamond by Atmospheric Annealing at 1800 °C*, *physica status solidi (a)* **222**, 5 (2025).
- [96] J. F. Geus *et al.*, *Low-noise short-wavelength pumped frequency downconversion for quantum frequency converters*, *Optica Quantum* **2**, 3 (2024).
- [97] A. Ruskuc *et al.*, *Multiplexed entanglement of multi-emitter quantum network nodes*, *Nature* **639**, 54 (2025).
- [98] G. Pieplow *et al.*, *Quantum electrometer for time-resolved material science at the atomic lattice scale*, *Nat Commun* **16**, 6435 (2025).

- [99] W. Gambling, *The rise and rise of optical fibers*, IEEE Journal of Selected Topics in Quantum Electronics **6**, 6 (2000).
- [100] A. Tchebotareva *et al.*, *Entanglement between a Diamond Spin Qubit and a Photonic Time-Bin Qubit at Telecom Wavelength*, Phys. Rev. Lett. **123**, 063601 (2019).
- [101] A. Stolk *et al.*, *Telecom-Band Quantum Interference of Frequency-Converted Photons from Remote Detuned NV Centers*, PRX Quantum **3**, 020359 (2022).
- [102] M. Iuliano *et al.*, *Qubit teleportation between a memory-compatible photonic time-bin qubit and a solid-state quantum network node*, npj Quantum Inf **10**, 1 (2024).
- [103] K. L. Van Der Enden, *Metropolitan-scale quantum networks with diamond qubits*, Ph.D. thesis (2025).
- [104] R. W. Boyd, *Nonlinear Optics*, 3rd ed. (Academic Press, USA, 2008).
- [105] R. Kaltenbaek, *Photonics II - Lectures*, University lecture (2020).
- [106] S. Zaske, *Quantum Frequency Down-Conversion of Single Photons in Nonlinear Optical Waveguides*, Ph.D. thesis (2013).
- [107] J. M. Brevoord, *Data underlying the dissertation "Control of the optical interface of color centers in diamond"*, (2025).

3

LASER-CUT PATTERNED, MICROMETER-THIN DIAMOND MEMBRANES WITH COHERENT COLOR CENTERS FOR OPEN MICROCAVITIES

**Y. Herrmann^{*}, J. M. Brevoord^{*}, J. Fischer^{*}, S. Scheijen, N. Codreanu, L.G. C. Wienhoven,
Y. M. Q. van der Graaf, C. F. J. Wolfs, R. Méjard, M. Ruf, N. de Jong, R. Hanson.**

Micrometer-scale thin diamond devices are key components for various quantum sensing and networking experiments, including the integration of color centers into optical microcavities. In this work, we introduce a laser-cutting method for patterning microdevices from millimeter-sized diamond membranes. The method can be used to fabricate devices with micrometer thicknesses and edge lengths of typically $10\ \mu\text{m}$ to $100\ \mu\text{m}$. We compare this method with an established nanofabrication process based on electron-beam lithography, a two-step transfer pattern utilizing a silicon nitride hard mask material, and reactive ion etching. Microdevices fabricated using both methods are bonded to a cavity Bragg mirror and characterized using scanning cavity microscopy. We record two-dimensional cavity finesse maps over the devices, revealing insights about the variation in diamond thickness, surface quality, and strain. The scans demonstrate that devices fabricated by laser-cutting exhibit similar properties to devices obtained by the conventional method. Finally, we show that the devices host optically coherent Tin- and Nitrogen-Vacancy centers suitable for applications in quantum networking.

^{*}These authors contributed equally to this work

The results of this chapter, excluding section 3.8 have been published in *Materials for Quantum Technology*, 5, 035001 (2025), ¹.

3.1. INTRODUCTION

Single-crystal (sub) micrometer-thin diamond samples hosting coherent color centers are relevant for several quantum technology applications spanning from quantum networking to sensing. In quantum networking, such platforms can be used to engineer the photonic environment of color centers for enhanced photon collection²⁻⁵. This includes photonic crystal cavities, fabricated directly into the diamond⁶⁻⁹ and thinned-down membranes, coated from both sides with a dielectric layer, which can function as an optical antenna¹⁰. Furthermore, such platforms can be incorporated into open microcavities¹¹⁻¹³ and they facilitate the manufacturing of heterogeneous photonic structures such as solid immersion lenses¹⁴, nanophotonic resonators^{15,16} or plasmonic nanogap cavities¹⁷.

In quantum sensing, chemically inert and bio-compatible, thin diamond samples can bring color centers near other materials, while still providing optical access. This can be used in sensing of living cells¹⁶, wide-field microscopy of electrical currents¹⁸, or magnetic fields¹⁹⁻²³.

In this work, our main focus is on the fabrication of diamond microdevices for open microcavities to Purcell-enhance color centers hosted inside the device. While pioneering work made use of color centers in nanodiamonds²⁴⁻²⁶, a micrometer-thin diamond sample is beneficial to maintain good optical coherence, especially in the case of Nitrogen-Vacancy centers^{27,28}. Such diamond samples have been used to couple Nitrogen-Vacancy and group-IV vacancy centers to open microcavities²⁹⁻³². The coupling of color centers to the cavity is quantified by the Purcell factor, which is proportional to Q/V , where Q denotes the cavity quality factor and V is the cavity mode volume. To demonstrate significant Purcell enhancement of color centers, the following microdevice properties must be taken into consideration: (1) A thickness of a few micrometers (or less) is desired to minimize the cavity mode volume. (2) A smooth surface (roughness $R_q \lesssim 1$ nm) is needed to maintain a high cavity quality factor (finesse). (3) Large lateral dimensions (tens of micrometers) with a small wedge are beneficial to provide an area to probe several cavity spots (cavity beam waist is on the order of a micrometer). (4) Bonding to a cavity Bragg mirror at a micrometer distance to a stripline for delivering microwaves³³ or static electric fields³⁴ is necessary. (5) The sample should contain color centers with good optical properties for quantum science and technology applications. While these criteria are relevant for the microcavity platform, they are also relevant to most of the applications mentioned.

Several fabrication methods have been developed to realize (sub) micrometer-thin diamond samples. These include the fabrication methods listed in the following: smart cut makes use of the implantation of light ions (like Carbon³⁵ or Helium³⁶) to produce a sacrificial layer of amorphous carbon, which can be removed electrochemically^{7,37}. Additional overgrowth is necessary for a high crystalline quality thin film diamond released from the sacrificial layer³⁸. In a diamond-on-insulator approach, a thin diamond membrane is bonded to a host (e.g. silicon) substrate and subsequently thinned

down to the required thickness^{6,8,39–41}. Furthermore, $\sim 50\ \mu\text{m}$ diamond microdevices can be patterned in a one-step (e.g. with a hydrogen silsesquioxane (HSQ) mask⁴²) or two-step pattern transfer process (e.g. with a silicon nitride (Si_xN_y) hard mask⁴³) and thinned down by dry etching and a heterogeneously integrated mask (e.g. a fused quartz mask⁴⁴). Alternatively, such diamond membranes can be first bonded to the cavity mirror and then thinned down with a fused quartz²⁷ or diamond⁴⁵ mask. Other methods start from bulk diamond and use an undercutting process (via angled plasma etching⁴⁶ or quasi-isotropic plasma etching⁴⁷). Moreover, the production of free-standing diamond nanoslabs with a Chromium protection mask and dry etching has been demonstrated⁴⁸. These fabrication methods are typically complex, labor-intensive, and necessitate additional equipment for the pattern transfer, lithography tools, and deposition tools to define microstructures in lateral dimensions.

In this work, we present a fabrication method for patterning microdevices of different sizes and shapes using laser-cutting to engrave $\sim 50\ \mu\text{m}$ thick diamond membranes. This approach utilizes only two fabrication tools (a femtosecond pulsed laser writer and a reactive ion etcher), significantly simplifying the process, reducing its duration, and increasing accessibility. The method allows to achieve feature sizes of approximately $3\ \mu\text{m}$, limited by the laser spot size. We compare this new fabrication method with an already established method of patterning the diamond membrane with electron-beam lithography (EBL) based on two-step patterning: the desired design is EBL patterned into a resist, followed by a reactive ion etch (RIE) to transfer the pattern into a hard mask material. Next, the hard mask pattern is transferred into the diamond membrane via RIE⁴³. Diamond microdevices obtained from both fabrication methods are then subsequently bonded to a cavity Bragg sample mirror, equipped with striplines for microwave delivery, see Fig. 3.1 (a) and (b). To demonstrate that the laser-cut microdevices are suitable for microcavity applications, we characterize the microdevices by scanning cavity microscopy (SCM)^{49–51}, see Fig. 3.1 (d). This demonstrates that both methods lead to microdevices with comparable cavity quality factors (cavity finesses). Furthermore, we study the optical properties of negatively charged Tin-Vacancy (SnV) and negatively charged Nitrogen-Vacancy (NV) centers embedded in diamond microdevices at low temperatures. Both methods result in devices suitable for microcavity applications in quantum networking.

3.2. FABRICATION OF DIAMOND MICRODEVICES

The two fabrication methods are compared and described in detail in the following. The process flow of both methods can be divided into five steps: sample preparation, patterning, color center creation, device release etch, and bonding. Specifically, the two methods majorly differ in the patterning fabrication step, where the method presented here foresees a design pattern transfer via laser-cutting. In contrast, the conventional fabrication method foresees a two-step transfer pattern based on EBL. The laser-cut method with SnV center creation is schematically summarized in Fig. 3.1 (c). The conventional EBL-based fabrication method is detailed in⁴³. Detailed fabrication steps and parameters can be found in the Appendix Tab. 3.1.

3.2.1. SAMPLE PREPARATION

For both methods, we follow the sample preparation step outlined in Ref.²⁷. We start with commercially available single-crystal, electronic-grade bulk diamonds, measuring $(2 \times 2) \text{ mm}^2$ and 0.5 mm in thickness with a face-orientation of $\langle 100 \rangle$, grown by chemical vapor deposition. The diamonds are laser-sliced into three $\sim 50 \mu\text{m}$ thick membranes and polished on both sides (Almax EasyLab). The roughness of the polished surface is typically $R_q < 1 \text{ nm}$. Before patterning, the membranes are cleaned by fuming nitric acid (65 %) at room temperature (step (1) in Fig. 3.1 (c)).

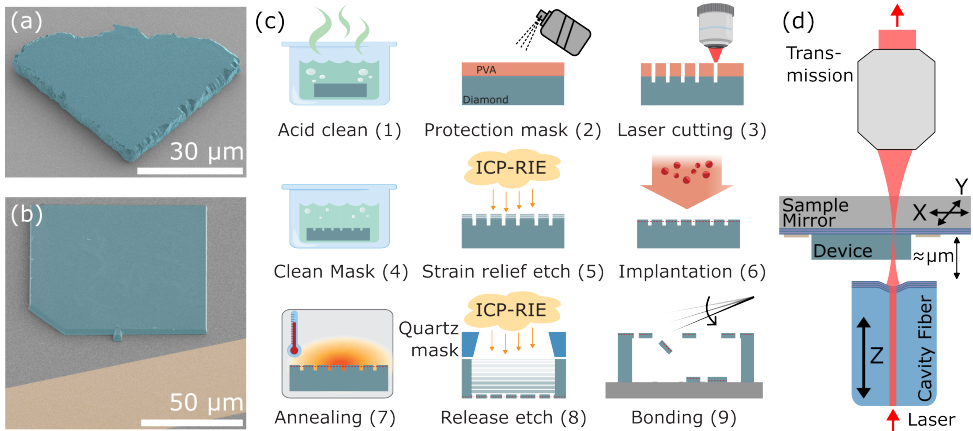


Figure 3.1: False-colored (cyan) scanning electron microscope (SEM) images of diamond microdevices obtained by laser-cutting (device originated from a parent diamond membrane named: *Vincent Vega*) in (a) and electron-beam lithography, and dry etching with a silicon nitride hard mask (*Pai Mei*) in (b). The devices are bonded to the cavity mirror. A gold stripline (yellow false-colored) can be used for microwave delivery. (c) Process flow to fabricate laser-cut diamond microdevices with Tin-Vacancy centers bonded to the cavity mirror. PVA: polyvinyl alcohol, ICP-RIE: inductively coupled plasma reactive ion etching. (d) Schematic of the scanning cavity microscope. The cavity is optically probed from the fiber side, and the transmission is detected. The sample mirror with the bonded diamond microdevices is scanned laterally in front of the fiber.

3.2.2. PATTERNING

Patterns of arbitrary microdevice designs are transferred into the $\sim 50 \mu\text{m}$ thick diamond membrane via the two methods by selectively removing diamond material. In the case of the laser-cutting method, the diamond membrane is coated with a polyvinyl alcohol (PVA) mask using standard PVA-based hairspray (step (2)). Next, approximately $10 \mu\text{m}$ to $15 \mu\text{m}$ deep trenches are created with a femtosecond-pulsed laser (Lasertec), transferring an arbitrary design into the diamond membrane (step (3))⁵². After patterning, the PVA mask is removed via an ultrasonic bath in de-ionized (DI) water (H_2O) and acetone for 10 min each at room temperature (step (4)), followed by inorganic wet cleaning in a Piranha mixture (ratio 3:1 of H_2SO_4 (95 %) : H_2O_2 (31 %)) at 80°C for 20 min. In the next step, the surface is treated with a strain relief etch for cleaning and to remove the residual polishing-induced strain from the membrane surface (step (5))⁴². The membrane is mounted with PMMA495 A4 on a fused quartz carrier wafer and etched

with inductively coupled plasma reactive ion etching (ICP/RIE) for 35 min in Ar/Cl₂ plasma chemistry, followed by 7 min etch in O₂ plasma chemistry (Oxford Instruments, Plasmalab System 100). This removes ~ 1.4 μm and ~ 2.1 μm, respectively, of diamond material from the surface. Alternatively, the strain relief etch can also be performed with a cyclic Ar/Cl₂ and O₂ recipe to improve surface roughness, as demonstrated in Ref. ⁴⁵.

The EBL method starts with processing the diamond membrane with a strain relief etch as described above (with different etching times). After the color center creation (described below), a ~ 320 nm thin Si_xN_y layer hard mask material is deposited on the top diamond surface by plasma-enhanced chemical vapor deposition (PECVD, Oxford Instruments Plasmalab 80 Plus). Next, CSAR-13 (AR-P 6200.13) positive tone resist is spin-coated, followed by the spin coating of Electra 92 (AR-PC 5090) conductive polymer to prevent charging effects during EBL exposure (Raith EPBG-5200). Before the development step, the Electra 92 is removed in deionized water and blow-dried with nitrogen. The resist is then developed by immersing the sample for 1 min in pentyl acetate, 5 s in ortho-xylene, 1 min in isopropyl alcohol (IPA), and blow-drying with nitrogen. The pattern is transferred into the Si_xN_y hard mask layer via ICP/RIE (Adixen AMS 100 I-speeder) in a CHF₃/O₂ based plasma chemistry⁵³. The resist is removed in a two-fold step: first, a coarse resist removal is executed by immersing the sample in a PRS 3000 positive resist stripper solution, followed by a second fine resist removal in a Piranha mixture clean, which is executed two times. Next, the pattern is transferred from the Si_xN_y hard mask into the diamond membrane by ICP/RIE with an O₂ plasma (Oxford Instruments, Plasmalab System 100), resulting in a trench depth of around 6 μm to 10 μm. The Si_xN_y hard mask is then removed by wet inorganic etch in hydrofluoric (HF) acid (40 %) for 15 min at room temperature.

3.2.3. COLOR CENTER CREATION

SnV centers are created in the diamond membrane by ion implantation of Tin (¹²⁰Sn) at an implantation energy of 350 keV and a dose of 3×10^{10} ions/cm² under an implantation angle of 7° (step (6)). The desired implantation energy is determined using Stopping Range of Ions in Matter (SRIM) simulations⁵⁴, resulting in an implantation depth of ~ 90 nm (straggle of ~ 17 nm), and the implantation angle is adopted to prevent ion channeling effects. For laser-cut samples, ion implantation is performed after patterning and strain relief etch. For EBL samples, the ion implantation is performed after the strain relief etch, but before the patterning step.

For the generation of NV centers with high optical coherence, we employ electron irradiation with minimal crystal damage to generate NV centers from the native nitrogen concentration^{27,34,55}. We irradiate and anneal the bulk diamonds before laser-slicing into membranes, but this step can also be performed later in the process. Irradiation is realized at the Reactor Institute in Delft with an electron-beam acceleration energy of 2 MeV and a dose of 4×10^{13} e⁻/cm². The energy leads to penetration of electrons through the full diamond (for both substrates used in this study, the 0.5 mm thick bulk and ~ 50 μm membranes). This results in lattice vacancies formed over the full thickness extent of the diamond substrates.

After the implantation and the irradiation steps, the diamond substrates are processed with a tri-acid clean (mixture of 1:1:1 ratio of H_2SO_4 (97 %): HNO_3 (65 %): HClO_4 (60 %)) at 120 °C for one hour. To enable vacancy migration and to activate color centers, as well as to remove defects (such as divacancies from the lattice), the samples are high-temperature annealed (at a pressure of $\sim 1 \times 10^{-6}$ mBar) with a temperature of up to 1100 °C (step (7)), followed by a tri-acid clean to remove any created graphite during the annealing step²⁷. Both ways to create color centers (implantation and electron irradiation) are compatible with the two demonstrated fabrication methods.

3.2.4. DEVICE RELEASE ETCH

To release the structures, the membrane with the patterned side facing down is placed on a fused quartz wafer. A 0.5 mm thick fused quartz mask with a 1.4 mm rectangular central opening and angled sidewalls (30°) is positioned and aligned on top of the back surface of the diamond membrane²⁷. The mask allows the etching plasma to access the back surface of the diamond membrane over the entire opening area, whereas areas of the membrane covered yield a supporting diamond frame. The center part of the membrane is etched with an ICP/RIE process (Oxford Instruments, Plasmalab System 100) composed of Ar/ Cl_2 for 45 min for cleaning and smoothening the surface, followed by consecutive multiple rounds of O_2 plasma deep etching (step (8), depending on the diamond membrane thickness). Between etching rounds, the membrane is inspected under an optical light microscope to assess the progressing thickness and verify the release of the microdevices, connected to the parent membrane by a small tether by design. The device release etch step is concluded when the target thickness is reached.

3.2.5. BONDING

Prior to the diamond microdevice bonding to the cavity sample mirrors¹³, microwave striplines can be fabricated on top of the mirrors. These are produced by an EBL and lift-off fabrication process, resulting in 5 nm titanium and 75 nm thick, 50 μm wide gold striplines. A wet inorganic Piranha clean concludes the microwave stripline fabrication, improving the bonding quality of the diamond microdevices. The stripline fabrication process does not reduce the cavity mirror reflectivity, as demonstrated in Ref.³³.

The bonding is performed by a four-degrees-of-freedom, piezo micromanipulator (Imina Technologies SA, miBots), used to controllably break the tether and release the diamond microdevices from the parent membrane (shown in Appendix Fig. 3.7 (a), see also Supplementary Video 1). As a result, the microdevices land on the cavity mirror, aligned and positioned under the parent diamond membrane such that proximity to the microwave striplines is ensured (step (9)). The micromanipulator is equipped with a 0.6 μm fine tungsten needle (Ted Pella, Ultrafine Tungsten Manipulator Probe). To increase the probability of obtaining well-bonded devices, the surface of the cavity mirror can be activated for 30 min inside an Ozone chamber (BioForce Nanosciences UV/Ozone ProCleaner), which removes organic contamination on the molecular level. In addition, the overall parent diamond membrane with the released microdevices can

be cleaned in HF (40 %) at room temperature. A well-bonded device exhibits a color matching with the mirror surface and does not show any interference patterns. Furthermore, these devices do not move when a lateral force with the micromanipulator tip is applied. Bonded microdevices from both fabrication methods are shown in Fig. 3.1 (a) and (b), measured with an SEM, and in Fig. 3.2 (a) and (c) with a light microscope.

In contrast, devices that are not fully bonded are typically identified by wave-like interference patterns (Newton's rings) or an opaque appearance (see Appendix Fig. 3.7 (b) and (c)). Unbonded devices can be repositioned on the mirror surface for alignment, such as placement near the stripline. For some devices, gentle force or tapping with the micromanipulator has resulted in bonding. Both fabrication methods, laser-cutting (Fig. 3.2 (a)) and EBL (Fig. 3.2 (c)), produce well-bonded devices.

3.2.6. FABRICATION RESULTS

Representative examples of bonded microdevices fabricated with the two methods presented in the previous sections are shown in Fig. 3.2. A laser-cut (70×70) μm^2 , ~ 2.5 μm thin microdevice shown in Fig. 3.2 (a) hosts SnV centers. The corresponding height map in Fig. 3.2 (b) is measured by a white light interferometer (Bruker ContourX-500) and yields a wedge with a slope of ~ 0.7 $\mu\text{m}/100\mu\text{m}$. The second microdevice, fabricated by EBL is (90×90) μm^2 in size and around 3.5 μm thin, shown in Fig. 3.2 (c) and contains NV centers. The height maps (Fig. 3.2 (d)) shows a wedge of ~ 1.4 $\mu\text{m}/100\mu\text{m}$. The higher gradient wedge indicates that this device originated from the outer region of the parent diamond membrane, where the etched profile is less homogeneous, because of the proximity effect due to the fused quartz mask. The determined wedge of both microdevices enables the investigation of the two different mode types, which are formed in the diamond-microcavity system (air-like and diamond-like, see next section).

The laser-cutting method yields devices with a significantly higher surface roughness for an extent of ~ 10 μm from the edges when compared to the EBL method obtained devices (compare Fig. 3.2 (a) to (c)). Beyond the high surface roughness extent of ~ 10 μm , the inner area of the laser-cut microdevice shows a comparable surface quality to the devices fabricated by EBL.

Both methods lead to the successful fabrication of microdevices with high-quality surfaces in the center, suitable for microcavity experiments (next section).

3.3. SCANNING CAVITY MICROSCOPY

In this section, we use SCM (see Supplementary Video 2) to study the quality of the bonded diamond microdevices. The experiments involve finesse measurements of the microcavity that give insights into cavity losses and allow us to conclude the diamond device surface wedge and quality. For this, we first introduce a cavity loss model to describe the finesse determined in length as done in our cavity finesse measurements.

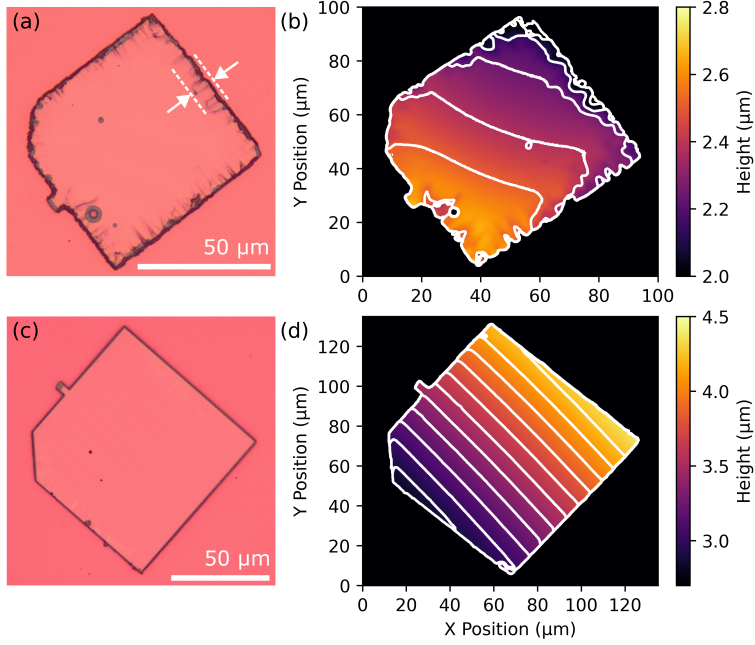


Figure 3.2: Comparison of diamond microdevices fabricated by laser-cutting and EBL. (a) Optical light microscope picture of the laser-cut microdevice (*Vincent Vega*). The rougher edge (indicated by the $10\ \mu\text{m}$ spaced, dashed lines) of the laser-cut microdevice is visible. (b) The corresponding height map is measured with a white light interferometer. The white lines are overlaid and indicate a microdevice thickness matching air-like modes with $q = 16$ to $q = 19$, calculated by equation (3.1). (c) Optical light microscope picture of the EBL microdevice (*Pai Mei*). (d) Corresponding height map with diamond thicknesses leading to an air-like mode of $q = 22$ to $q = 32$, calculated by equation (3.1). Both devices are well-bonded to the underlying (pink) cavity mirror. The height data of the white light interferometer is stated with respect to the mirror surface.

3.3.1. CAVITY LOSS MODEL

We consider a hemispherical plano-concave microcavity, where both Bragg mirrors are terminated with a high refractive index material and the diamond microdevices are bonded to the (flat) sample mirror (see Fig. 3.1 (d)). The cavity finesse $\mathcal{F} = 2\pi/\mathcal{L}_{\text{eff}}$ is inversely proportional to the sum of the effective losses \mathcal{L}_{eff} . Together with the known mirror transmission loss values, this results in a complete understanding of the system. Most fundamentally, the diamond devices change the sample mirror transmission loss for a given probe laser wavelength depending on their thickness. Hereby so-called air-like and diamond-like mode^{11,56} thicknesses can be defined:

$$t_d = q \frac{\lambda}{2n_d} \quad (\text{air-like}), \quad t_d = (2q+1) \frac{\lambda}{4n_d} \quad (\text{diamond-like}), \quad (3.1)$$

with a corresponding fundamental mode number q and the refractive index of diamond $n_d = 2.41$ ⁵⁷ (for our laser wavelength of $\lambda = 637\ \text{nm}$). For the air-like (diamond-like) modes, the mirror transmission loss is minimal (maximal). This phenomenon is associated with the electric field intensity ratio of the air and the diamond part of the cavity.

A consecutive air-like and diamond-like mode is separated by a diamond thickness of $\lambda/(4n_d) \approx 66$ nm and hence can indicate a device thickness wedge.

To include further diamond-related loss mechanisms, we can model the effective losses for the here conducted finesse measurements with:

$$\mathcal{L}_{\text{eff}} = \mathcal{L}_{M,a} + \frac{n_d E_{\text{max,d}}^2}{E_{\text{max,a}}^2} (\mathcal{L}_{M,d} + \mathcal{L}_{A,d} + \mathcal{L}_{S,\text{eff,d}}) + \mathcal{L}_{\text{add}}. \quad (3.2)$$

In this equation, $\mathcal{L}_{M,a}$ accounts for the loss through the air-side mirror and \mathcal{L}_{add} considers any additional losses. The fraction $n_d E_{\text{max,d}}^2 / E_{\text{max,a}}^2$ describes the electric field intensity ratio between the air and diamond part, and can be calculated by⁵⁶:

$$\left(\frac{n_d E_{\text{max,d}}^2}{E_{\text{max,a}}^2} \right)^{-1} = \frac{1}{n_d} \sin^2 \left(\frac{2\pi n_d t_d}{\lambda} \right) + n_d \cos^2 \left(\frac{2\pi n_d t_d}{\lambda} \right). \quad (3.3)$$

The ratio depends on the diamond thickness and leads to the modulation of the finesse values between air-like ($n_d E_{\text{max,d}}^2 / E_{\text{max,a}}^2 = 1/n_d$) and diamond-like modes ($n_d E_{\text{max,d}}^2 / E_{\text{max,a}}^2 = n_d$). The modulated losses are: the diamond-side sample mirror loss $\mathcal{L}_{M,d}$, the absorption losses $\mathcal{L}_{A,d}$ and the scattering losses at the air-diamond interface $\mathcal{L}_{S,\text{eff,d}}$. The absorption losses can be calculated with the diamond absorption coefficient α to $\mathcal{L}_{A,d} \approx 2\alpha t_d$, while the scattering losses can be calculated by⁵⁶:

$$\mathcal{L}_{S,\text{eff,d}} \approx \sin^2 \left(\frac{2\pi n_d t_d}{\lambda} \right) \frac{(n_d + 1)(n_d - 1)^2}{n_d} \left(\frac{4\pi\sigma_{DA}}{\lambda} \right)^2. \quad (3.4)$$

Here, σ_{DA} includes the device surface roughness at the air-diamond interface. For an air-like mode, the scattering losses are zero, while they become maximal in a diamond-like mode. The cavity finesse on the diamond is thus also a measure of the surface roughness.

3.3.2. CAVITY FINESSE MEASUREMENTS

We characterize the diamond microdevices by two-dimensional scans, in which the cavity finesse is measured on each lateral spot with a room temperature fiber-based Fabry-Pérot microcavity, schematically depicted in Fig. 3.1(d) (scanning cavity microscopy⁵⁸). The (1×1) cm² sample mirror, on which the diamond devices are bonded, is scanned laterally with a piezo nanopositioning stage in steps of 0.2 μm . Technical details about the microcavity setup can be found in 3.7.3. An individual finesse measurement is performed by scanning the cavity length over two fundamental modes while probing the cavity transmission with a resonant laser, shown in Appendix Fig. 3.9 (a). We record all measurements with cavity lengths below 15 μm , to ensure that the cavity finesse is not limited by clipping losses (see Appendix Fig. 3.9 (b) for characterization of the cavity fiber). A scan of the two devices fabricated by laser-cutting and EBL is presented in Fig. 3.3 (a) and (c).

The mirror coatings (Laseroptik) are designed to be maximally reflective for 637 nm light with $\mathcal{L}_{M,a} = 50$ ppm ($\mathcal{L}_{M,d} = 670$ ppm for diamond termination) losses for the fiber tip

(sample) mirror. As follows from equation (3.2), in a bare cavity ($t_d = 0 \mu\text{m}$), scattering and absorption losses vanish and the sample mirror transmission losses translate to the air-terminated value of $1/n_d \times \mathcal{L}_{M,d} = 280 \text{ ppm}$. The measured finesse around 8000 (see green distributions in Fig. 3.3 (b) and (d)) indicates additional losses around $\mathcal{L}_{\text{add}} = 470 \text{ ppm}$. We attribute these additional losses to the quality of the concave fiber tip.

On both diamond microdevices in Fig. 3.3 (a) and (c), the finesse shows a clear modulation with the same pattern as in the diamond thickness variation from Fig. 3.2 (b) and (d). We associate the variation in finesse values with the alternation between air-like modes (higher finesse) and diamond-like modes (lower finesse). In the air-like modes, only a slight reduction of the cavity finesse compared to the bare cavity is observed. For the diamond-like modes, the finesse is much reduced. The cavity transmission on the EBL device (*Pai Mei*) is reduced around diamond-like mode regions so much that no finesse can be determined. Some thin lines with reduced finesse are visible in the scan in Fig. 3.3 (c), which are attributed to transverse-mode mixing⁵⁸.

To study the effect of the diamond microdevices more quantitatively, we investigate the finesse depending on the device thickness. This data is obtained by overlaying the white light interferometer data from Fig. 3.2 (b) and (d) with the finesse scans from Fig. 3.3 (a) and (c). The interferometer data has a sufficient lateral resolution of about $0.13 \mu\text{m}$ per step. For every measured finesse value, within the white rectangle in the scan, we take the corresponding diamond thickness from the interferometer data. This is shown in Fig. 3.4 for both diamond devices.

We notice that the absolute thickness values from the white light interferometer do not directly match the expected positions of the air-like and diamond-like modes according to equation (3.1). The measured values might be distorted due to the multilayer Bragg mirror on which the devices are bonded. We compensate for this by measuring the diamond thickness using the cavity mode dispersion (Appendix Fig. 3.10) on an air-like mode on the diamond (indicated in Fig. 3.3) to determine an offset for the diamond thickness values. The absolute thickness from the white light interferometer and the thickness determined by the cavity dispersion differ by $0.16 \mu\text{m}$ to $0.32 \mu\text{m}$.

We fit the measured finesse values depending on the diamond thickness in Fig. 3.4 with the effective losses from equation (3.2). In the fit, we use the known mirror losses from the coating design as stated above, and a small diamond thickness translation of $< 20 \text{ nm}$ is allowed. Furthermore, for the used high-purity, electronic-grade diamonds grown by chemical vapor deposition, no absorption losses are expected⁵⁹. This leaves the additional losses \mathcal{L}_{add} and the diamond surface roughness σ_{DA} as free parameters in the fit.

For the laser-cut microdevice, the fit yields a diamond surface roughness value of 0.9 nm and additional losses of 610 ppm . The EBL device fit yields values of 1.2 nm surface roughness and 820 ppm additional losses. For both devices, a distribution of finesse values for a fixed diamond thickness is observed, leading to the band-like structure in

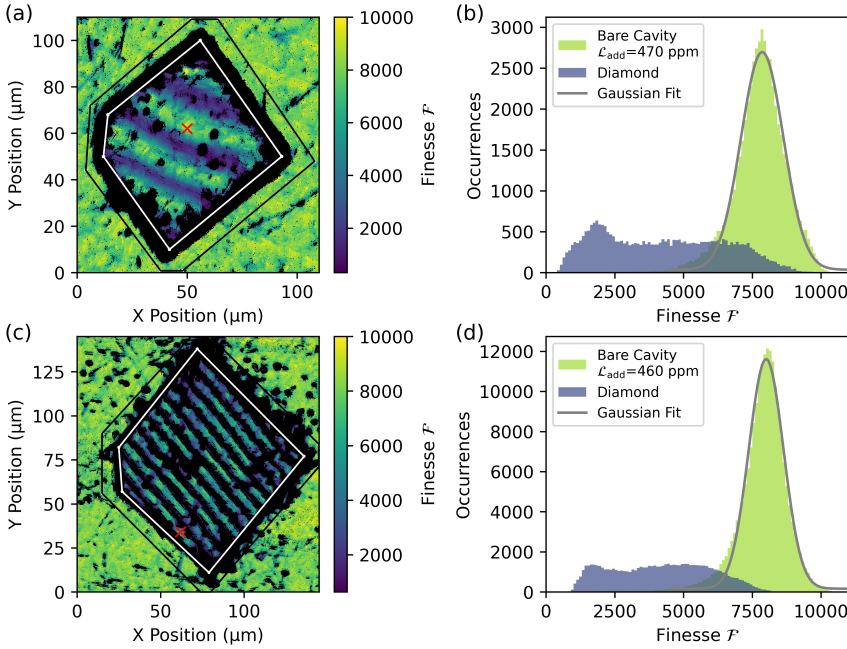


Figure 3.3: Scanning cavity microscopy of the diamond microdevices. Both devices show a clear modulation of the finesse due to the alternation between air-like and diamond-like modes. (a) Measured two-dimensional finesse scan on a laser-cut diamond microdevice (*Vincent Vega*). (b) Histogram of the finesse values measured in (a). Values on the diamond (bare cavity) are taken from inside the white rectangle (outside the black rectangle). (c) Measured two-dimensional finesse scan on an EBL diamond microdevice (*Pai Mei*). (d) Histogram of finesse values measured in (c). Finesse values on the diamond (bare cavity) are taken from inside the white rectangle (outside the black rectangle). For the bare cavity, a finesse centered around 8000 is determined by the Gaussian fits in (b) and (d). The red crosses in (a) and (c) indicate the positions where the cavity length measurements presented in 3.7.5 are taken. The histograms are plotted in bins of 100.

Fig. 3.4. This means that for a specific diamond thickness, lateral cavity positions with varying surface quality are found. To quantify the spread in surface roughness of the data presented in Fig. 3.4, we use the following procedure: the finesse values for a thickness segment of 10 nm are binned into a histogram, which is fitted with a Gaussian function. This fit determines for every thickness segment a mean value and a standard deviation. We fit the mean plus (minus) the standard deviation values of all segments with the model losses of equation (3.2), to determine the upper yellow (lower bright green) curves in Fig. 3.4. With that, we find that our laser-cut (EBL) device exhibits areas with surface roughness values as low as 0.6 nm (1.1 nm), which are common values for these fabrication methods. For both samples finesse values similar to the bare cavity are reached in the air-like modes, whereas in the diamond-like modes scattering losses of $\mathcal{L}_{S,\text{eff,d}} = 390$ ppm (1330 ppm) limit the achievable finesse in the laser-cut (EBL) device.

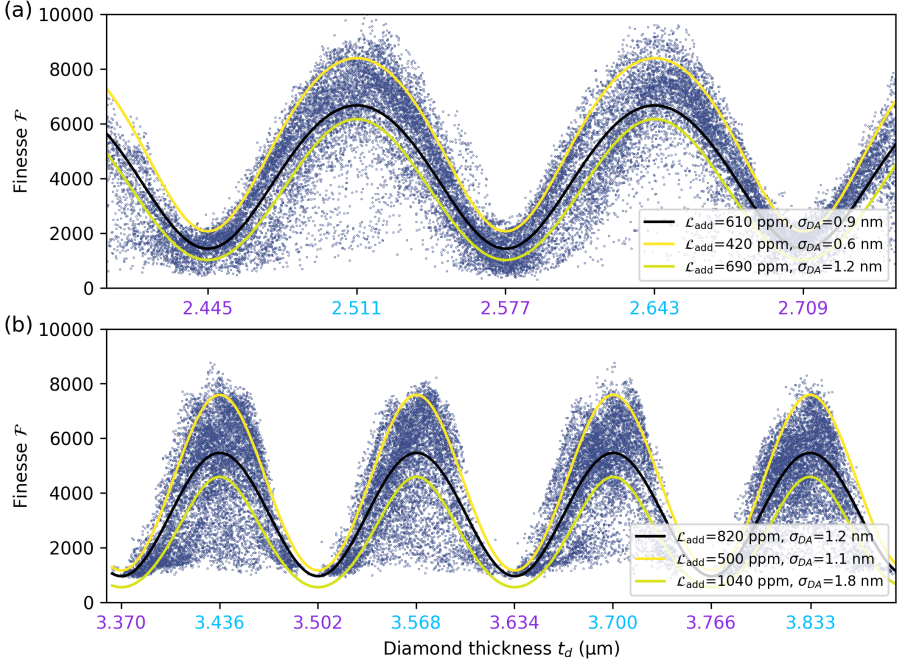


Figure 3.4: Diamond thickness dependent finesse values observed by SCM. Finesse values are taken from inside the white rectangle in Fig. 3.3. The black line is a fit of the finesse values with losses from equation (3.2). The modulation of the finesse values between high-finesse air-like modes and low-finesse diamond-like modes is visible. The diamond thickness values that correspond to an air-like (diamond-like) mode are indicated by the bright blue (purple) axis ticks, determined by equation (3.1). By determining the mean and standard deviation of the finesse values in 10 nm segments (see text), we also give an upper (yellow) and lower finesse curve (bright green) for both devices. More than 60 % of the finesse values lie between the two curves. The diamond thickness measurement by the cavity dispersion is performed for the displayed first air-like mode for both samples (see Appendix Fig. 3.10). (a) Finesse measured on the laser-cut diamond microdevice (*Vincent Vega*). (b) Finesse measured on the EBL diamond microdevice (*Pai Mei*). Note that the black fit is lowered due to the higher spread in finesse values.

3.3.3. FREQUENCY SPLITTING OF THE POLARIZATION CAVITY MODES

In addition to the finesse, the frequency splitting of the two orthogonal polarization modes of the microcavity is studied. Strain-induced birefringence in the diamond microdevice can cause a splitting of the horizontal and vertical polarization cavity mode⁶⁰. In general, diamond color centers couple differently to these modes depending on their electric dipole overlap with the electric field of the cavity. These polarization modes are used in cross-polarization resonant excitation and detection schemes, and the magnitude of polarization splitting becomes relevant for excitation laser power considerations²⁹.

We investigate the polarization splitting of the fundamental modes within the same scan used for the finesse measurements. To measure the splitting, the cavity is resonantly

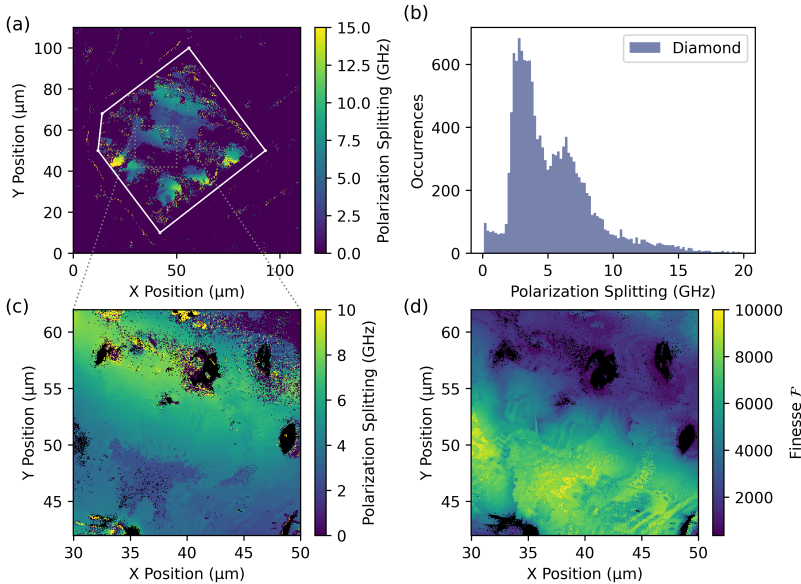


Figure 3.5: Polarization splitting on the laser-cut diamond microdevice (*Vincent Vega*). (a) Polarization splitting is measured on the bare mirror and the diamond device. Data is taken within the same scan as shown in Fig. 3.3 (a). (b) Histogram of the polarization splitting measured on the diamond device inside the white rectangle in (a). Around half of the measured lateral points do not show a polarization splitting (zero bin not included in the histogram). The bin size is 0.2 GHz. (c) Polarization splitting, separately measured with a 70 nm resolution in the $(20 \times 20) \mu\text{m}^2$ area indicated in (a). (d) Corresponding finesse values of the same area as shown in (c). The air-like modes with a higher finesse show a smaller polarization splitting compared to the diamond-like modes.

probed using laser light with frequency-modulated sidebands, generated by a phase electro-optic modulator. The cavity length is scanned around the fundamental mode, and a typical measurement is shown in 3.7.6. The spacing of the sidebands is set by the modulator driving frequency and is used to determine the frequency splitting of the polarization modes.

Figure 3.5 (a) shows the polarization splitting measured on and around the laser-cut microdevice. On the bare mirror, no polarization splitting is measured, while on the diamond device, polarization splittings up to 15 GHz can be observed (histogram shown in Fig. 3.5 (b)). It seems that regions with higher polarization splitting in Fig. 3.5 (a) are closer to the device edges, which can be explained by higher strain, possibly induced by the damage of the laser-cutting. Figure 3.5 (c) shows a selected part of the device with the corresponding finesse scan in Fig. 3.5 (d). It is observed that the polarization splitting is higher in the low-finesse, diamond-like mode part (upper area in the scan). This can be explained by the higher electric field intensity inside the diamond for diamond-like modes, leading to a more pronounced effect of the birefringence⁵⁸.

For the EBL microdevices presented here, we do not observe significant polariza-

tion splitting beyond the cavity linewidth. However, we have also seen polarization splittings up to 10 GHz on other EBL-fabricated devices. To understand the origin of the different strain values, further investigations are needed.

3.4. OPTICALLY COHERENT COLOR CENTERS

For quantum network applications, the color centers in the diamond microdevices must show a (close to) transform-limited optical emitter linewidth. Noise in the environment of the color center (such as fluctuating charges) broadens the emitter linewidth. We can decompose the linewidth broadening into a slow noise contribution, spectral diffusion, and a fast noise contribution, pure dephasing⁶¹. The former leads to a Gaussian broadening and can be mitigated by active tracking and feedback on the emitter transition frequency^{62–65}. Whereas pure dephasing leads to a Lorentzian broadening with a more fundamental influence, as it directly determines the indistinguishability in a two-photon quantum interference experiment of color centers^{66,67} and limits the achievable remote entanglement fidelity in emission-based entanglement protocols^{61,68}. Moreover, the pure dephasing linewidth enters the coherent cooperativity determining fidelities of quantum information protocols⁶⁹.

We study the optical emitter linewidth of the color centers in our diamond microdevices with photoluminescence excitation (PLE) measurements. These measurements are performed in a home-built confocal microscope setup, where the samples are mounted in a closed-cycle Helium cryostat. In the PLE measurements, a resonant laser is scanned over the zero-phonon line (ZPL) of the color center, and the fluorescence is detected in the phonon sideband.

Figure 3.6 (a) shows a confocal scan of the laser-cut diamond microdevice hosting SnV centers. Note that this device is a different microdevice than shown before, but it originated from the same fabrication run and parent membrane (*Vincent Vega*). For the PLE measurements, an off-resonant, 515 nm laser is used before each resonant laser scan to initialize the SnV center in its negatively charged state. The application of a green laser pulse is known to change the charge environment of the color center, resulting in spectral diffusion. We acquire 100 of these scans on three different SnV centers (Fig. 3.6 (b)) and average all scans to get a measure of the spectral diffusion linewidth. In some of these measurements, a bistability of the SnV center transition frequency is observed. These discrete jumps between two spectral positions separated by about 100 MHz might be caused by a charge trap near the SnV center^{70,71}.

To quantify the pure dephasing linewidth, scans that show a complete Lorentzian fluorescence peak are manually selected (more than 50 %), fitted, and centered before averaging. The SnV centers of Fig. 3.6 (b) show good optical coherence with pure dephasing linewidths close to the transform limit around 32 MHz. The corresponding excited state lifetime was determined in previous work³², which also demonstrated the coherent cavity coupling of a single SnV center in a device obtained from the same diamond membrane. These results demonstrate that coherent SnV centers are created

in the laser-cut microdevices.

Figure 3.6 (c) shows the confocal scan of an EBL diamond microdevice hosting NV centers. Note that this device is fabricated in a second run with the EBL method (device originated from parent membrane named *Mr. Orange*). For NV centers, we probe the spin-conserving E_x or E_y emitter transition of the ZPL, which involves the application of intermediate off-resonant, 515 nm, laser pulses at every resonant laser scan frequency to mitigate spin state pumping. These off-resonant laser pulses initialize the NV center predominantly in the negatively charged and spin ground state⁷². Because of the intermediate application of green laser pulses, we can experimentally not measure spectral diffusion and pure dephasing linewidth separately. We thus analyze the emitter fluorescence peaks by fitting a Voigt profile, which is a convolution of a Gaussian and a Lorentzian function. In the fit routine, the Lorentzian linewidth is lower bound to the transform-limited linewidth of 13 MHz of the NV center⁷³. Typical scan results with their corresponding Voigt fits are shown in Fig. 3.6 (d).

We analyze 20 different NV centers at several lateral diamond microdevices positions and find linewidths between 38 MHz and 130 MHz with a median linewidth of 62 MHz (statistics shown in Appendix Fig. 3.12). These results are in line with former work with larger (2×2) mm² thinned-down diamond membranes²⁷, indicating that the much tighter lateral dimensions do not induce additional optical decoherence.

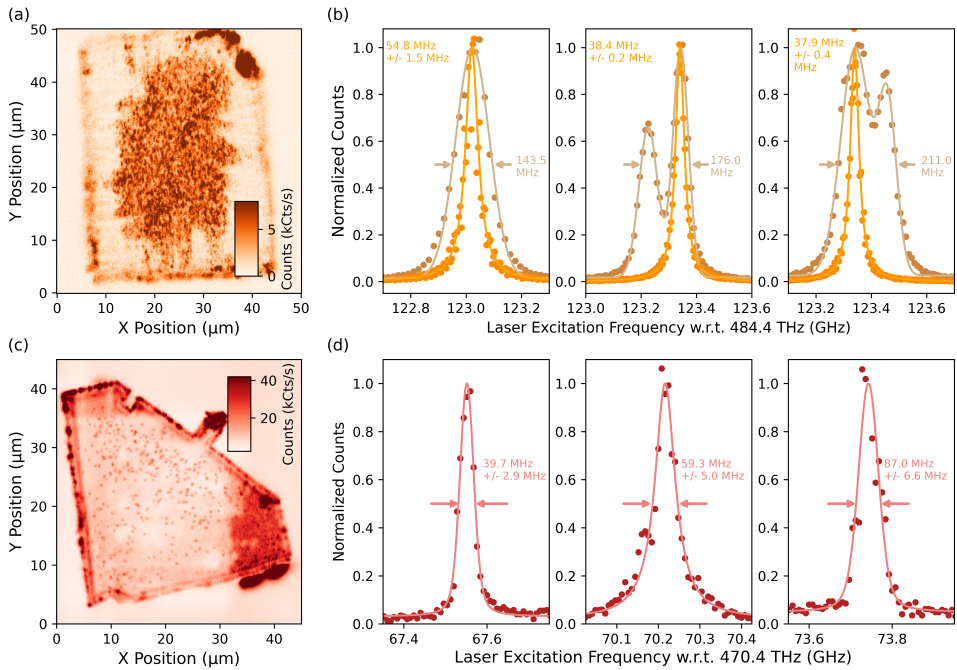


Figure 3.6: Optical properties of SnV centers inside a laser-cut diamond microdevice (*Vincent Vega*) and NV centers inside an EBL patterned diamond device (*Mr. Orange*). The emitter linewidth measurements are performed at ~ 4 K with a confocal microscope. (a) A map of the SnV device with off-resonant, 515 nm excitation. The fluorescence is filtered with a 620 nm bandpass filter (full-width half maximum of 10 nm) to detect predominantly fluorescence of SnV centers. A high SnV center density is observed in the center of the device, while the SnV center layer is removed at the wedged edges. Note that this map was measured in a room-temperature scanning confocal microscope. (b) Typical PLE laser scans of SnV centers, fitted with a Gaussian (ocher) and Lorentzian (orange) function to obtain the spectral diffusion and dephasing linewidth, respectively. (c) Confocal map of the electron-beam patterned device, showing individual, spatially separated NV centers. (d) Typical PLE laser scans of NV centers, fitted with a Voigt function to extract the linewidth. To initialize the NV center into the bright state, a green laser pulse is applied in every repetition. The relevant measurement parameters for the scans in (b) and (d) can be found in 3.7.7.

3.5. CONCLUSION

We present a method for patterning high-quality micrometer-thin diamond devices utilizing laser-cutting. This method significantly simplifies the fabrication process compared to previously reported methods. Also, the process step of laser-cutting can be readily outsourced. We show that these microdevices can be successfully bonded to a dielectric cavity Bragg sample mirror using a micromanipulator. SCM scans reveal a high surface quality of the fabricated devices, reflected by high cavity finesse values. In addition, we demonstrate that the devices host coherent color centers, which are suitable for quantum optical experiments and applications.

For quantum spin-photon interfaces, the expected microdevice performance in microcavities can be estimated with the measured finesse of 9000 (2000) in the air-like (diamond-like) mode. With the $17.3\ \mu\text{m}$ radius of curvature of the used fiber mirror, these values translate to a maximum Purcell factor of about 30 (39) for a NV center and, with adjusted mirror coatings, also for a SnV center. The Purcell enhancement would be combined with a high outcoupling efficiency through the sample mirror of 40 % (51 %) for the air-like (diamond-like) modes and the used mirror coatings. The performance values could be further improved by using a fiber tip mirror that shows lower additional losses^{74–76}.

Combined with the integrated gold striplines on the sample mirror for microwave control of the spin qubits^{33,77,78}, the presented approach can enable the realization of an efficient spin-photon interface with diamond color centers.

3.6. ACKNOWLEDGEMENT

The authors thank Alexander Stramma for proofreading the manuscript. Furthermore, the authors thank the Quentin Tarantino movie universe for providing the sample names. The authors acknowledge financial support from the Dutch Research Council (NWO) through the Spinoza prize 2019 (project number SPI 63-264) and from the Dutch Ministry of Economic Affairs and Climate Policy (EZK), as part of the Quantum Delta NL programme. The authors gratefully acknowledge that this work was partially supported by the joint research program “Modular quantum computers” by Fujitsu Limited and Delft University of Technology, co-funded by the Netherlands Enterprise Agency under project number PPS2007. This research was supported by the Early Research Program of the Netherlands Organisation for Applied Scientific Research (TNO) and by the Top Sector High Tech Systems and Materials.

3.6.1. AUTHOR CONTRIBUTIONS

Y. H., J. M. B., and J. F. contributed equally to this work. M. R. and N. C. developed the EBL fabrication process used in this work. N. d. J. contributed to developing the laser-cutting method. J. M. B., C. S., and Y. H. fabricated the diamond devices. C. S. and L. G. C. W. characterized the devices with the white light interferometer. J. F., Y. vd. G., C. F. J. W., and S. S. built the cavity characterization setup. S. S. measured the two-dimensional cavity

scans and characterized the cavity fiber. C. S., Y. H., J. M. B., and J. F. characterized the color centers. R. M. fabricated the cavity fiber. J. F. derived the used cavity loss model. Y. H., J. F., and S. S. analyzed the data. Y. H., J. M. B., J. F., S. S., and R. H. wrote the manuscript with input from all authors. R. H. supervised the experiments.

3.6.2. DATA AVAILABILITY STATEMENT

The datasets of this study and the Python software for analysis and plotting are publicly available on 4TU.ResearchData under Ref.⁷⁹.

3

3.7. APPENDIX

3.7.1. OUTLINE OF FABRICATION

The detailed steps of both fabrication methods are summarized in table 3.1.

Fab. Step	Electron-Beam Lithography (EBL)	Laser-Cutting
I. Cleaning	Fuming nitric acid (1): 10 min in HNO ₃ (65 %) at room temperature	
(II. Strain Relief Etch, Implantation, Annealing)	Strain relief etch as described in subsection 3.2.2, followed by tri-acid clean, implantation, annealing, and a post-anneal tri-acid clean as detailed in subsection 3.2.3	-
III. Application of Protection Mask	PECVD ~ 320 nm silicon nitride Si _x N _y	Application of PVA layer (2)
IV. Spin Coating	Sample mounted with PMMA495 A4 on silicon piece, resist CSAR-13 (AR-P 6200.13), 3500 rpm (thickness of ~ 430 nm), bake 3 min at 150 °C Spin coat Electra 92 (AR-PC 5090), 4000 rpm (thickness of ~ 30 nm), bake 2 min at 90 °C	-
V. Exposure	Electron-beam: Dose of 400 uC/cm ² with 3 nm spot size	-
VI. Development	Remove Electra 92 with 1 min deionized water, blow dry with nitrogen. CSAR-13 development: 1 min in pentyl-acetate, 5 s in ortho-xylene, 1 min in IPA, blow dry with nitrogen	-
VII. Patterning Hard Mask	Si _x N _y etch with plasma composed of CHF ₃ /O ₂ ⁸⁰	-
VIII. Resist Removal	PRS 3000 for 2 h at 80 °C, followed by overnight PRS 3000 at room temperature	-
IX. Cleaning	Double Piranha clean: Mixture with ratio 3:1 of H ₂ SO ₄ (95 %) : H ₂ O ₂ (31 %) at 80 °C for 20 min	-
X. Transfer Pattern into Diamond	Anisotropic ICP/RIE: Sample mounted with PMMA495 A4 on fused quartz carrier wafer, 30 min O ₂ plasma chemistry	Laser-cutting (3) with a femtosecond pulsed laser
XI. Cleaning	Removal of the Si _x N _y hard mask: Hydrofluoric (HF) acid (40 %) clean 15 min at room temperature	Removal of PVA: Ultrasonic bath in de-ionized water and acetone for 10 min, each at room temperature (4), followed by Piranha clean
(XII. Strain Relief Etch, Implantation, Annealing)	-	Strain relief etch (5) as described in subsection 3.2.2, followed by tri-acid clean, implantation (6), annealing (7), and post-anneal tri-acid clean as detailed in subsection 3.2.3
XIII. Release Etch	ICP/RIE (8): Membrane protected by fused quartz mask with central opening, 45 min Ar/Cl ₂ . Multiple rounds of O ₂ etch until individual microdevices are released. Etch rates can be found in Ref. ²⁷ .	
XIV. Cleaning	HF clean	
XV. Bonding	Micromanipulator (9)	

Table 3.1: Detailed fabrication steps and process parameters of the two fabrication methods to obtain diamond microdevices, starting with ~ 50 μm membranes. All wet processing steps are followed by a dip in acetone and IPA and blow-drying with a nitrogen gun. The numbers in brackets for the laser-cutting refer to Fig. 3.1 (c) of the main text. Fabrication step II. (XII.) of the EBL (laser-cutting) method is used to create SnV centers. In the case of NV centers, the color centers are created in the bulk diamond, before slicing into membranes, as described in subsection 3.2.3.

3.7.2. BONDING OF MICRODEVICES TO CAVITY MIRROR

Figure 3.7 (a) shows the breaking out of individual microdevices by a micromanipulator. Supplementary Video 1 shows the process with devices from a second laser-cut membrane. We observe that up to 30 % of the devices bond fully to the cavity mirror. Figure 3.7 (b) and (c) show diamond devices that are not fully bonded to the mirror. When approached by the cavity fiber, such devices can be moved or picked up accidentally.

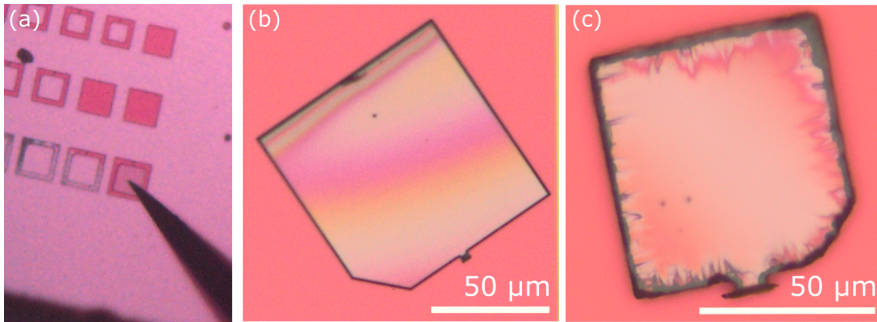


Figure 3.7: Bonding of diamond microdevices to the cavity mirror. (a) Released, thinned-down diamond devices above the cavity mirror. Individual devices can be broken out with the tip of a micromanipulator. An ill-bonded device fabricated by EBL (*Pai Mei*) in (b) and by laser-cutting (*Vincent Vega*) in (c). Both devices show interference fringes and an opaque color.

3.7.3. EXPERIMENTAL SETUP: ROOM TEMPERATURE MICROCAVITY

The cavity sample mirror with the microdevices (Fig. 3.8 (a)) is mounted on a piezo nanopositioning stage (Physik Instrumente P-542.2SL) with a range of 200 μm in both the X - and Y -direction. The other cavity mirror is a coated, laser-ablated fiber tip⁷⁴, which can be moved in the axial direction by a high-precision objective scanner (Physik Instrumente P-721) to change the cavity length along the Z -direction.

Figure 3.8 (b) shows a sketch of the optical setup and the microcavity. The cavity can be probed with resonant 637 nm light (Newport New Focus Velocity TLB-6300-LN) or with a white light supercontinuum source (NKT Photonics SC-450-2), spectrally filtered for 600 nm to 700 nm. The excitation light is combined in fiber and sent via the fiber side into the cavity. The transmitted light is collimated with an objective (100X Mitutoyo Plan Apochromat Objective) and collected on a photodiode (Thorlabs APD130A2) or sent via fiber to a spectrometer (Princeton Instruments SP-2500i). In addition, the microcavity can be imaged from the sample mirror side by a lamp and a camera for lateral alignment. Supplementary Video 2 shows a two-dimensional cavity finesse scan over an exemplary device recorded with the camera.

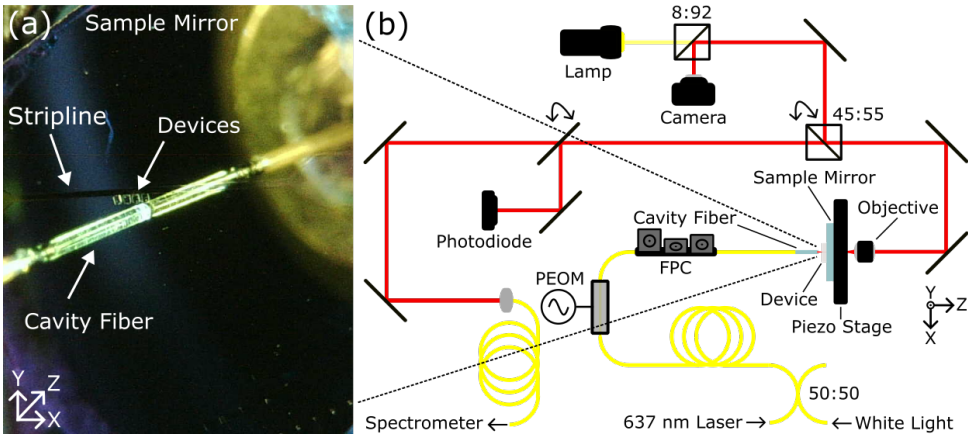


Figure 3.8: (a) Microscope picture of the microcavity with exemplary microdevices on the sample mirror next to a gold stripline. The cavity fiber can be seen on the left side, while the reflection in the mirror is on the right side. (b) Sketch of the home-built SCM setup. Excitation light (resonant laser or white light) is sent into the cavity via the fiber. The light can be modulated with a phase electro-optic modulator (PEOM), and the polarization is set manually with a 3-paddle fiber polarization controller (FPC). The outcoupled detection beam is collimated with an objective and sent either to a photodiode or coupled into a single-mode fiber for the spectrometer.

3.7.4. EXPERIMENTAL METHODS: FINESSE MEASUREMENTS AND CAVITY FIBER PROPERTIES

To measure the finesse, the cavity is probed with a resonant 637 nm laser, and the transmission signal is recorded on the photodiode. We record the time trace of the photodiode voltage with an oscilloscope (Picotech Picoscope 3403). The cavity length is scanned by a triangular voltage with a frequency of 300 Hz over approximately five fundamental modes to ensure that the middle of these modes is not affected by nonlinearities occurring at the edges of the scanning range. The middle modes are fitted with Lorentzian functions, resulting in a measured cavity finesse defined as the ratio of the mode distance to the linewidth in time. An exemplary trace with two fundamental modes is shown in Fig. 3.9 (a). The resonance peak with the higher coefficient of determination (R^2) is used to determine the finesse. The data is filtered by requiring the mode distance to be within an acceptance range to ensure that only the fundamental modes are fitted.

As discussed in the main text, birefringence in diamond microdevices can cause polarization splitting, which is observed as a frequency splitting of the fundamental cavity mode. To correctly fit these modes in the finesse measurements, two Lorentzian functions are fitted (see Fig. 3.11 (a)).

The same cavity fiber is used for all the presented measurements. From an interferometric measurement of the concave fiber tip, we extract a spherical radius of curvature ROC of $17.3 \mu\text{m}$ with an asymmetry of 7.8 %. To determine the range in which

the fiber exhibits a stable finesse, we measure the cavity length-dependent finesse in Fig. 3.9 (b) on the bare mirror. The cavity length is determined by taking white light transmission spectra, which directly yield the cavity free spectral range and thereby the cavity length. For longer cavity lengths L_{cav} clipping losses \mathcal{L}_{clip} emerge which dependent on the diameter of the concave feature D_d and the ROC of the fiber mirror and can be calculated by⁵⁶:

$$\mathcal{L}_{clip} = e^{-2\left(\frac{D_d}{2\omega_m}\right)^2}. \quad (3.5)$$

In this formula, ω_m denotes the cavity beam width on the fiber mirror and can be calculated by the beam waist on the sample cavity mirror ω_0 ⁸¹:

$$\omega_m = \omega_0 \sqrt{1 + \left(\frac{L_{cav}\lambda}{\pi n\omega_0^2}\right)^2}, \quad \omega_0 = \sqrt{\frac{\lambda}{\pi}} (L_{cav}(ROC - L_{cav}))^{1/4}. \quad (3.6)$$

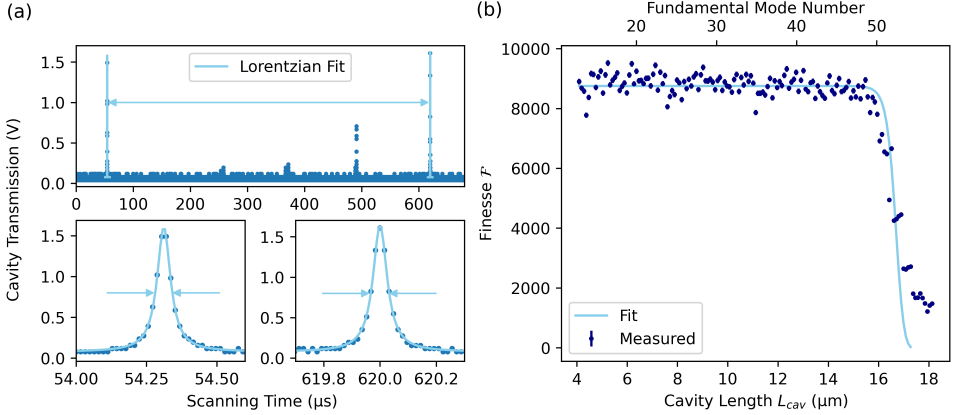


Figure 3.9: (a) Typical cavity finesse measurement recorded with an oscilloscope. The cavity length is scanned with a triangular voltage and two fundamental modes with a few higher-order modes are visible in the upper panel. The peaks of the fundamental modes are fitted with a Lorentzian function, yielding the cavity linewidth in time. The free spectral range in time is given by the spacing of the fundamental modes. From the shown measurement, a finesse of 9500 is determined. (b) Cavity length-dependent measured finesse of the fiber used to characterize the diamond microdevices. The coating limited finesse is 19000 with 330 ppm losses. A clear plateau of finesse values of ~ 8700 is reached for a cavity length smaller than $15 \mu\text{m}$.

We fit the measured finesse values in Fig. 3.9 (b), with the losses determined by equation (3.2) plus the clipping losses \mathcal{L}_{clip} . Like in section 3.3.2 of the main text, we set $t_d = 0 \mu\text{m}$ and leave the additional losses and the diameter of the concave feature as free parameters. The radius of curvature is set to the measured value as stated above.

Note that the finesse values measured on the plateau in Fig. 3.9 (b) are a bit higher than the average bare cavity finesse values due to a local optimization on the lateral spot and reveal additional losses of 390 ppm determined by the fit.

3.7.5. EXPERIMENTAL METHODS: HYBRID CAVITY MODES

To determine the cavity length and the thickness of incorporated devices, we probe the cavity with broadband white light and send the transmitted light to a spectrometer. The cavity length is changed by applying a voltage to the objective scanner, which holds the cavity fiber.

For the broadband white light, the cavity acts as a spectral filter, and fundamental modes appear as bright lines. We fit the fundamental modes with an analytic formula¹¹, yielding the length of the air gap and the device thickness. The measurements are shown in Fig. 3.10.

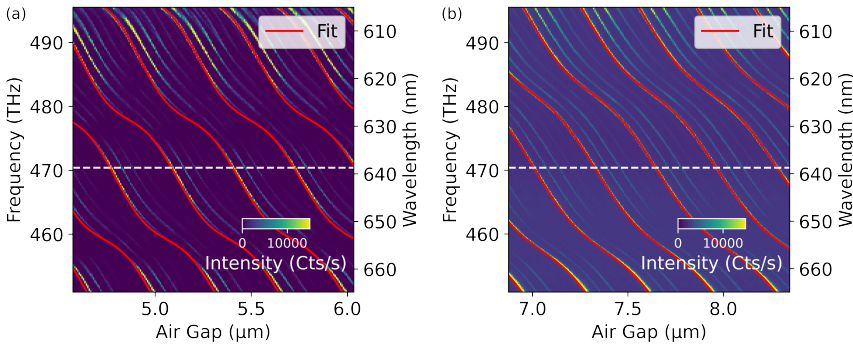


Figure 3.10: Cavity dispersion measured by transmission spectra of a broadband light source. (a) On the EBL microdevice (*Pai Mei*), we measure a device thickness of $3.31\ \mu\text{m}$. (b) On the laser-cut microdevice (*Vincent Vega*), the fit determines a thickness of $2.51\ \mu\text{m}$. Both devices are probed in the air-like mode (steeper slope) at $637\ \text{nm}$, indicated by the white, dashed line. The positions on the devices of these measurements are indicated in Fig. 3.3 (a) and (c) with a red cross.

3.7.6. EXPERIMENTAL METHODS: POLARIZATION SPLITTING

To measure the cavity polarization splitting, a second trace of the resonance peaks is measured at each lateral scan point with the resonant $637\ \text{nm}$ laser, modulated by sidebands. The sidebands are imprinted by a phase electro-optic modulator (Jenoptik PM635) with a microwave source (Rohde & Schwarz SGS100A) at a frequency of $6\ \text{GHz}$. The obtained modes are fitted with three (or six) Lorentzian peaks, and the sidebands are used to convert the polarization splitting from scanning time to frequency. The data are filtered by requiring $R^2 > 0.95$ to ensure the fit succeeded. An example measurement is shown in Fig. 3.11.

3.7.7. EXPERIMENTAL METHODS: PLE SCANS

Measurements are performed in a home-built, cryogenic confocal microscope, whose excitation and detection path can be adapted for the measurements of SnV and NV centers. Details about the low-temperature setup and the measurement methods are described in the Supplementary Information of Ref. ⁶³ and ²⁷.

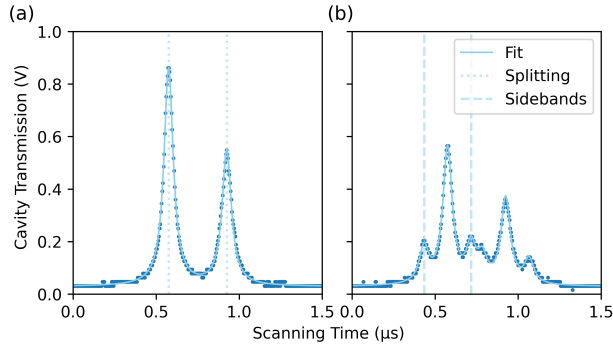


Figure 3.11: Exemplary measurement of the polarization splitting of the two orthogonal cavity modes on the diamond device. The cavity length is scanned with a triangular voltage over the fundamental mode, and the transmission is measured on a photodiode. (a) The length-dependent polarization splitting of the fundamental mode. (b) The same measurement with the sideband modulation. The fixed distance of the sidebands (indicated by the dashed lines) is used to determine the cavity linewidth and polarization splitting in frequency. In this measurement, a linewidth of 2.9 GHz and polarization splitting of 14.9 GHz (dotted lines in (a)) is extracted.

The parameters for the SnV center measurements shown in Fig. 3.6 (b) are: $1\ \mu\text{W}$ green repump for 100 ms and 0.5 nW to 1 nW resonant laser excitation power for 10 ms integration. The resonant laser is detuned in steps between 10 MHz to 20 MHz with a speed of $\sim 2\ \text{GHz/s}$.

The parameters of the NV center measurements in Fig. 3.6 (d) are: $40\ \mu\text{W}$ green repump for $10\ \mu\text{s}$ and 40 nW resonant laser excitation power for $20\ \mu\text{s}$ integration. At each frequency step between 8 MHz to 20 MHz, a sequence of repump, waiting of $10\ \mu\text{s}$, and readout is repeated for a total time of 200 ms. The statistics of the NV center measurements can be found in Fig. 3.12.

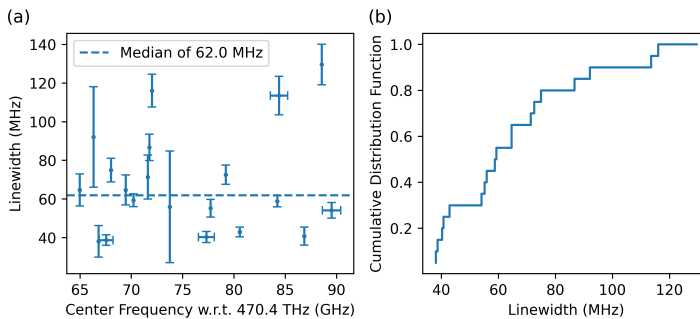


Figure 3.12: Statistics of the optical coherence of 20 different NV centers in an EBL patterned diamond microdevice (*Mr. Orange*), measured at $\sim 4\ \text{K}$ with a confocal microscope. (a) ZPL center frequencies and linewidth values, obtained by a Voigt fit to the individual NV center resonances (see Fig. 3.6 for exemplary data and fit). The errors are also obtained by the fit. (b) The linewidth values are plotted as a cumulative distribution function (CDF). The measurement parameters can be found in 3.7.7.

3.7.8. MEASUREMENTS ON THE LASER-CUT MICRODEVICE

An overview of all measurements performed on the laser-cut microdevice (*Vincent Vega*) is shown in Fig. 3.13.

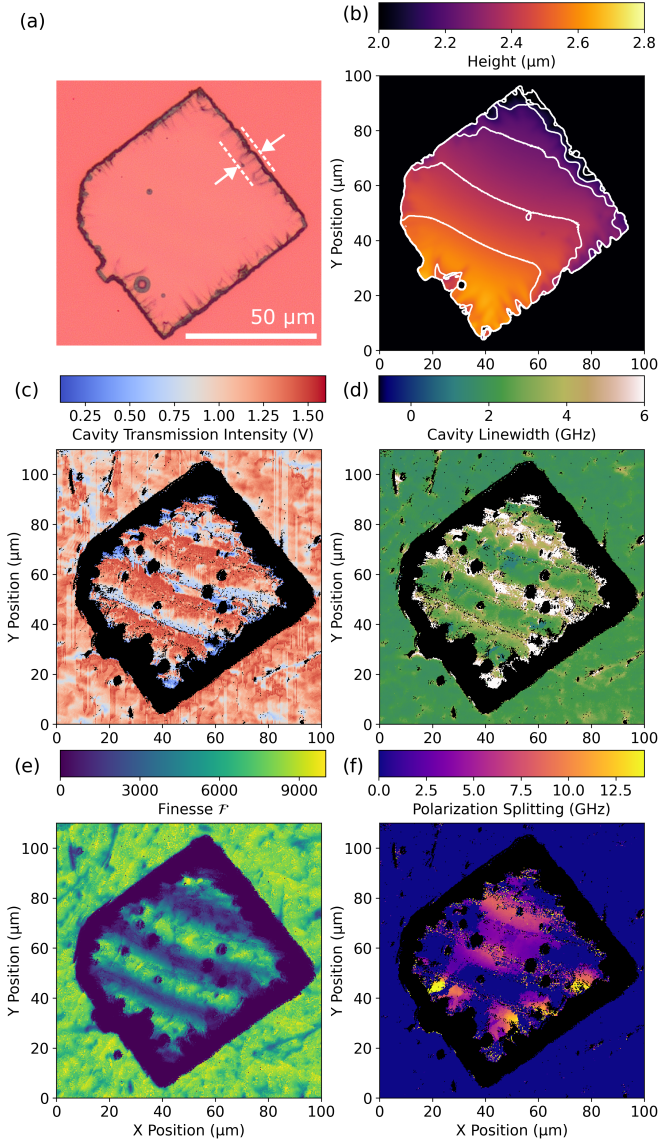


Figure 3.13: Summary of different measurements of the laser-cut diamond microdevice (*Vincent Vega*). (a) Light microscope image. (b) Height map measured by a white light interferometer. (c)-(f) Scanning cavity microscopy. All data is measured within one scan and by probing the cavity with a resonant laser. (c) Cavity transmission intensity is measured on a photodiode. Note that the laser power is varied during the measurement. (d) Cavity linewidth. (e) Cavity finesse. (f) Cavity polarization splitting.

3.8. ADDITIONAL DATA

This section presents additional figures on the fabrication process and data of the laser-cut and EBL microdevices shown in this chapter. The underlying data can be found in the repository accompanying this thesis⁸².

3.8.1. CREATION OF NV CENTERS

Systematic studies have shown that NV centers formed from nitrogen naturally occurring in the diamond lattice show much narrower optical linewidth than NV centers created by ion implantation^{81,83}.

We therefore employ electron irradiation with minimal crystal damage to generate NV centers from the native nitrogen concentration³⁴ to obtain NV centers with high optical coherence²⁷. As described in section 3.2.3, the bulk diamond is irradiated with electrons at the Reactor Institute in Delft. A van de Graaff electron accelerator produces a 2 MeV electron beam, in which the diamonds are placed for a certain time, determining the irradiation dose. The energy is large enough that electrons fully penetrate the sample and vacancies are formed homogeneously throughout the diamond. The sample is afterward processed with a tri-acid clean and annealed under vacuum (see section 3.2.3). To assess the NV center density, confocal microscopy scans are conducted

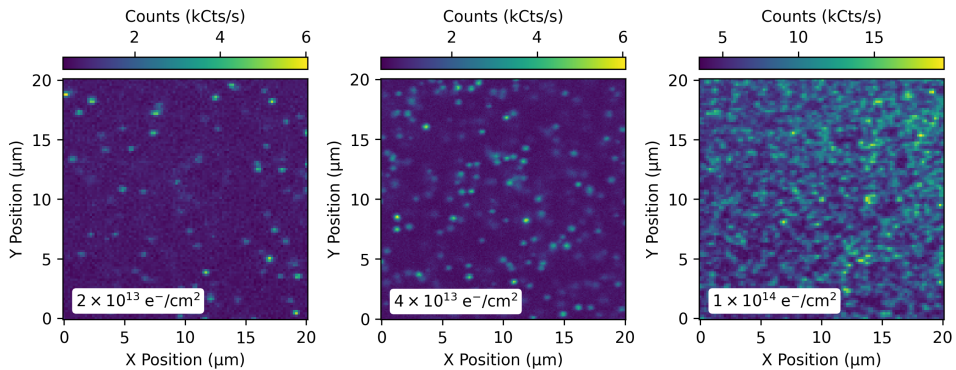


Figure 3.14: Confocal microscopy scans of three bulk diamond samples, after electron irradiation and annealing. An energy of 2 MeV is used, and the respective electron irradiation doses are indicated in the inset box. Confocal scans are performed under ambient conditions with 400 μ W off-resonant, green excitation at a focal depth of about 5 μ m below the diamond surface. A higher electron dose leads to the creation of more vacancies and subsequently more NV centers in the sample, despite the unknown starting nitrogen density of the commercial samples, which is specified to be below 5 ppb. The native NV center density in these samples is even smaller, with typical numbers below 0.03 ppb.

of the bulk samples after annealing. Typical confocal scans are shown in Fig. 3.14 with different electron irradiation doses. Irradiation with a higher electron dose with subsequent annealing can be repeated until a sufficient NV density is reached. Afterwards, the 0.5 mm thick bulk diamonds are sliced and polished into three membranes as described in section 3.2.1.

3.8.2. FABRICATION OF EBL MICRODEVICES

Parts of the EBL fabrication process are shown in Fig. 3.15. The membrane after transferring the pattern from the silicon nitride hard mask into the diamond surface with the anisotropic inductively coupled plasma reactive ion etching is shown in Fig. 3.15 (a) (fabrication step X. in tab. 3.1). Figure 3.15 (b) shows the membrane during the device release etch with the quartz mask from the backside (fabrication step XIII. in tab. 3.1). Note that the release etch is used for both fabrication methods, laser-cutting and EBL.

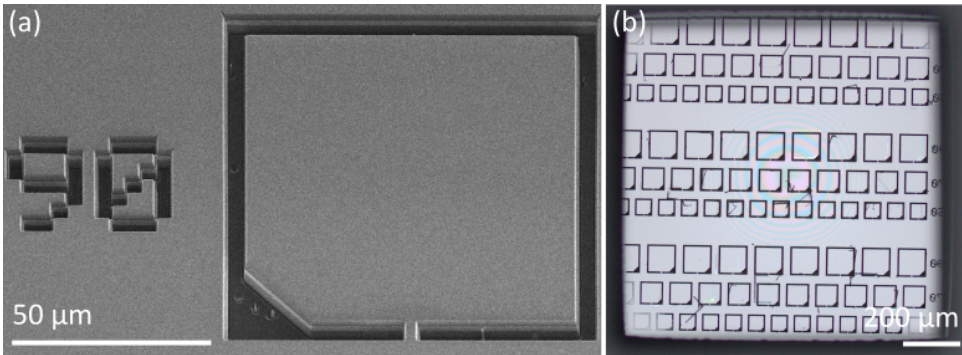


Figure 3.15: Diamond microdevices patterned by electron beam lithography (EBL) during the fabrication process (*Pai Mei*). (a) Scanning electron microscope image of the sample after etching the trenches with the silicon nitride hard mask. (b) Light microscope image from the backside of the sample after multiple rounds of the release etch. The quartz mask protecting the outer frame of the membrane is visible on the edges. Most of the trenches have opened, and the interference pattern in the center of the sample indicates a thickness of up to a few micrometers or less. Figure adapted from Sauerzapf⁸⁴.

3.8.3. FABRICATION OF LASER-CUT MICRODEVICES

For the laser-cutting method, the diamond membranes are protected with a polyvinyl alcohol (PVA) layer. Figure 3.16 (a) shows a diamond membrane after laser-cutting (fabrication step X. in tab. 3.1). The protection layer is removed by de-ionized water and acetone, and the sample is subsequently cleaned in a Piranha mixture (Fig. 3.16 (b)). Finally, to obtain a smooth and clean surface, a strain-relief etch is conducted as shown in Fig. 3.16 (c) (fabrication step XII. in tab. 3.1). For SnV centers, the membranes are, after this step, implanted with tin ions, followed by annealing (see section 3.2.3).

3.8.4. SnV CENTERS IN LASER-CUT MICRODEVICES

Confocal microscopy scans are performed under ambient conditions to assess the SnV center density in the microdevices after bonding to the cavity mirror. A confocal scan is shown in Fig. 3.17 (b), while room temperature spectrum is shown in Fig. 3.17 (c). A clear peak in the spectrum around 620 nm confirms the ZPL emission of SnV centers, accompanied by the phonon sideband emission towards longer wavelengths.

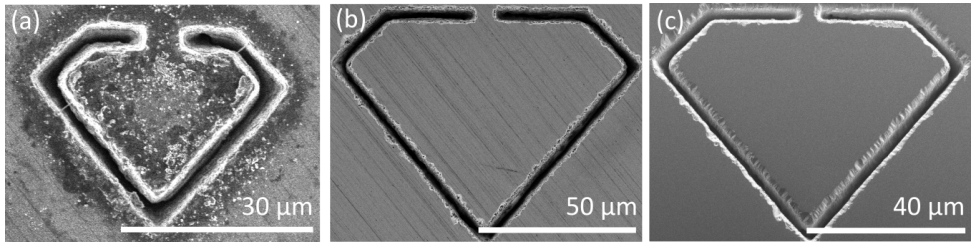


Figure 3.16: Diamond microdevices patterned by laser-cutting during the fabrication process (*Vincent Vega*), investigated by scanning electron microscopy. The membrane is protected with a PVA mask. (a) The membrane is shown directly after laser cutting, with debris created by the irradiation. (b) The protection layer and debris are removed by a Piranha clean. The membrane still exhibits marks from the polishing process. (c) A strain relief etch (see section 3.2.2) leads to a smooth and clean diamond surface. The laser-cutting results in wedged edges with a higher surface roughness. However, the center of the devices maintains a high quality. Figure adapted from Sauerzapf⁸⁴.

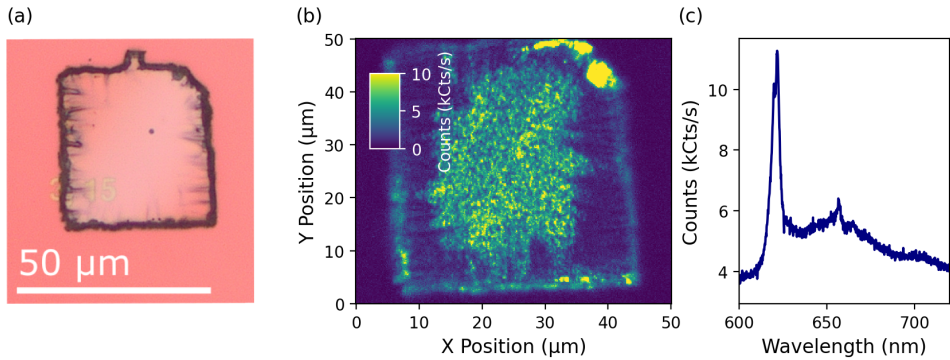


Figure 3.17: SnV centers in a laser-cut diamond microdevice (*Vincent Vega*) bonded to the cavity mirror. (a) Light microscope image of the device. (b) Scanning confocal microscopy of the device. Off-resonant, green excitation is used, and the fluorescence is filtered with a 620 nm bandpass filter (full-width half maximum of 10 nm) to select only the light of SnV centers. A high SnV density is observed in the center of the platelet, while the SnV layer is removed at the wedged edges. Note that this scan is also shown in Fig. 3.6 (a). (c) A spectrum is recorded in the center of the device, showing a peak around 620 nm of the SnV centers emission (detection light only filtered with a long pass filter at 600 nm). The measurements are performed at room temperature.

The optical properties of SnV centers are further investigated at low temperatures in Fig. 3.18. A series of PLE laser scans are conducted at low temperatures for three different SnV centers. The spectral wandering of the SnV centers can be observed, as well as the bistability as mentioned in section 3.4.

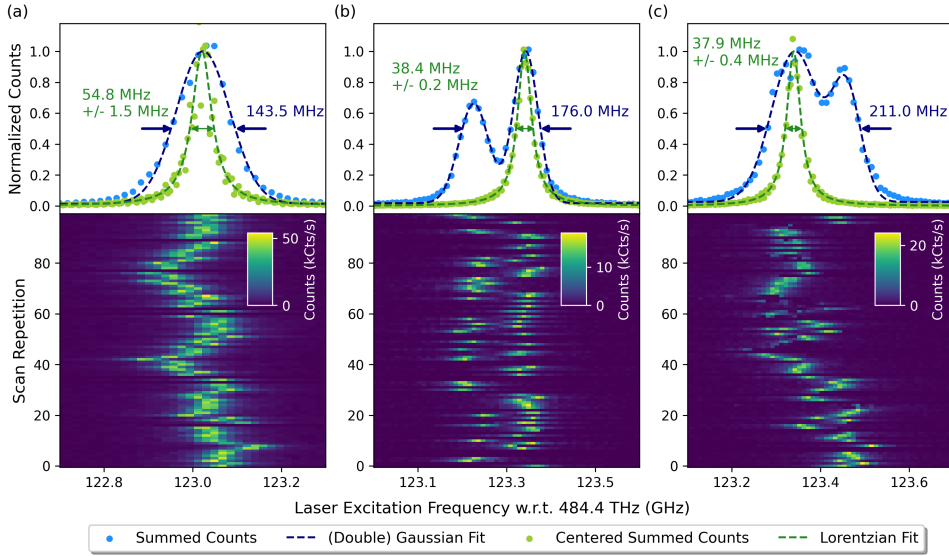


Figure 3.18: Lower panel: hundred consecutive PLE laser scans of three different SnV centers hosted in a laser-cut diamond microdevice (*Vincent Vega*) at a temperature of 4 K. To initialize the charge state, the off-resonant green repump laser is applied at the beginning of each scan. Upper panel: Integrated counts (in blue) fit with a Gaussian function to determine the spectral diffusion. An individual scan is fit with a Lorentzian function and centered to sum (in green), yielding the SnV center's dephasing linewidth. Scans with a full Lorentzian lineshape peak are manually selected. The data of the upper panel is shown in Fig. 3.6 (b). Measurement parameters can be found in section 3.7.7.

3.8.5. NV CENTERS IN EBL MICRODEVICES

The light microscope image and a two-dimensional confocal microscopy scan of the EBL-fabricated microdevice are shown in Fig. 3.19. The scan reveals the NV center density.

Figure 3.20 (a) shows a broad PLE laser scan with several NV center transitions. The spectrum is relatively clean, confirming the low density of NV centers as expected from the two-dimensional confocal scan shown in Fig. 3.19 (b).

A thickness of $5\mu\text{m}$ to $6\mu\text{m}$ of the microdevice is measured with a white light interferometer.

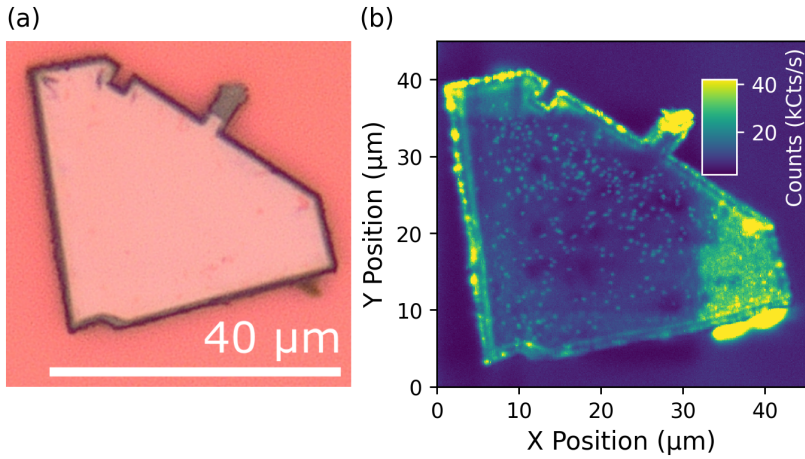


Figure 3.19: NV centers in an EBL-fabricated diamond microdevice (*Mr. Orange*) bonded to the cavity mirror. (a) Light microscope image of the device. (b) Scanning confocal microscopy. Off-resonant, green excitation is used, and the fluorescence at longer wavelengths is detected. A moderate NV center density is observed. Note that this scan is also shown in Fig. 3.6 (c).

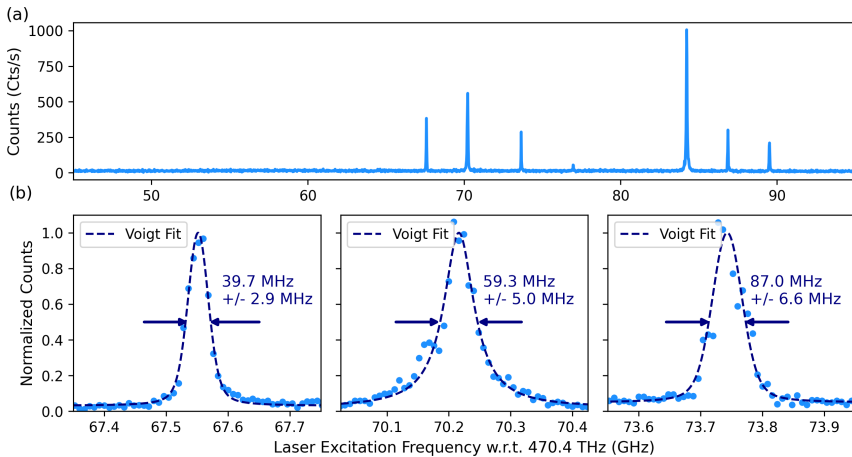


Figure 3.20: Optical properties of NV centers inside the EBL patterned diamond microdevice (*Mr. Orange*) measured by PLE laser scan at low temperatures with a confocal microscope. At each frequency step, the NV center is initialized with a green laser pulse into the negative charge state and predominantly in the spin ground state. (a) Wide frequency scan in steps of 20 MHz showing the optical resonances of several NV centers. (b) Narrower scans in steps of 8 MHz over the three peaks on the left side of (a). Each peak is fit with a Voigt profile, and the extracted linewidth is displayed next to it. The same data is shown in Fig. 3.6 (d). Measurement parameters can be found in section 3.7.7.

3.8.6. NV CENTERS IN LASER-CUT MICRODEVICES

This section presents preliminary data on NV centers in laser-cut microdevices. Note that this device has not been included in the measurements so far. NV centers are created by electron irradiation with a dose of $4 \times 10^{13} \text{ e}^-/\text{cm}^2$. A thickness of $6 \mu\text{m}$ to $7 \mu\text{m}$ of the microdevice is measured with a white light interferometer. The device is placed on the mirror at a distance of about $50 \mu\text{m}$ to a gold stripline, which can be used for microwave delivery.

Figure 3.21 shows measurements under ambient conditions, confirming that the device contains NV centers and that they can be addressed by microwaves applied through the stripline. The spin-excited states of the NV center have a higher probability of decaying through the intersystem crossing, which leads to reduced fluorescence in the optical signal. When the driving frequency of the microwaves becomes resonant with the spin transition around 2.88 GHz, a reduced fluorescence due to the intersystem crossing can be observed.

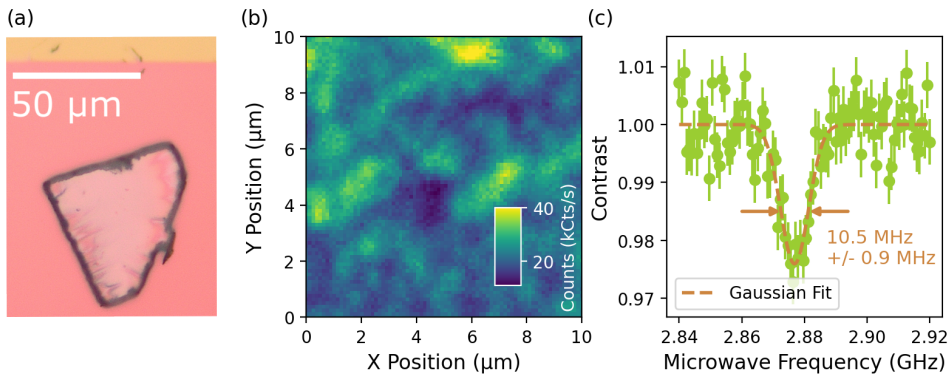


Figure 3.21: NV centers in a diamond microdevice, fabricated by laser cutting (*Ringo*). (a) Light microscope image of the device bonded to the cavity mirror. Before bonding, a gold stripline is deposited on the mirror for microwave control. (b) A confocal microscopy scan of the center of the device shows a high NV center density under off-resonant, 515 nm excitation. (c) Optically detected magnetic resonance measurement of NV centers under off-resonant, continuous wave excitation without a magnetic field. The microwave frequency is changed in steps of 0.8 MHz with an integration time of 100 ms per step. A microwave power of 25 dBm is used, integrated over ten repetitions. The measurements are conducted at room temperature.

Figure 3.22 (a) presents PLE laser scan conducted at low temperatures over a frequency range covering around 65 GHz. The optical transitions of multiple NV centers are visible. This confirms the high density of the device as indicated by the confocal scan.

The stability of one NV center's transition is further investigated by repetitive scans in Fig. 3.22 (b). We use constant microwave driving at the NV center's resonance frequency during the measurement to mix the spin state. Without the microwave driving, the resonant laser would optically pump the NV center to a different spin state, which appears dark during the resonant scan. The stable count trace in the lower panel of

Fig. 3.22 (a) indicates that the NV centers are not spin pumped into the dark state.

To conclude about the NV center quality in laser-cut devices, further investigation is required to gather more statistics.

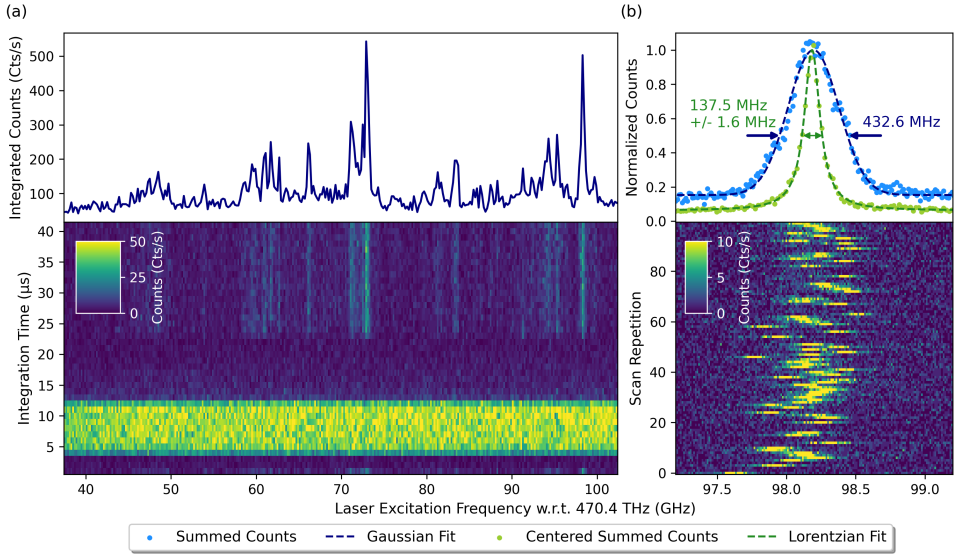


Figure 3.22: Optical properties of NV centers in a laser-cut diamond microdevice (*Ringo*). (a) PLE scan at low temperatures. The lower panel shows the obtained counts during the measurement sequences: at each frequency point, an off-resonant, green laser is used to repump with 5 μW for 10 μs . After a wait time of 10 μs , the resonant laser is applied with 30 nW for 20 μs . 10000 repetitions are averaged over time per frequency step of 0.2 MHz. The upper panel shows the integrated counts during the time of the application of the resonant laser pulse. (b) Consecutive PLE scans around the dominant peak on the right side of the spectrum of (a). Scans with a full Lorentzian peak are manually selected and summed up in blue, which is fit by a Gaussian function. In green: each scan is separately fit with a Lorentzian function and centered before summation. The obtained spectrum is fitted with a Lorentzian function. Measurement parameters: before each scan, an off-resonant, green laser pulse is applied with 10 μW for 200 ms. The resonant laser is detuned in steps of ~ 12 MHz with a speed of ~ 0.3 GHz/s. Per frequency step, the counts are integrated for 40 ms with 1 nW resonant laser power. In both measurements of (a) and (b), microwaves at 2.877 GHz with 25 dBm are constantly applied.

BIBLIOGRAPHY

- [1] Y. Herrmann *et al.*, *Laser-cut patterned, micrometer-thin diamond membranes with coherent color centers for open microcavities*, Mater. Quantum. Technol. **5**, 035001 (2025).
- [2] E. Janitz, M. K. Bhaskar and L. Childress, *Cavity quantum electrodynamics with color centers in diamond*, Optica **7**, 10 (2020).
- [3] S. Mi, M. Kiss, T. Graziosi and N. Quack, *Integrated photonic devices in single crystal diamond*, J. Phys. Photonics **2**, 042001 (2020).
- [4] M. Ruf, N. H. Wan, H. Choi, D. Englund and R. Hanson, *Quantum networks based on color centers in diamond*, Journal of Applied Physics **130**, 070901 (2021).
- [5] P. K. Shandilya *et al.*, *Diamond Integrated Quantum Nanophotonics: Spins, Photons and Phonons*, J. Lightwave Technol. **40**, 23 (2022).
- [6] J. Riedrich-Möller *et al.*, *One- and two-dimensional photonic crystal microcavities in single crystal diamond*, Nature Nanotech **7**, 69 (2012).
- [7] J. C. Lee, A. P. Magyar, D. O. Bracher, I. Aharonovich and E. L. Hu, *Fabrication of thin diamond membranes for photonic applications*, Diamond and Related Materials **33**, 45 (2013).
- [8] A. Faraon *et al.*, *Quantum photonic devices in single-crystal diamond*, New J. Phys. **15**, 2 (2013).
- [9] S. W. Ding *et al.*, *High-Q cavity interface for color centers in thin film diamond*, Nat Commun **15**, 6358 (2024).
- [10] P. Fuchs, T. Jung, M. Kieschnick, J. Meijer and C. Becher, *A cavity-based optical antenna for color centers in diamond*, APL Photonics **6**, 8 (2021).
- [11] E. Janitz *et al.*, *Fabry-Perot microcavity for diamond-based photonics*, Phys. Rev. A **92**, 043844 (2015).
- [12] S. Bogdanović *et al.*, *Design and low-temperature characterization of a tunable microcavity for diamond-based quantum networks*, Appl. Phys. Lett. **110**, 17 (2017).
- [13] D. Riedel *et al.*, *Deterministic Enhancement of Coherent Photon Generation from a Nitrogen-Vacancy Center in Ultrapure Diamond*, Phys. Rev. X **7**, 031040 (2017).
- [14] D. Riedel *et al.*, *Low-Loss Broadband Antenna for Efficient Photon Collection from a Coherent Spin in Diamond*, Phys. Rev. Applied **2**, 064011 (2014).
- [15] A. Butcher *et al.*, *High-Q Nanophotonic Resonators on Diamond Membranes using Templated Atomic Layer Deposition of TiO₂*, Nano Lett. **20**, 6 (2020).
- [16] X. Guo *et al.*, *Direct-bonded diamond membranes for heterogeneous quantum and electronic technologies*, Nat Commun **15**, 8788 (2024).

- [17] A. M. Boyce *et al.*, *Plasmonic Diamond Membranes for Ultrafast Silicon Vacancy Emission*, *Nano Lett.* **24**, 12 (2024).
- [18] S. Asif *et al.*, *Diamond micro-chip for quantum microscopy*, *AVS Quantum Science* **6**, 4 (2024).
- [19] Y. Schluskel *et al.*, *Wide-Field Imaging of Superconductor Vortices with Electron Spins in Diamond*, *Phys. Rev. Applied* **10**, 034032 (2018).
- [20] J. J. Carmiggelt *et al.*, *Broadband microwave detection using electron spins in a hybrid diamond-magnet sensor chip*, *Nat Commun* **14**, 490 (2023).
- [21] T. S. Ghiasi *et al.*, *Nitrogen-vacancy magnetometry of CrSBr by diamond membrane transfer*, *npj 2D Mater Appl* **7**, 62 (2023).
- [22] M. Borst *et al.*, *Observation and control of hybrid spin-wave–Meissner-current transport modes*, *Science* **382**, 6669 (2023).
- [23] J. Zhou *et al.*, *Quantum sensing of local stray field environment of micron-scale magnetic disks*, *Applied Physics Letters* **123**, 024003 (2023).
- [24] R. Albrecht, A. Bommer, C. Deutsch, J. Reichel and C. Becher, *Coupling of a Single Nitrogen-Vacancy Center in Diamond to a Fiber-Based Microcavity*, *Phys. Rev. Lett.* **110**, 24 (2013).
- [25] H. Kaupp *et al.*, *Scaling laws of the cavity enhancement for nitrogen-vacancy centers in diamond*, *Phys. Rev. A* **88**, 053812 (2013).
- [26] S. Johnson *et al.*, *Tunable cavity coupling of the zero phonon line of a nitrogen-vacancy defect in diamond*, *New J. Phys.* **17**, 122003 (2015).
- [27] M. Ruf *et al.*, *Optically Coherent Nitrogen-Vacancy Centers in Micrometer-Thin Etched Diamond Membranes*, *Nano Lett.* **19**, 6 (2019).
- [28] V. Yurgens *et al.*, *Spectrally stable nitrogen-vacancy centers in diamond formed by carbon implantation into thin microstructures*, *Applied Physics Letters* **121**, 234001 (2022).
- [29] V. Yurgens *et al.*, *Cavity-assisted resonance fluorescence from a nitrogen-vacancy center in diamond*, *npj Quantum Inf* **10**, 112 (2024).
- [30] R. Zifkin, C. D. Rodríguez Rosenblueth, E. Janitz, Y. Fontana and L. Childress, *Lifetime Reduction of Single Germanium-Vacancy Centers in Diamond via a Tunable Open Microcavity*, *PRX Quantum* **5**, 030308 (2024).
- [31] R. Berghaus *et al.*, *Cavity-enhanced emission and absorption of color centers in a diamond membrane with selectable strain*, *Phys. Rev. Appl.* **23**, 034050 (2025).
- [32] Y. Herrmann *et al.*, *Coherent Coupling of a Diamond Tin-Vacancy Center to a Tunable Open Microcavity*, *Phys. Rev. X* **14**, 041013 (2024).

- [33] S. Bogdanović *et al.*, *Robust nano-fabrication of an integrated platform for spin control in a tunable microcavity*, *APL Photonics* **2**, 12 (2017).
- [34] P. Tamarat *et al.*, *Stark Shift Control of Single Optical Centers in Diamond*, *Phys. Rev. Lett.* **97**, 083002 (2006).
- [35] N. R. Parikh *et al.*, *Single-crystal diamond plate liftoff achieved by ion implantation and subsequent annealing*, *Applied Physics Letters* **61**, 26 (1992).
- [36] A. H. Piracha *et al.*, *Scalable Fabrication of Integrated Nanophotonic Circuits on Arrays of Thin Single Crystal Diamond Membrane Windows*, *Nano Lett.* **16**, 5 (2016).
- [37] B. A. Fairchild *et al.*, *Fabrication of Ultrathin Single-Crystal Diamond Membranes*, *Advanced Materials* **20**, 24 (2008).
- [38] X. Guo *et al.*, *Tunable and Transferable Diamond Membranes for Integrated Quantum Technologies*, *Nano Lett.* **21**, 24 (2021).
- [39] A. Faraon, P. E. Barclay, C. Santori, K.-M. C. Fu and R. G. Beausoleil, *Resonant enhancement of the zero-phonon emission from a colour centre in a diamond cavity*, *Nature Photon* **5**, 301 (2011).
- [40] B. J. M. Hausmann *et al.*, *Integrated Diamond Networks for Quantum Nanophotonics*, *Nano Lett.* **12**, 3 (2012).
- [41] P. Ouartchaiyapong, L. M. A. Pascal, B. A. Myers, P. Lauria and A. C. Bleszynski Jayich, *High quality factor single-crystal diamond mechanical resonators*, *Applied Physics Letters* **101**, 163505 (2012).
- [42] P. Appel *et al.*, *Fabrication of all diamond scanning probes for nanoscale magnetometry*, *Rev. Sci. Instrum.* **87**, 6 (2016).
- [43] M. Ruf, *Cavity-enhanced quantum network nodes in diamond*, Ph.D. thesis, Delft University of Technology (2021).
- [44] Y. Tao, J. M. Boss, B. A. Moores and C. L. Degen, *Single-crystal diamond nanomechanical resonators with quality factors exceeding one million*, *Nat Commun* **5**, 3638 (2014).
- [45] J. Heupel *et al.*, *Fabrication of High-Quality Thin Single-Crystal Diamond Membranes with Low Surface Roughness*, *Physica Status Solidi (a)* **220**, 4 (2023).
- [46] M. J. Burek *et al.*, *Free-Standing Mechanical and Photonic Nanostructures in Single-Crystal Diamond*, *Nano Lett.* **12**, 12 (2012).
- [47] B. Khanaliloo, M. Mitchell, A. C. Hryciw and P. E. Barclay, *High-Q/V Monolithic Diamond Microdisks Fabricated with Quasi-isotropic Etching*, *Nano Lett.* **15**, 8 (2015).
- [48] J. S. Hodges *et al.*, *Long-lived NV⁻ spin coherence in high-purity diamond membranes*, *New J. Phys.* **14**, 093004 (2012).

- [49] C. Toninelli *et al.*, *A scanning microcavity for in situ control of single-molecule emission*, Applied Physics Letters **97**, 021107 (2010).
- [50] M. Mader, J. Reichel, T. W. Hänsch and D. Hunger, *A scanning cavity microscope*, Nat Commun **6**, 7249 (2015).
- [51] J. Benedikter, T. Moosmayer, M. Mader, T. Hümmer and D. Hunger, *Transverse-mode coupling effects in scanning cavity microscopy*, New J. Phys. **21**, 103029 (2019).
- [52] S. M. Eaton *et al.*, *Quantum Micro–Nano Devices Fabricated in Diamond by Femtosecond Laser and Ion Irradiation*, Adv Quantum Tech **2**, 1900006 (2019).
- [53] R. Norte, J. Moura and S. Gröblacher, *Mechanical Resonators for Quantum Optomechanics Experiments at Room Temperature*, Phys. Rev. Lett. **116**, 147202 (2016).
- [54] J. F. Ziegler, M. Ziegler and J. Biersack, *SRIM – The stopping and range of ions in matter (2010)*, Nuclear Instruments and Methods in Physics Research Section B: Beam Interactions with Materials and Atoms **268**, 1818 (2010).
- [55] S. van Dam, *Optical cavities, coherent emitters, and protocols for diamond-based quantum networks*, Ph.D. thesis, Delft University of Technology (2019).
- [56] S. B. van Dam, M. Ruf and R. Hanson, *Optimal design of diamond-air microcavities for quantum networks using an analytical approach*, New J. Phys. **20**, 115004 (2018).
- [57] A. M. Zaitsev, *Optical Properties of Diamond* (Springer Berlin Heidelberg, Berlin, Heidelberg, 2001).
- [58] J. Körber *et al.*, *Scanning Cavity Microscopy of a Single-Crystal Diamond Membrane*, Phys. Rev. Applied **19**, 064057 (2023).
- [59] I. Friel, S. L. Geoghegan, D. J. Twitchen and G. A. Scarsbrook, *Development of high quality single crystal diamond for novel laser applications*, in *Optics and Photonics for Counterterrorism and Crime Fighting VI and Optical Materials in Defence Systems Technology VII*, edited by C. Lewis, D. Burgess, R. Zamboni, F. Kajzar and E. M. Heckman (Toulouse, France, 2010) p. 783819.
- [60] D. Howell, *Strain-induced birefringence in natural diamond: a review*, ejm **24**, 575 (2012).
- [61] H. K. Beukers *et al.*, *Remote-Entanglement Protocols for Stationary Qubits with Photonic Interfaces*, PRX Quantum **5**, 010202 (2024).
- [62] B. Hensen *et al.*, *Loophole-free Bell inequality violation using electron spins separated by 1.3 kilometres*, Nature **526**, 682 (2015).
- [63] J. M. Brevoord *et al.*, *Heralded initialization of charge state and optical-transition frequency of diamond tin-vacancy centers*, Phys. Rev. Applied **21**, 5 (2024).

- [64] J. M. Brevoord *et al.*, *Large-range tuning and stabilization of the optical transition of diamond tin-vacancy centers by in situ strain control*, Appl. Phys. Lett. **126**, 17 (2025).
- [65] G. L. Van De Stolpe *et al.*, *Check-probe spectroscopy of lifetime-limited emitters in bulk-grown silicon carbide*, npj Quantum Inf **11**, 31 (2025).
- [66] H. Bernien *et al.*, *Two-Photon Quantum Interference from Separate Nitrogen Vacancy Centers in Diamond*, Phys. Rev. Lett. **108**, 4 (2012).
- [67] A. Sipahigil *et al.*, *Indistinguishable Photons from Separated Silicon-Vacancy Centers in Diamond*, Phys. Rev. Lett. **113**, 113602 (2014).
- [68] H. Bernien *et al.*, *Heralded entanglement between solid-state qubits separated by three metres*, Nature **497**, 86 (2013).
- [69] J. Borregaard, A. S. Sørensen and P. Lodahl, *Quantum Networks with Deterministic Spin–Photon Interfaces*, Adv. Quantum Technol. **2**, 5 (2019).
- [70] G. Pieplow *et al.*, *Quantum electrometer for time-resolved material science at the atomic lattice scale*, Nat Commun **16**, 6435 (2025).
- [71] Z. Li *et al.*, *Atomic optical antennas in solids*, Nat. Photon. **18**, 1113 (2024).
- [72] D. M. Irber *et al.*, *Robust all-optical single-shot readout of nitrogen-vacancy centers in diamond*, Nat Commun **12**, 532 (2021).
- [73] S. L. N. Hermans *et al.*, *Entangling remote qubits using the single-photon protocol: an in-depth theoretical and experimental study*, New J. Phys. **25**, 013011 (2023).
- [74] D. Hunger *et al.*, *A fiber Fabry–Perot cavity with high finesse*, New J. Phys. **12**, 065038 (2010).
- [75] M. Uphoff, M. Brekenfeld, G. Rempe and S. Ritter, *Frequency splitting of polarization eigenmodes in microscopic Fabry–Perot cavities*, New J. Phys. **17**, 013053 (2015).
- [76] P. Maier, S. Rupp, N. Lettner, J. H. Denschlag and A. Kubanek, *Fabrication of customized low-loss optical resonators by combination of FIB-milling and CO₂ laser smoothing*, Opt. Express **33**, 19205 (2025).
- [77] X. Guo *et al.*, *Microwave-Based Quantum Control and Coherence Protection of Tin-Vacancy Spin Qubits in a Strain-Tuned Diamond-Membrane Heterostructure*, Phys. Rev. X **13**, 041037 (2023).
- [78] Y. Herrmann *et al.*, *A low-temperature tunable microcavity featuring high passive stability and microwave integration*, AVS Quantum Science **6**, 041401 (2024).
- [79] Y. Herrmann *et al.*, *Data and software underlying the publication "Laser-cut Patterned, Micrometer-thin Diamond Membranes with Coherent Color Centers for Open Microcavities"*, (2025).

- [80] M. Ruf, M. Weaver, S. van Dam and R. Hanson, *Resonant Excitation and Purcell Enhancement of Coherent Nitrogen-Vacancy Centers Coupled to a Fabry-Perot Microcavity*, Phys. Rev. Applied **15**, 024049 (2021).
- [81] S. B. Van Dam *et al.*, *Optical coherence of diamond nitrogen-vacancy centers formed by ion implantation and annealing*, Phys. Rev. B **99**, 161203 (2019).
- [82] J. M. Brevoord, *Data underlying the dissertation "Control of the optical interface of color centers in diamond"*, (2025).
- [83] M. Kasperczyk *et al.*, *Statistically modeling optical linewidths of nitrogen vacancy centers in microstructures*, Phys. Rev. B **102**, 075312 (2020).
- [84] C. Sauerzapf, *Fabrication and characterization of micrometerthin, color center-enriched diamonds for open microcavity quantum network nodes*, Master's thesis, Delft University of Technology (2023).

4

HERALDED INITIALIZATION OF CHARGE STATE AND OPTICAL TRANSITION FREQUENCY OF DIAMOND TIN VACANCY CENTERS

J. M. Brevoord*, L. De Santis*, T. Yamamoto, M. Pasini, N. Codreanu, T. Turan, H. K. C. Beukers, C. Waas, R. Hanson.

Diamond Tin-Vacancy centers have emerged as a promising platform for quantum information science and technology. A key challenge for their use in more complex quantum experiments and scalable applications is the ability to prepare the center in the desired charge state with the optical transition at a pre-defined frequency. Here we report on heralding such successful preparation using a combination of laser excitation, photon detection, and real-time logic. We first show that fluorescence photon counts collected during an optimized resonant probe pulse strongly correlate with the subsequent charge state and optical transition frequency, enabling real-time heralding of the desired state through threshold photon counting. We then implement and apply this heralding technique to photoluminescence excitation measurements, coherent optical driving, and an optical Ramsey experiment, finding strongly improved optical coherence with increasing threshold. Finally, we demonstrate that the prepared optical frequency follows the probe laser across the inhomogeneous linewidth, enabling tuning of the transition frequency over multiple homogeneous linewidths.

*These authors contributed equally to this work

The results of this chapter have been published in Phys. Rev. Applied **21**, 054047 (2024) ¹.

4.1. INTRODUCTION

In the past decade, color centers in diamond have become a leading platform for quantum networking experiments²⁻⁴. The first demonstrations relied on the nitrogen-vacancy center, ranging from the first loophole-free Bell test⁵ to a multinode-network experiments^{6,7}. However, the nitrogen-vacancy center suffers from a low Debye-Waller factor and strong spectral diffusion close to surfaces, making its optical interface inefficient. Group-IV vacancy centers emerged as a favorable alternative due to their high Debye-Waller factor^{3,8,9} and inversion symmetry¹⁰, resulting in first-order insensitivity to charge noise¹¹ and thus compatibility with nanophotonics integration^{12,13}. Pioneering experiments showing basic network-node operation in a dilution refrigerator have been performed with the silicon-vacancy center in nanophotonic devices¹⁴⁻¹⁶. More recently, the negatively charged tin-vacancy (SnV^-) center in diamond has attracted significant interest because of a high quantum efficiency^{8,12,17} and significant spin-orbit coupling, which allows operation at elevated temperatures compared with the silicon-vacancy center^{8,18,19}. In recent experiments, the integration of SnV centers into nanophotonic devices²⁰⁻²³ and coherent SnV spin-qubit control have been demonstrated^{24,25}.

It has been widely reported that under resonant optical excitation the SnV^- center can go into a dark state^{8,18,19,21,26}, possibly the SnV^{2-} state²⁷. Off-resonant excitation (typically around 515-532 nm) is routinely used for repumping to the SnV^- state^{11,18,20,21}. The optical-transition frequency of the SnV^- center after the repump is, in general, not the same as before (spectral diffusion), possibly caused by the capture or release of nearby charges in the repump process or by the direct impact of the pump excitation on the charge environment²⁷. The sensitivity of the SnV^- center to its charge environment persists in higher orders, despite being first-order insensitive due to inversion symmetry¹¹. These processes pose two challenges for future use in quantum protocols: i) the charge-state repump is probabilistic, leading to initialization errors, and ii) spectral diffusion hinders efficient optical spin initialization and readout and causes reduced photon indistinguishability, which negatively impacts key protocols requiring photon interference such as remote entanglement generation²⁸. In this work, we overcome these challenges by realizing heralded initialization into the desired charge state and preset the optical-transition frequency.

4.2. EXPERIMENTAL SETUP

A simplified level structure of the SnV center in the negatively charged state (SnV^-) is shown in Fig. 4.1(a). In the absence of a magnetic field, the ground and optically excited states consist of spin-degenerate orbital doublets, leading to four optical transitions. Of main interest for a spin-photon interface is the zero-phonon line (ZPL) transition at 619 nm, linking the lowest-branch ground and optically excited states. Besides the ZPL path, photon emission can be accompanied by the excitation of vibronic modes (phonon-sideband (PSB) emission).

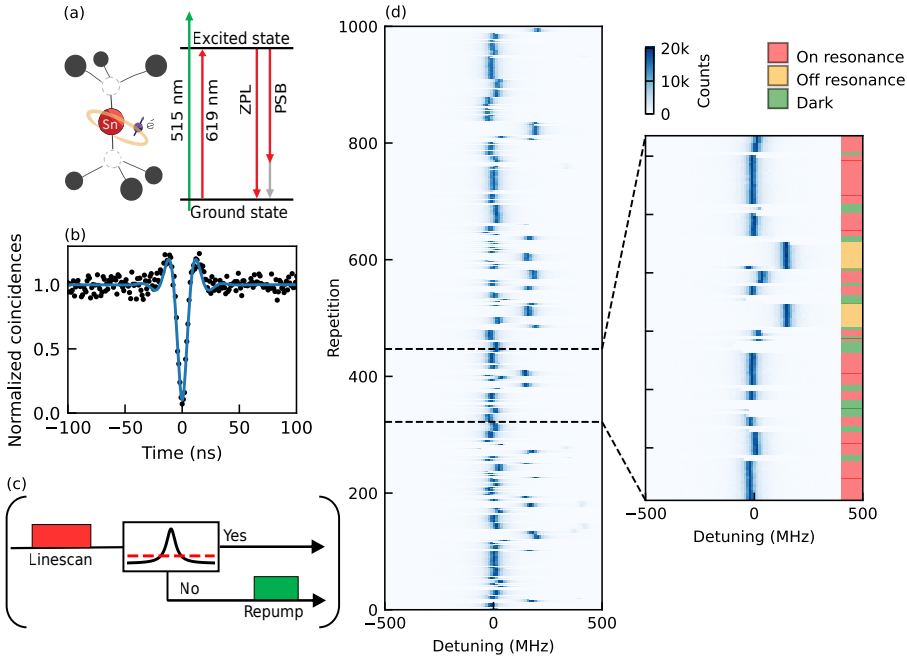


Figure 4.1: (a) Color-center structure and the optical transition of interest of a SnV^- center in diamond. Resonant excitation at 619 nm results in emission in the ZPL or PSB decay channels. (b) Second-order correlation measurement of the emission from a single SnV^- under continuous resonant excitation of 80 nW, fitted by $g^{(2)}(\tau) = 1 - e^{-\frac{3\tau\gamma}{4}} (\cos(\omega\tau) + \frac{3\gamma}{4\omega} \sin(\omega\tau))$, yielding $g^{(2)}(0) = 0.10 \pm 0.02$, without background correction. (c) Pulse sequence for the conditional PLE measurements, where we apply a repump pulse if the maximum number of photon counts detected during a single frequency step is less than 1.5 times the mean number of photons detected. (d) Fluorescence from 1000 PLE scans taken at approximately 1.3 GHz/s over the optical transition. The state of the emitter is estimated from the counts detected during each scan. If the emitter is flagged as dark, an off-resonant 515 nm pulse is applied before the following scan.

Our main investigation focuses on a SnV^- center (labeled $\text{SnV}^- \text{A}$) in an $\text{IIa} \langle 111 \rangle$ -oriented diamond, where Sn ions are implanted approximately 1 nm below the surface. Subsequently, overgrowth of the diamond by chemical-vapor deposition²⁹ results in SnV^- centers approximately 550 nm below the surface. All experiments on $\text{SnV}^- \text{A}$ are performed in an optical confocal setup at 4 K (see Supplemental Material for experimental setup details, which includes Ref.³⁰). Fig. 4.1(b) shows the second-order correlation function $g^{(2)}$ of the PSB emission of the SnV^- center under continuous resonant excitation. We find $g^{(2)}(0) = 0.10 \pm 0.02$ without any background subtraction showing that the light indeed originates from an individual emitter.

4.3. DYNAMICS OF CHARGE STATE AND RESONANCE FREQUENCY

We investigate the SnV^- center by performing photoluminescence-excitation (PLE) scans, where the optical transition is scanned with a resonant laser of 3 nW at approxi-

mately 1.3 GHz/s while the PSB emission is recorded. In this experiment, a conditional repump is used: we apply a repump pulse if the peak photon count detected during the PLE is below a preset threshold; see pulse sequence in Fig. 4.1(c).

Fig. 4.1(d) shows 1000 consecutive resonant scans. We identify three different regimes, which we label by color on the right for a subset of scans. Red indicates that the optical transition is found near zero detuning ('on resonance') and the photon-count threshold is met. This condition constitutes the desired state. Green indicates scans with counts below the threshold, indicating the emitter has gone into the dark state. A 515 nm repump pulse of 50 ms and 1 μ W is applied before the following scan. It can be seen that the repump pulse indeed brings the emitter back to the bright SnV^- -state with good probability, often accompanied by a shift of the resonant frequency of the emitter. We highlight scans in orange in which the threshold of counts is met, but the detected resonance is significantly detuned, more than 100 MHz ('off resonance'). Importantly, we find that the SnV^- center exhibits high spectral stability both for the on-resonance condition and for the off-resonance condition, up to the point that ionization occurs.

4.4. PROBE PULSES FOR CHARGE-STATE AND RESONANCE-CONDITION DETECTION

Motivated by the observed spectral stability before ionization, we explore the possibility of using photon counts during a resonant probe pulse as a heralding signal for the successful preparation of the SnV^- center in the negative charge state with its optical transition at a desired frequency. To gain quantitative insights into the predictive capabilities of such a heralding signal, we implement the pulse sequence shown in Fig. 4.2(a). A 515 nm 'repump' pulse is followed by two identical resonant-laser pulses, named here 'pulse 1' and 'pulse 2'. The sequence in Fig. 4.2(a) is repeated 10 000 times in our experimental runs.

In Fig. 4.2(b) we plot on a logarithmic scale the distributions of the photons detected during pulse 2, C_2 , as a function of the number of photons detected during the preceding pulse 1, C_1 , for three different resonant-laser powers. We quantitatively describe the relation between the two distributions C_1 and C_2 via the correlation coefficient $R_{1,2}$ (see Supplemental Material for details). For the lowest power (top panel), we find an almost-perfect correlation of $R_{1,2} = 0.961$. This observation implies that the number of photons scattered by the SnV^- center during these pulses is dictated by their charge state and their instantaneous detuning from the laser frequency. By increasing the resonant-laser power (middle and lower panel), we observe a change in the distribution of photon counts. As expected, the mean number of photon counts is increased. In addition, while the correlation between C_1 and C_2 is still present, we can see the effect of ionization, resulting in vertical and horizontal regions of uncorrelated photon distributions with decreasing correlations coefficients $R_{1,2}$ of 0.857 and 0.798 respectively. The vertical band is due to ionization during pulse 2 after several photons have already been detected. The horizontal band corresponds mainly to cases where ionization occurred during pulse 1; those cases could lead to an incorrect heralding

signal and should thus be minimized. Having confirmed that the probe signal strongly correlates to the state of the SnV^- center after the probe, we now use this to condition our dataset to cases where the SnV^- center is on resonance with the probe laser (i.e. a high number of photon counts in the detection window). As shown in Fig. 4.2(c), if conditioning is done on $C_1 > 100$, the photon-count distribution of pulse 2 follows a Poisson distribution centered at 110 counts, while the reverse conditioning shows a broader, lower-count distribution mixed with a peak near zero counts. The thresholding approach demonstrated here allows us to filter the desired bright-state condition of the color center out of the statistical distribution of possible charge-resonance states. We determine a lower bound for the initialization fidelity of $(96 \pm 4)\%$ (see Supplemental Material for details). Tighter thresholding can be done at the expense of a decrease in efficiency, as shown in Fig. 4.2(d). For instance, for the threshold value of 100 used above, we observe a success probability of passing the threshold of 33%.

Similarly to the analysis above, we study the effect of the repump laser (see pulse sequence in Fig. 4.2(e)) by plotting the number of photons detected during pulse 4, C_4 , as a function of the number of photons detected in the probe pulse (C_3) preceding a pump pulse, see Fig. 4.2(f). For weak repump pulses (top panel), some correlation between the probe and pump signals is visible, as the repump in this case does not significantly affect the SnV^- center and its environment. For sufficiently strong repump pulses (middle and lower panels), no correlations are observed, showing that the state following the repump pulse is independent of the state before the repump. This is confirmed by the histograms shown in Fig. 4.2(g), where we plot the count distribution C_4 of the data in the middle panel in Fig. 4.2(f) for the two shaded areas. We see that the distributions are similar for low and high counts detected in pulse 3.

Using again the data from the middle panel of Fig. 4.2(f), we estimate how efficiently the repump reinitializes the SnV^- center in the negative charge state if it was in the dark state before. For this, we set a threshold of 20 counts to distinguish between the desired charge state and the dark state. Conditioning on a dark state being detected on pulse 3, we find the probability of detecting a bright state on pulse 4 reaches about 75%.

4.5. OPTICAL RABI DRIVING

Next we investigate the correlation between probe-pulse counts and the SnV^- optical coherence. We apply the pulse sequence as shown in Fig. 4.3(a), where the repump pulse and probe pulse are now followed by 500 repetitions of a 30 ns resonant pulse used to drive optical Rabi oscillations. Fig. 4.3(b) shows a histogram of the number of photons detected during the probe pulse, where three peaks are present. We allocate the instances of high detected photon counts (rightmost peak) to the emitter being in the 'on-resonance' state. The instances of the middle and left peak instead correspond respectively to the 'off-resonant' and 'dark' cases. On the basis of this, we divide the histogram into four parts, as highlighted by the shaded background colors in Fig. 4.3(b) corresponding to the three peaks described above plus an intermediate region between the center peak and the rightmost peak.

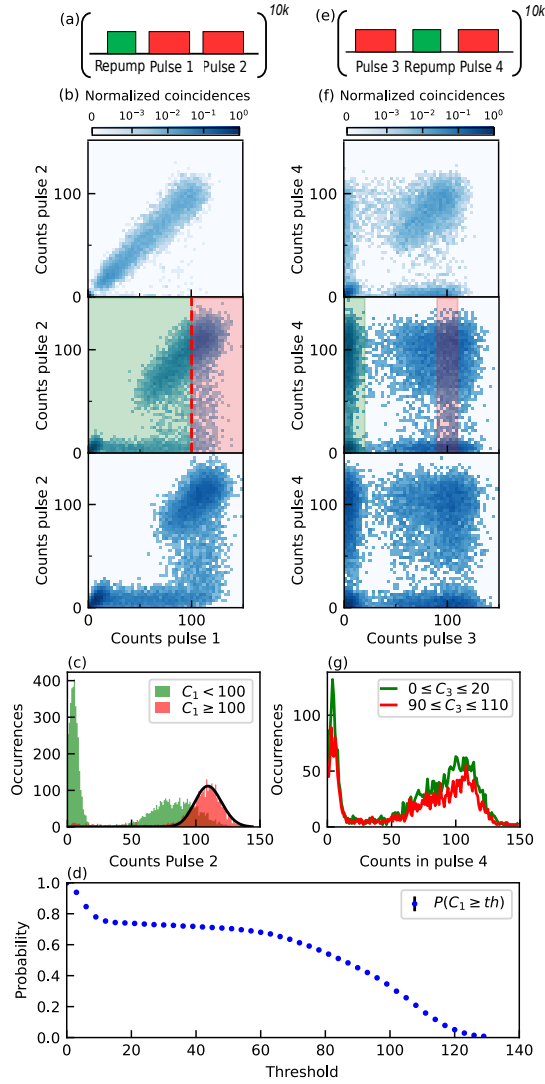


Figure 4.2: (a) Pulse sequence used for the data in (b), consisting of an off-resonant pump pulse followed by two identical resonant probe pulses (1 and 2). (b) Two-dimensional histogram of photon counts C_2 , as a function of C_1 for increasing resonant-laser powers (10 nW, 100 nW, 200 nW) and a fixed duration of 50 μ s. (c) Histogram of C_2 conditioned on C_1 above or below a threshold of 100 counts of the data from the middle panel of (b). From the former, we determine the lower-bound initialization fidelity of $(96 \pm 4)\%$. The total variance distance of the two histograms is 0.68, which indicates a high degree of orthogonality between the two distributions. (d) Probability of passing the threshold used for heralded bright-state initialization; the error bars fall within the data points. (e) Pulse sequence used for the data in (f), consists of two identical resonant probe pulses (3 and 4) with an off-resonant pump pulse in between. (f) Two-dimensional histogram of photon counts C_4 , as a function of C_3 for increasing repump duration and powers (50 μ s at 10 μ W, 500 μ s at 100 μ W, 750 μ s at 200 μ W). (g) Histogram of C_4 conditioned on C_3 being a low or high number of counts. The total variance distance of the two histograms is 0.09, which indicates a low degree of orthogonality between the two distributions.

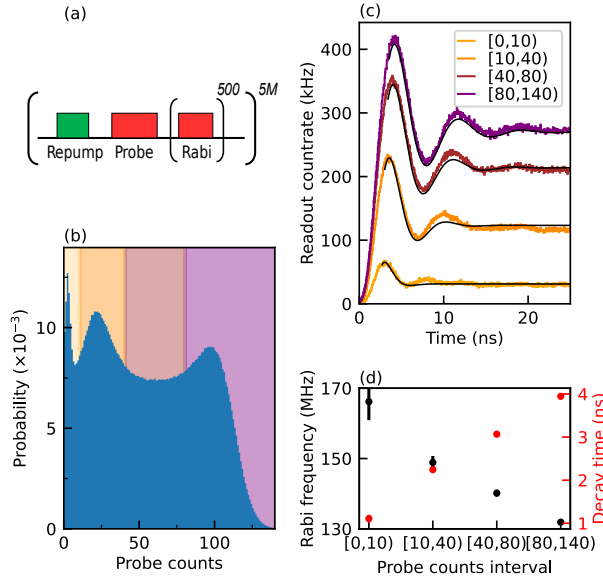


Figure 4.3: (a) Pulse sequence used for the Rabi driving experiment conditioned on the probe-pulse counts (Repump: 500 μ s, 100 μ W, Probe: 500 μ s, 100 nW, Rabi pulse: 30 ns at 17.5 nW). (b) Histogram of the photon counts detected during the probe pulse normalized by the number of sequence iterations. (c) Time-resolved histograms of photon counts during Rabi driving, conditioned on the number of photons detected in the preceding probe pulse. Solid lines are exponentially decaying sine fits to the data. (d) Decay times and Rabi frequencies were obtained by fitting the time traces in (c), including the error of the fits.

Fig. 4.3(c) shows time traces of the detected photons during the 30 ns resonant readout pulse conditioned on the four threshold intervals. Each curve reveals coherent driven oscillations with different amplitude, frequency, and decay times. As expected, by thresholding for higher probe counts we obtain higher count rates in the readout, as we are selecting for cases where the SnV^- is on resonance with the driving laser. By fitting these curves with an exponentially damped sine function we extract the Rabi frequency and decay time of the oscillations. These values are summarized in Fig. 4.3(d). Since the Rabi frequency is higher for nonzero detuning, this is consistent with the SnV^- center being closer to resonance for an increasing number of detected photons in the probe pulse. These results demonstrate a clear relation between the probe counts and the measured coherence.

4.6. REAL-TIME HERALDING OF CHARGE STATE AND OPTICAL-TRANSITION FREQUENCY

In the experiments reported so far, the conditioning on probe-pulse counts was done in postselection. For scalable applications in quantum protocols, it is key that the selection is done in real time i.e. before quantum protocols are run^{6,7,31,32}. In the

following, we report implementation of live thresholding on the probe counts using the programmable logic of a fast microcontroller (running on a $10\ \mu\text{s}$ clock cycle, see Supplemental Material) and use this as a charge-resonance-check (CRC) routine to herald the desired charge-resonance state before each experimental run.

The CRC sequence (see Fig. 4.4(a)) starts with a resonant probe pulse and live counting. Below we report on an implementation using two threshold values instead of just one, which allows more freedom in trading off heralding efficiency (rate) and accuracy. If the number of counts detected during the resonant probe pulse is below C_{repump} , an off-resonant 515 nm repump pulse is applied, followed by a resonant probe pulse. If the counts detected during the probe pulse are above C_{repump} but below C_{pass} , the resonant probe pulse is applied again. C_{repump} probes whether the emitter is in the correct charge state and the threshold C_{pass} functions to filter for instances that the emitter is not on resonance with the driving field. This procedure is repeated until the threshold C_{pass} is met.

We first implement the CRC in conjunction with PLE scans to show its effect on spectral diffusion and ionization; see Fig. 4.4(b). The CRC repump and probe pulses are of the same power and duration as in Fig. 4.3. Fig. 4.4(b) depicts two panels with 250 PLE scans each. Before every scan, a CRC is performed with a threshold (C_{pass} , C_{repump}) of (50, 10) counts for the left panel and (110,10) counts for the right panel.

For a low CRC threshold, $C_{\text{pass}} = 50$, the SnV^- resonant frequency shows spectral jumps less frequently than for a high CRC threshold, $C_{\text{pass}} = 110$, but jumps with higher magnitude. Because of the lower threshold, enough photons can be scattered to pass the CRC even when the SnV^- center is off-resonance. As a result, these off-resonant cases affect the PLE experiment, while the repump pulse is applied only once the emitter is dark.

With higher CRC thresholding, more repump cycles are required to reach a configuration where the SnV^- detuning to the driving laser is small enough to scatter more photons than the threshold value, C_{pass} . This leads to more-frequent spectral jumps of the resonance frequency but the jumps are of significantly lower magnitude. It can be seen how this improves the effective spectral diffusion probed by our experiment by one looking at the distribution of SnV^- resonance frequencies in the PLE scans (top panels in Fig. 4.4(b)). Here we have filtered for the resonance of the other emitter. In Fig. 4.4(c), we show the standard deviation of the distribution in the top panel in Fig. 4.4(b) as a function of the CRC threshold, C_{pass} . A clear trend towards a single-peaked distribution and lower variance is visible for higher thresholds (see Supplemental Material for the PLE scans). We note that use of a CRC threshold $C_{\text{pass}} < 50$ resulted in too few repump pulses to reliably determine the repump-induced spectral diffusion.

In addition, we applied the CRC on a different SnV center ($\text{SnV}^- \text{B}$) which is embedded in a nanophotonic waveguide (see Ref. ²³ for the device and experimental-setup details). When setting a high C_{pass} , we observe similar stable lines as for $\text{SnV}^- \text{A}$,

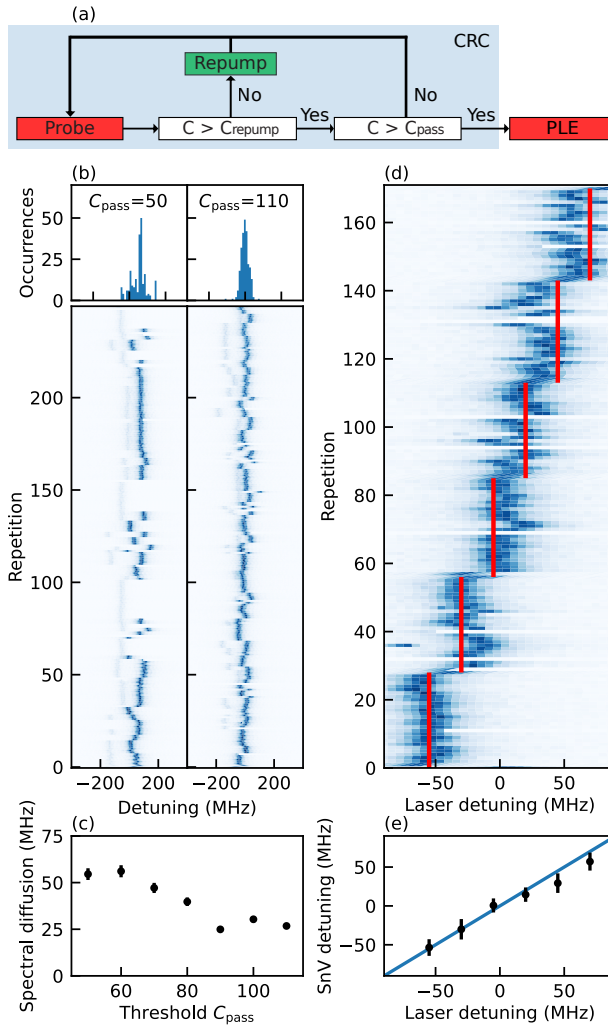


Figure 4.4: (a) Real-time logic pulse sequence for the CRC used to herald the charge-resonance state of the SnV. (b) Bottom: Fluorescence from 250 PLE scans each taken at approximately 1.3 GHz/s over the optical transition of SnV⁻A, preceded by a CRC for a threshold C_{pass} of 50 (left) and 110 (right) counts and a threshold $C_{\text{repump}} = 10$. We highlight the presence of a second weaker resonance in the scans, red-detuned with respect to the main one, that we attribute to another nearby emitter. Top: The distribution of the fitted centers of the individual scans, filtered for the bright emitter. (c) The standard deviation of the centers of the individual fitted scans as a function of the CRC threshold. The error bar is the standard error of the standard deviation. (d) The fluorescence of PLE scans each taken at approximately 1.3 GHz/s over the optical transition of SnV⁻B, preceded by a CRC for different resonant frequencies indicated by the red vertical lines. (e) Emitter's mean central frequency as a function of the set laser frequency, showing the shift of the SnV⁻ center's emission by CRC conditioning. The error bar is 1 standard deviation over the repetitions shown in panel (d).

see Fig. 4.4(d) and Supplemental Material for more PLE scans obtained with different CRC thresholds. Furthermore, we show on $\text{SnV}^- \text{B}$ that the CRC can be used to tune the heralded optical-transition frequency. In Fig. 4.4(d), we increase the frequency of the resonant laser during the CRC about every 30 scans, while using a high C_{pass} . As a consequence the heralding value of the emitter frequency will also change. The resonant-peak center detected in the subsequent PLE follows the frequency set point indicated by the solid red lines as shown in Fig. 4.4(d). In Fig. 4.4(e), we plot the mean center frequency of the individual scans for the different laser-detuning set points. This experiment shows that using CRC heralding we can tune the emitter by more than 100 MHz, which is several times greater than the measured mean single-scan (homogeneous) linewidth of 31 MHz. The effective tuning range of this method is determined by the inhomogeneous (or spectral-diffusion-limited) linewidth (which can be measured by one setting the CRC threshold to zero), as the probability for the repump pulse bringing the optical transition to more-detuned frequencies decreases rapidly.

4.7. OPTICAL RAMSEY EXPERIMENT USING REAL-TIME HERALDING

Finally, we directly probe the coherence of the optical transition for different CRC thresholds, by performing Ramsey-interferometry experiments using the pulse sequence depicted in Fig. 4.5(a). First, coherence between the ground state and the optically excited state is created with an optical $\pi/2$ pulse. After letting this state evolve for time τ we apply a second $\pi/2$ to map the remaining coherence onto populations that we read out by integrating the fluorescence in a 5 ns window after the second $\pi/2$ -pulse. This signal is then normalized to twice the fluorescence measured for a mixed state (i.e. for large τ).

We run this experiment for different delays τ and phase differences ϕ of the pulses. The resulting data are shown in Fig. 4.5(b), where the dependence of the readout signal on τ (x-axis value) and ϕ (plot color) is shown for a C_{pass} of 10, 60, and 110 counts in the left, center, and right panels, respectively, and fixed $C_{\text{repump}} = 10$. With increasing CRC threshold C_{pass} , we observe both a higher contrast of the oscillations and a slower decay of this contrast with increasing τ .

We extract a quantitative measure for the coherence between the ground state and the excited state by fitting the phase dependence for each value of τ to a sine function²¹. The amplitude of the sine is plotted in Fig. 4.5(c) as a function of τ . From a Gaussian fit to the data we determine the dephasing time T_2^* of the optical transition. For the CRC threshold $C_{\text{pass}} = 10$ we obtain T_2^* of (4.3 ± 1.7) ns, where the large uncertainty is a consequence of the low contrast. For a high CRC threshold $C_{\text{pass}} = 100$, we determine $T_2^* = (6.3 \pm 0.4)$ ns. This is, to our knowledge, the highest measured optical T_2^* for a SnV^- center to date. This demonstrates that implementation of a CRC can mitigate the effects of spectral detuning leading to an increase in optical coherence time, which is key to improving photon-interference experiments.

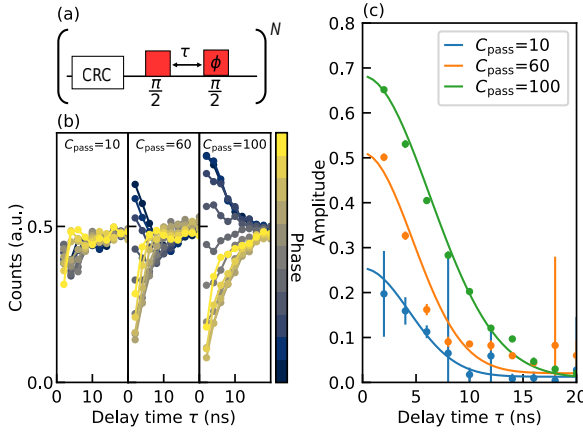


Figure 4.5: Optical Ramsey experiment conditioned on CRC. (a) Pulse sequence used for the data in (b), (c) (see Supplemental Material for further details) (b) Counts detected during an integration window after the second $\pi/2$ -pulse for a set C_{repump} of 10 and different C_{pass} , for different phases of the second $\pi/2$ -pulse, normalized to twice the counts detected in a mixed state. (c) Contrast decay envelopes for different CRC thresholds, C_{pass} , and a fixed C_{repump} of 10. The fitted envelopes show an increase of the T_2^* from (4.3 ± 1.7) ns for a low threshold, C_{pass} , to $T_2^* = (6.3 \pm 0.4)$ ns for the highest $C_{\text{pass}} = 100$. The error bars are fit errors.

4.8. CONCLUSION AND OUTLOOK

The ability to reliably prepare color-center qubits in the desired charge state at a set optical-transition frequency, as demonstrated here, is a key requirement for efficiently running complex quantum experiments as well for future quantum technologies. Taken together with recent diamond-SnV-center demonstrations of nanophotonic integration²⁰, spin-qubit control, and coherence beyond a 1 ms^{24,25}, our results complete a quantum control toolkit for scaling current single-center experiments. Compared with the experimentally maturer diamond nitrogen-vacancy center^{5,6,31,32} and diamond silicon-vacancy center^{15,16,33,34}, the SnV center adds the combination of compatibility with nanophotonic integration and relatively high quantum efficiency and operating temperature, making it a compelling platform for future exploration of multiqubit quantum networking and quantum computing protocols.

4.9. ACKNOWLEDGEMENT

We thank Henri Ervasti for software support. We thank Yanik Herrmann and Julius Fisher for proofreading the manuscript. We gratefully acknowledge support of this work by the Dutch Research Council (NWO) through the Spinoza Prize 2019 (Project No. SPI 63-264), by the Dutch Ministry of Economic Affairs and Climate Policy (EZK) as part of the Quantum Delta NL program, by the joint research program “Modular quantum computers” of Fujitsu Limited and Delft University of Technology, cofunded by the Netherlands Enterprise Agency under Project No. PPS2007, and by the QIA-Phase 1 project through the European Union’s Horizon Europe research and innovation program under Grant Agreement No. 101102140. L.D.S. acknowledges funding from the European Union’s Horizon

2020 research and innovation program under Marie Skłodowska-Curie Grant Agreement No. 840393.

4.9.1. AUTHOR CONTRIBUTIONS

J. M. B. and L. D. S. conducted the experiments and analyzed the data. T. Y. performed the diamond overgrowth. J. M. B. prepared the diamond sample with Sn centers, (SnV⁻)-A. T. T. helped with the measurements on the waveguide sample, (SnV⁻)-B, which was fabricated by N. C., and M. P. designed and built the waveguide setup. C. W., H. K. C. B., J. M. B., L. D. S., and M. P. were involved in building parts of the setup used for the main part of the measurements. J. M. B., L. D. S., and R. H. wrote the manuscript with input from all authors. L. D. S. and R. H. supervised the experiments.

4.9.2. DATA AVAILABILITY STATEMENT

The datasets of this study and the Python software for analysis and plotting are publicly available on 4TU.ResearchData under Ref.³⁵.

4.10. SUPPLEMENTARY MATERIAL

4.10.1. FABRICATION METHOD

The IIa <111>-oriented almost dislocation-free diamond substrate used for these measurements was cleaned in a piranha solution for 20 minutes before and after a plasma etch was performed using an Ar/Cl₂-plasma and an O₂-plasma removing ~8 μm of the surface to relief it from polishing induced strain. The (120)Sn ions were implanted at CuttingEdge with an energy of 5 keV and a dose of 1e11 ions/cm². After implantation and subsequent acid cleaning, a ~550 nm thick diamond layer was overgrown in-house using chemical vapor deposition (CVD). The growth was employed by a methane gas concentration of 0.04%, a gas pressure of 120 torr, and the surface temperature was maintained at 920°C. Impurity profiling via secondary ion mass spectroscopy on samples from similar growth experiments revealed silicon levels below 100 ppb, nitrogen concentrations below 20 ppb, and hydrogen content below 200 ppb, all below background levels. Boron concentrations were potentially near 10 ppb or at the detection limit. During the diamond growth, the sample is brought to temperatures where the vacancies become mobile and SnV centers are formed.

4.10.2. EXPERIMENTAL SET-UP

All measurement data in this work has been taken in a closed-cycle S50-Montana cryostat at a baseplate temperature of 4 K. The optical set-up consists of a room-temperature confocal microscope objective that is mounted in a home-built housing with xyz-positioners (Physik Instrumente P-615K011) to allow movement of the objective. An aluminum heat shield around the room-temperature objective is used to shield the 4 K diamond sample stage from heating by the objective. Resonant excitation around 619 nm is performed using a Toptica TA-SHG Pro. The wavelength is stabilized by feedback through a wavemeter (HighFinesse WS/U-10U). The off-resonant 515 nm green exci-

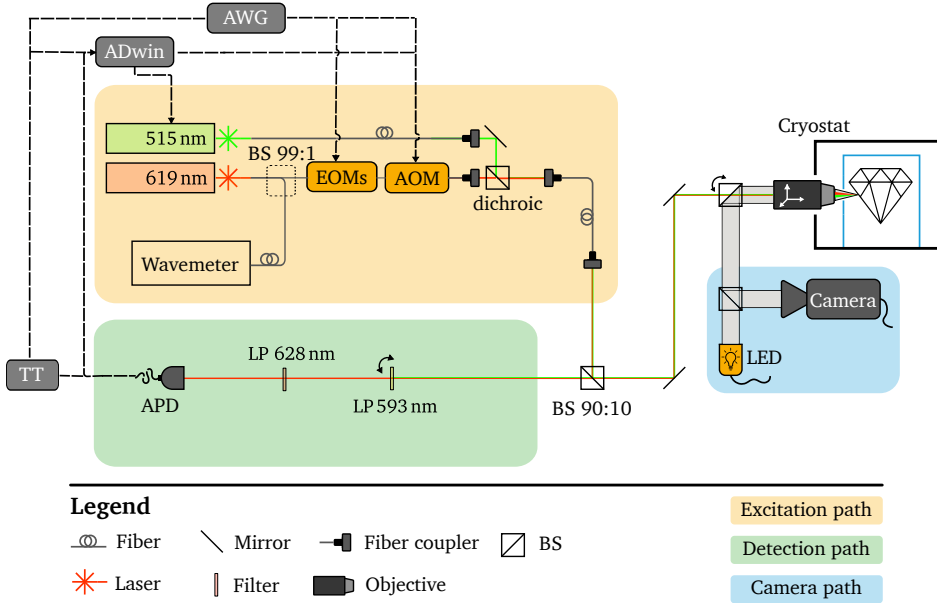


Figure 4.6: Confocal set-up

tation is performed using a Hubner Photonics Cobolt 06-MLD. To create μs resonant pulses, we use an in-fiber acousto-optic modulator (Gooch and Housego) controlled by a microcontroller (Jaeger ADwin Pro II). For ns-pulses, we use in addition an in-fiber amplitude electro-optic modulator (aEOM) (Jenoptik AM635) controlled by an arbitrary wave generator (Tektronix AWG5014). For phase modulation, we use an in-fiber phase EOM (pEOM) (Jenoptik PM635). The EOMs are stabilized for maximum transmission. All laser paths are combined and focused on the emitter of interest. In the detection path the resonant and off-resonant laser light is filtered by a 593 nm long-pass (Thorlabs, FELH0600) and a 628 nm long-pass (Semrock, TLP01-628) filter. The resulting PSB photons are detected by an APD (Laser Components), which generates analog pulses that can be recorded by both a timetagger (Hydraharp, PicoQuant) and the microcontroller. The setup is controlled and measurements are performed with a PC and the python 3 framework QMI 0.37³⁰.

4.10.3. CORRELATIONS BETWEEN THE HERALDING SIGNAL AND THE READ-OUT SIGNAL

To quantitatively describe the degree of correlation in Fig. 2(b) and 2(f) of the main text we calculate the Pearson correlation coefficients between the relevant datasets (using the `numpy.corrcoef()` function). The resulting coefficients quantifies the correlation between the two counts distributions (pulse 1 and pulse 2 in the case of Fig. 2(b), pulse 3 and pulse 4 in the case of Fig. 2(f)). For Fig. 2(b), we obtain 0.961, 0.857, 0.798 respectively for the top, middle, bottom plot. This confirms the high degree of correlation

between the two distributions, slightly reduced with increasing resonant laser power due to ionization. For Fig. 2(f), we obtain 0.584, 0.002, 0.015 respectively for the top, middle, bottom plot. This confirms that, while some correlation is still present at low green repump powers, with sufficiently high green power the counts distributions are uncorrelated.

Similarly to the analysis above, to quantify the orthogonality of the two distributions shown in Fig. 2(c) and in Fig. 2(g) of the main text, we calculate the total variation distance between the green and red histogram in each figure. For Fig. 2(c) the total distance is 0.68, and for Fig. 2(g) the total distance is 0.09. This confirms the high (low) degree of orthogonality between the two distributions in Fig. 2c (Fig. 2(g)).

4

4.10.4. INITIALIZATION FIDELITY

The lower bound initialization fidelity discussed in section IV of the main text is determined by conservatively attributing all runs in which the second pulse yields a dark state to an initialization error (i.e. assuming that the SnV was already dark at the end of the first pulse). The reason that this provides a lower bound is that ionization could also have occurred at the start of the second pulse leading to low number of total counts; this case would be an error in the analyzing pulse, not in the actual initialization. Performing above estimate yields (for Fig. 2(c) of the main text) a lower bound to the initialization fidelity of $F \geq (96 \pm 4)\%$.

4.10.5. OPTICAL PULSE CHARACTERIZATION AND OPTIMIZATION

To create the optical π -pulses, a 26 ns AOM-pulse (25 ns rise time of the AOM and 1 ns optical pulse) is applied, during which an aEOM suppresses the light during the ramping up and ramping down of the AOM pulse. During the window in which the aEOM is not suppressing a short 1 ns resonant light pulse is transmitted. All pulses are generated by the AWG.

The suppression of the light by the aEOM is optimized by sweeping the amplitude of the aEOM pulse and optimizing for the minimal number of photon counts detected during the ramping-up time of the AOM. An identical but reverse sign pulse is applied after the pulse sequence to prevent charging of the aEOM.

The optical $\pi/2$ -pulses are characterized by fixing the amplitude of AOM wave, sweeping the amplitude of the pulse of the aEOM and, integrating the PSB-photons counts after the pulse. This results in a sinusoid response which we fit to determine the amplitude of the aEOM wave corresponding to a $\pi/2$ -pulse.

For the Ramsey experiments, we noticed the amplitude of the second $\pi/2$ -pulse to vary with waiting time, τ , most likely to be caused by charging of the aEOM. We mitigate this effect by calibrating the amplitude of the second $\pi/2$ -pulse as a function of waiting time. We sweep the amplitude of the pulse of the aEOM and minimize the difference in detected photon counts between the first optimized pulse and the second $\pi/2$ -pulse.

4.10.6. CRC OPTICAL RAMSEY INTERFEROMETRY MEASUREMENTS

Additional data to Fig. 5 of the main text. We sweep the CRC threshold, C_{pass} , while keeping $C_{\text{repump}} = 10$. For $C_{\text{pass}} = 1$, we implement $C_{\text{repump}} = 1$, which is effectively equivalent to not implementing a CRC sequence but instead use a conditional repump, where we only repump once the emitter is in the dark state.

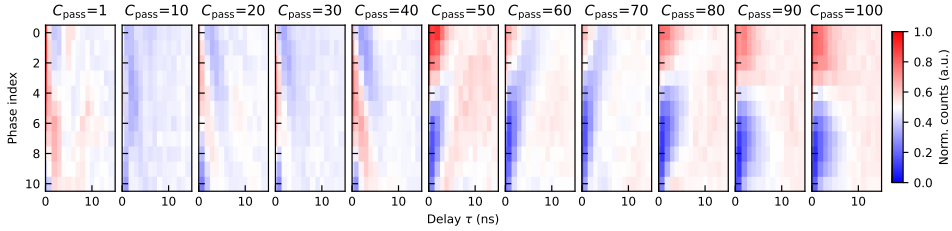


Figure 4.7: CRC Ramsey additional data, the phase index is based on the voltage step applied to the pEOM. Phase index 0 represents no phase difference between the $2 \pi/2$ -pulses, which should result in maximum counts detected at $\tau=0$.

4.10.7. CRC LINESCANS

Additional data to Fig. 4 of the main text.

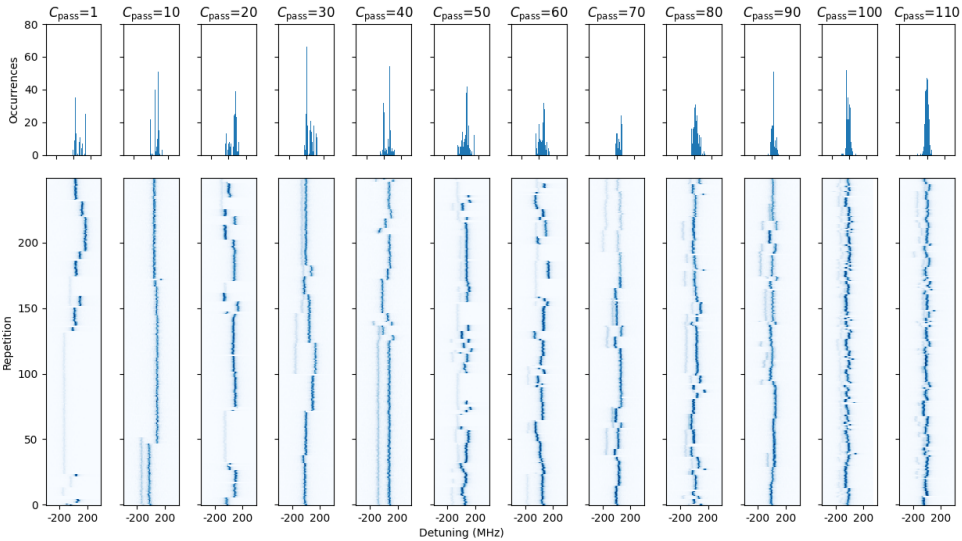


Figure 4.8: CRC linescan additional data of $\text{SnV}^- \text{A}$. Bottom: The fluorescence of 250 PLE scans each taken in $\sim 1.3 \text{ GHz/s}$ over the optical transition of $\text{SnV}^- \text{A}$, preceded by a CRC for various threshold C_{pass} and a fixed threshold $C_{\text{repump}} = 10$. We attribute the second red-detuned resonance detected to another nearby emitter. Top: The distribution of the fitted centers of the individual scans, filtered for the bright emitter.

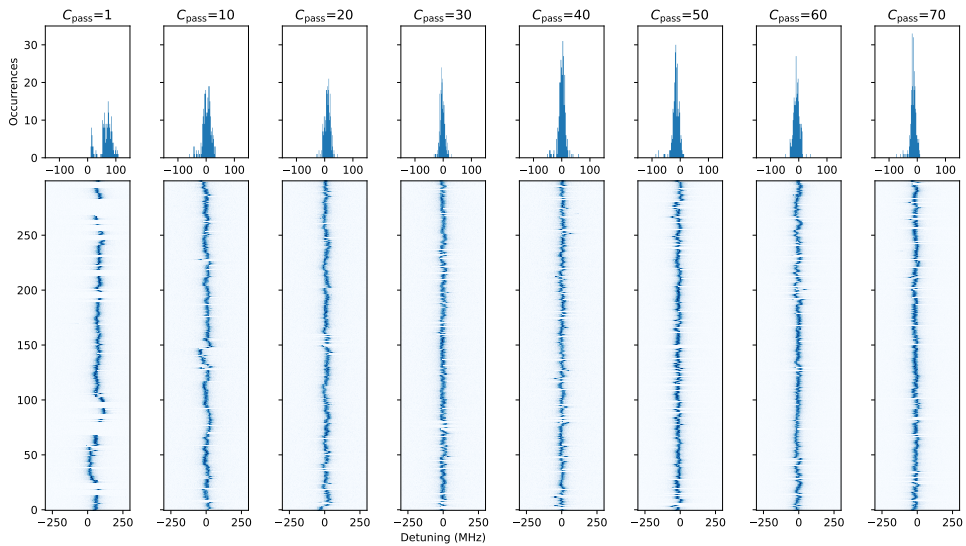


Figure 4.9: CRC linescan additional data of an in a waveguide embedded SnV^- B. Bottom: The fluorescence of 300 PLE scans each taken in ~ 1.3 GHz/s over the optical transition of SnV^- A, preceded by a CRC for various threshold C_{pass} and a fixed threshold $C_{\text{repump}} = 10$. Top: The distribution of the fitted centers of the individual scans.

BIBLIOGRAPHY

- [1] J. M. Brevoord *et al.*, *Heralded initialization of charge state and optical-transition frequency of diamond tin-vacancy centers*, *Phys. Rev. Applied* **21**, 5 (2024).
- [2] M. Atatüre, D. Englund, N. Vamivakas, S.-Y. Lee and J. Wrachtrup, *Material platforms for spin-based photonic quantum technologies*, *Nat Rev Mater* **3**, 38 (2018).
- [3] M. Ruf, N. H. Wan, H. Choi, D. Englund and R. Hanson, *Quantum networks based on color centers in diamond*, *Journal of Applied Physics* **130**, 070901 (2021).
- [4] G. Wolfowicz *et al.*, *Quantum guidelines for solid-state spin defects*, *Nat Rev Mater* **6**, 10 (2021).
- [5] B. Hensen *et al.*, *Loophole-free Bell inequality violation using electron spins separated by 1.3 kilometres*, *Nature* **526**, 682 (2015).
- [6] M. Pompili *et al.*, *Realization of a multinode quantum network of remote solid-state qubits*, *Science* **372**, 6539 (2021).
- [7] S. L. N. Hermans *et al.*, *Qubit teleportation between non-neighbouring nodes in a quantum network*, *Nature* **605**, 663 (2022).
- [8] T. Iwasaki *et al.*, *Tin-Vacancy Quantum Emitters in Diamond*, *Phys. Rev. Lett.* **119**, 253601 (2017).

- [9] C. Bradac, W. Gao, J. Forneris, M. E. Trusheim and I. Aharonovich, *Quantum nanophotonics with group IV defects in diamond*, Nat. Commun. **10**, 5625 (2019).
- [10] C. Hepp *et al.*, *Electronic Structure of the Silicon Vacancy Color Center in Diamond*, Phys. Rev. Lett. **112**, 036405 (2014).
- [11] L. De Santis, M. Trusheim, K. Chen and D. Englund, *Investigation of the Stark Effect on a Centrosymmetric Quantum Emitter in Diamond*, Phys. Rev. Lett. **127**, 14 (2021).
- [12] A. Sipahigil *et al.*, *An integrated diamond nanophotonics platform for quantum-optical networks*, Science **354**, 6314 (2016).
- [13] R. E. Evans *et al.*, *Photon-mediated interactions between quantum emitters in a diamond nanocavity*, Science **362**, 6415 (2018).
- [14] D. Sukachev *et al.*, *Silicon-Vacancy Spin Qubit in Diamond: A Quantum Memory Exceeding 10 ms with Single-Shot State Readout*, Phys. Rev. Lett. **119**, 223602 (2017).
- [15] M. K. Bhaskar *et al.*, *Experimental demonstration of memory-enhanced quantum communication*, Nature **580**, 60 (2020).
- [16] P.-J. Stas *et al.*, *Robust multi-qubit quantum network node with integrated error detection*, Science **378**, 6619 (2022).
- [17] M. Nguyen *et al.*, *Photodynamics and quantum efficiency of germanium vacancy color centers in diamond*, AP **1**, 066002 (2019).
- [18] J. Görlitz *et al.*, *Spectroscopic investigations of negatively charged tin-vacancy centres in diamond*, New J. Phys. **22**, 013048 (2020).
- [19] M. E. Trusheim *et al.*, *Transform-Limited Photons From a Coherent Tin-Vacancy Spin in Diamond*, Phys. Rev. Lett. **124**, 023602 (2020).
- [20] A. E. Rugar *et al.*, *Quantum Photonic Interface for Tin-Vacancy Centers in Diamond*, Phys. Rev. X **11**, 031021 (2021).
- [21] J. Arjona Martínez *et al.*, *Photonic Indistinguishability of the Tin-Vacancy Center in Nanostructured Diamond*, Phys. Rev. Lett. **129**, 17 (2022).
- [22] K. Kuruma *et al.*, *Coupling of a single tin-vacancy center to a photonic crystal cavity in diamond*, Applied Physics Letters **118**, 230601 (2021).
- [23] M. Pasini *et al.*, *Nonlinear Quantum Photonics with a Tin-Vacancy Center Coupled to a One-Dimensional Diamond Waveguide*, Phys. Rev. Lett. **133**, 023603 (2024).
- [24] E. I. Rosenthal *et al.*, *Microwave Spin Control of a Tin-Vacancy Qubit in Diamond*, Phys. Rev. X **13**, 031022 (2023).
- [25] X. Guo *et al.*, *Microwave-Based Quantum Control and Coherence Protection of Tin-Vacancy Spin Qubits in a Strain-Tuned Diamond-Membrane Heterostructure*, Phys. Rev. X **13**, 041037 (2023).

- [26] T. Lühmann *et al.*, *Charge-State Tuning of Single SnV Centers in Diamond*, ACS Photonics **7**, 12 (2020).
- [27] J. Görlitz *et al.*, *Coherence of a charge stabilised tin-vacancy spin in diamond*, npj Quantum Inf **8**, 45 (2022).
- [28] H. K. Beukers *et al.*, *Remote-Entanglement Protocols for Stationary Qubits with Photonic Interfaces*, PRX Quantum **5**, 010202 (2024).
- [29] A. E. Rugar *et al.*, *Generation of Tin-Vacancy Centers in Diamond via Shallow Ion Implantation and Subsequent Diamond Overgrowth*, Nano Lett. **20**, 3 (2020).
- [30] I. T. Raa *et al.*, *QMI - Quantum Measurement Infrastructure, a Python 3 framework for controlling laboratory equipment*, (2023).
- [31] S. L. N. Hermans *et al.*, *Entangling remote qubits using the single-photon protocol: an in-depth theoretical and experimental study*, New J. Phys. **25**, 013011 (2023).
- [32] A. Stolk *et al.*, *Telecom-Band Quantum Interference of Frequency-Converted Photons from Remote Detuned NV Centers*, PRX Quantum **3**, 020359 (2022).
- [33] B. Pingault *et al.*, *Coherent control of the silicon-vacancy spin in diamond*, Nat Commun **8**, 15579 (2017).
- [34] S. Meesala *et al.*, *Strain engineering of the silicon-vacancy center in diamond*, Phys. Rev. B **97**, 205444 (2018).
- [35] J. M. Brevoord *et al.*, *Data underlying the publication "Heralded initialization of charge state and optical transition frequency of diamond tin-vacancy centers"*, (2023).

5

LARGE-RANGE TUNING AND STABILIZATION OF THE OPTICAL TRANSITION OF DIAMOND TIN-VACANCY CENTERS BY *in situ* STRAIN CONTROL

J. M. Brevoord, L. G. C. Wienhoven, N. Codreanu, T. Ishiguro, E. van Leeuwen, M. Iuliano,
L. De Santis, C. Waas, H. K. C. Beukers, T. Turan, C. Errando-Herranz, K. Kawaguchi, R. Hanson

*The negatively charged tin-vacancy (SnV^-) center in diamond has emerged as a promising platform for quantum computing and quantum networks. To connect SnV^- qubits in large networks, *in situ* tuning and stabilization of their optical transitions are essential to overcome static and dynamic frequency offsets induced by the local environment. Here, we report on the large-range optical frequency tuning of diamond SnV^- centers using micro-electro-mechanically mediated strain control in photonic integrated waveguide devices. We realize a tuning range of >40 GHz, covering a major part of the inhomogeneous distribution. In addition, we employ real-time feedback on the strain environment to stabilize the resonance frequency and mitigate spectral wandering. These results provide a path for on-chip scaling of diamond SnV -based quantum networks.*

5.1. INTRODUCTION

Spin qubits in the solid state are promising building blocks for the realization of large-scale quantum systems²⁻⁹, with potential applications in computing and communication^{2,3}. An early workhorse for the field has been the nitrogen-vacancy (NV) in diamond, which was used for a loophole-free Bell test¹⁰, the realization of a multi-node quantum network⁶ and heralded entanglement over metropolitan distances⁷. However, the relatively low Debye-Waller factor and the incompatibility with nanophotonic integration due to a first-order sensitivity to electrical noise limits the development of large-scale quantum networks and the integration into scalable photonic circuits based on NV-centers in diamond. Next-generation color centers in solid state materials have started to emerge over the last decade to drive scaling of quantum systems^{9,11-14}. The negatively charged tin-vacancy (SnV^-) center in diamond has attracted much recent attention due to its excellent optical properties¹⁵⁻¹⁷, high quantum efficiency^{18,19}, and significant spin-orbit coupling^{20,21}, which allows for operation above dilution refrigerator temperatures^{20,22,23}. Furthermore, the SnV^- center lacks a first-order sensitivity to electrical noise due to its inversion symmetry, making it compatible with nanophotonic integration^{8,24-28}. The recent demonstration of entanglement between the electron spin-1/2 SnV^- center and a nearby ¹³C nuclear spin opens a path toward multi-qubit experiments using this platform²³.

5

For connecting SnV^- qubits into larger networks, photonic links mediating entanglement generation provide a modular and scalable path²⁹⁻³². The entanglement generation requires the qubits to emit indistinguishable photons. However, the photon emission of spin qubits in solids is typically not indistinguishable due to different local strain in the material resulting in a broad inhomogeneous distribution. In addition, the optical resonance frequency variations over time due to changes in e.g. local strain and variations in the local electronic environment limit the indistinguishability of the emitted photons. This poses challenges for the realization of large-scale quantum networks. SnV^- centers in diamond are first-order insensitive to electric fields, therefore conventional tuning using DC Stark tuning is limited^{33,34}. Previous work on strain engineering of other group-IV defects in diamond demonstrated frequency tuning^{11,35,36}, the mitigation of phonon interactions³⁷, and quantum interference of electromechanical stabilized emitters³⁸. Recent work on strain engineering of SnV^- centers shows heterogeneous integration with efficient state preparation and readout^{8,26} and a tuning range up to ≈ 25 GHz. Here, we integrated diamond waveguide devices containing SnV^- centers with local optical frequency control via electromechanically induced strain. We demonstrate a tuning range of >40 GHz and use the strain control in a feedback loop realizing a 12-fold improvement in the stabilization of the optical transition.

The SnV^- center in diamond consists of a tin-atom at the interstitial position between two missing carbon atoms with a captured electron, as shown in Fig. 5.1(a). A simplified level structure of the SnV^- center is given in Fig. 5.1(b). In the absence of a magnetic field, the ground and optically excited states are composed of spin-degenerate orbital doublets, resulting in four optical transitions^{18,39}. In the presence of strain, the

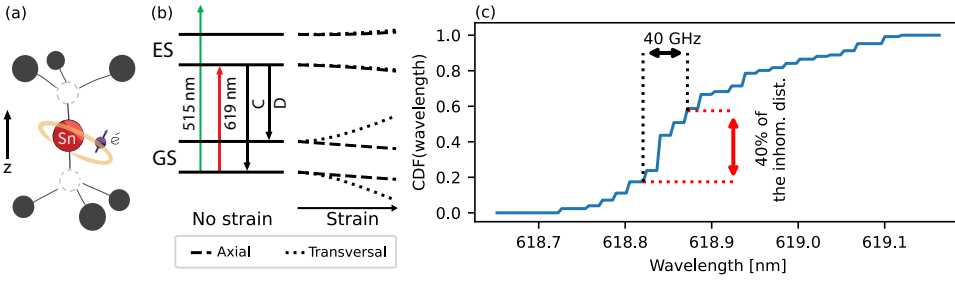


Figure 5.1: (a) Schematic of the SnV^- center structure. (b) The energy level scheme of an SnV^- center in diamond, indicating the ground state (GS) splitting and the excited state (ES) splitting. We focus on tuning and stabilizing the C-transition, which is the most relevant for quantum technology applications. Resonant excitation at 619 nm results in zero-phonon line (ZPL) emission via the C-transition and the D-transition, as well as their respective phonon side bands (PSB, not shown). Strain alters the energy levels. (c) The cumulative distribution function (CDF) of the inhomogeneous distribution from resonances obtained with PL.

energy levels shift. In this work, we control the optical transition linking the lowest branch of the ground and the optically excited state, zero-phonon line (ZPL), the C-transition. The C-transition is well suited for spin readout and photon emission for photon-mediated entanglement generation. We study SnV^- centers in our device in an optical confocal set-up at an operating temperature of 4 K, see the supplementary material for more details on the experimental set-up.

5.1.1. INHOMOGENEOUS DISTRIBUTION

The variation in optical resonances between different color centers in the diamond sample (inhomogeneous distribution) will determine the tuning range required to produce indistinguishable photons from multiple color centers within the same diamond sample. The inhomogeneous distribution of the SnV^- centers in the devices fabricated on a diamond sample used for this work is determined by photoluminescence (PL) measurements. We collect the emission in free space using a spectrometer while illuminating the sample with an off-resonant 515 nm laser with 200 μW and integrating over 10 s at 173 different laser spot locations on different devices. We determine the resonances of the C-transition using a peak-finding algorithm. The cumulative inhomogeneous distribution is plotted in Fig. 5.1(c). About 40% of the resonances detected in the region of interest are within a 40 GHz window. This range is not a fundamental limitation, in the recent work of Li et al.⁸, they found 40% of the resonances in a ≈ 20 GHz window. Moreover, Görlitz et al. reported a linewidth of 15 GHz for the ZPL transition of an ensemble of SnV^- centers in a high-pressure, high-temperature annealed diamond implanted with Sn atoms¹⁹. In addition to overcoming this static inhomogeneity, spectral diffusion and bi-stability pose a second challenge, as reported by others^{16,25,27,40–42}. In this work, we target both challenges using *in situ* strain engineering of the SnV^- including real-time feedback.

5.2. SnV CENTER STRAIN THEORY

Following Meesala, Sohn et al.³⁶ and Guo, Stramma, et al.²², considering an infinitesimal strain regime, we use the Hamiltonian describing strain in the basis of the SnV⁻:

$$\mathbb{H}_{\text{strain}} = \sum_{i,j} A_{ij} \epsilon_{ij}, \quad (5.1)$$

where ϵ_{ij} is a component of the strain tensor, $\boldsymbol{\epsilon}$, and A_{ij} operators that act on the electronic levels. Using group theory, we can write the Hamiltonian in the irreducible representations of the D_{3d} point group, in the basis $\{|e_x \uparrow\rangle, |e_x \downarrow\rangle, |e_y \uparrow\rangle, |e_y \downarrow\rangle\}$, where e_x, e_y represent the orbital and \downarrow, \uparrow the electronic spin-1/2 states. This shows that strain does not couple the ground and excited states, resulting in identical strain Hamiltonians forms for the ground and excited states. In this basis and in the local coordinate frame of the SnV⁻ center, where z is along the high-symmetry axis, the [111] crystallographic direction, the part of the Hamiltonian describing the presence of strain is,

$$\mathbb{H}_{\text{strain}} = \begin{bmatrix} \epsilon_{A_{1g}} - \epsilon_{E_{gx}} & \epsilon_{E_{gy}} \\ \epsilon_{E_{gy}} & \epsilon_{A_{1g}} + \epsilon_{E_{gx}} \end{bmatrix} \otimes \mathbb{1}_2, \quad (5.2)$$

where $\epsilon_{A_{1g}}, \epsilon_{E_{gx}}, \epsilon_{E_{gy}}$ represent the strain induced deformation modes in the D_{3d} point group. Rewriting each term as a linear combination of the strain tensor results in,

$$\begin{aligned} \epsilon_{A_{1g}} &= t_{\perp}(\epsilon_{xx} + \epsilon_{yy}) + t_{\parallel} \epsilon_{zz}, \\ \epsilon_{E_{gx}} &= d(\epsilon_{xx} - \epsilon_{yy}) + f \epsilon_{zx}, \\ \epsilon_{E_{gy}} &= -2d \epsilon_{xy} + f \epsilon_{yz}, \end{aligned} \quad (5.3)$$

where $t_{\perp}, t_{\parallel}, d$ and f are the strain susceptibilities, with different values in the ground and excited state. Diagonalizing the Hamiltonian and including spin-orbit coupling results in expressions for the mean ZPL frequency, ν_{ZPL} , and ground and excited state splitting, $\Delta_{u,g}$,

$$\begin{aligned} \nu_{\text{ZPL}} &= \nu_0 + \epsilon_{A_{1g}}^u - \epsilon_{A_{1g}}^g, \\ \Delta_u &= \sqrt{(\lambda_{\text{SO}}^u)^2 + 4(\epsilon_{E_{gx}}^u)^2 + 4(\epsilon_{E_{gy}}^u)^2}, \\ \Delta_g &= \sqrt{(\lambda_{\text{SO}}^g)^2 + 4(\epsilon_{E_{gx}}^g)^2 + 4(\epsilon_{E_{gy}}^g)^2}, \end{aligned} \quad (5.4)$$

where ν_0 is the mean ZPL frequency in the absence of strain and $\lambda_{\text{SO}}^{g,(u)}$ is the spin-orbit coupling of the ground (excited) state. The superscript g (u) indicates the ground (excited) state contribution.

5.3. DIAMOND WAVEGUIDE DEVICE FOR STRAIN TUNING

Our investigation focuses on SnV⁻ centers embedded in waveguide-based microelectromechanical systems (MEMS) devices. Fig. 5.2(a) shows a false-colored scanning electron microscope (SEM) image of the full MEMS device. The SnV⁻ incorporated waveguide is on one side connected via a mechanical spring-like structure to the bulk,

and on the other side clamped by two bars to two diamond bulk support platforms. Niobium electrodes (with titanium as the adhesion layer) are deposited on the spring (top electrode), indicated by the blue-colored region in Fig. 5.2(a), and below the spring (bottom electrode), indicated by the purple shaded region on Fig. 5.2(a). These electrodes form a capacitive electromechanical actuator when a bias voltage is applied between the electrodes. According to Eq. 5.4, by varying the applied bias voltage we can tune the optical resonance frequency of the SnV^- center due to the induced strain in the crystal.

Our device is fabricated from an electronic grade $\langle 001 \rangle$ -surface-orientated diamond sample. The Sn-atoms are uniformly implanted with a dose of 10^{11} ions/cm². After vacuum-annealing to activate the SnV^- centers, the color centers are predicted to end up at a mean depth of 90 nm below the surface with a straggle of 17 nm from stopping and range of ions in matter (SRIM) simulations⁴³. Due to substantial graphite formation during vacuum-annealing, an additional short plasma etching step was performed to remove the graphitic layer, resulting in SnV^- centers closer to the surface. Fabrication details can be found in the Supplementary Material. The waveguides used in this work are longitudinally aligned along the [110] direction. The four possible orientations of the SnV^- centers in the diamond crystal are [111], $\bar{1}11$, $1\bar{1}1$, and $\bar{1}\bar{1}1$. Considering the dominant uniaxial strain along the [110] direction when a voltage is applied, two groups of color centers that respond similarly to strain remain, indicated in Fig. 5.2(b). We denote the SnV^- centers with a component of the dipole along (perpendicular) the long axis of the beam as axial (transversal) color centers.

5.4. STRAIN SIMULATION OF THE DIAMOND DEVICE

We perform a finite element method (FEM) simulation using Ansys⁴⁴ to determine the strain in the waveguide when a voltage is applied over the electrodes. The ϵ_{xx} (lab frame) component of the strain tensor on the surface of the beam is shown in Fig. 5.2(c) when 75 V is applied, resulting in a maximal strain of $\epsilon_{xx} = 7 \times 10^{-5}$. Additional information on the simulations can be found in the supplementary material. We have indicated the estimated position of the SnV^- centers, positioned in different waveguides, evaluated in this work.

By rotating the strain tensor obtained from the FEM simulation from the lab frame to the axial/transversal SnV^- center reference frame and using Eq. 5.3 and Eq. 5.4, we simulate the resonance frequency shift of SnV^- centers in our device as a function of applied voltage. We use the strain susceptibilities d and f determined by Guo and Stramma et al.²² and t_{\parallel} from studies on other group-IV color centers by Meesala and Sohn et al.,³⁶ and Maity and Shao et al.³⁵. We note that using the single reported value for t_{\parallel} for SnV^- in Ref.²⁶ resulted in a discrepancy with the data well outside the uncertainty margin. For t_{\perp} , we take a lower and an upper bound based on reported values for other group-IV color centers^{35,36}, and incorporate this into the uncertainty margins of our simulations.

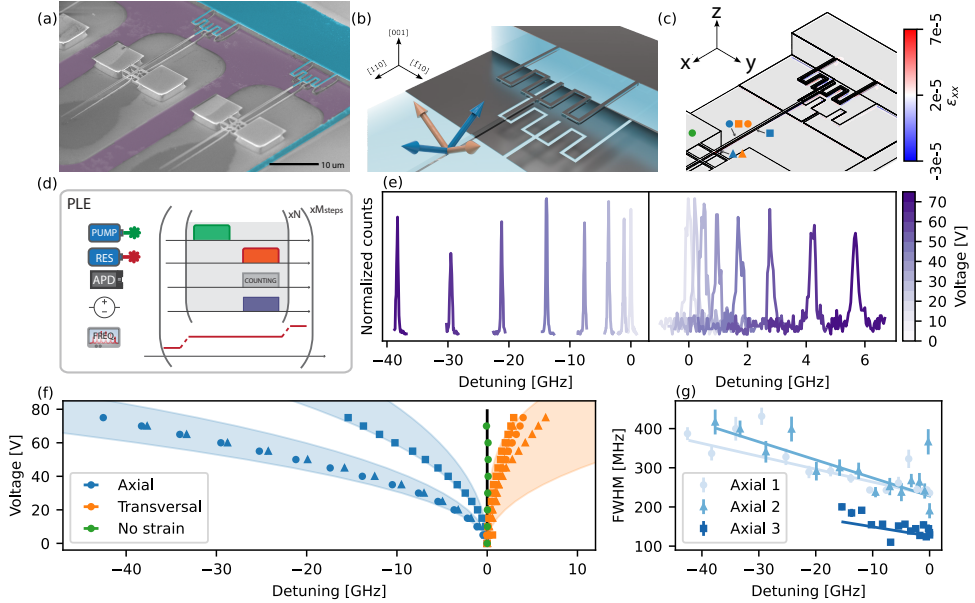


Figure 5.2: (a) False colored scanning electron microscope (SEM) image of the devices. (b) Orientation of the axial (transversal) SnV^- centers in the waveguide, indicated by the blue (orange) arrows. (c) Finite element method (FEM) simulation of the strain distribution (ϵ_{xx} component) over the surface of the device when 75 V is applied. The estimated positions of the SnV^- centers evaluated in (f) are indicated. (d) Pulse sequence of a photoluminescence excitation (PLE) scan, consisting of a pump off-resonant green pulse, a resonant (res) laser pulse, and photon counting by an avalanche photodiode (APD). (e) Fluorescence of PLE scans taken at different bias voltages of an axial (blue triangle) (transversal (orange triangle)) SnV^- center in the left (right) panel, showing an optical frequency shift of almost -40 GHz (6 GHz). The fluorescence is normalized to the maximal count rate of the 0V scan for the axial (8680 counts/s) and transversal emitter (2320 counts/s). (f) Summary of the measured optical resonance frequency detuning of several SnV^- centers, indicated by different shaped data points, as a function of the applied bias voltage, the error bars lie within the data points. The shaded areas are the simulated frequency shift as a function of the applied bias voltage for the SnV^- center 20 nm below the surface at the hinge point (orange and blue triangle) and 4 μm away from it (blue square), the uncertainty is in the depth of the color center and the strain susceptibility parameter t_{\perp} . (g) A summary of the obtained full-width half maximum (FWHM) from fitting PLE scan fluorescence as a function of detuning, for multiple axial oriented SnV^- centers, which we have fitted with a linear function.

5.5. TUNING RANGE VIA LOCAL STRAIN ENGINEERING

To determine the tuning range of the SnV^- centers in this sample, we perform photoluminescence excitation (PLE) scans using the pulse sequence shown in Fig. 5.2(d). We record the phonon-sideband (PSB) emission during the PLE scans. The bias voltage is applied in a pulsed way concurrent with the resonant readout to avoid heating originating from leakage current in the system. We have calibrated the pulse time and the time between subsequent pulses to eliminate the effects of heating. More information on the calibration can be found in the supplementary material.

Fig. 5.2(e) shows the PSB collection during PLE scans for different applied bias voltages. We observe the two distinct tuning behaviors attributed to the axial and transversal-oriented groups. The results of multiple SnV^- centers are summarized in Fig. 5.2(f), where we plot the detuning as a function of the applied bias voltage. In the Supplementary Material, we plot the absolute frequency shift as a function of the applied voltage. From the emitters evaluated, we can tune 4 pairs of emitters to the same absolute frequency. For an axial and a transversal SnV^- center positioned close to the hinge point (indicated by the orange and blue triangles in Fig. 5.2(c)) and an axial SnV^- center further away from the hinge point (indicated by the blue square), we simulate the expected frequency shift, indicated by the shaded areas in Fig. 5.2(f). We included an error bar representing our uncertainty in the depth of the color centers in the beam and the strain susceptibility values. The optical resonance of an SnV^- in the bulk (indicated by the green circle), which should not experience strain due to the bias voltage, is recorded for reference. This reference SnV^- indeed shows no frequency shift with increasing voltage. We find that SnV^- centers that show axial SnV^- center behavior can be tuned up to ≈ 43 GHz and transversal centers up to ≈ 6 GHz, covering a substantial part of the inhomogeneous distribution.

5.6. OPTICAL RESONANT FREQUENCY STABILITY

We observe a linear increase in the linewidth with frequency shift and hence strain in Fig. 5.2(g), where we summarize the fitted full-width half maximum (FWHM) of the linewidth obtained from the PLE scans of several axial SnV^- centers. We observe a similar trend for these color centers, with a mean linewidth increase in 3.42 MHz/GHz. We did not see this behavior for the reference emitter evaluated in the bulk. Further investigation is needed to determine whether this behavior is intrinsic to SnV^- centers or device-related (e.g., induced by local heating).

The second challenge that we address in this work is the optical transition frequency drift over time. Drifts of the optical resonance frequency due to changes in the local charge environment can be compensated by real-time logic protocols, called charge resonance (CR) checks, that can herald the desired resonance condition^{16,45}. This method relies on applying an off-resonant pulse, which alters the local charge environment. However, drifts beyond the local charge-induced distribution will lead to vanishing heralding success probabilities for these protocols. In those cases, the drift can be

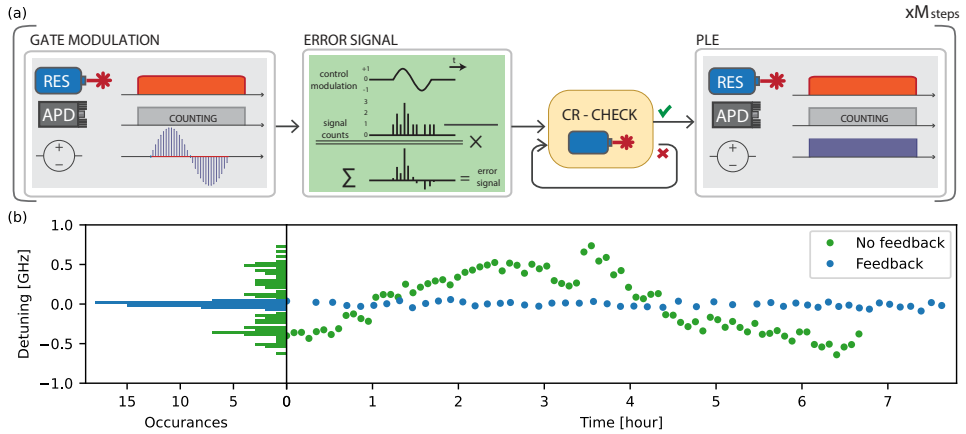


Figure 5.3: (a) Pulse sequence and real-time logic of the gate modulated CR-checked PLE. (b) (Right panel) Fitted centers of the fluorescence of 50 gate modulated CR-checked PLE scans, taken over 7 hours. For comparison the fitted centers of PLE scans with no active feedback in green. The error bar lies within the data points. (Left panel) Histogram of the fitted centers.

5

compensated for by dynamically adjusting the local strain⁴⁶. We implement a real-time feedback loop, utilizing strain tuning to stabilize the SnV^- center at a desired resonant optical frequency. The experimental protocol is schematically depicted in Fig. 5.3(a). It starts with a resonant readout pulse at the target resonance frequency while counting the PSB photons. We superimpose the strain-inducing DC bias voltage with a sinusoidal signal and correlate the number of counts with the phase of the control modulation signal. This is followed by a CR check. Once this is passed, the experimental sequence is started. By averaging the photon counts obtained during the gate modulation phase of this sequence, we obtain an error signal to adjust the static DC bias voltage using a standard proportional – integral – derivative (PID) feedback loop. The strain-inducing DC bias voltage is updated at a 5 Hz rate. This method effectively compensates for slow drifts limited by the update rate and can be used complementarily to the CR check, which addresses faster and smaller drifts in the optical resonance frequency.

To test the stability, we probe the resonance frequency of an SnV^- for more than 7 h by PLE scans. We fit the photon counts recorded per scan with a Voigt function and plot the fitted center frequency as a function of time in Fig. 5.3(b) right panel. The stability observed over the 7-h duration demonstrates the robustness of the system, and there are no intrinsic limitations that would preclude maintaining this stability over extended time periods. When no active feedback is applied, the drifts of the optical resonance are larger than can be compensated for by changes in the local charge environment. We compare the gate-modulated CR-checked PLE scans with PLE scans when no active feedback or CR checks are applied. The standard deviation of the fitted centers with active feedback is 30 MHz, while for the non-feedback case, the standard deviation is 365 MHz. In the left panel of Fig. 5.3(b), we plot a histogram of the fitted centers. The FWHM of the summed counts is 229 ± 2 MHz and the mean of the FWHM

of the individual fitted scans is 225 MHz. Comparing the standard deviation in fitted centers with the non-feedback case results in a 12-fold increase in optical frequency stability with this feedback technique.

5.7. CONCLUSION AND OUTLOOK

In summary, we have presented and demonstrated fabricated devices that show a tunability up to >40 GHz, covering a significant part of the inhomogeneous distribution of the SnV^- centers in this sample. We have stabilized the optical resonance of an SnV^- using a dynamic strain feedback loop and demonstrated a 12-fold improvement in stability. The strain tuning is applied locally to SnV^- embedded in waveguides and can be extended to tune numerous SnV^- on the same chip simultaneously. The methods demonstrated here pave the way toward the generation of heralded indistinguishable photons from many integrated SnV^- qubits, providing an important element for scaling SnV^- -based quantum technologies.

5.8. ACKNOWLEDGEMENT

The authors thank R. Schouten and B. Otto for electronic support, N. Albers for machining parts of the experimental setup, and O. Benningshof and J. Mensingh for cryogenics matter. The authors thank V. V. Dobrovitski for the fruitful discussions and A. Stramma for proofreading the manuscript. We acknowledge support from the joint research program “Modular quantum computers” by Fujitsu Limited and Delft University of Technology, co-funded by the Netherlands Enterprise Agency under Project No. PPS2007, from the Dutch Research Council (NWO) through the Spinoza prize 2019 (Project No. SPI 63-264), from the Dutch Ministry of Economic Affairs and Climate Policy (EZK) as part of the Quantum Delta NL program, from the Quantum Internet Alliance through the Horizon Europe program (Grant Agreement No. 101080128), and from the European Union’s Horizon Europe research and innovation program under Grant Agreement No. 101102140—QIA Phase 1.

5.8.1. AUTHOR CONTRIBUTIONS

J. M. B.: Conceptualization (lead); Data curation (lead); Formal analysis (lead); Investigation (lead); Methodology (lead); Software (lead); Validation (lead); Visualization (lead); Writing – review & editing (lead). L. G. C. W.: Conceptualization (lead); Formal analysis (equal); Investigation (lead); Methodology (equal); Software (equal); Validation (equal); Visualization (lead); Writing – review & editing (equal). N. C.: Conceptualization (equal); Investigation (supporting); Methodology (equal); Writing – review & editing (supporting). T. I.: Conceptualization (equal); Investigation (equal); Methodology (equal); Writing – review & editing (supporting). E. v. L.: Conceptualization (equal); Investigation (supporting); Methodology (equal); Writing – review & editing (supporting). M. I.: Methodology (equal); Software (supporting); Writing – review & editing (supporting). L. D. S.: Conceptualization (equal); Methodology (equal); Writing – review & editing (supporting). C. W.: Investigation (equal); Methodology (equal); Software (supporting); Writing – review & editing (supporting). H. K. C. B.: Methodology (equal); Software (sup-

porting); Writing – review & editing (supporting). T. T.: Methodology (equal); Software (supporting); Writing – review & editing (supporting). C. E-H.: Methodology (equal); Writing – review & editing (supporting). K. K.: Methodology (equal); Supervision (equal); Writing – review & editing (supporting). R. H.: Conceptualization (lead); Funding acquisition (lead); Project administration (lead); Resources (lead); Supervision (lead); Validation (equal); Writing – review & editing (equal).

5.8.2. DATA AVAILABILITY STATEMENT

The datasets of this study and the Python software for analysis and plotting are publicly available on 4TU.ResearchData under Ref.⁴⁷.

5.9. SUPPLEMENTARY MATERIAL

5.9.1. DEVICE FABRICATION

The fabrication of the diamond MEMS devices is divided into three main stages: incorporating coherent SnVs⁻ in diamond, fabricating diamond waveguides, and defining thin-film electrodes onto the diamond nanostructures. The SnV incorporation process starts from a $\langle 001|001 \rangle$ surface-oriented electronic-grade single-crystal diamond (supplied by Element 6) and follows the same general process as described in²⁵. After an inorganic surface pre-clean and an inductively-coupled-plasma reactive-ion-etching (ICP-RIE) strain relieve etch, the diamond is implanted with $^{120}\text{Sn}^+$ ions at an acceleration voltage of 350 keV and an implantation dose of 10^{11} ions/cm², under an angle of 7°. Following the $^{120}\text{Sn}^+$ implantation, the diamond is cleaned in a boiling tri-acid solution (ratio 1:1:1 of HNO₃ (65%):HClO₄ (70%):H₂SO₄ (95%)) and the SnVs are activated via vacuum-annealing. The graphitized diamond surface post-vacuum-annealing is removed with a combination of a boiling tri-acid clean and a short ICP-RIE O₂ etch.

The diamond waveguide fabrication is based on the crystallographic-plane-dependent quasi-isotropic etch undercut method, developed in^{11,25,29,48–50}. We again follow the same general process as described in²⁵, but here, the quasi-isotropic undercut etch is performed at a sample holder temperature of 250 °C, completing the total undercut in only 64 minutes. The fabricated waveguides are longitudinally aligned along the [110] direction.

Finally, we fabricate thin-film electrodes onto the diamond nanostructures via lift-off. A bi-layer positive-tone electron-beam resist stack consisting of methyl methacrylate (MMA) and polymethyl methacrylate (PMMA) is used to facilitate the lift-off of the electrodes. The electrode material stack consists of a 6 nm thick titanium adhesion layer and 10 nm thick niobium film, both deposited via electron-beam evaporation in a single evaporation run. These films are deposited at the lowest rate possible with the used evaporator tool to minimize stresses in the films, which could lead to detachment of the electrodes during lift-off. The lift-off process of the electrodes is performed in a heated bath of acetone. A schematic overview of the device and the relevant parameters are given in Fig. 5.4 and Tab. 5.1.

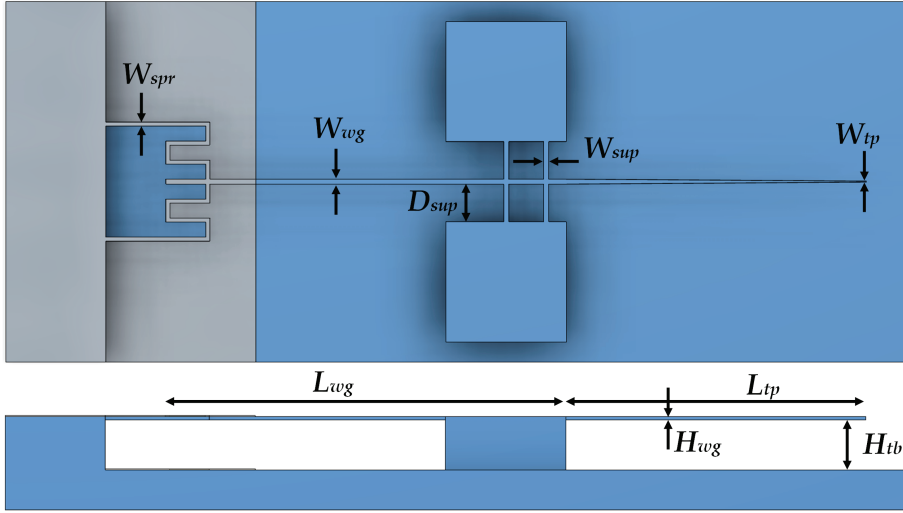


Figure 5.4: Schematic overview of the device and the relevant parameters of the geometry.

Parameter	Value
W_{spr}	200 nm
W_{wg}	250 nm
W_{sup}	250 nm
W_{tp}	50 nm
D_{sup}	2 μm
L_{wg}	20 μm
L_{tp}	15 μm
H_{tb}	$\approx 2.5 \mu\text{m}$
H_{wg}	160 nm

Table 5.1: Parameters of the device geometry corresponding to the dimensions indicated in Fig. 5.4.

5.9.2. EXPERIMENTAL SET-UP

All measurement data in this work has been taken in a closed-cycle attoDry800 cryostat at a baseplate temperature of 4 K. The diamond sample is glued on a printed circuit board (PCB) that is mounted on attocube positioners (ANPz102, ANPx101 (2x), AN-Sxyz100). The positioner stack and the PCB are enclosed by an aluminum heat shield to block radiation from the objective. All resonant excitation (619 nm) is done by using a Toptica TA-SHG Pro and a Toptica TA-SHG. The wavelength of the excitation light is stabilized by feedback through a wavemeter (HighFinesse WS-6). All off-resonant 515 nm excitation is done by a Hubner Photonics Cobolt 06-MLD. The resonant optical pulses are created using in-fiber acousto-optic modulators (Gooch and Housego) controlled by a microcontroller (Jaeger ADwin Pro II). The laser paths of the different lasers are combined in a single path and focussed on the diamond region of interest. To obtain only the

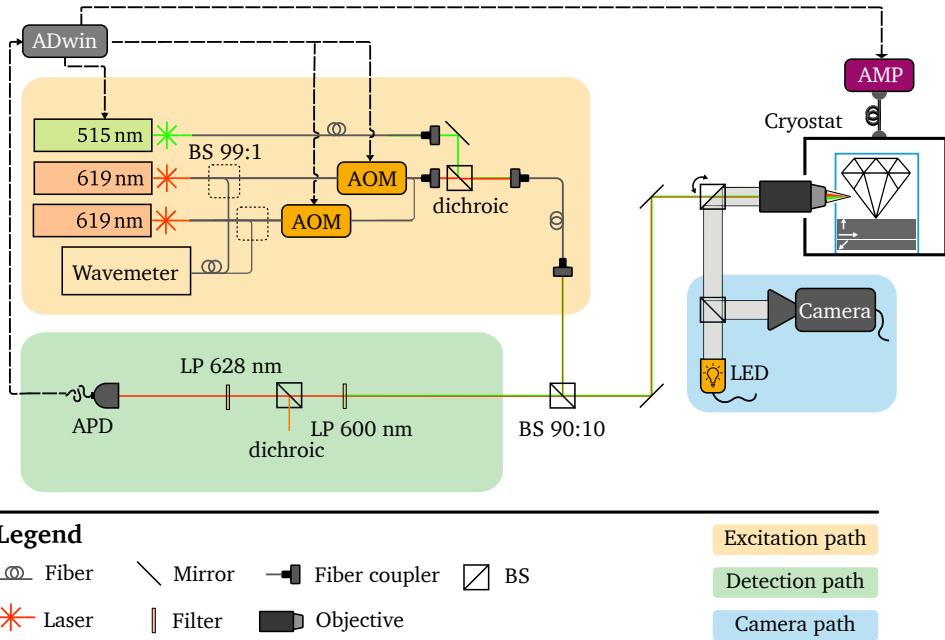


Figure 5.5: Experimental confocal set-up.

PSB light, the resonant and off-resonant laser photons are filtered by a long-pass (Thorlabs, FELH0600), dichroic beamsplitter (Semrock, FF625-SDi01), and 2 tunable 628 nm long-pass (Semrock, TLP01-628) filters in the detection path. We use an APD for photon detection which is connected to the microcontroller for photon counting. We use the DAC channel of the microcontroller and an in-house build voltage amplifier (x10, 2 μ s ramp time) to deliver the voltage pulses for strain engineering. The experimental setup is controlled by a PC and the Python 3 framework QMI 0.37⁵¹. A schematic overview of the set-up is depicted in Fig. 5.5.

5.9.3. VOLTAGE PULSE CALIBRATION

We observe that for large applied voltages leakage current through the system caused significant resistive heating. We note that on this chip 48 strain-tune devices are biased in parallel so that a leakage current at one of the devices affects the operation of all of them. This effect can be mitigated in future chips by adding individual voltage biasing to each device. This local increased temperature lowers the optical resonance frequency of Sn^- and broadens the optical linewidth, which is detrimental for quantum applications that rely on indistinguishable photons. By pulsing the applied bias voltage to induce local strain, the effect of the heat can be minimized. We calibrate the minimal required cool-down time after the voltage pulse by sweeping a waiting time after the voltage pulse during PLE scans. For cool-down times longer than 1500 μ s, no significant change in the

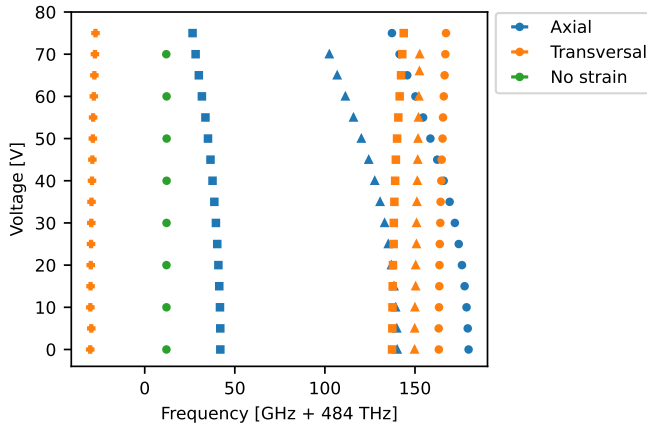


Figure 5.6: Summary of measured absolute frequency shift as a function of applied voltage, of several emitters. The data is of the same emitters as in Fig. 5.2(f).

resonance frequency is obtained. Secondly, we calibrate the voltage pulse duration to eliminate heat during the voltage pulse, by sweeping the pulse duration. We evaluate the resonance frequency and FWHM by fitting the collected PSB photons during the pulse in $1 \mu\text{s}$ time bins, for different durations of the pulse. For pulses of $50 \mu\text{s}$, we observe no change in resonance frequency and FWHM during the duration of the pulse. In addition, we observed no hysteresis in the voltage when it was applied in a pulsed way.

5.9.4. FREQUENCY SHIFT AS A FUNCTION OF VOLTAGE

We re-plot the data from Fig. 5.2(f) of the main text in Fig. 5.6 to depict the absolute frequency shift as a function of the applied voltage. In this way, it can be seen that 4 pairs of emitters can be tuned to the same absolute frequency. As the measurements have been done in a confocal arrangement, 1 emitter can be measured simultaneously.

5.9.5. FEM SIMULATIONS

The FEM simulations in the main text are performed using the simulation software Ansys⁴⁴. The FEM simulation solves for an equilibrium of the restoring forces of the dielectric and the electrostatic forces. The electrostatic field between the top and bottom electrode is 0.3 MV/cm at a voltage of 70 V . The model outputs the components of the strain tensor in the geometry of our device. The effective thermal expansion coefficients for diamond and niobium are determined from the data in^{52,53}, by fitting the data and then integrating the fit from room temperature, 293 K , to the temperature at which the measurements were performed, 4 K .

Material paramters	Diamond	Niobium
Young's modulus (MPa)	1050×10^3 ⁵⁴	105×10^3 ⁵⁵
Poisson's ratio	0.2 ⁵⁴	0.35 ⁵⁵
Electrical resistivity (Ωm)	-	1.52×10^{-7} ⁵⁵
Thermal expansion coefficient (1/K)	0.282×10^{-6} ⁵³	5.06×10^{-6} ⁵²
Dielectric constant	5.68	-

Table 5.2: Material properties used for the FEM simulations.

BIBLIOGRAPHY

- [1] J. M. Brevoord *et al.*, *Large-range tuning and stabilization of the optical transition of diamond tin-vacancy centers by in situ strain control*, Appl. Phys. Lett. **126**, 17 (2025).
- [2] H. J. Kimble, *The quantum internet*, Nature **453**, 1023 (2008).
- [3] S. Wehner, D. Elkouss and R. Hanson, *Quantum internet: A vision for the road ahead*, Science **362**, 6412 (2018).
- [4] P.-J. Stas *et al.*, *Robust multi-qubit quantum network node with integrated error detection*, Science **378**, 6619 (2022).
- [5] C. T. Nguyen *et al.*, *An integrated nanophotonic quantum register based on silicon-vacancy spins in diamond*, Phys. Rev. B **100**, 165428 (2019).
- [6] M. Pompili *et al.*, *Realization of a multinode quantum network of remote solid-state qubits*, Science **372**, 6539 (2021).
- [7] A. J. Stolk *et al.*, *Metropolitan-scale heralded entanglement of solid-state qubits*, Science Advances **10**, 44 (2024).
- [8] L. Li *et al.*, *Heterogeneous integration of spin–photon interfaces with a CMOS platform*, Nature **630**, 70 (2024).
- [9] M. K. Bhaskar *et al.*, *Experimental demonstration of memory-enhanced quantum communication*, Nature **580**, 60 (2020).
- [10] B. Hensen *et al.*, *Loophole-free Bell inequality violation using electron spins separated by 1.3 kilometres*, Nature **526**, 682 (2015).
- [11] N. H. Wan *et al.*, *Large-scale integration of artificial atoms in hybrid photonic circuits*, Nature **583**, 226 (2020).
- [12] J. Heiler *et al.*, *Spectral stability of V2 centres in sub-micron 4H-SiC membranes*, npj Quantum Mater. **9**, 34 (2024).
- [13] S. Simmons, *Scalable Fault-Tolerant Quantum Technologies with Silicon Color Centers*, PRX Quantum **5**, 010102 (2024).

- [14] M. Bhaskar *et al.*, *Quantum Nonlinear Optics with a Germanium-Vacancy Color Center in a Nanoscale Diamond Waveguide*, Phys. Rev. Lett. **118**, 22 (2017).
- [15] M. E. Trusheim *et al.*, *Transform-Limited Photons From a Coherent Tin-Vacancy Spin in Diamond*, Phys. Rev. Lett. **124**, 023602 (2020).
- [16] J. M. Brevoord *et al.*, *Heralded initialization of charge state and optical-transition frequency of diamond tin-vacancy centers*, Phys. Rev. Applied **21**, 5 (2024).
- [17] A. E. Rugar *et al.*, *Quantum Photonic Interface for Tin-Vacancy Centers in Diamond*, Phys. Rev. X **11**, 031021 (2021).
- [18] T. Iwasaki *et al.*, *Tin-Vacancy Quantum Emitters in Diamond*, Phys. Rev. Lett. **119**, 253601 (2017).
- [19] J. Görlitz *et al.*, *Spectroscopic investigations of negatively charged tin-vacancy centres in diamond*, New J. Phys. **22**, 013048 (2020).
- [20] E. I. Rosenthal *et al.*, *Microwave Spin Control of a Tin-Vacancy Qubit in Diamond*, Phys. Rev. X **13**, 031022 (2023).
- [21] I. Karapatzakis *et al.*, *Microwave Control of the Tin-Vacancy Spin Qubit in Diamond with a Superconducting Waveguide*, Phys. Rev. X **14**, 031036 (2024).
- [22] X. Guo *et al.*, *Microwave-Based Quantum Control and Coherence Protection of Tin-Vacancy Spin Qubits in a Strain-Tuned Diamond-Membrane Heterostructure*, Phys. Rev. X **13**, 041037 (2023).
- [23] H. K. Beukers *et al.*, *Control of Solid-State Nuclear Spin Qubits Using an Electron Spin-1/2*, Phys. Rev. X **15**, 021011 (2025).
- [24] A. E. Rugar, C. Dory, S. Sun and J. Vučković, *Characterization of optical and spin properties of single tin-vacancy centers in diamond nanopillars*, Phys. Rev. B **99**, 205417 (2019).
- [25] M. Pasini *et al.*, *Nonlinear Quantum Photonics with a Tin-Vacancy Center Coupled to a One-Dimensional Diamond Waveguide*, Phys. Rev. Lett. **133**, 023603 (2024).
- [26] G. Clark *et al.*, *Nanoelectromechanical Control of Spin–Photon Interfaces in a Hybrid Quantum System on Chip*, Nano Letters **24**, 4 (2024).
- [27] J. Arjona Martínez *et al.*, *Photonic Indistinguishability of the Tin-Vacancy Center in Nanostructured Diamond*, Phys. Rev. Lett. **129**, 17 (2022).
- [28] C. Bradac, W. Gao, J. Forneris, M. E. Trusheim and I. Aharonovich, *Quantum nanophotonics with group IV defects in diamond*, Nat. Commun. **10**, 5625 (2019).
- [29] M. Ruf, N. H. Wan, H. Choi, D. Englund and R. Hanson, *Quantum networks based on color centers in diamond*, Journal of Applied Physics **130**, 070901 (2021).

- [30] H. Choi, M. Pant, S. Guha and D. Englund, *Percolation-based architecture for cluster state creation using photon-mediated entanglement between atomic memories*, npj Quantum Inf **5**, 104 (2019).
- [31] N. H. Nickerson, J. F. Fitzsimons and S. C. Benjamin, *Freely Scalable Quantum Technologies Using Cells of 5-to-50 Qubits with Very Lossy and Noisy Photonic Links*, Phys. Rev. X **4**, 041041 (2014).
- [32] K. Nemoto *et al.*, *Photonic Architecture for Scalable Quantum Information Processing in Diamond*, Phys. Rev. X **4**, 031022 (2014).
- [33] L. De Santis, M. Trusheim, K. Chen and D. Englund, *Investigation of the Stark Effect on a Centrosymmetric Quantum Emitter in Diamond*, Phys. Rev. Lett. **127**, 14 (2021).
- [34] S. Aghaeimeibodi, D. Riedel, A. E. Rugar, C. Dory and J. Vučković, *Electrical Tuning of Tin-Vacancy Centers in Diamond*, Phys. Rev. Applied **15**, 6 (2021).
- [35] S. Maity *et al.*, *Spectral Alignment of Single-Photon Emitters in Diamond using Strain Gradient*, Phys. Rev. Appl. **10**, 024050 (2018).
- [36] S. Meesala *et al.*, *Strain engineering of the silicon-vacancy center in diamond*, Phys. Rev. B **97**, 205444 (2018).
- [37] Y.-I. Sohn *et al.*, *Controlling the coherence of a diamond spin qubit through its strain environment*, Nat Commun **9**, 2012 (2018).
- [38] B. Machielse *et al.*, *Quantum Interference of Electromechanically Stabilized Emitters in Nanophotonic Devices*, Phys. Rev. X **9**, 031022 (2019).
- [39] C. Hepp *et al.*, *Electronic Structure of the Silicon Vacancy Color Center in Diamond*, Phys. Rev. Lett. **112**, 036405 (2014).
- [40] G. Pieplow *et al.*, *Quantum electrometer for time-resolved material science at the atomic lattice scale*, Nat Commun **16**, 6435 (2025).
- [41] Y. Herrmann *et al.*, *Coherent Coupling of a Diamond Tin-Vacancy Center to a Tunable Open Microcavity*, Phys. Rev. X **14**, 041013 (2024).
- [42] Z. Li *et al.*, *Atomic optical antennas in solids*, Nat. Photon. **18**, 1113 (2024).
- [43] J. F. Ziegler, M. Ziegler and J. Biersack, *SRIM – The stopping and range of ions in matter (2010)*, Nuclear Instruments and Methods in Physics Research Section B: Beam Interactions with Materials and Atoms **268**, 1818 (2010).
- [44] Ansys® Academic Research Mechanical, Release 18.1, .
- [45] H. Bernien *et al.*, *Heralded entanglement between solid-state qubits separated by three metres*, Nature **497**, 86 (2013).
- [46] V. M. Acosta *et al.*, *Dynamic Stabilization of the Optical Resonances of Single Nitrogen-Vacancy Centers in Diamond*, Phys. Rev. Lett. **108**, 20 (2012).

- [47] J. M. Brevoord *et al.*, *Data underlying the publication "Large-Range Tuning and Stabilization of the Optical Transition of Diamond Tin-Vacancy Centers by In-Situ Strain Control"*, (2024).
- [48] B. Khanaliloo, M. Mitchell, A. C. Hryciw and P. E. Barclay, *High-Q/V Monolithic Diamond Microdisks Fabricated with Quasi-isotropic Etching*, *Nano Lett.* **15**, 8 (2015).
- [49] M. Mitchell, D. P. Lake and P. E. Barclay, *Realizing $Q > 300\,000$ in diamond microdisks for optomechanics via etch optimization*, *APL Photonics* **4**, 1 (2019).
- [50] S. Mouradian, N. H. Wan, T. Schröder and D. Englund, *Rectangular photonic crystal nanobeam cavities in bulk diamond*, *Applied Physics Letters* **111**, 021103 (2017).
- [51] I. T. Raa *et al.*, *QMI - Quantum Measurement Infrastructure, a Python 3 framework for controlling laboratory equipment*, (2023).
- [52] M. S. Dias and J. R. L. d. Mattos, *Uranium-zirconium based alloys part I: reference points for thermophysical properties*, (Brazil, 2015).
- [53] P. Jacobson and S. Stoupin, *Thermal expansion coefficient of diamond in a wide temperature range*, *Diamond and Related Materials* **97**, 107469 (2019).
- [54] C. A. Klein and G. F. Cardinale, *Young's modulus and Poisson's ratio of CVD diamond*, *Diamond and Related Materials* **2**, 918 (1993).
- [55] I. L. Shabalín, *Ultra-High Temperature Materials I: Carbon (Graphene/Graphite) and Refractory Metals* (Springer Netherlands, Dordrecht, 2014).

6

QUANTUM FREQUENCY CONVERSION OF SINGLE PHOTONS FROM A TIN-VACANCY CENTER IN DIAMOND

J. M. Brevoord*, J. F. Geus*, T. Turan, M. Guerrero Romero, D. Bedialauneta Rodríguez,
N. Codreanu, A. M. Stramma, R. Hanson, F. Elsen, B. Jungbluth

Diamond tin-vacancy (SnV) centers are promising candidates for building quantum network nodes. However, their native photon emission at 619 nm is incompatible with metropolitan-scale networks operating at low-loss telecom wavelengths. To address this, we demonstrate highly efficient, low-noise quantum frequency conversion (QFC) of 619 nm photons to the telecom S-band at 1480 nm. The conversion process combines 619 nm photons with 1064 nm pump light in an actively stabilized cavity containing a bulk monocrystalline potassium titanyl arsenate (KTA) crystal. We achieve an internal (external) conversion efficiency of $(48 \pm 3)\%$ ($(28 \pm 2)\%$) and a noise photon rate per wavelength of (2.2 ± 0.9) cts/s/pm, which is spectrally flat in the investigated frequency range of 40 GHz. Furthermore, we demonstrate that the efficiency remains above 80% of its maximum over a frequency range of 70 GHz. Finally, we generate a string of photons from a single waveguide-embedded SnV⁻ center using a train of excitation pulses and send these through the QFC. After the QFC, we observe a string of telecom photons displaying the SnV lifetime, confirming successful conversion. These results represent a critical step towards metropolitan-scale fiber-based quantum networks using SnV⁻ centers.

*These authors contributed equally to this work

6.1. INTRODUCTION

Quantum networks, consisting of quantum processors interconnected via optical links, have the potential to enable a wide range of applications, including secure communication, distributed quantum computing, networked quantum sensing, and novel tests of fundamental physics¹⁻⁶. Significant progress toward realizing such networks has led to demonstrations of key building blocks of a metropolitan quantum network⁷⁻¹².

To date, the state-of-the-art multi-node quantum network comprises three nodes¹³, with quantum teleportation demonstrated between non-neighboring nodes¹⁴. In terms of on-chip capabilities, Li *et al.* demonstrated an architecture for large-scale heterogeneous integration, calibration, and spectral tuning of spin qubits, and high-fidelity spin state initialization and readout¹⁵. Long-distance heralded quantum entanglement over metropolitan scales has also been achieved, notably using two nitrogen-vacancy (NV) centers in diamond separated by approximately 10 km and connected via 25 km of deployed fiber infrastructure¹⁶. In addition, the entanglement of two nanophotonic quantum memories was demonstrated between nearby nodes connected by a 35 km deployed fiber loop¹⁷.

6

A key element in many quantum networking protocols is the generation and interference of single photons, so-called flying qubits, that are entangled with stationary qubits¹⁸. These photons are typically transmitted through optical fibers, where propagation losses ultimately limit the entanglement generation rate for longer distances. However, most optically active quantum color centers emit photons outside the telecom spectrum^{13,19,20}, where fiber transmission loss is significantly higher than in the telecom band. Quantum frequency conversion (QFC) offers a viable solution by coherently shifting the photon wavelength into the low-loss telecom regime while preserving its quantum properties^{17,21,22}.

Among the emerging spin-photon interfaces, the negatively charged tin-vacancy (SnV^-) center in diamond has gained attention due to its relatively high quantum efficiency^{23,24}, large spin-orbit coupling²⁵⁻²⁷, and its inversion symmetry²⁸, which allows for nanophotonic integration^{15,29-32}. The SnV^- center consists of a tin atom positioned at the interstitial site between two adjacent missing carbon atoms in the diamond lattice. In the absence of a magnetic field, the SnV^- has four optical transitions originating from spin-degenerate orbital doublets in the optically ground and excited states. The coherent emission, which is useful for entanglement protocols and quantum applications, is the zero-phonon line (ZPL) transition at 619 nm, also known as the C-transition, which links the lowest branch of the ground and excited states.

In this work, we demonstrate low-noise, efficient quantum frequency conversion of single photons emitted from an SnV^- center in diamond. By converting these photons from 619 nm to the telecom S-band at 1480 nm, our approach overcomes a major bottleneck for SnV^- -based metropolitan quantum networks with deployed fiber interconnects.

6.2. METHODS & RESULTS

6.2.1. QUANTUM FREQUENCY CONVERTER

The QFC setup implemented in this work is adapted from the design reported in³³ and implemented in¹⁶, modified to enable frequency down-conversion of photons emitted from the zero-phonon line (ZPL) of an SnV^- center at $\lambda_{\text{SnV}} = 619 \text{ nm}$ by a change in the crystal's cut orientation. The process relies on three-wave mixing in a bulk monocrystalline potassium titanyl arsenate (KTA) crystal using a strong intermediate-wavelength pump laser at $\lambda_p = 1064 \text{ nm}$ (NKT Adjustik Y10 and Boostik Y10). The output wavelength, λ_{out} , is calculated via energy conservation as,

$$\lambda_{\text{out}} = (\lambda_{\text{SnV}}^{-1} - \lambda_p^{-1})^{-1} = 1480 \text{ nm}. \quad (6.1)$$

Efficient conversion is achieved via birefringent phase matching in the KTA crystal, which is placed within a bow-tie cavity to enhance the pump laser power to the required levels for efficient conversion. The crystal is cut such that the wave vectors of the incident light lie in the plane defined by the crystal's x- and y-axes at a phase matching angle of $\phi = 40^\circ$ (measured from x towards y), enabling type-II phase matching, where pump laser (extraordinary) and frequency-converted photons (ordinary) exhibit perpendicular polarization. The nomenclature follows the convention where $n_x < n_y < n_z$. A schematic of the complete setup is shown in Fig. 6.1.

The 619 nm input is coupled from a polarization-maintaining single-mode fiber to the free-space setup of the QFC via a collimator and mode-shaped with a telescope for optimal overlap with the cavity mode at the focus position located at the crystal's center. The polarization of the 619 nm photons is adapted by a half-waveplate to optimize the conversion efficiency.

One mirror of the bow-tie cavity is mounted on a piezoelectric actuator for active stabilization using the Hänsch-Couillaud locking scheme³⁴. With an enhancement-factor of about 40 (60), more than 350 W of pump laser power is available inside the cavity from the 9 W input power (6 W coupled power) delivered by the laser. The enhancement factor and thus conversion efficiency can be increased further by optimizing the impedance matching. To suppress noise from pump scattering and other nonlinear processes (e.g., Raman and spontaneous parametric down-conversion (SPDC)), the converted light is filtered. The filtering setup consists of a combination of 1400 nm long-pass filters, polarization filtering, a narrowband bandpass filter (FWHM = 12 nm), and a narrowband in-fiber Bragg grating (FBG) bandpass filter (TeraXion, FWHM = 5 GHz).

6.2.2. CONVERSION EFFICIENCY AND BANDWIDTH

When the conversion efficiency is measured, a laser emitting at a wavelength of $\lambda_{\text{SnV}} = 619 \text{ nm}$ (Toptica DLC TA pro) is used instead of the SnV^- center. The internal (external) conversion efficiency is then calculated by the ratio of converted light power in front of the output fiber-collimator (in-fiber behind the narrowband filter) to the red laser power entering the free-space part of the QFC, corrected for the ratio of photon ener-

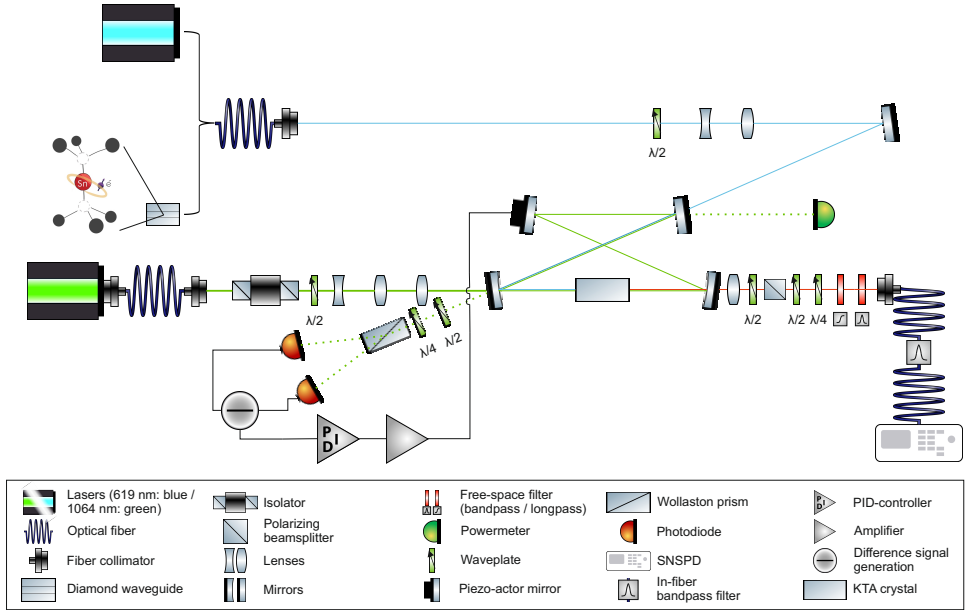


Figure 6.1: **Schematic of the frequency conversion setup.** Single photons from an SnV^- center are launched into free space and mode-matched via a telescope before entering the KTA crystal. A half-waveplate is used to align the polarization for maximal conversion efficiency. The converted telecom light is filtered using polarization optics, long-pass filters, and a bandpass filter (FWHM = 12 nm), and then coupled into a polarization-maintaining fiber. An additional in-fiber bandpass filter (FWHM = 5 GHz) precedes detection by a superconducting nanowire single-photon detector (SNSPD). The pump light originates from a continuous wave single-frequency laser, which is beam-shaped to be coupled to the bow-tie cavity containing the KTA crystal. This cavity is locked via the Hänsch-Couillaud technique to maintain resonance. When the internal and external conversion efficiency are measured, the SnV^- -emitter setup is replaced with a laser, and the converted light power is measured before the output fiber-collimator and in-fiber, respectively.

6

gies ($\eta_Q = 1480/619$). To approximate the internal efficiency (i.e., the process' efficiency inside the nonlinear material), the results are corrected for the residual reflectivity of optical coatings of 8%. Fig. 6.2(a) shows the conversion efficiency as a function of circulating pump power. At a circulating pump power of (360 ± 17) W, an internal efficiency of (48 ± 3) % is achieved. The error bars are calculated from the accuracy of the power measurements. A maximum external efficiency of (28 ± 2) % is observed at a pump power of (344 ± 16) W in the cavity. The conversion efficiency η_{QFC} for a nonlinear material of length L is expected to exhibit the following dependency on the pump laser power P :

$$\eta_{\text{QFC}} = \eta_{\text{max}} \sin^2(L\sqrt{\alpha P}), \quad (6.2)$$

with the maximum conversion efficiency η_{max} and the normalized power efficiency α ³⁵. The linear increase of the conversion efficiency with pump laser power suggests an unaccounted dependency on either η_{QFC} or α . Sweeping the incident pump laser power affects both the thermal load to the nonlinear crystal and the power reaching the photodiodes, which generate the error signal for cavity locking, resulting in a change in the

temperature distribution inside the crystal and potentially the spatial properties of the cavity mode.

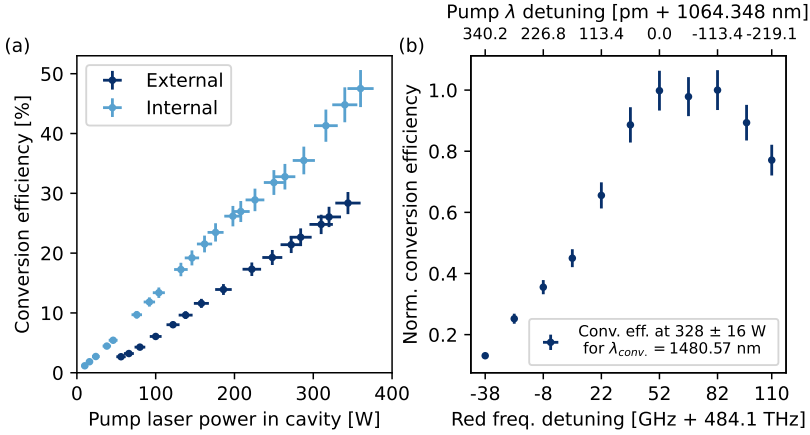


Figure 6.2: **Conversion efficiency measured using classical 619 nm laser light.** (a) Internal and external efficiencies as a function of circulating pump power. A maximum internal (external) efficiency of $(48 \pm 3)\%$ ($(28 \pm 2)\%$) is achieved. The error bars represent the accuracy of the detectors used. (b) Spectral bandwidth of the QFC setup, measured by varying the red laser input frequency while adjusting the pump wavelength to keep the converted output fixed. Within a 70 GHz range, conversion efficiency remains above 80% of its maximum.

Next, we probe the spectral bandwidth of the conversion setup, which is relevant in conjunction with the properties of SnV^- center emission. Due to varying local strain in the diamond lattice, different SnV^- centers may exhibit different emission frequencies, indicated by the inhomogeneous distribution. Depending on the SnV^- center creation process, the inhomogeneous distribution can vary from 4 GHz to more than 100 GHz^{15,36–39}. In addition, SnV^- centers' resonant frequencies can drift over time. For both scenarios, these frequency differences can be compensated for by simply adjusting the pump laser wavelength and thereby maintaining converted photons with the same frequency. We measure the spectral acceptance bandwidth by scanning the input signal frequency while compensating with the pump wavelength, thus keeping the target wavelength fixed. As shown in Fig. 6.2(b), the system maintains over 80% of its maximum efficiency across a 70 GHz tuning range.

6.2.3. QFC NOISE CHARACTERIZATION

With the pump laser wavelength being much shorter than the wavelength of frequency-converted photons, Raman-scattered pump photons are not expected to contribute significantly to the generation of noise, leaving SPDC as the expected dominant source of noise photons. To quantify the noise introduced by the QFC process, we measure the count rate (averaged over 20 s) on an SNSPD (Quantum Opus, detection efficiency $\eta_{\text{SNSPD}} = 75\%$) connected to the QFC setup after the in-fiber narrowband filter while only the pump laser is operating and no red light enters the QFC. All counts in this config-

uration, therefore, arise either from SPDC of the pump laser light in the crystal or can be attributed to black-body radiation and detector dark counts. The noise density is determined by normalizing the count rate, N , to the detector efficiency, η_{SNSPD} , and the bandwidth of the spectral filter stack, $\Delta\lambda_{\text{BP}}$,

$$\frac{dn}{d\lambda} = \frac{N}{\eta_{\text{SNSPD}}\Delta\lambda_{\text{BP}}}. \quad (6.3)$$

When the additional narrowband FBG is used, the data is further corrected for its transmission ($T_{\text{FBG}} = 81\%$) for comparability between the two filter setups. The results are depicted in Fig. 6.3(a). We observe a linear increase of the noise density with the pump laser power in the cavity up to a value of (2.2 ± 0.9) cts/s/pm, which indicates SPDC as the leading noise contribution⁴⁰. Measurements with and without the 5 GHz in-fiber bandpass filter yield similar results. Additionally, the center frequency of the FBG is swept at maximum pump laser power (see Fig. 6.3(b)), yielding no significant dependency on the measured noise rate as a function of the center wavelength of the filter. Both investigations indicate spectral homogeneity of the SPDC-generated noise.

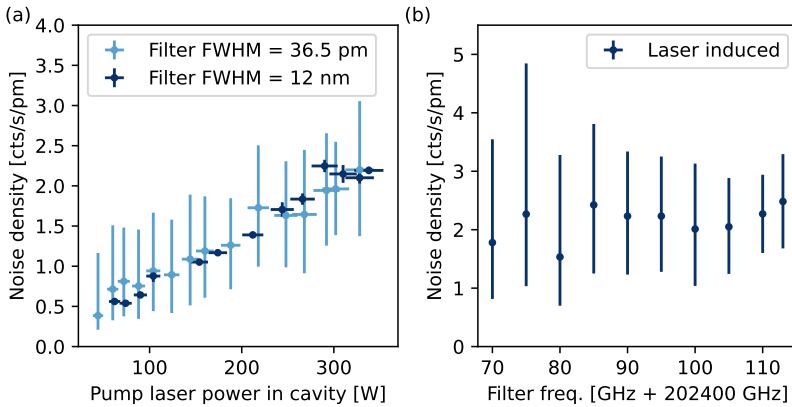


Figure 6.3: **Noise characterization.** All measurement data depicted here is corrected for the SNSPD-efficiency, detector dark-counts, and (if applicable) thermal noise and losses introduced by the tunable narrowband in-fiber filter. A Bayesian approach to error analysis is implemented to prevent a non-physical noise density error bar. (a) Noise density as a function of the pump laser power. The noise increases linearly with the pump laser power up to a value of (2.2 ± 0.9) cts/s/pm. The data depict measurements with (without) the narrowband in-fiber filter, resulting in a FWHM of the spectral pass-band of 36.5 pm (12 nm). (b) Noise density as a function of center frequency of the narrowband in-fiber filter. Within the accuracy of this measurement, spectrally flat noise is measured in the investigated regime.

6.2.4. CONVERSION OF SINGLE SnV^- CENTER PHOTONS

We finally apply our quantum frequency conversion process to photons emitted by a single SnV^- center. We first describe the generation and characterization of those photons. The SnV^- center studied in this work is embedded in a suspended diamond waveguide device fabricated as described in Ref.³¹. In short, the SnV^- centers are

created via tin-ion implantation, followed by acid cleaning and high-temperature vacuum annealing. The waveguide devices are fabricated by a quasi-isotropic undercut etch-based fabrication process.

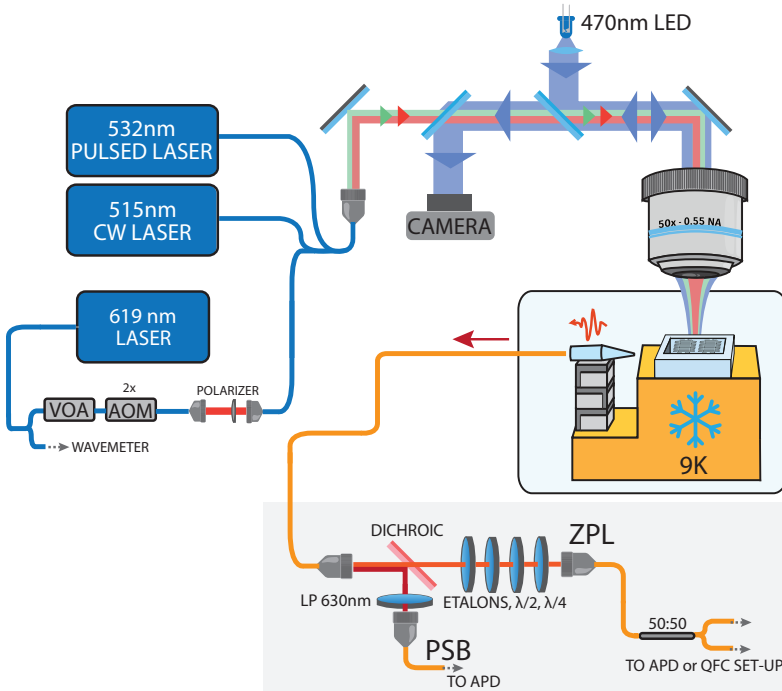


Figure 6.4: SnV^- setup used for the SnV^- experiments. The SnV^- centers are embedded in suspended diamond waveguides, with a tapered fiber positioned via nano-positioners in a lensed configuration in front of the tapered waveguide. This is mounted in a 9 K closed-cycle cryostat. Off-resonant excitation is performed in free space using an external objective, with a CW 515 nm laser and a pulsed 532 nm laser (1 MHz repetition rate). A camera and LED enable sample imaging. Resonant excitation is done with a 619 nm Toptica TA-SHG Pro laser. PSB and ZPL light are separated by a dichroic mirror, with an LP630 nm filter removing leaked excitation light. In the ZPL path, narrowband etalons select the C-transition ZPL photons from an SnV^- center.

Photon collection from the waveguide is achieved using a tapered single-mode optical fiber. The fiber is chemically etched into a conical shape via hydrofluoric acid, producing a lensing effect when positioned in front of the waveguide taper. The diamond sample and fiber are mounted inside a closed-cycle optical cryostat operating at 9 K, see Ref. ³¹ for details.

Resonant excitation of the SnV^- is performed using a Toptica DLC TA-SHG Pro laser at 619 nm from a free-space objective above the sample. Off-resonant excitation is provided using either a continuous-wave laser (Cobolt 06-MLD, 515 nm) or a pulsed laser (NKT Onefive Katana Advanced Laser Diode Systems PiLas, 532 nm, 65 ps pulse width, 1 MHz repetition rate, attenuated to $\sim 500 \mu\text{W}$ average power) for lifetime and second-order correlation measurements.

Emission is collected via the tapered fiber and separated into the ZPL and Phonon-Side-Band (PSB) paths using a dichroic mirror, see Fig. 6.4. The ZPL photons are further filtered using a free space etalon combination, consisting of a 40 GHz and a 4 GHz narrowband etalon in series, to suppress photon counts from other SnV^- centers. For the experiments where frequency conversion is not performed, the photons are detected using Laser Component COUNT-T avalanche photodetectors (APD) with a timing-jitter of ~ 400 ps, connected to a time-correlated single-photon counting module PicoQuant MultiHarp 150 for time-resolved photon detection. For the conversion experiments, the ZPL photons are routed to the QFC setup via a 35 m polarization-maintaining optical fiber.

To generate a train of single photons, we apply pulsed off-resonant excitation at 532 nm and time-resolve the filtered ZPL emission. The ZPL photons are collected and spectrally filtered to a window of 4 GHz. Fig. 6.5(a) shows a histogram of photon detection times relative to the excitation pulse at $t=0$. The counts are normalized to counts per bin over the bin width. The probability of photon detection per excitation pulse is $9.33\text{e-}04$. An exponential fit indicates that the lifetime is (7.47 ± 0.11) ns. The signal-to-noise (SNR) right after the optical pulse exceeds 1000.

6

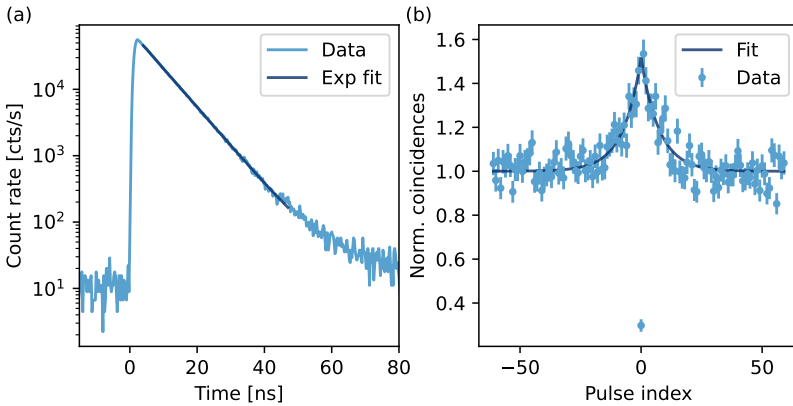


Figure 6.5: **Lifetime and second-order correlation function $g^{(2)}(\tau)$ measurements.** (a) Unconverted lifetime measurement results of the SnV^- center under investigation. The optical decay is fitted with an exponential function $f(t) = A \cdot e^{-t/\tau} + B$, resulting in an optical lifetime of the SnV^- center of $\tau = (7.47 \pm 0.11)$ ns and $A = (54394 \pm 1112)$ cts/s and $B = (22 \pm 8)$ cts/s. (b) The second-order correlation function $g^{(2)}(\tau)$ performed in a pulsed fashion. The data is fitted with a bunching model, $g^{(2)}(t) = 1 + A \cdot e^{-t/\tau}$, following the procedure of Ref. ⁴¹ resulting in $g^{(2)}(0) = (0.298 \pm 0.004)$, without background correction. The fit results include $A = (0.51 \pm 0.04)$ and $\tau = (7.50 \pm 0.85)$ pulses.

Single-photon statistics are validated via a second-order correlation measurement $g^{(2)}(\tau)$. The emitted photons are split with a 50:50 in-fiber beamsplitter and detected with two detectors. We determine the time difference between detected photons in the different detectors. We integrate the photon counts where the time difference corresponds to a specific pulse index separation. The resulting histogram in Fig. 6.5(b) shows

a clear dip at zero delay. Note that the data also shows bunching, as the off-resonant excitation leads to an imperfect initialization into the optically bright negatively charged SnV^- state. We obtain $g^{(2)}(0) = (0.298 \pm 0.004)$ without any background correction, confirming single-photon emission.

We send the SnV^- center ZPL photons generated by the off-resonant laser pulses to the QFC setup, where we convert the photons to the telecom S-band. The pump laser power in the cavity is maintained at approximately 350 W. Fig. 6.6 shows the time-resolved histogram of the converted photons, detected using the SNSPDs. An exponential fit reveals a lifetime of (7.58 ± 0.14) ns, in line with the unconverted value. We determine an SNR of 20 right after the excitation pulse. The signal is reduced to 0.04 of the value before conversion, mainly due to the conversion efficiency (0.28), losses at the free space launching (estimated to be around 0.5), and losses in the 35 m visible and 90 m telecom optical fiber and connectors. In addition, the noise increased from 22 cts/s to 102 cts/s, primarily due to pump-laser-induced noise. The combination of a filter with a FWHM of 36.5 pm and the pump-laser induced noise of (2.2 ± 0.9) cts/s/pm determined above, yield ~ 73 cts/s noise counts. The remaining noise counts are attributed to noise photons in the 90 m fiber linking the QFC setup to the SNSPD.

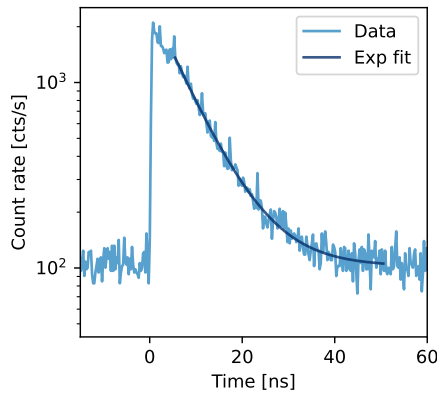


Figure 6.6: **SnV^- center emitted converted photons.** The photons from the SnV^- center are converted by the QFC setup and measured with the SNSPDs at a pump laser power of about 350 W. The optical decay is fitted with an exponential function $f(t) = A \cdot e^{-t/\tau} + B$, resulting in an optical lifetime of the SnV^- center of $\tau = (7.58 \pm 0.14)$ ns and $A = (243 \pm 6) \cdot 10^1$ cts/s and $B = (102 \pm 3)$ cts/s. The resulting lifetime is similar to the lifetime measured before conversion. This indicates that we have successfully converted photons originating from an SnV^- center to the telecom S-band. We attribute the small periodic peaks to either electronic or optical reflections.

6.3. CONCLUSION

We have demonstrated efficient and low-noise frequency down-conversion of single photons emitted from an SnV^- center in diamond, translating its natural wavelength from the visible regime (619 nm) to the telecom S-band (1480 nm). This conversion process is based on the three-wave mixing between a cavity-enhanced pump laser and

the single photons in a KTA crystal, with birefringent phase matching enabling high conversion efficiencies.

We achieve an internal conversion efficiency of $(48 \pm 3)\%$ and an external conversion efficiency of $(28 \pm 2)\%$, while suppressing noise from the scattering process of the high-intensity pump laser through polarization filtering and extensive spectral filtering to (2.2 ± 0.9) cts/s/pm. The conversion efficiency can be further improved by increasing the pump laser power or improving cavity enhancement.

The cavity resonance is tunable to the pump laser frequency, allowing for spectral tunability of the converted photons. This flexibility is crucial for generating indistinguishable photons from multiple quantum emitters with differing emission wavelengths, a key requirement for entanglement generation between different quantum nodes in a quantum network. We demonstrate a conversion bandwidth of 70 GHz within which the conversion efficiency remains above 80% of the maximum, enabling compensating for spectral inhomogeneity between SnV^- centers and spectral drift over time while keeping the target wavelength fixed.

Altogether, these results represent an important step toward implementing long-distance, deployed fiber-based quantum networks based on SnV^- centers in diamond.

6.4. ACKNOWLEDGEMENT

This research was funded by Fraunhofer-Gesellschaft zur Förderung der angewandten Forschung e.V. and by the Dutch Research Council (NWO) through the project “QuTech Part II Applied-oriented research” (project number 601.QT.001) and the Zwaartekracht program Quantum Software Consortium (project no. 024.003.037/3368). We further acknowledge funds from the Dutch Ministry of Economic Affairs and Climate Policy (EZK), as part of the Quantum Delta NL programme, and Holland High Tech through the TKI HTSM (20.0052 PPS) funds. We acknowledge support from the Dutch Research Council (NWO) through the Spinoza prize 2019 (Project No. SPI 63-264).

6.4.1. DATA AVAILABILITY STATEMENT

The datasets of this study and the Python software for analysis and plotting are publicly available on 4TU.ResearchData under Ref.⁴².

BIBLIOGRAPHY

- [1] H. J. Kimble, *The quantum internet*, Nature **453**, 1023 (2008).
- [2] S. Wehner, D. Elkouss and R. Hanson, *Quantum internet: A vision for the road ahead*, Science **362**, 6412 (2018).
- [3] A. Ekert and R. Renner, *The ultimate physical limits of privacy*, Nature **507**, 443 (2014).
- [4] L. Jiang, J. M. Taylor, A. S. Sørensen and M. D. Lukin, *Distributed quantum computation based on small quantum registers*, Phys. Rev. A **76**, 062323 (2007).
- [5] D. Gottesman, T. Jennewein and S. Croke, *Longer-Baseline Telescopes Using Quantum Repeaters*, Phys. Rev. Lett. **109**, 070503 (2012).
- [6] H. Buhrman, R. Cleve, J. Watrous and R. d. Wolf, *Quantum Fingerprinting*, Phys. Rev. Lett. **87**, 167902 (2001).
- [7] H. Bernien *et al.*, *Heralded entanglement between solid-state qubits separated by three metres*, Nature **497**, 86 (2013).
- [8] J. Hofmann *et al.*, *Heralded Entanglement Between Widely Separated Atoms*, Science **337**, 6090 (2012).
- [9] D. L. Moehring *et al.*, *Entanglement of Single-Atom Quantum Bits at a Distance*, Nature **449**, 7158 (2007).
- [10] S. Ritter *et al.*, *An elementary quantum network of single atoms in optical cavities*, Nature **484**, 195 (2012).
- [11] M. H. Abobeih *et al.*, *Fault-tolerant operation of a logical qubit in a diamond quantum processor*, Nature **606**, 884 (2022).
- [12] C. Bradley *et al.*, *A Ten-Qubit Solid-State Spin Register with Quantum Memory up to One Minute*, Phys. Rev. X **9**, 3 (2019).
- [13] M. Pompili *et al.*, *Realization of a multinode quantum network of remote solid-state qubits*, Science **372**, 6539 (2021).
- [14] S. L. N. Hermans *et al.*, *Qubit teleportation between non-neighbouring nodes in a quantum network*, Nature **605**, 663 (2022).
- [15] L. Li *et al.*, *Heterogeneous integration of spin–photon interfaces with a CMOS platform*, Nature **630**, 70 (2024).
- [16] A. J. Stolk *et al.*, *Metropolitan-scale heralded entanglement of solid-state qubits*, Science Advances **10**, 44 (2024).
- [17] C. M. Knaut *et al.*, *Entanglement of nanophotonic quantum memory nodes in a telecom network*, Nature **629**, 573 (2024).

- [18] H. K. Beukers *et al.*, *Remote-Entanglement Protocols for Stationary Qubits with Photonic Interfaces*, PRX Quantum **5**, 010202 (2024).
- [19] S. Daiss *et al.*, *A Quantum-Logic Gate between Distant Quantum-Network Modules*, Science **371**, 6529 (2021).
- [20] V. Krutyanskiy *et al.*, *Light-matter entanglement over 50 km of optical fibre*, npj Quantum Inf **5**, 72 (2019).
- [21] A. Tchebotareva *et al.*, *Entanglement between a Diamond Spin Qubit and a Photonic Time-Bin Qubit at Telecom Wavelength*, Phys. Rev. Lett. **123**, 063601 (2019).
- [22] A. Stolk *et al.*, *Telecom-Band Quantum Interference of Frequency-Converted Photons from Remote Detuned NV Centers*, PRX Quantum **3**, 020359 (2022).
- [23] T. Iwasaki *et al.*, *Tin-Vacancy Quantum Emitters in Diamond*, Phys. Rev. Lett. **119**, 253601 (2017).
- [24] Y. Herrmann *et al.*, *Coherent Coupling of a Diamond Tin-Vacancy Center to a Tunable Open Microcavity*, Phys. Rev. X **14**, 041013 (2024).
- [25] I. Karpatzakis *et al.*, *Microwave Control of the Tin-Vacancy Spin Qubit in Diamond with a Superconducting Waveguide*, Phys. Rev. X **14**, 031036 (2024).
- [26] X. Guo *et al.*, *Microwave-Based Quantum Control and Coherence Protection of Tin-Vacancy Spin Qubits in a Strain-Tuned Diamond-Membrane Heterostructure*, Phys. Rev. X **13**, 041037 (2023).
- [27] E. I. Rosenthal *et al.*, *Microwave Spin Control of a Tin-Vacancy Qubit in Diamond*, Phys. Rev. X **13**, 031022 (2023).
- [28] G. Thiering and A. Gali, *Ab Initio Magneto-Optical Spectrum of Group-IV Vacancy Color Centers in Diamond*, Physical Review X **8**, 021063 (2018).
- [29] A. E. Rugar *et al.*, *Quantum Photonic Interface for Tin-Vacancy Centers in Diamond*, Phys. Rev. X **11**, 031021 (2021).
- [30] J. Arjona Martínez *et al.*, *Photonic Indistinguishability of the Tin-Vacancy Center in Nanostructured Diamond*, Phys. Rev. Lett. **129**, 17 (2022).
- [31] M. Pasini *et al.*, *Nonlinear Quantum Photonics with a Tin-Vacancy Center Coupled to a One-Dimensional Diamond Waveguide*, Phys. Rev. Lett. **133**, 023603 (2024).
- [32] G. Clark *et al.*, *Nanoelectromechanical Control of Spin-Photon Interfaces in a Hybrid Quantum System on Chip*, Nano Letters **24**, 4 (2024).
- [33] J. F. Geus *et al.*, *Low-noise short-wavelength pumped frequency downconversion for quantum frequency converters*, Optica Quantum **2**, 3 (2024).
- [34] T. Hansch and B. Couillaud, *Laser frequency stabilization by polarization spectroscopy of a reflecting reference cavity*, Optics Communications **35**, 441 (1980).

- [35] R. V. Roussev, C. Langrock, J. R. Kurz and M. M. Fejer, *Periodically poled lithium niobate waveguide sum-frequency generator for efficient single-photon detection at communication wavelengths*, Opt. Lett. **29**, 1518 (2004).
- [36] J. M. Brevoord *et al.*, *Large-range tuning and stabilization of the optical transition of diamond tin-vacancy centers by in situ strain control*, Appl. Phys. Lett. **126**, 17 (2025).
- [37] J. Görlitz *et al.*, *Spectroscopic investigations of negatively charged tin-vacancy centres in diamond*, New J. Phys. **22**, 013048 (2020).
- [38] Y. Narita *et al.*, *Multiple Tin-Vacancy Centers in Diamond with Nearly Identical Photon Frequency and Linewidth*, Phys. Rev. Applied **19**, 024061 (2023).
- [39] V. Bushmakin *et al.*, *Two-Photon Interference of Photons from Remote Tin-Vacancy Centers in Diamond*, (2024), arXiv:2412.17539.
- [40] C. K. Hong and L. Mandel, *Theory of parametric frequency down conversion of light*, Phys. Rev. A **31**, 2409 (1985).
- [41] M. Ruf, M. Weaver, S. van Dam and R. Hanson, *Resonant Excitation and Purcell Enhancement of Coherent Nitrogen-Vacancy Centers Coupled to a Fabry-Perot Microcavity*, Phys. Rev. Applied **15**, 024049 (2021).
- [42] J. M. Brevoord *et al.*, *Data underlying the publication "Quantum Frequency Conversion of Single Photons from a Tin-Vacancy Center in Diamond"*, (2025).

7

CONCLUSIONS AND OUTLOOK

I may not be your ideal woman
- Celeste

7.1. SUMMARY

In this thesis, we explore the use of the tin-vacancy (SnV) center in diamond as a platform for quantum network nodes within a future quantum internet. We investigated the challenges associated with operating spin qubits in this solid-state platform, with a particular focus on controlling the optical interface of SnV centers for applications in metropolitan-scale quantum networks. We have demonstrated the control over the resonance frequency of coherent photons to generate indistinguishable photons from different emitters for entanglement generation, achieving tunability across small (**Chapter 4**), intermediate (**Chapter 5**), and large (**Chapter 6**) frequency ranges.

The main contributions of this work are summarized below:

- In **Chapter 3**, we introduce a novel fabrication method for producing thin diamond plates that host optically coherent color centers. The novelty of this technique is based on laser cutting patterns into diamond, as opposed to techniques relying on electron beam lithography and hard mask etching. This technique reduces fabrication complexity, improves device yield, and shortens production time. We demonstrated the incorporation of optically coherent NV and SnV centers into these structures, which have applications in quantum sensing, communication, and computing.
- In **Chapter 4**, we investigate the charge dynamics of single SnV centers in diamond. By combining resonant excitation, photon detection, and real-time feedback logic, we achieved heralded initialization of both the charge state and the optical resonance frequency with a fidelity of $(96 \pm 4)\%$. We showed that increasing the pass threshold in the real-time logic improves optical coherence and enables fine-tuning of the resonance frequency within the inhomogeneous linewidth of a single emitter (>100 MHz).
- In **Chapter 5**, we demonstrated wide-range tuning of the optical resonance frequency of SnV centers by dynamically controlling the local strain environment. Due to variations in their surrounding lattice, SnV centers typically emit at distinct frequencies, resulting in a broad inhomogeneous distribution. By precisely adjusting strain, we tuned different emitters to the same optical frequency, with a tunability >40 GHz. Furthermore, we showed that this approach allows stabilization of the resonance frequency over a timescale exceeding seven hours.
- **Chapter 6** describes the Quantum Frequency Conversion (QFC) of single photons originating from a SnV center at 619 nm to 1480 nm, which is in the optical telecom S-band. This conversion facilitates low-loss photon transmission over long distances, as required for scalable quantum networking. We report a total external conversion efficiency of $(28 \pm 2)\%$, while maintaining a noise photon rate per wavelength of (2.2 ± 0.9) cts/s/pm. The system exhibits a relative conversion efficiency above 80% over a frequency range of 70 GHz.

Overall, this work establishes a versatile toolkit for controlling the optical interface of SnV centers in diamond, with a view toward enabling long-distance entanglement

generation within metropolitan quantum networks. While the generation of indistinguishable telecom photons from separate nodes is making progress, we have not yet demonstrated entanglement over metropolitan distances using SnV centers, an achievement that requires integration of multiple additional components^{1,2}.

In the following sections, we outline the current limitations of the methods developed in this work and provide an outlook on recent and future advances that could enable the realization of scalable quantum networks for real-world deployment. We first address scaling in terms of quantum links, highlighting the motivation for developing SnV-based photonic chips. We then outline the key challenges that remain for realizing such chips. Finally, we examine the obstacles associated with extending quantum networks to large distances.

7.2. SCALING QUANTUM LINKS

An important figure of merit for scaling up quantum internet demonstrations is the link efficiency, defined as $\eta_{\text{link}} = r_{\text{entanglement}}/r_{\text{decoherence}}$, which describes the ratio between the rate at which entanglement can be generated over the rate at which it decoheres. A link efficiency below 1 indicates that the decoherence occurs faster than entanglement can be generated. However, this does not exclude entanglement generation. The multi-node network experiment of Pompili and Hermans et al., did show that it is possible to generate two entangled links simultaneously in a probabilistic manner³. However, the implementation with a link efficiency below one comes with the price of a reduced entanglement rate and makes it infeasible to scale to more nodes in a quantum network, as the probability of having entangled links simultaneously between many nodes vanishes.

7.2.1. IMPROVING THE MEMORY

Reducing the decoherence rate directly improves the link efficiency. In the work of Beukers and Waas et al., the nuclear ^{13}C spins are controlled using the electron spin-1/2 system of the SnV center⁴. The nuclear spin is a long-lived memory that enhances the functionality of the electron spin^{3,5-7}. A requirement is maintaining the electron spin coherence during electron-nuclear gate operations⁸. Two commonly used techniques to extend the electron spin coherence to perform electron-nuclear gates are dynamical decoupling (DD)⁹ and dynamically decoupled radio frequency (DDRF) control¹⁰. The selectivity of the control methods depends on the magnitude of the electron spin, which is lower for the SnV center compared to the NV center. Beukers and Waas et al. demonstrate that the DDRF control method provides improved selectivity over the DD technique for spin-1/2 systems. In their work, the electron-nuclear gate fidelity is limited by the electron coherence, which is attributed to the presence of an electron spin bath. These unwanted interactions may originate from crystal imperfections, which could be reduced during the fabrication.

Controlling the nuclear ^{13}C spin requires microwave pulses on the electron spin, which may cause heating of the diamond sample. The cooling power of the cryostat limits both the number of pulses and the repetition rate of the pulses on different

electron spins of SnV centers. To address this, advances are needed to efficiently drive the electron spin with minimal power dissipation, such as using superconducting coplanar waveguides¹¹.

7.2.2. IMPROVING THE ENTANGLEMENT RATE

The work in this thesis focuses on improving the entanglement rate $r_{\text{entanglement}}$ via various mechanisms. In Chap. 3, a novel fabrication method for realizing thin diamond microdevices for open microcavity applications is introduced. This approach enhances the photon extraction rate both by increasing the emission rate through Purcell enhancement and by efficient collection of the emitted photons.

The detection efficiency of a coherent photon from a SnV center coupled to a microcavity using the diamond devices is defined as the product of the emission into the cavity mode, β_{cavity} and the outcoupling efficiency, η_{out} , which is determined to be 51% (Chap. 3). The emission into the cavity mode β_{cavity} is the ratio between the cavity-enhanced emission, C , compared to the total emission $(C + 1)$ ¹². The cavity-enhanced emission for an optimally positioned and coupled SnV center to the cavity is defined by the Purcell factor, F_p^{ZPL} , which is $F_p^{\text{ZPL}} = 39$, times the Debye-Waller factor, quantum efficiency, and orbital branching ratio. These emitter properties result in a factor of 0.36¹³. This results in a cooperativity, $C = 39 \times 0.36 = 14$. Therefore, the total probability of extracting a resonant, cavity outcoupled photon from the SnV center, $\eta_{\text{photon}} = \eta_{\text{out}} \times \frac{C}{C+1} = 0.51 \times \frac{14}{15} = 0.48$.

For comparison, the collectable photon probability from a SnV center in a solid immersion lens (SIL) is given by the emitter photon probability (0.36) multiplied by a typical collection efficiency (0.1)¹⁴, resulting in 0.036. Thus, the microcavity combined with the devices of Chap. 3 would result in a more than ten times higher photon detection efficiency.

In Chap. 4 we present a heralded initialization scheme to prepare the SnV center in the negatively charge state and allows probing of its optical resonance. This initialization scheme can be used for other solid-state optically active qubit platforms and has been widely used for NV experiments^{3,15,16}, and first silicon-carbide experiments¹⁷. The method avoids post-processing and mitigates spectral diffusion, which increases the duty cycle of experiments. Characterization of the optimal probe and off-resonant pulse conditions also provides insight into the spectral and charge dynamics of the system.

Future improvements to the entanglement rate could come from further enhancing photon extraction and using other methods for enhancing the ZPL photon emission rate, for example, by using photonic crystal cavities. In the next sections, we discuss methods to realize a large number of SnV center-based qubits on a single quantum node. These next steps will involve SnV centers embedded in nanophotonic structures. A key challenge ahead is the deterministic placement of SnV centers at desired positions within nanophotonic structures.

7.3. SNV-BASED PHOTONICS CHIP

7.3.1. DETERMINISTIC PLACEMENT OF SNV CENTERS

To complement advances in spectral stability of the SnV center and material purity, a crucial step toward scalable integration is the deterministic creation of SnV centers with high spatial precision. The current low conversion yield from tin to SnV centers makes advances in deterministic creation essential for scalable integration into nanophotonic devices. For an optimal coupling of the SnV to the cavity or waveguide mode, SnV centers must be placed within specific spatial regions. Several techniques offer varying levels of precision for the 3D placement of SnV centers within diamond.

One approach involves implanting Sn atoms into diamonds patterned with reference markers. After color center formation, the emitters are identified and characterized. The device pattern designs are aligned accordingly to the pre-characterized SnV centers. While effective, this method is time-consuming and limited by localization accuracy relative to the markers. To ensure single Sn-ion occupancy per device, the ion implantation dose can be reduced such that, statistically, only one Sn-ion is implanted per device.

Single SnV creation at specific locations can be achieved by masking the diamond, e.g., with electron beam resist and defining nanoscale apertures^{18,19}. Other strategies include implantation through apertures in an atomic force microscope (AFM) tip^{20,21}, or focused ion beam (FIB) implantation for targeted positioning. Recently, Cheng et al. showed site-controlled ion implantation followed by local femtosecond laser annealing with in-situ spectral monitoring, where they realized featuring 50 nm resolution and believe it is possible to bring it down to 20 nm²².

However, two main challenges remain:

- **Implantation stochasticity:** Due to the Poissonian distribution of the number of Sn ions implanted, it is not guaranteed that a single ion will be implanted and convert to a color center. This can be addressed by detecting secondary electrons upon ion impact or using systems that pre-select and deliver single ions, such as ion traps with laser cooling^{23,24}. These methods offer high-fidelity single-ion implantation but require significant technical overhead.
- **Straggle:** Collisions between implanted ions and crystal lattice atoms cause deviation from the intended trajectory. Straggle increases with implantation energy, so low-energy implantation is preferred, albeit at the cost of reduced depth²⁵. Heavier ions, such as tin, experience less straggle than lighter ones.

To minimize straggle while maintaining good optical properties, incorporation during CVD growth has been used for NV, SiV, and GeV centers. These centers tend to exhibit narrower linewidths and better stability when formed in situ. While SnV formation during growth has not yet been reported, it remains an avenue of interest. In terms of lateral placement, targeted laser-based techniques can localize defect formation. For example, high-power laser pulses can generate vacancies at a defined spot, followed by

low-power annealing pulses to form color centers^{26,27}.

A variety of techniques exist for the creation and positioning of SnV centers in diamond, each offering different advantages in terms of yield, spatial precision, and scalability. Full three-dimensional control over SnV placement will likely require a combination of methods, such as low-energy implantation, precision masking, targeted annealing, or CVD diamond overgrowth. The optimal approach depends not only on the desired device architecture but also on the available fabrication tools and capabilities.

7.3.2. DIAMOND NANOPHOTONICS FABRICATION

Besides creating SnV centers at the optimal location with the desired environment, for scaling to a large number of qubits per chip, diamond must be shaped into a nanophotonic structure. This allows for on-chip routing, improves spin-photon interfaces, and collection efficiencies.

The field of diamond nanophotonic fabrication is a fast-moving field²⁸⁻³⁰. Current fabrication methods for bulk diamond often rely on techniques such as angled plasma etching or quasi-isotropic undercut etching, as presented in Chap. 5. While effective for certain geometries, these approaches impose limitations on device design. Etch rates can vary with geometry, for example, narrower structures etch faster than wider ones in quasi-isotropic undercut processes, leading to inhomogeneous diamond thicknesses across a device. Furthermore, compatibility with other fabrication steps is limited: metal layers, for instance, must be avoided before etching to prevent cross-contamination in the diamond etching chambers. These constraints restrict the flexibility of the overall device architecture. Despite the challenges, the fabrication of diamond suspended waveguides^{31,32}, photonic crystal cavities³³, and phononic crystal cavities³⁴ has been realized using the quasi-isotropic undercut method.

7.3.3. HYBRID INTEGRATION

Other approaches to realize large photonic quantum chips are by combining different fabricated chips instead of fabricating the whole chip out of a diamond substrate. Photonic integrated circuits (PICs) are emerging as a key platform for scaling quantum systems toward many-qubit architectures. PICs offer a wide range of low-loss on-chip components, including waveguides, filters, modulators, detectors, lasers, and optical switches³⁵⁻³⁹. Over the past decade, significant investment from foundries has driven improvements in manufacturability, reproducibility, and component complexity⁴⁰. Moreover, PIC platforms can incorporate nonlinear materials for on-chip frequency conversion^{41,42}, as well as metal layers for electrical signaling and qubit control and on-chip photon detection^{43,44}.

By hybridizing high-quality diamond nanophotonic devices, such as waveguides or photonic crystal cavities, with advanced PICs, it becomes possible to combine the strengths of both platforms: the quantum properties of diamond with the scalability and comprehensiveness of silicon photonics.

However, fabricating thin diamond films (~200 nm) for efficient optical mode confinement remains challenging. The technique presented in Chap. 3, based on laser writing and subsequent isotropic plasma etching, suffers from inhomogeneous etch rates that produce wedge-shaped plates with varying thicknesses, limiting device uniformity. However, it has been shown that better uniformity is possible⁴⁵.

Recent progress has been made using smart-cut techniques in combination with diamond overgrowth to fabricate thin diamond films with low surface roughness^{46–48}. The smart-cut technique realized diamond thin-films of a thickness of 10 nm which can be bonded to a variety of substrates⁴⁹. This technique relies on the helium ion implantation, which creates a damage layer at a very confined depth. This damage layer can be electrochemically etched away, resulting in thin, high-quality suspended diamond plates. Although technically demanding and requiring various fabrication steps, this method has enabled the creation of 2D photonic crystal cavities in diamond with a high quality factor, which cannot be realized with angled or quasi-isotropic etching techniques⁵⁰. Despite its promise, further development is needed to make this technique scalable for large-scale device fabrication.

Integration of diamond devices with PICs can be achieved through transfer printing⁵¹ or pick-and-place techniques^{52,53}. In transfer printing, a flexible stamp is used to transfer diamond components onto the PIC. In pick-and-place, a microneedle positions individual diamond devices. Although both techniques are currently labor-intensive, they offer the advantage of pre-characterizing SnV centers in the diamond devices before integration, which greatly increases the yield and performance of the final photonic system.

7.3.4. PHOTONIC PACKAGING

For quantum communication in a longer-distance quantum network, the photons entangled with the spin systems need to be routed off-chip. Several techniques can be used to achieve this. A commonly used technique is to route the photons off-chip using tapered fibers. This technique was also used in Chap. 6, and the chip design of the diamond devices used in Chap. 5 also has tapered waveguides for the possibility of efficiently routing the light off-chip using tapered fibers. Coupling efficiencies of >90% can be achieved^{54,55}. However, tapered fibers are challenging to fabricate and are mechanically fragile. Nanopositioners are typically required to align the tapered fiber with the diamond device.

An alternative, and more scalable, technique involves using fiber arrays in combination with grating couplers. However, this technique typically results in a bit lower coupling efficiency than using tapered fibers. Moreover, precise alignment of the fiber array to the chip necessitates multiple degrees of freedom by nanopositioners inside the fridge.

Another potential approach is to permanently attach tapered fibers to the diamond

devices using adhesive bonding. This would enable light extraction from multiple SnV qubits on the same chip. However, this technique is still in its early stages and requires further development to become reliable for integration into diamond-based devices.

Promising progress has been made in fabricating centimeter-scale, low-loss suspended waveguides⁵⁶. These structures offer the possibility of photonic interconnection between spatially separated chips, potentially operating at different temperature stages. These photonic “ribbons” could serve as the photonic analog of electrical wirebonding, allowing for modular and flexible interconnection of independently fabricated components.

7.4. OTHER PLATFORMS

While this thesis focuses on SnV and NV centers in diamond, several other solid-state systems are emerging as candidates for scalable quantum networks. For instance, spins in silicon-based materials are attractive due to their compatibility with the current mature silicon fabrication techniques. Color centers in silicon and silicon carbide have been shown to be promising^{17,57–61}. Recently, entanglement between two T-centers in silicon has been demonstrated, highlighting the potential of this platform⁶².

Furthermore, rare-earth ion-based emitters in various host materials have demonstrated the capabilities required for quantum networking by multiplexed entanglement of remote ion pairs in nanophotonic crystal cavities has led to improved entanglement distribution rates^{63,64}.

7.5. GOING THE DISTANCE

Distributing entanglement over long distances requires a low-loss medium for photon transmission. There are two approaches to realizing a long-distance optical link: a free-space optical link or the transmission of light via fiber. The emission of diamond color centers is outside of the telecom band, and thus relies on frequency conversion to reduce the photon loss in long optical fibers. The conversion demonstrated in Chap. 6 significantly improves the transmission probability of a flying qubit photon to arrive at an end station at large distances. The loss over long distances is improved from about 10 db/km at 619 nm to about 0.3 db/km at 1480 nm. However, this conversion does introduce noise, mainly from pump laser-induced noise, and the conversion efficiency is less than unity, so some photon loss remains unavoidable. The added noise rate presented in Chap. 6 is comparable to the added noise due to the QFC of the work of Stolk et al., where they have demonstrated heralded entanglement over a metropolitan quantum network¹⁵, indicating that even with these added noise rates, entanglement is possible over large distances.

Another limitation is the current size of the QFC setup, which limits its scalability and integration into compact quantum devices. Future developments should focus on low-noise, high-efficiency, on-chip QFC systems. Promising results have already been shown by Wang et. al, who demonstrated on-chip conversion of visible light at 863 nm

to the telecom L-band at 1550 nm, using a 1950 nm pump laser⁶⁵.

7.6. THE QUANTUM ECO SYSTEM

Over the past decade, key experiments have demonstrated the feasibility of building a quantum internet. Translating these achievements from laboratory demonstrations to real-world deployment is a major challenge. Scaling of these systems is challenging too, as a higher performance of the qubit systems is needed. Therefore, focus on scaling and improving the performance of the qubit systems is needed.

Researchers should continue to explore and develop new techniques without being constrained by current practical limitations. Once a particular platform proves itself as a leading candidate for a future quantum internet, industry will follow. Substantial financial resources are available in this sector and will flow toward platforms that are enabled by scientific breakthroughs.

The research community should avoid making decisions based on present-day practicalities. For example, if the community comes to a consensus that the SnV center in diamond is the most viable candidate for quantum networking, industry will pick up on diamond foundries, and today's challenges, such as the complexity of diamond fabrication, will be addressed. Likewise, decisions should not be driven by convenience, such as favoring native telecom emitters. Instead, research should focus on advancing fundamental capabilities, trusting that engineering solutions will follow.

7.7. EPILOGUE

Looking back, the dream of building scalable quantum networks once felt distant and uncertain. Today, with continued advances in quantum devices, material science, and integration techniques, the building blocks are more tangible than ever. As the field moves forward, the next generation of quantum network nodes is no longer a distant vision but a rapidly approaching reality. It's an exciting time to be part of this journey!

BIBLIOGRAPHY

- [1] H. J. Kimble, *The quantum internet*, Nature **453**, 1023 (2008).
- [2] S. Wehner, D. Elkouss and R. Hanson, *Quantum internet: A vision for the road ahead*, Science **362**, 6412 (2018).
- [3] M. Pompili *et al.*, *Realization of a multinode quantum network of remote solid-state qubits*, Science **372**, 6539 (2021).
- [4] H. K. Beukers *et al.*, *Control of Solid-State Nuclear Spin Qubits Using an Electron Spin-1/2*, Phys. Rev. X **15**, 021011 (2025).
- [5] M. K. Bhaskar *et al.*, *Experimental demonstration of memory-enhanced quantum communication*, Nature **580**, 60 (2020).
- [6] M. H. Abobeih *et al.*, *Fault-tolerant operation of a logical qubit in a diamond quantum processor*, Nature **606**, 884 (2022).
- [7] S. L. N. Hermans *et al.*, *Entangling remote qubits using the single-photon protocol: an in-depth theoretical and experimental study*, New J. Phys. **25**, 013011 (2023).
- [8] T. Van Der Sar *et al.*, *Decoherence-protected quantum gates for a hybrid solid-state spin register*, Nature **484**, 82 (2012).
- [9] T. H. Taminiau *et al.*, *Detection and Control of Individual Nuclear Spins Using a Weakly Coupled Electron Spin*, Phys. Rev. Lett. **109**, 137602 (2012).
- [10] C. Bradley *et al.*, *A Ten-Qubit Solid-State Spin Register with Quantum Memory up to One Minute*, Phys. Rev. X **9**, 3 (2019).
- [11] I. Karpatzakis *et al.*, *Microwave Control of the Tin-Vacancy Spin Qubit in Diamond with a Superconducting Waveguide*, Phys. Rev. X **14**, 031036 (2024).
- [12] M. Fox, *Quantum optics: an introduction*, Oxford master series in physics No. 15 (Oxford University Press, Oxford ; New York, 2006).
- [13] Y. Herrmann *et al.*, *Coherent Coupling of a Diamond Tin-Vacancy Center to a Tunable Open Microcavity*, Phys. Rev. X **14**, 041013 (2024).
- [14] B. Hensen *et al.*, *Loophole-free Bell inequality violation using electron spins separated by 1.3 kilometres*, Nature **526**, 682 (2015).
- [15] A. J. Stolk *et al.*, *Metropolitan-scale heralded entanglement of solid-state qubits*, Science Advances **10**, 44 (2024).
- [16] M. Iuliano *et al.*, *Qubit teleportation between a memory-compatible photonic time-bin qubit and a solid-state quantum network node*, npj Quantum Inf **10**, 1 (2024).
- [17] G. L. Van De Stolpe *et al.*, *Check-probe spectroscopy of lifetime-limited emitters in bulk-grown silicon carbide*, npj Quantum Inf **11**, 31 (2025).

- [18] M. Schukraft *et al.*, *Invited Article: Precision nanoimplantation of nitrogen vacancy centers into diamond photonic crystal cavities and waveguides*, *APL Photonics* **1**, 020801 (2016).
- [19] E. van Leeuwen, *Fabrication of a Nano-Electro-Mechanical System to strain individual tin-vacancy centres in diamond*, Master's thesis, Delft University of Technology (2023).
- [20] S. Pezzagna *et al.*, *Nanoscale Engineering and Optical Addressing of Single Spins in Diamond*, *Small* **6**, 19 (2010).
- [21] T. Jung *et al.*, *Spin measurements of NV centers coupled to a photonic crystal cavity*, *APL Photonics* **4**, 120803 (2019).
- [22] X. Cheng *et al.*, *Laser activation of single group-IV colour centres in diamond*, *Nat Commun* **16**, 5124 (2025).
- [23] W. Schnitzler *et al.*, *Deterministic Ultracold Ion Source Targeting the Heisenberg Limit*, *Phys. Rev. Lett.* **102**, 070501 (2009).
- [24] K. Groot-Berning, G. Jacob, C. Osterkamp, F. Jelezko and F. Schmidt-Kaler, *Fabrication of $^{15}\text{N}^-$ NV centers in diamond using a deterministic single ion implanter*, *New J. Phys.* **23**, 063067 (2021).
- [25] A. E. Rugar *et al.*, *Generation of Tin-Vacancy Centers in Diamond via Shallow Ion Implantation and Subsequent Diamond Overgrowth*, *Nano Lett.* **20**, 3 (2020).
- [26] C. A. McLellan *et al.*, *Patterned Formation of Highly Coherent Nitrogen-Vacancy Centers Using a Focused Electron Irradiation Technique*, *Nano Lett.* **16**, 4 (2016).
- [27] Y.-C. Chen *et al.*, *Laser writing of individual nitrogen-vacancy defects in diamond with near-unity yield*, *Optica* **6**, 5 (2019).
- [28] S. Mi, M. Kiss, T. Graziosi and N. Quack, *Integrated photonic devices in single crystal diamond*, *J. Phys. Photonics* **2**, 042001 (2020).
- [29] C. Bradac, W. Gao, J. Forneris, M. E. Trusheim and I. Aharonovich, *Quantum nanophotonics with group IV defects in diamond*, *Nat. Commun.* **10**, 5625 (2019).
- [30] A. H. Piracha *et al.*, *Scalable Fabrication of Integrated Nanophotonic Circuits on Arrays of Thin Single Crystal Diamond Membrane Windows*, *Nano Lett.* **16**, 5 (2016).
- [31] M. Pasini *et al.*, *Nonlinear Quantum Photonics with a Tin-Vacancy Center Coupled to a One-Dimensional Diamond Waveguide*, *Phys. Rev. Lett.* **133**, 023603 (2024).
- [32] J. Arjona Martínez *et al.*, *Photonic Indistinguishability of the Tin-Vacancy Center in Nanostructured Diamond*, *Phys. Rev. Lett.* **129**, 17 (2022).
- [33] A. E. Rugar *et al.*, *Quantum Photonic Interface for Tin-Vacancy Centers in Diamond*, *Phys. Rev. X* **11**, 031021 (2021).

- [34] K. Kuruma *et al.*, *Controlling interactions between high-frequency phonons and single quantum systems using phononic crystals*, Nat. Phys. **21**, 77 (2025).
- [35] W. Bogaerts *et al.*, *Programmable photonic circuits*, Nature **586**, 207 (2020).
- [36] N. C. Harris *et al.*, *Linear programmable nanophotonic processors*, Optica **5**, 1623 (2018).
- [37] D. J. Blumenthal, R. Heideman, D. Geuzebroek, A. Leinse and C. Roeloffzen, *Silicon Nitride in Silicon Photonics*, Proc. IEEE **106**, 2209 (2018).
- [38] A. W. Elshaari, W. Pernice, K. Srinivasan, O. Benson and V. Zwiller, *Hybrid integrated quantum photonic circuits*, Nat. Photonics **14**, 285 (2020).
- [39] E. Pelucchi *et al.*, *The potential and global outlook of integrated photonics for quantum technologies*, Nat Rev Phys **4**, 194 (2021).
- [40] A. H. Atabaki *et al.*, *Integrating photonics with silicon nanoelectronics for the next generation of systems on a chip*, Nature **556**, 349 (2018).
- [41] D. Zhu *et al.*, *Integrated photonics on thin-film lithium niobate*, Adv. Opt. Photon. **13**, 242 (2021).
- [42] X. Guo, C.-L. Zou, H. Jung and H. X. Tang, *On-Chip Strong Coupling and Efficient Frequency Conversion between Telecom and Visible Optical Modes*, Phys. Rev. Lett. **117** (2016).
- [43] M. Schwartz *et al.*, *Fully On-Chip Single-Photon Hanbury-Brown and Twiss Experiment on a Monolithic Semiconductor–Superconductor Platform*, Nano Lett. **18**, 6892 (2018).
- [44] S. Gyger *et al.*, *Reconfigurable photonics with on-chip single-photon detectors*, Nat Commun **12** (2021).
- [45] A. Corazza *et al.*, *Homogeneous Free-Standing Nanostructures from Bulk Diamond over Millimeter Scales for Quantum Technologies*, Nano Lett. **25**, 14526 (2025).
- [46] X. Guo *et al.*, *Tunable and Transferable Diamond Membranes for Integrated Quantum Technologies*, Nano Lett. **21**, 24 (2021).
- [47] A. P. Magyar *et al.*, *Fabrication of thin, luminescent, single-crystal diamond membranes*, Appl. Phys. Lett. **99**, 081913 (2011).
- [48] I. Aharonovich *et al.*, *Homoepitaxial Growth of Single Crystal Diamond Membranes for Quantum Information Processing*, Advanced Materials **24** (2012).
- [49] X. Guo *et al.*, *Direct-bonded diamond membranes for heterogeneous quantum and electronic technologies*, Nat Commun **15**, 8788 (2024).
- [50] S. W. Ding *et al.*, *High-Q cavity interface for color centers in thin film diamond*, Nat Commun **15**, 6358 (2024).

- [51] L. Li *et al.*, *Heterogeneous integration of spin–photon interfaces with a CMOS platform*, *Nature* **630**, 70 (2024).
- [52] N. Lettner *et al.*, *Controlling All Degrees of Freedom of the Optical Coupling in Hybrid Quantum Photonics*, *ACS Photonics* **11**, 696 (2024).
- [53] D. Riedel *et al.*, *Efficient Photonic Integration of Diamond Color Centers and Thin-Film Lithium Niobate*, *ACS Photonics* **10**, 4236 (2023).
- [54] M. J. Burek *et al.*, *Fiber-Coupled Diamond Quantum Nanophotonic Interface*, *Phys. Rev. Appl.* **8**, 024026 (2017).
- [55] B. Zeng *et al.*, *Cryogenic packaging of nanophotonic devices with a low coupling loss <1 dB*, *Applied Physics Letters* **123**, 161106 (2023).
- [56] G. Clark *et al.*, *Scalable integration and control of diamond color centers in a piezoelectric photonic platform*, in *Quantum 2.0* (Optica Publishing Group, 2025) pp. QTu4B–2.
- [57] A. DeAbreu *et al.*, *Waveguide-integrated silicon T centres*, *Opt. Express*, *OE* **31**, 15045 (2023).
- [58] D. B. Higginbottom *et al.*, *Optical observation of single spins in silicon*, *Nature* **607**, 266 (2022).
- [59] Y. Baron *et al.*, *Detection of Single W-Centers in Silicon*, *ACS Photonics* **9**, 2337 (2022).
- [60] W. Redjem *et al.*, *Single artificial atoms in silicon emitting at telecom wavelengths*, *Nat Electron* **3**, 738 (2020).
- [61] C. Babin *et al.*, *Fabrication and nanophotonic waveguide integration of silicon carbide colour centres with preserved spin-optical coherence*, *Nat. Mater.* **21**, 67 (2022).
- [62] F. Afzal *et al.*, *Distributed Quantum Computing in Silicon*, (2024), arXiv:2406.01704.
- [63] A. Ruskuc *et al.*, *Multiplexed entanglement of multi-emitter quantum network nodes*, *Nature* **639**, 54 (2025).
- [64] J. M. Kindem *et al.*, *Control and single-shot readout of an ion embedded in a nanophotonic cavity*, *Nature* **580**, 201 (2020).
- [65] X. Wang *et al.*, *Quantum frequency conversion and single-photon detection with lithium niobate nanophotonic chips*, *npj Quantum Inf* **9**, 38 (2023).

ACKNOWLEDGEMENTS

Ik kan het niet alleen
- De Dijk

This thesis is the result of so many people being part of my life in various ways. Each one of you played a part, changed the way I felt and thought. And all of you being in my life, therefore, contributed to the work presented in this thesis. The wonderful thesis cover designed by **Studio Angelineau** depicts that the data of this work is literally created by all of you. Thank you **Jord**, for this amazing work. This is the part of the thesis where I get to thank all of you and share my personal thoughts on this journey.

Ronald, I want to thank you for all the freedom you have given me. The hands-off approach and perfect amount of steering at the right moment gave me the confidence and faith that allowed me to grow as a scientist. You were always there to listen and guide, without any judgment, creating a very safe space. Your flexibility regarding working remotely during the time I needed to be with my family was greatly appreciated. I wish you all the best with the new combo of being a professor and CEO. **Alexander**, you are the initiator of this PhD journey. Your enthusiasm for teaching the course "Introduction to quantum mechanics" in the bachelor's sparked my interest in quantum mechanics, but the time during my bachelor's and master's thesis in your group made me (unexpectedly) realize that a PhD was what I wanted. You and your group have had a massive impact on this, and I am very grateful for this. Thank you for being part of the committee; it is very special to me. **Tim**, thank you for being my co-promotor. Your group has been a large influence on my daily life at QuTech, both in technical discussions as well as all the fun we had. Thank you, my former (almost) neighbor **Lieven**, for taking the time to be part of this committee. I do not think there are many PhD candidates who can say that they sang karaoke with their committee member. Thank you for contributing to this great atmosphere at QuTech and for being part of this special day. **Miriam**, it is great to have you as part of the committee. I really appreciate the time you took to get to know each other in the preparation for the defense. It comforted me a lot, and I am sure that you have the same effect on many others in the Applied Physics program. **Ralf**, thank you for taking the time to travel to Delft and being part of the committee.

Hans Bartling, you have been there for the whole PhD journey, starting by recommending Team Diamond for a PhD, to being part of this special day. You know me as a physics colleague and as a friend. You know all the struggles, and you have comforted me many times. It was fantastic to have a friend who knows the ins and outs. Thank you

for always being there for me and all the great conversations we have had. Your humor, goodbye my lover-singer skills, passion for good food, and amazing music taste need to be continued to be shared. All the concerts and festivals we have been to, I'm so glad we got to experience this together.

Yanik, you are the diamond of the team. Your humor is fantastic, and your passion for particular things is legendary. You have been a big driving force in many social activities, which have contributed a lot to the social environment. If quantum network nodes could be jealous, they would all be jealous of your memory capabilities; it is extremely impressive. I hope you never lose your passion for Spaghetti Eis and Mocha coffee. Thank you for introducing me to R&AB, Mr. McGovern, Weihnachtsmarkts, the tropical Germany, Fulda, Red Roofs (although I am happy I came out there alive), and the global Team Diamond sticker community! I will never forget all the fun trips we made! And if I do, I know I can count on you!

Supervising master's students during their final year project has meant a lot to me. I am thankful for the trust that they had that together we could learn from each other. The time spent with all four of you was special, and I have learned a lot from all of you. **Colin**, you were the brave first. Your skills in the cleanroom and in the lab were, luckily, better than your spatial orientation. Your ambition for everything in life was clear from the beginning, and I really enjoyed going to Makkum and seeing the one and only *Roy Bianco & Die Abbrunzati Boys*. Good luck in Stuggi! **Elvis**, your critical view and passion were present from day one, whether it was cleanroom safety or fermenting food or bouldering. I really enjoyed working together, exploring the fabrication process of completely new devices. It was very brave to start this project with us. Quantware is lucky to have you on board! Thank you for jumping into the deep together! **Leo**, you Hanson lab fan boy. I am happy you did not listen to me when I advised you not to do a Master's project in the Hanson lab, but instead explore other labs, hoping you would return for a PhD in the group. I will never ever forget the emotional first time we measured strain tuning. Your enthusiasm and appreciation for the physics wonders are contagious. Your loyalty to the group is endless, and your fab is fabulous. **Miguel**, we had a blast fighting the cavity lock and searching for converted light. Thank you for encouraging me to explore vegan food and making me realize that there is very much wrong with the bio-industry; the vegan chocolate croissants from the Spar were my favorite reflection walk snack!

I want to thank everyone that have (had) their office in the F007. We have shared our measurement ups and downs, and it was a great safe place where we could rant freely about our day. Thank you to all the members of the full house, kwartet, three musketeers, and quad squad. May we never forget to wish each other "Happy Friday, Big Guy!".

Nic, my dear friend, thank you for all our conversations about life, pairs, your love for London, lab struggles, the future, during our (almost) daily Spar sessions for lunch, drinking GTs, or going for a beer. Playing in the band together was a blast, and I am

honored that I have made it to the selective list of people in your phone contacts. You were always there for me, and knowing that was a great comfort.

I want to thank the whole SnV-team, we made such great progress over the last years, starting from our first SnV samples to realizing quantum nodes with endless possibilities (and their challenges). The one who taught me all the ins and outs of a quantum optics lab is the most calm Italian you will ever meet: **Lorenzo**. You were a great teacher, and I had a blast working with you and learning from you. I hope Grenoble is treating you well with plenty of skiing! **Nina**, our fab queen! Your passion and determination are inspiring. I really enjoyed going to conferences around the world together; they are one of my favorite memories of this journey! Still can't believe we actually went to Hawaii. Thank you for teaching me all the fab magic! **Tim**, Buuurlin boy, thank you for being a patient listener and a truly honest and kind person. I enjoyed working with you on the QFC project, although driving the laser to Aachen was quite stressful. I know with you on board, anything is possible in VLT2. **Dani**, our energy bomb, always in for a little dance in the lab, I am so happy you joined the team as a cavity enthusiast. San Fran 2025 road trip together with **Alex** was amazing! I really enjoyed all our conversations and discussions. Next trip, I will make sure my hiking skills are on par with your pro-level. So glad will still have all the amazing pictures of Alex. I am happy I got to know the two of you so much better during that trip. **Hans Beukers**, your passion for discussing and never-ending energy were of great importance to the team. I was happy to be sitting across from you in the office, having an expert available at all times. The sailing trip you organized was the best group outing we could have had. I am sure you will continue to achieve amazing things. **Matteo Jr.**, I really enjoy playing in the band with you, and a scroppino will always be the best dessert. I hope they can also make them in Barcelona. **Christopher**, your dedication to the team and the project is extremely admirable. Anything can be done with you in the lab. I am curious to see what is next for you! **Niv**, I find it very brave that you, as a resident of Theory Land, moved to the Experimental Land. Your happiness and bright smile light up every meeting. Thank you for teaching me everything about cavity-based entanglement schemes. **Timo**, our latest addition to the team and to the office, you are a remarkably talented and skilled physicist. I can't wait to see what will come out of VLT1 with you joining the F-14 team. **Jan**, although not working officially for Ronald, I do think you belong in this part of the acknowledgment! You never run out of energy and enthusiasm, whether it is about fiber arrays, photonic chips, hiking, qube-lunch, or ultimate frisbee, nothing will stop you. Thank you for being so active in organizing all social events; they are always a lot of fun. The power kiting was amazing! I also really enjoyed the hiking in Heimbach! I'm glad you and Sjoerd took over LT5. My precious lab is in great hands with the two of you in charge!

Although not working (primarily) on SnV centers, the rest of the Hanson lab has also been of great importance in my life. **Christian**, you are the brave tamer of the defects in the Silicon-zoo, which is a very promising adventure. I have a lot of respect for your determination and motivation for making this happen. If anyone can do it, it is you. In addition, this makes you the record holder for the fastest sample swap. I've really enjoyed sharing the office, discussing politics, stock markets, and other random

things. **Julius**, together we got to bond over supervising Colin, which kick-started many of the trips we have made together. Thank you for showing me all the German culture. I am really happy that together we are responsible for helping Yanik with his big day! **Mariagrazia**, it is super impressive to see what you have achieved during your PhD. Your dedication to making these experiments happen deserves a lot of respect, and I am excited to see where you will continue making a big impact!

Although not currently present in the Hanson lab anymore, but for sure, those who deserve a spot in this section are the NV alumni, who either taught me a lot and/or were a lot of fun to be around. **Max**, the legend and expert on many, many topics, whether it is cavities (micro and nano-size), fabrication, optics, you name it, and you were the one to go to. But also for advice on how to deal with situations during the PhD journey, I gained a lot from your advice, for which I am thankful to you. **Kian**, I mean Kiiiiiiiiiiiiiiiieggjaan, I really enjoyed the road trip we did together, and your enthusiasm and happy vibes light up every day! **Marie-Christine**, the patience and kindness with which you can explain difficult physics is admirable. And I will never ever forget your EPIC wedding in Vienna. I am so grateful that we could be part of it. **Alejandro**, my forever second favorite post-doc, without ever announcing who my favorite is. I do not know where to start; your iconic lunch habits, ninja-style walking through the lab, and jump scaring me many times, the sunglasses, and your lab safety violations, Coolio's imitation, all of the Spanish cursing, and lastly the World Cup Cup. We have had so many iconic conversations in B-07. Thank you for making it so much fun to work with you! **Matteo Sr.**, it was so great to watch from the sideline all the amazing projects you have completed and now hearing about all the cool things you do at IonQ! **Arian**, the encyclopedia of the Hanson Lab, you were always there to help in the lab and to give mental support when needed. Your advice on future steps is very valuable. I also really enjoy our discussions, although we might not agree on everything, you ensure that all discussions happen in a respectful way, essential for them to happen. Thank you for introducing me to all your techno. I enjoyed going to the shows and meeting the famous Vinkeveen Boys. I know you will achieve great things in Singapore, and I wish you and Vincy all the best. **Sophie**, your passion and drive for research are impressive. I really enjoyed having you around at the start of my PhD, and to have an overlap at the end is amazing. Thank you for all our conversations about science and future steps. You have been very inspiring to me. Anyone who gets to work in your group can count themselves as a very lucky person, and I am so curious to see what will come out of the lab, with you leading it; only great things can happen!

Thank you to all the former master's students who have been in the group. It was always a lot of fun, chilling with you in the master's room, learning from each other, and having great lunch discussions. Thank you **Stijn** for being the best fiber whisperer, for your amazing BBQ skills, and for sharing the best carnival experience. It was fantastic! **Pepijn**, I had a blast working with you on LTFiber, your laugh and vibe are contagious. **Caroline** is always down for a conversation about anything! It is great to see that you have joined DelftNetworks, continuing with your passion for cleanroom work. Thank you for never getting mad for singing your name like it is sung in songs. Thank you:

Alexandre, Constantijn, Cees, Joan, Sezer, Sarel, Otmar, Lisa, Laurens, Annick, Jonas, Leanne, Mark, Bram, Zarije, Adria, Valentino, Sara, Rana, Charlotte, Thomas, Tijmen.

Team Diamond(+), consists of more than just Hanson Lab members. I have experienced the interaction with the rest of the community in Delft, not only very valuable science and technology-wise, but also a lot of fun. The famous TimTams were a big part of the fun vibes at QuTech. Starting with thanking the former post-docs. **Damian**, it was great sharing the office with you and discussing random quantum theory, you were always down to dive deep into a topic! **Benjamin P.**, your name very often pops up on the author list of interesting papers. It was an honor to have you work with us in Delft. I will not forget the great road trip we went on, and your lifehack skills on how to get down a slippery, snowy road! **Anta**, your happiness shines very bright and far. Your enthusiasm and motivation are contagious; it was a joy to have you around. Thanks to you, describing an unstable emitter will forever be la-la-la. I hope one day you will understand the beauty of a cheese sandwich for lunch. **Dr. Bradley (Cooper)**, aka **Conor on the dancefloor**, it is great to have you back in Delft. The calmness and friendliness with which you can describe something is on another level. I really enjoyed discussing random things with you.

Guido, holder of the record of speedwalking in the hallway, I had a lot of fun learning the basics of Quantum Information with you, driving with you from Bad Honnef (glad I survived after all your stories), going on a road trip, and of course, cycling through San Francisco last summer. That scooter of yours is really scary, but you seem to handle it very well! Your passion, knowledge, and enthusiasm for physics are huge, and it all pays off very well! Thank you for revealing Sjoerd's secrets to me in your acknowledgement, the best joke of the PhD that I fell for. Speaking of **Sjoerd**, thank you for aaalllll the fun we had. Cleaning out LT5 was a party, going on a road trip with you was amazing, you are always in for a nice activity, and always ready to help people out when you can. You are always curious to learn new things, and you are not scared to ask questions. I will never forget Bad Honnef for the 527 different ways of announcing that "Sjörd Lön" from the online audience has a question. Thank you for all the fun we had; without you, I would have laughed quite a bit less over the last four years! Delft Networks is really lucky to have you on board!

To all the current members of the TimTams, thank you for all the great lunch conversations, random optics and physics discussions in the hallway. **Jiwon**, fending machines are not the same after your GST presentations. Thank you for all the tips about where to go in South Korea. **Dan**, I really enjoyed our discussions over lunch. We have not always agreed on everything, but that never stopped us from being open to seeing where the other person comes from. I really value this! **Gerben**, it is very impressive to see at what speed you kick-started the SiC fab. The amazing cavities that are coming out of the cleanroom are amazing. You are always fun to be around! I love your dry way of presenting! **Laurens**, you are always busy, getting yourself involved in solving lab challenges or helping with art exhibitions, teacher projects, etc, etc. In addition to your passion, you also always have an eye open to check in with your

colleagues to see how they are doing. I really appreciate that! **Tobi**, it is so great to share the office with you! I love sharing music with you and being hyped about going to concerts or shows! The best work breaks are going to the massage chairs with you! Your ambition and dedication to bring the SiC project to the next level are real! Remember that it is a marathon, not a sprint! **Benjamin v. O.**, your coding skills are magic, and the speed at which you can solve a physics challenge is impressive. You will do great things! I am still hoping for the day I get invited to chill with the climbing crew without having to climb. Speaking of climbing, **Margriet**, it is great to see how passionate you have gotten about climbing. I really enjoyed all our discussions, and I really find it cool how you always have interesting questions ready when people give talks! Thank you for showing us around in the world of GST! **Madhu**, while we have not had that much overlap, I always see you around with a big content smile. I know you will do great things during your PhD! **Christina**, it was a lot of fun going for runs with you! Especially the Dam tot Damloop, although the pictures suggest something else. Also, I really enjoyed going to the DPG with you! **Jasper aka Kevin**, thank you for all the tips about what to do in Singapore. Thank you for not getting mad for calling you by the wrong name. You always have a lot of energy, and your dedication to the SiC project is very present!

Fabian, thank you for introducing me to the world of QFC. It was fantastic working with you on this project. Your knowledge of the setup and the process is very impressive. I am very happy that all our hard work has paid off! I wish you many, many happy (accident-free) bike rides! Thank you, **Sal**, for all the fun discussions we have had, and I am very curious about all the cool things your group will do!

Without the amazing support team, the research we be nowhere! Some of the 10 and 3 o'clock coffee drinkers have given me a rough time, but I know it was just a sign of love. I knew that I could count on you no matter what. There were the wirebonding experiments with **Jason**, disassembling and assembling of LT5 with **Olaf**, magical voltage amplifiers from the electronic wizards (**Raymond, Raymond, Berend**) and discussing VLT1 purchasing with **Roy**, EVERY morning a happy **Vinod** wishing me a good morning making everyone feel a bit better and happier, **Nico** always down for a good conversation and making sure all custom pieces of the fridge were perfect, **Siebe** and **Jelle** always ready to help with all the random requests of the lab. **Hitham**, your door was always open to hear about how we thought we could improve the safety in the lab. Your happy and kind energy is making this environment intrinsically safe. Thank you for sharing so much about the Egyptian culture. I have learned so much from this. **Regis**, I need to apologize for complaining so much to you about having to fill out another form. I understand that you didn't like our high-power IR free-space laser in a cavity. But together we made it work, and I want to thank you for your patience and dedication to this very important job!

Sara helped me out many times, whether it was making sure our precious diamonds were shipped across the ocean, booking rooms, handling finances, and much more. I knew I could count on you. This made our work so much easier. Thank you for doing such a fantastic job helping us out. Thank you, **Shannon**, for your happy vibes and all

the events you have organized. I wish you all the best with your new adventure!

Eugene, you were an absolute legend in the cleanroom. Since you have left, I have not been in the cleanroom, as I can't seem to realize that you have actually retired and other people are taking over your role. Thank you for helping out with all the tri-acid set-ups while discussing all your favorite beers. I hope you are enjoying your very well-deserved retirement. I also need to thank all the other members of the cleanroom staff who have trained me on many machines and given me advice on fabrication processes. Thank you **Charles, Pauline, Roald, Bas, Marc, Arnold, Hozanna, Lodi, Esther**. Thank you **Zahra** for all the help with the cleanroom processes.

I want to thank all the members of the Q2 band that I have played with. It was always a lot of fun practicing with you and going to Pepperoncino afterwards. Your energy had me feeling good every Wednesday!! Thank you **Anne-Marije, Bart, Christina, Christopher, Colin, Conor, Desa, Floor, Guido, Gustavo, Hanifa, Hans, Laurens, Luc, Maia, Margriet, Matteo, Nic, Pablo, Sander, Timo, Tzula, Zarije!**

Thank you **Pablo** and **Ralf** for being the best neighbors and becoming good friends. I have really enjoyed all our board game nights, having great (and sometimes experimental) dinners. It was always a blast hanging out with you. I hope our paths will continue to cross.

Bram, my brother from another mother, living with you together in Spoorzicht, representing L'Angelille was amazing. All the memories we have together mean a lot to me. From uneatable cheese quiche to going to festivals, epic Christmas dinners, interactions with Pris, C-H-A-R-G-E-D, and many more memories. I love seeing you being so happy with Maebhvtvbt.

To the best BLIKsems, thank you to sweet **Laura** for being the best listener. I am so happy that with you there, anything is okay, and everything can always be discussed. Always down to go to JoVo together with **Roos**. I loved going skiing with you, and that your enthusiasm didn't end where that of others might have! **Bink**, best singer there is, that I can never get enough of. You were always ready to help out where you could, and I am sad that my body cannot handle our borrels no longer. I am so happy you, Job, and Guusje are so close by and for recommending us to the best house we might ever live in. **Tynke** your passion for everything you love is an inspiration. There is never a dull moment when you are around! I am so excited to see how your van will turn out! **Hanneke**, you were right there when the physics basis was founded. I will never forget our epic bachelor time, where we spent so much time together. Our trip to Australia was a definite highlight, and I am thankful we got to do it together. I can't wait to see your young family grow. **Aly**, thank you for always being so sweet and kind and organized! I love seeing how your house has transformed, and I can't wait for the wedding!

To the PH, I am grateful COVID happened and that I got to parasite in the PH12. The bond we formed over that period is priceless, and I will never get enough of Pro&O,

the uncontrollable laughter, dakteras borrels, loodwater, huisweekendjes, kapsalon, Aperol, everything through the mandoline, unforgettable P&M diners, your fashion, Arkie, and **Angie**. **Juul**, **Yaar**, **Jord**, and **Jord**, you mean a lot to me. Thank you for being there.

The **Vento** girls, we have been on many adventures, and you have made me laugh too much. The epic trips to Croatia, Hungary, Belgium, and the recent unforgettable Gala in Friesland. Your interest in my research, showing your support and hype, and wanting to know how the quantum internet works, means a lot to me. Each one of you has a special place in my heart. I am grateful to be a Vento for life.

To my family-in-law, you never know what you get when you start dating somebody, but you are beyond what I could have hoped for. You were always supportive and interested in this PhD journey. Your theatrical way of being able to replay parts of movies, situations, and memories is too extra, and I love it. **Hein** and **Kiek**, thank you for taking me into the family and showing me that there is no such thing as too much scrabble, and "gebergte" is the best opening word that will ever be played. **Renske**, your drawing skills are unbelievable, your way of living life to the absolute fullest is contagious, love the vibe. Never slow down. **Wouter**, I will never forget the Spiderman moment. Please never change; you are a gem of the world. Sweet **Elaine**, my partner in crime, so happy you and Wouter met, DTRH was unforgettable.

To my family, your unconditional love and support are the foundation of this thesis, for which I am forever grateful. **Mama** and **Papa**, you have set the example in life and ensured that I could grow into the person I have become. Your constant support for all decisions I have made throughout my studies and PhD, and your constant interest in what I was doing, was very comforting. Thank you for holding down the fort in Oldemarkt, **Frederique**. I'm so happy that you found what you love to do and didn't follow the path you thought you had to follow. I love coming home, getting spoiled, and cuddling with **Huub**. All the evening-long dinners and pizza parties are precious to me.

Sophie, my fellow Reigâh, I am so happy that we are so close. Thank you for all the support over the last years. Traveling the world with you is the best, and singing (screaming) along to all the classics is one of my favorite memories. I love going to parties with you and eating the best food everywhere. Keep following your heart. It's gonna be alright, it's gonna be alright, music is medicine.

Bart, you are the person who needs to be thanked the most. You are the best that has happened to me. You have supported me on a daily basis throughout this journey, being my biggest fan. You are the never-ending comedy show that I hope will never end. Without all the laughter, life would be much heavier. I love how we can discuss everything and make our big decisions in a structured Excel sheet. A home without a Home Assistant is no home. With you by my side, I am not scared to jump into the deep. Together we can do anything. You make me a better person. You make me laugh, feel happy, and very much loved. You have had by far the biggest influence on this thesis,

and I am forever thankful for that. I am so happy that I get to share life with you, as it is so good with you in it, and I am excited to see what it will bring us. Totdat het niet meer leuk is en dan nog even.

LIST OF PUBLICATIONS

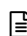
JOURNAL ARTICLES

9. *Quantum Frequency Conversion of Single Photons from a Tin-Vacancy Center in Diamond*,
J. M. Brevoord*, J. F. Geus*, T. Turan, M. Guerrero Romero, D. Bedialauneta Rodríguez, N. Codreanu, A. M. Stramma, R. Hanson, F. Elsen, B. Jungbluth, [arXiv: 2509.01661](#), [currently under review](#),
8. *Laser-cut Patterned, Micrometer-thin Diamond Membranes with Coherent Color Centers for Open Microcavities*,
Y. Herrmann*, **J. M. Brevoord***, J. Fischer*, S. Scheijen, C. Sauerzapf, N. Codreanu, L. G. C. Wienhoven, Y. M. Q. van der Graaf, C. F. J. Wolfs, R. Méjard, M. Ruf, N. de Jong, and R. Hanson, [Materials for Quantum Technology](#), **5**, 035001, (2025),
7. *Large-range tuning and stabilization of the optical transition of diamond tin-vacancy centers by in situ strain control*,
J. M. Brevoord, L. G. C. Wienhoven, N. Codreanu, T. Ishiguro, E. van Leeuwen, M. Iuliano, L. De Santis, C. Waas, H. K. C. Beukers, T. Turan, C. Errando-Herranz, K. Kawaguchi, and R. Hanson, [Applied Physics Letters](#), **126**, 174001, (2025), [cover of journal and featured as the editor's suggestion](#),
6. *Control of Solid-State Nuclear Spin Qubits Using an Electron Spin-1/2*,
H. K. C. Beukers*, C. Waas*, M. Pasini, H. B. van Ommen, Z. Ademi, M. Iuliano, N. Codreanu, **J. M. Brevoord**, T. Turan, T. H. Taminiau, and R. Hanson, [Phys. Rev. X](#), **15**, 021011, (2025),
5. *A low-temperature tunable microcavity featuring high passive stability and microwave integration*,
Y. Herrmann*, J. Fischer*, S. Scheijen, C. F. J. Wolfs, **J. M. Brevoord**, C. Sauerzapf, L. G. C. Wienhoven, L. J. Feije, M. Eschen, M. Ruf, M. J. Weaver, and R. Hanson, [AVS Quantum Science](#), **6**, 4, (2024),
4. *Coherent coupling of a diamond tin-vacancy center to a tunable open microcavity*,
Y. Herrmann*, J. Fischer*, **J. M. Brevoord**, C. Sauerzapf, L. G. C. Wienhoven, L. J. Feije, M. Pasini, M. Eschen, M. Ruf, M. J. Weaver, and R. Hanson, [Phys. Rev. X](#), **14**, 041013, (2024),
3. *Nonlinear quantum photonics with a tin-vacancy center coupled to a one-dimensional diamond waveguide*,
M. Pasini, N. Codreanu, T. Turan, A. Riera Moral, C. F. Primavera, L. De Santis, H. K. C. Beukers, **J. M. Brevoord**, C. Waas, J. Borregaard, and R. Hanson, [Phys. Rev. Lett.](#), **133**, 023603, (2024),

2. *Heralded initialization of charge state and optical-transition frequency of diamond tin-vacancy centers*,
J. M. Brevoord*, L. De Santis*, T. Yamamoto, M. Pasini, N. Codreanu, T. Turan, H. K. C. Beukers, C. Waas, and R. Hanson, [Phys. Rev. Applied](#), **21**, 054047, (2024),
1. *Phase interference for probing topological fractional charge in a BiSbTeSe₂-based Josephson junction array*,
J. M. Brevoord, D. H. Wielens, M. Lankhorst, J. Díez-Mérida, Y. Huang, C. Li and A. Brinkman, [Nanotechnology](#) **32**, 43, (2021).

PATENTS

1. *A hybrid methodology to produce diamond membranes, using a combination of reactive ion etching and laser engraving*,
Y. Herrmann, **J. M. Brevoord**, N. de Jong, C. Sauerzapf, M. Ruf, J. Fischer, and R. Hanson, (2024).

 Included in this thesis.

* Equally contributing authors.

CURRICULUM VITAE



Julia Maria BREVOORD

May 31st, 1995, IJsselham, The Netherlands

- 2014-2017 **Bachelor of Science**, Applied Physics
University of Twente, Enschede, The Netherlands
Thesis: *"Solving the Schrödinger and Poisson equations for a LaAlO₃-SrTiO₃ interface using Comsol Multi Physics."*
Supervisor: Prof. dr. ir. Alexander Brinkman
- 2017-2021 **Master of Science**, Applied Physics
University of Twente, Enschede, The Netherlands
Thesis: *"Fractional charge of Josephson vortices in a Josephson junction array at a superconducting-topological insulator interface"*
Supervisor: Prof. dr. ir. Alexander Brinkman
- 2017-2021 **Master of Science**, Applied Mathematics
University of Twente, Enschede, The Netherlands
Thesis: *"A vehicle routing problem of electric towing trucks at airports"*
Supervisor: Prof. dr. Richard J. Boucherie
- Summer 2019 **Internship**, Quantum Walks
Hokkaido University, Sapporo, Japan
Subject: *Theoretical modeling of the physical and statistical characteristics of 2-dimensional quantum walks*
Supervisors: Prof. dr. ir. Alexander Brinkman, Prof. dr. Richard J. Boucherie and Prof. dr. Kousuke Yakubo
- 2021-2025 **Ph.D**, Applied Physics
QuTech, Delft University of Technology, Delft, The Netherlands
Thesis: *"Control of the optical interface of color centers in diamond."*
Promotors: Prof. dr. ir. Ronald Hanson and Dr. ir. Tim Taminiau.

Control of the optical interface of color centers in diamond

Julia Maria Brevoord

